

David Taylor Research Center

Bethesda, MD 20884-5000

DTRC-91/002 January 1991

Technical Conference Proceedings

Proceedings of the Sixth International Cryocoolers Conference

Plymouth, Massachusetts

October 25-26, 1990

Volume I

Edited by
Geoffrey Green and
Margaret Knox

CRYCOOLERS
6



Approved for public release; distribution is unlimited

REPORT DOCUMENTATION PAGE

Form Approved
OMB No. 0704-0188

Public reporting burden for this collection of information is estimated to average 1 hour per response, including the time for reviewing instructions, searching existing data sources, gathering and maintaining the data needed, and completing and reviewing the collection of information. Send comments regarding this burden estimate or any other aspect of this collection of information, including suggestions for reducing this burden, to Washington Headquarters Services, Directorate for Information Operations and Reports, 1215 Jefferson Davis Highway, Suite 1204, Arlington, VA 22202-4302, and to the Office of Management and Budget, Paperwork Reduction Project (0704-0188), Washington, DC 20503.

1. AGENCY USE ONLY (Leave blank)	2. REPORT DATE January 1991	3. REPORT TYPE AND DATES COVERED Conference proceedings	
4. TITLE AND SUBTITLE Proceedings of the Sixth International Cryocoolers Conference		5. FUNDING NUMBERS	
6. AUTHOR(S) Geoffrey Green and Margaret Knox, Editors		8. PERFORMING ORGANIZATION REPORT NUMBER DTRC-91/002	
7. PERFORMING ORGANIZATION NAME(S) AND ADDRESS(ES) David Taylor Research Center Annapolis, Maryland 21402-5067		10. SPONSORING / MONITORING AGENCY REPORT NUMBER	
9. SPONSORING / MONITORING AGENCY NAME(S) AND ADDRESS(ES)		11. SUPPLEMENTARY NOTES	
12a. DISTRIBUTION / AVAILABILITY STATEMENT Approved for public release; distribution is unlimited.		12b. DISTRIBUTION CODE	
13. ABSTRACT (Maximum 200 words) <p style="margin-left: 40px;">This document contains the proceedings of the Sixth International Cryocoolers Conference, held October 25-26, 1990, in Plymouth, Massachusetts. About 260 people attended, representing many government and private laboratories (both foreign and domestic) as well as numerous universities and industrial companies. Fifty-four papers were presented.</p> <p style="margin-left: 40px;">The speakers described advances in many areas of cryocooler technology, mostly in the temperature range below 80 K. Topics included advanced regenerators, pulse tube and sorption coolers, and Stirling, Joule-Thomson, magnetic, and hybrid coolers. The discussions also covered a broad range of applications and component technologies.</p>			
14. SUBJECT TERMS Cryocoolers, cryogenics, cryopumps, Gifford-McMahon coolers, helium, infrared detectors, Joule-Thomson coolers, magnetic coolers, pulse tube coolers, rare earths, refrigeration, regenerators, sorption coolers, space coolers, Stirling coolers, superconductors.		15. NUMBER OF PAGES	
17. SECURITY CLASSIFICATION OF REPORT		16. PRICE CODE	
18. SECURITY CLASSIFICATION OF THIS PAGE	19. SECURITY CLASSIFICATION OF ABSTRACT	20. LIMITATION OF ABSTRACT	

CONFERENCE COMMITTEE

Chairman

Peter J. Kerney
CTI-CRYOGENICS
Waltham, MA 02254-9171
(617) 622-5391

Program Committee

Geoffrey Green, Chairman
David Taylor Research Center
Annapolis, MD 21402-5067
(301) 267-3632

Ronald White, WRDC/FIVEA

Jill Ludwigsen, Nichols Research Corp

Walter Swift, CREARE R&D Inc.

Frank Kadl, Leybold Vacuum Products, Inc.

Local Arrangements

George Y. Robinson, Nichols Research Corp.

Advisory Board

John Barclay
Astronautics

Stephen Castles
NASA/Goddard

Gordon Davey
University of Oxford, U.K.

Alfred Johnson
Aerospace Corp.

Hiroshi Nagano
Toyama University, Japan

Ralph Longsworth
APD-Cryogenics

Martin Nisenoff
Naval Research Laboratory

Joseph L. Smith
MIT

Michael Superczynski
DTRC

Klaus Timmerhaus
University of Colorado

Paul Scheihing
DOE

William Shields
Janix Research Inc.



Dr. Howard O. McMahon

In Memoriam

The world of cryogenic engineering and small cryocooler technology was saddened by the death on August 5, 1990, of Dr. Howard O. McMahon, former President of Arthur D. Little, Inc., and a member of the Board of Directors of Helix Technology Corporation. He was 75 years old.

Dr. McMahon's pioneering efforts in the field of cryogenics made possible important contributions to the advancement of science and technology. In the late 1940's and 1950's, Dr. McMahon was responsible for developing and commercializing the Collins-ADL Helium Cryostat. The first commercial helium liquefier permitted universities and research laboratories throughout the world to conduct experiments at low temperatures and make important advances in the fields of chemistry, physics, biology, metallurgy, electronics and astronomy.

It was in the late 1950's at Arthur D. Little, Inc., that Dr. McMahon and William E. Gifford invented the Gifford-McMahon cryogenic refrigeration cycle—a unique method of reliably providing closed-cycle refrigeration at temperatures below 10 degrees kelvin. Initially, Gifford-McMahon cryogenic refrigerators were used for a variety of applications including the cooling of infrared detectors, low-noise ground-based receivers for satellite communication networks and experiments in low-temperature spectroscopy at long wavelengths.

With the birth of the microelectronics industry came the need for processing silicon wafers in clean, high-vacuum chambers. The ability to achieve ultra-clean conditions in vacuum processing chambers using Gifford-McMahon cryopumps has had a significant impact on the development of the complex high-speed, high-capacity integrated circuits of today. Subsequently, the Gifford-McMahon cryogenic refrigeration cycle became the industry standard refrigeration cycle for cryopump applications in the rapidly growing semiconductor industry.

A native of Alberta, Canada, and a naturalized citizen of the United States, Dr. McMahon received his B.A. and M.A. from the University of British Columbia in 1935 and 1937, and his Ph.D. in Physical Chemistry from the Massachusetts Institute of Technology in 1941. In 1943 he joined Arthur D. Little, Inc. and in 1964 became President, continuing as a Director until 1978.

Dr. McMahon was the author of many technical papers and held 22 patents on a wide variety of inventions. In 1979, Dr. McMahon was awarded the S.C. Collins Award in recognition of his outstanding technical contributions and dedicated service to the cryogenic community.

Dr. McMahon's inspiration and influence reached into many aspects of cryogenic engineering, especially into the advancement of small cryogenic coolers for commercial applications. In grateful recognition of his contributions, the Proceeding of the Sixth International Cryocooler Conference is dedicated Dr. Howard O. McMahon.

FOREWORD

These two volumes contain the proceedings of the Sixth International Cryocooler Conference (ICC), held in Plymouth, Massachusetts, on October 25–26, 1990. Peter J. Kenney of CTI-CRYOGENICS was the conference chairman; Geoffrey Green of the U.S. Navy's David Taylor Research Center served as program committee chairman.

The first cryocooler conference, held in 1980, was designed to stimulate interest and discussion in the scientific and engineering community about the latest developments and advances in refrigeration for cryogenic sensors and electronic systems at temperatures below 20 kelvin. Since then the ICC has been held every second year, and the topic has been expanded to include scientific and technological developments in small, closed-cycle refrigerators and components operating at temperatures up to about 80 K.

This year, close to 260 participants gathered from all over the world. They represented numerous universities, private companies, and government and commercial laboratories, both foreign and domestic.

Fifty-four papers were presented. The speakers described advances in many areas of cryocooler technology. The discussions included advanced regenerators, Gifford McMahon systems, pulse tube and sorption coolers, Stirling, Joule-Thomson, magnetic, and hybrid coolers, and a broad range of applications and component technologies.

The development of a small, compact, reliable and efficient cryocooler continues to be priority for cryogenics. We are pleased to present these proceedings, which we believe show further significant progress in the field.

—*The Editors*

ACKNOWLEDGMENTS

The Sixth International Cryocooler Conference Board would like to thank the following corporations, whose generous support contributed to the success of the 1990 Conference:

Arthur D. Little, Inc.

Creare Inc.

Cryomech, Inc.

CTI-CRYOGENICS, Division of Helix Technology Corporation

Janis Research Corporation

Lake Shore Cryotronics Inc.

Leyhold Vacuum Products Inc.

Magnavox Electro-Optical Systems

MMR Technologies Inc.

Nichols Research Corporation

CONTENTS -VOLUME I

SESSION I: APPLICATIONS

<i>Cryorefrigerator Evaluation for Future Magnetic Resonant Imaging Applications</i> , R.A. Ackermann	3
<i>4 K GM/JT Cryocooler for Cryogenic Sensors</i> , Yoon-Myung Kang, Tadashi Ogura, Satoru Uosaki, Katsumi Sakitani, Shuichi Sochi, Shuji Fujimoto, Ken-ichi Sata and Naoki Fukui	17
<i>Characterization of Miniature Stirling-Cycle Cryocoolers for Space Application</i> , R.G. Ross, Jr., D.L. Johnson and R.S. Sugimura	27
<i>The Use of Cryocooler for Computer Cooling</i> , Hsien-sheng Pei and Stephen Heng	39
<i>Performance of a Prototype, 5 Year Lifetime Stirling Cycle Refrigerator for Space Applications</i> , C. Keung, P.J. Patt, M. Starr and R. McFarlane	53

SESSION II: PULSE TUBE AND SORPTION COOLERS

<i>System Design Analysis of Pulse-Tube Cryocooler</i> , B.J. Huang, L.T. Lee and C.W. Lu	77
<i>Pulse Tube Cooler Modeling</i> , G.M. Harpole and C.K. Chan	91
<i>Activated Carbon Test Assembly</i> , Ben P.M. Halvensteijn and Ali Kashani	103
<i>Development of a High Density Activated Carbon-Carbon Composite for Cryogenic Applications</i> , Gilbert Brassell, James Lieberman and Josephine Curtis	115
<i>Reliability and Life of Sorbent Materials for Sorption Coolers</i> , G. Mon, L.C.Wen, J.J. Wu, S. Bard and A. Garnica	129

SESSION IIIA—SPACE COOLERS AND SESSION IIIB—REGENERATOR TECHNOLOGY

<i>Is the V-Groove Radiative Cooler Optimized?</i> Peter Kittel	145
<i>Long-Lifetime Stored Cryogen Systems Using Refrigerators to Reduce Parasitic Heat Input</i> , Richard A. Hopkins, Jeffrey H. Lee, Rodney L. Oonk, Chris D. Miller and Stephen J. Nieczkowski	153
<i>Effect of Void Volume in Regenerator</i> , Yoichi Matsubara and Yu Hiresaki	173
<i>Measurement of Regenerator Performance in a Pulse Tube Refrigerator</i> , Wayne Rawlins, K.D. Timmerhaus and Ray Radebaugh	183
<i>Ceramic Composite Regenerator Materials</i> , W.N. Lawless	193

CONTENTS—VOLUME I (continued)

SESSION IVA—STIRLING COOLERS I AND SESSION IVB—JOULE-THOMSON COOLERS I

<i>Stirling Cooler Optimization</i> , Gavid Gedeon	203
<i>Development of Stirling Cycle Cooler and Integration of this Cooler into a Biological Storage Freezer</i> , Russell C. Tipton	217
<i>Considerations in Using Joule-Thomson Coolers</i> , Glenn E. Bonney and Ralph C. Longworth	231
<i>Characterization of Coolants for Joule-Thomson Cryocoolers</i> , B. Maytal and S.W. Van Sciver	245
<i>Recent Developments in Clog Resistant and Demand Flow Cryostats</i> , J.W. Prentice, G. Walker and S.G. Zylstra	257

VOLUME II

SESSION V—REGENERATOR/RARE EARTH

<i>Two-Stage GM Refrigerator with Er₃Ni Regenerator for Helium Liquefaction</i> , Toru Kuriyama, Masahiko Takahashi and Hideki Nakagome	3
<i>High Efficient 4 K Refrigerator (GM Refrigerator with JT Circuit) Using Er₃Ni Regenerator</i> , Hideki Nakagome, Ryuichi Hakamada, Masahiko Takahashi and Toru Kuriyama	15
<i>Two-Stage Gifford-McMahon Cycle Cryocooler Operating at about 2 K</i> , Takashi Inaguchi, Masashi Nagao and Hideto Yoshimura	25
<i>Generation of Superfluid Helium by a Gifford-McMahon Cycle Cryocooler</i> , Masashi Nagao, Takashi Inaguchi, Hideto Yoshimura, Shirou Nakamura, Tadatoshi Yamada and Masatami Iwamoto	37

SESSION VIA: STIRLING COOLERS II AND SESSION VIB—JOULE-THOMSON COOLERS II

<i>Development of an Efficient, Bellows Driven Stirling Cycle Cryocooler</i> , Sibley C. Burnett, John R. Purcell and Carl J. Russo	51
<i>Superfluid Stirling Refrigerator: A New Method for Cooling Below 1 Kelvin</i> , V. Kotsubo and G.W. Swift	59
<i>A Linear Drive Stirling Cycle Cryocooler for EO/IR Applications</i> , Alan L. Weeks	71
<i>Vibration Characteristics of Small Rotary and Linear Cryogenic Coolers for IR Systems</i> , W.J. Gully and M.W. Hanes	85
<i>A Gas-Fired Duplex-Stirling Cryorefrigerator to Liquefy Natural Gas for Automotive Fuel</i> , Woody Ellison, Ernest E. Atkins, Dr. Graham Walker and Steven G. Zylstra	97

CONTENTS—VOLUME II (continued)

<i>Thermodynamic Analysis of Mixed Fluid Joule-Thomson Cryocoolers,</i> B. Maytal and S.W. Van Sciver	111
<i>A Long Life Oil Lubricated J-T Cryocooler for Space Applications,</i> James Lester, Robert Levenduski and Roger Scarlotti	137
<i>Development of a Fast Cooldown J-T Cooling System,</i> G. Pahler, H. Maier, R. Maier and M. Bareiss	153
<i>Development of a Fast Cooldown, Joule-Thomson Microminiature Refrigerator and Vacuum Package, for Operation of Infrared, Focal Plane Arrays at 70K,</i> W.A. Little and R.L. Paugh	161
<i>Recent Practical Applications of Open Cycle, Compressor Based Joule-Thomson Cooling,</i> Paul Benson	171

SESSION VIIA—MAGNETIC COOLERS AND SESSION VIIB—SPACE COOLERS II

<i>Design of the Regenerative Magnetic Refrigerator Operating Between 4.2 K and 1.8 K,</i> Sangkwon Jeong and Joseph L. Smith, Jr.	189
<i>Analysis of a Magnetic Refrigerator Operating Temperature Between 10 K and 1.4 K,</i> Takenori Numazawa, Hideo Kimura, Mitsunori Sato and Hiroshi Maeda	199
<i>A Preliminary Numerical Study of Magnetic Refrigeration,</i> C. Carpetis	215
<i>The Magnetocaloric Effect in Nanocomposites,</i> Robert D. Shull, Lydon J. Swartzendruber and Lawrence H. Bennett	231
<i>Rare-Earth Intermetallic Components for Magnetic Refrigerants,</i> Alexander Tishin	247
<i>Supercritical Helium Dewar Space Flight Results,</i> Paul Forney	251
<i>A Continuously-Operating Dilution Refrigerator for Space Applications,</i> Pat R. Roach	263
<i>Heat Driven Cryocooler for Satellite Bus Use,</i> Robert M. Lerner	273
<i>Key Attributes and Generic Requirements for Cryocooler Application on Microsats,</i> John Lester Miller	285
<i>Development of Small Vuilleumier Cryocoolers for Space Use,</i> Masakuni Kawada, Shunsuke Hosokawa and Isao Kudo	295
<i>Immersion vs Conduction Cooling of a Niobium Josephson Junction Integrated Circuit: Characterization and Performance Correlations at Low Frequencies,</i> Edward Hershberg, Kimberly Godshalk, Vallath Nandakumar, Soo Young Lee and Bruce Murdock	317
<i>Effect of Tube Temperature Profile on Thermal Acoustic Oscillations in Liquid Hydrogen Systems,</i> Y.F. Gu and K.D. Timmerhaus	329

CONTENTS—VOLUME II (continued)

Simulation of a Near-Isothermal Expander, M.G. Norris, J.L. Smith, Jr.
and J.A. Crunkleton 341

Development of a He II Gap Heat Switch for a 2K to 10K ADR,
Ali Kashani and Ben P.M. Helvensteijn 355

*Micro and Nanno Cryocoolers: Speculation on Future
Development*, Graham Walker and Edward R. Bingham 363

Session I — Applications

Chairperson: Marty Nisenoff, NRL

Co-Chairperson: Frank Kadi, Leybold Vacuum Products, Inc.

CRYOREFRIGERATOR EVALUATION FOR FUTURE MAGNETIC RESONANT IMAGING APPLICATIONS

R.A. Ackermann
GE Corporate Research and Development
Schenectady, New York 12301

ABSTRACT

Gifford McMahon cryorefrigerators are now used very successfully on all GE magnetic resonant imaging systems to reduce liquid helium consumption. However, this use has also demonstrated the need for a highly reliable and superior quality product. Noise, contamination, and disturbances have all created problems and have led to the need for costly product improvements to meet customer acceptance.

To characterize cryorefrigerator performance and evaluate reliability, GE Corporate Research and Development (GE-CRD) started an experimental program in 1988 to measure the capacity of commercially available two-stage Gifford McMahon (GM) cycle refrigerators and to define their primary modes of failure in a simulated magnetic resonance imaging environment. The program has included the performance mapping of six commercial refrigerators, life testing of three machines, and the evaluation of all failures as they occurred. Performance mapping was performed over a range of heat loads from 0 to 30 W on the first stage, and 0 to 5 W on the second stage. Endurance testing has consisted of accumulating over 28,000 hours of operation on three machines. Failure modes analysis has consisted of monitoring gas purity with a gas chromatograph and mass spectrometer and the close inspection of all failed units.

This paper describes the results of the load mapping and endurance testing performed, and compares these results with projected future requirements for GE-MRI applications. Testing has shown that the capacity of existing machines is too low for future applications, and that contamination failures caused by the slow buildup of CO₂ and N₂ in the cold head appears to be a major factor limiting reliability and shortening maintenance intervals of GM refrigerators.

INTRODUCTION

The use of a GM refrigerator on an MRI magnet has eliminated the need for liquid nitrogen cooling of a thermal shield and has reduced the liquid helium consumption from 0.5 L/h to less than 0.05 L/h for a 2.5-ton magnet and helium con-

tainer. This success has led to the use of a GM refrigerator on all GE-MRI systems and has made servicing and reliability a critical issue for overall product success.

The cryorefrigerator test program being conducted at GE-CRD is directed at characterizing the performance of commercially available two-stage GM refrigerators and establishing failure modes. The objective of this work is twofold:

1. To characterize commercial GM refrigerator performance for evaluation against future requirements.
2. To increase the field service interval to greater than 2 years, and depot maintenance - defined as requiring shipment of either the cold head or compressor to a central facility - to 4 years.

The assembly of a GM refrigerator on a GE-MRI system is shown in Fig. 1, and Fig. 2 shows the mounting of the refrigerator on the cryostat. In this mounting configuration, the refrigerator cold head extends into a sleeve in the cryostat and connects to the first- and second-stage thermal shields by flexible thermal straps. The two shields are maintained at temperatures of 40 to 50 K for the outer first stage shield and 12 to 15 K for the inner second stage shield. The mounting sleeve is used to separate the refrigerator from the main cryostat vacuum for easier refrigerator maintenance.

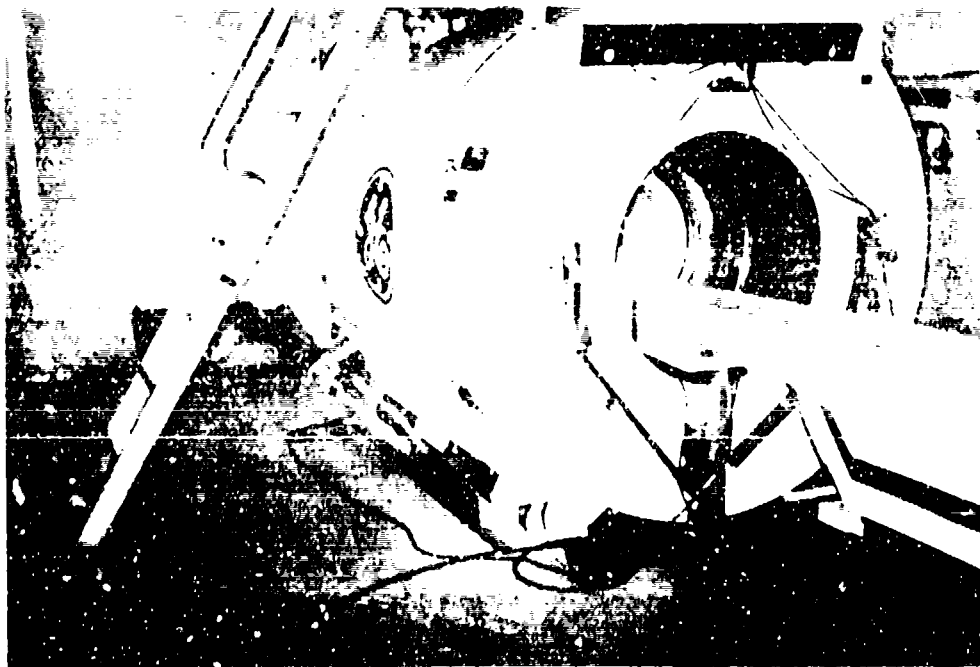


Fig. 1. MRI magnet system.

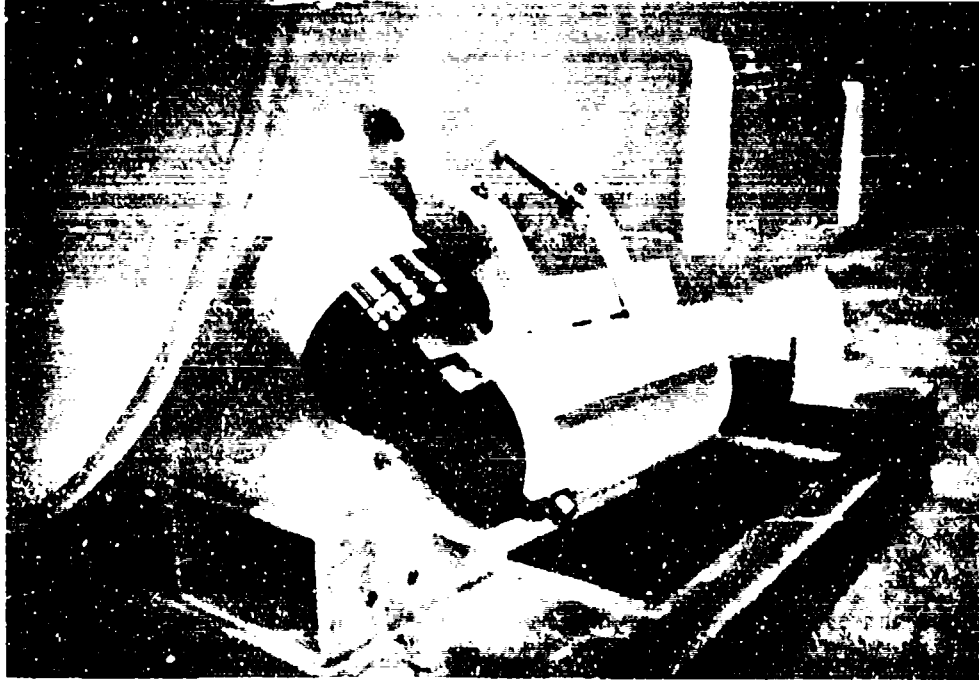


Fig. 2. MRI shield cooler.

TEST PROGRAM

The test program consisted of load mapping and endurance testing. The load mapping was performed by mounting the cold head in a liquid nitrogen-shielded vacuum vessel, and attaching a thermal shield to the first stage and a thermal station to the second stage of the cold head (Fig. 3). Electrical resistance heaters were attached to the thermal shield and to the second-stage thermal station, and calibrated carbon glass resistance temperature sensors were mounted on the cold head first and second stages to measure temperature. The load mapping was performed by applying heat to the first and second stages: 0 to 30 W on the first stage and 0 to 5 W on the second stage. The heat load and temperatures were monitored with a PC-based data acquisition system that was also programmed to automatically set the heat loads on each stage, based on a steady-state temperature criterion of less than 0.01 K over a 15-min interval. Fig. 4 depicts the test setup for the load mapping, and Table 1 lists the refrigerators that were tested along with their nominal ratings as given by the manufacturer.

Endurance testing has consisted of continuously running three refrigerators, two mechanically driven and one pneumatically driven, to accumulate operating hours at a fixed operating point. The refrigerators were run in a simulated MRI environment by setting a thermal load on the first and second stages, controlling the cooling water to 70°F, and operating the cold head in the vicinity of a stray magnetic field similar to that seen on a 0.5-T MRI system. The first- and second-stage temperatures were sampled every 2 h and checked daily for deviations. When a failure did occur, the

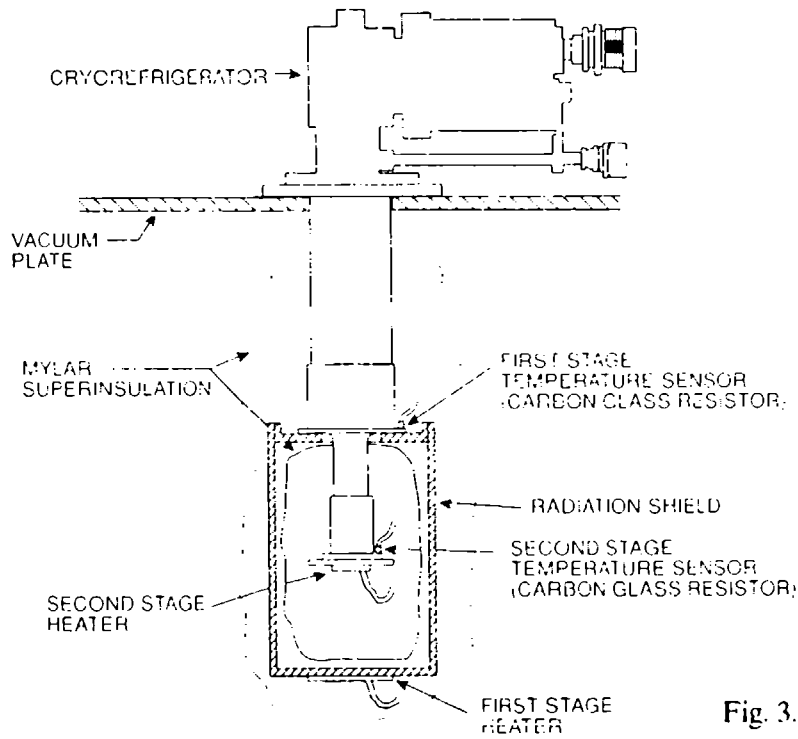


Fig. 3. Cryorefrigerator test setup.

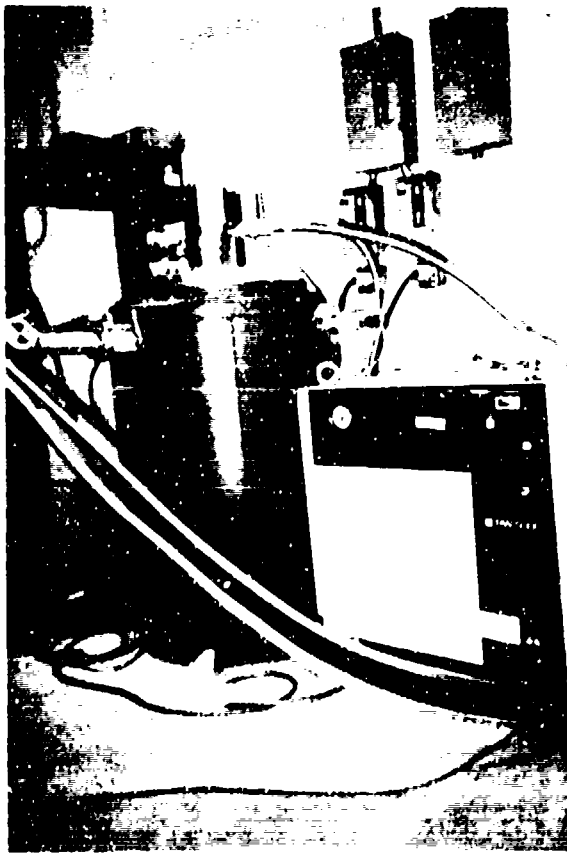


Fig. 4. Cryorefrigerator test apparatus.

Table 1. Manufacturer's specifications for GM refrigerators tested

Unit	Capacity (W)		Input Power (kW)
	80 K	20 K	
Balzers UC-110	100	10	7.0
Balzers (shield cooler)	70	7	4.0
CTI 1020C	40	12	5.0
Leybold			
RGD580-GE/RW4000	65	6.0	5.0
RGD580/RW5000	100	6.3	6.5
Cryomech GBO4	60	7	4.5

compressor was disconnected from the cold head, the system was allowed to warm to ambient temperature, gas samples were taken from both the cold head and compressor, and the unit was disassembled and inspected for damage and wear.

Temperature tracking consisted of averaging the bi-hourly data to determine the short-term, daily temperature deviations and plotting weekly averages to determine long-term temperature stability. It is projected that temperature stability will become more important in future applications as tighter helium boiloff specifications and longer maintenance intervals are sought. Planned specifications for future applications are given in the following section.

Schematic representations for the mechanical and pneumatic drives are shown in Fig. 5 and 6, respectively. The mechanical drives use a scotch yoke mechanism to provide a sinusoidal motion to the displacer, and mechanical valves that are timed to the displacer motion provide the cyclic pressure changes. Poppet valves, driven from the scotch yoke crank, are used in the first refrigerator tested, and a spool valve, driven by an end-of-stroke mechanism, is used in the second refrigerator. In the pneumatic refrigerator, a rotating disc valve and a stem volume (chamber 1 in Fig. 6) provide a net driving force to the displacer at precise times in the cycle to produce a square wave displacement. The rotating disc valve in the pneumatic refrigerators also provides the cyclic pressure changes over the cycle.

FUTURE GE-MRI CRYOREFRIGERATOR REQUIREMENTS

Future GE-MRI systems will strive for lower refrigerator temperatures and increased maintenance intervals to reduce operating and service expenses. In addition, new software for improved image resolution will require significant reductions in cryorefrigerator vibrations. Some of the more critical specifications that are contemplated are

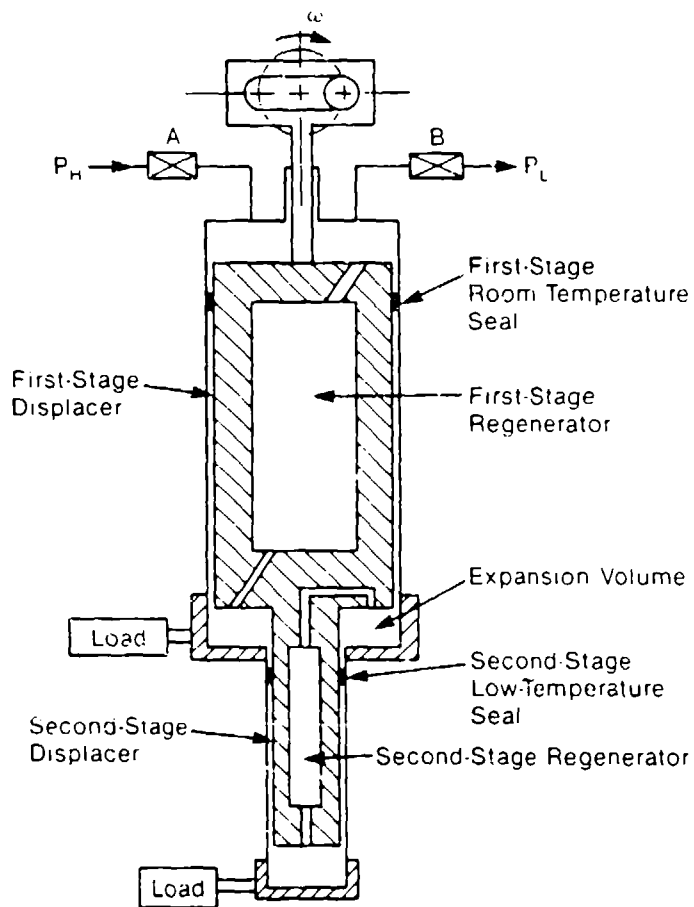


Fig. 5. Mechanically driven GM cold head.

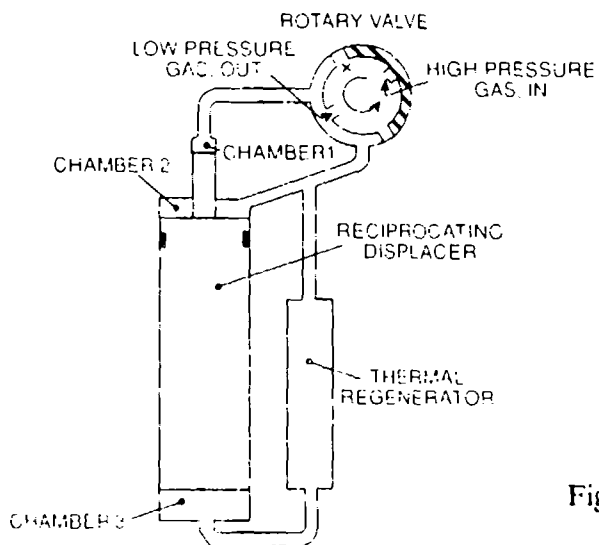


Fig. 6. Pneumatically driven GM cold head.

1. Capacity

2.5 W second stage
40.0 W first stage

2. Temperature Stability

Short term (<24.0-h period): 0.2 K second stage
2.0 K first stage

Long term (> 1-yr period): 0.5 K second stage
5.0 K first stage

3. Noise

The noise from the refrigerator, when installed in the cryostat, shall be less than 60 dBA at a distance of less than 3 m over the frequency range of 0 to 20 kHz.

4. Vibration

A vibration specification has not been established. However, this requirement is becoming more important because new software packages are improving the image resolution and refrigerator disturbances are beginning to noticeably impact the image quality.

5. Field Preventive Maintenance

Field preventive maintenance procedures shall not be required more often than once every 2 yr. Field service shall not require more than one service representative and shall not require more than a 6-h period.

6. Depot Maintenance

Depot maintenance (for which the part must be removed from the site and shipped to a central facility) shall be required for the cold head no more frequently than every 4 yr, and for the compressor, no more frequently than every 5 yr.

TEST RESULTS

The load maps obtained for the six refrigerators tested are shown in Fig. 7. Each load map represents several weeks of running to ensure that the refrigerator performance had stabilized and steady-state operation had been achieved. In addition, in all cases the maps were repeated several times to ensure the consistency of the data.

Comparing performance based on our test points of 2.5 W on the second stage and 40 W on the first stage, Table 2 shows that the Balzers UC-110 and Cryomech GB04 achieved the lowest temperatures. The performance of the other refrigerators was similar to the existing Balzers shield cooler; they provide no significant capacity increase for future applications.

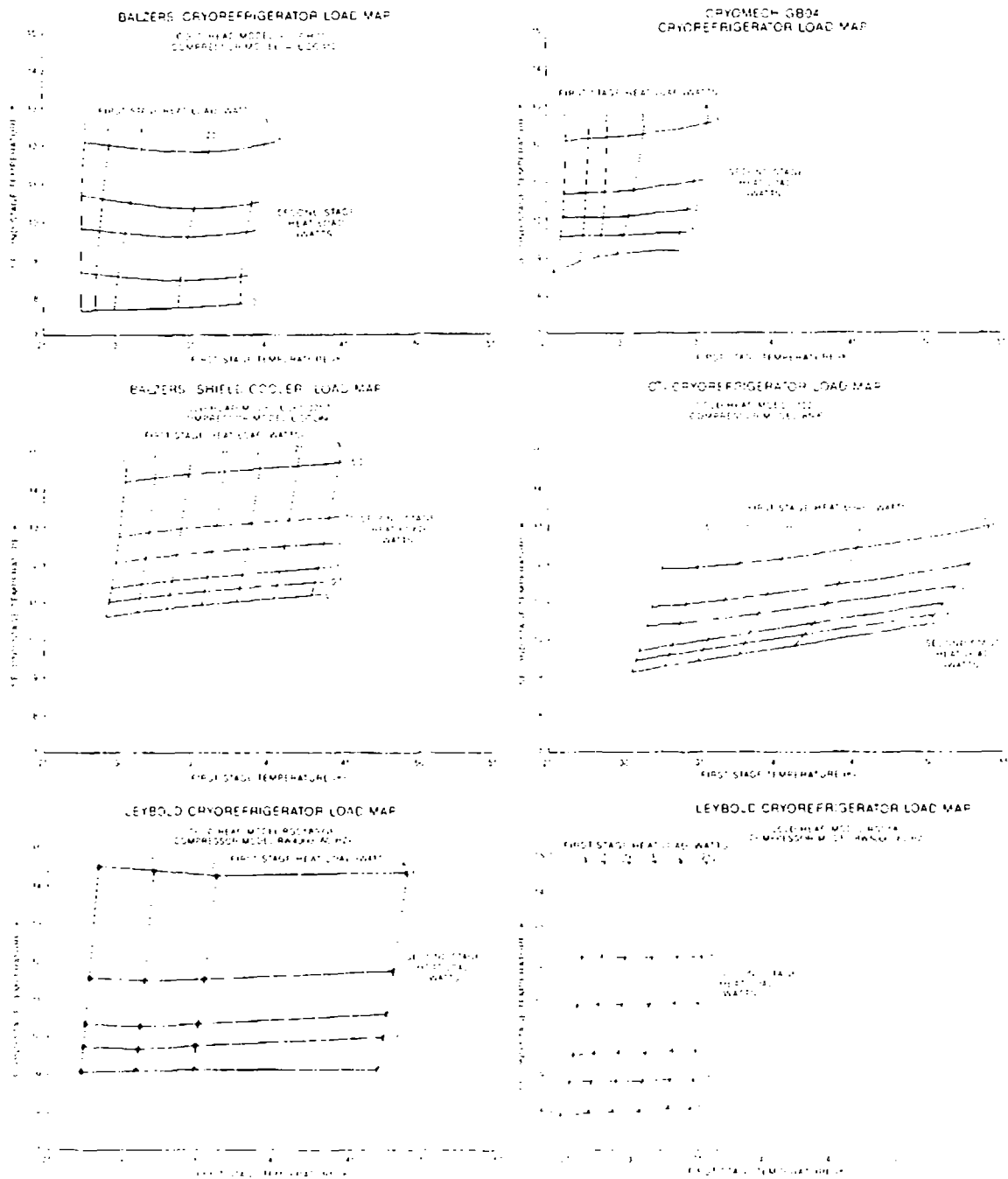


Fig. 7. Load maps from tests of commercial GM refrigerators.

Table 2. Cryorefrigerator test data

Unit	Temperature (K)	
	First Stage (at 40 W)	Second Stage (at 2.5 W)
Balzers UC-110	45.0	10.5
Balzers (shield cooler)	47.5	13.0
CTI 1020C	80.0	12.5
Leybold		
RGD580-GE/RW4000	48.0	12.5
RGD580/RW5000	46.0	11.5
Cryomech GBO4	34.5	10.5

Three refrigerators were selected for endurance testing. Two employed mechanically driven scotch yoke mechanisms and the third employed a pneumatic drive. Each refrigerator was set up in a simulated MRI environment with the first- and second-stage temperatures monitored every 2 h. The results of the temperature tracking for each of these machines are shown in Fig. 8, 9, and 10. The endurance and failures exhibited by these refrigerators were as follows:

1. First Mechanical Drive Refrigerator

A total of 12,360 h was accumulated on the first mechanical drive refrigerator with two failures occurring. The first failure, after 3.5 months of operation, was characterized by a severe temperature degradation on the first and second stages, leading to a temperature rise of 8.0 K and 0.7 K on the first and second stages, respectively. This degradation was considered sufficiently severe to terminate the test. The refrigerator was allowed to warm up, a gas sample was taken, and the cold head was disassembled and inspected for wear. No evidence of wear was found; however, the gas sample revealed high levels of N₂ (>400 ppm) and CO₂ (>50 ppm), which were considered responsible for the temperature degradations.

The refrigerator was returned to the manufacturer for servicing. Upon receipt of the repaired unit, endurance testing was continued. This second refrigerator test ran for 13.5 months, when the refrigerator again failed because of a severe rise in first- and second-stage temperatures that exceeded required operating levels. During this test, the refrigerator ran uninterrupted for 11 months, but 2.5 months prior to the termination of the test, it exhibited the strange behavior of suddenly reaching much lower temperatures on the first and second stages than had previously been measured. Since no physical parameters had changed, and no substantiated explanation could be given for the sudden change

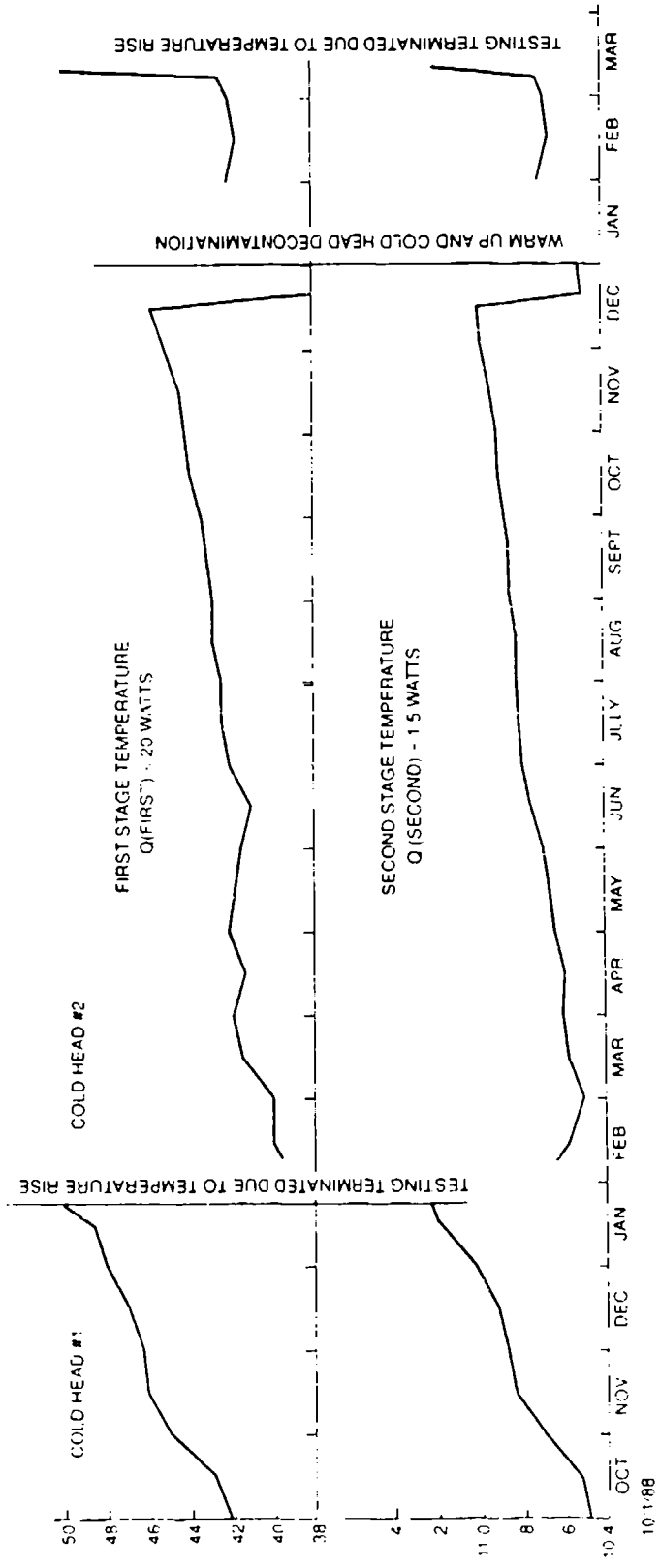


Fig. 8. Temperature tracking for the first mechanical drive GM refrigerator (max. uninterrupted operating time = 7,848 h).

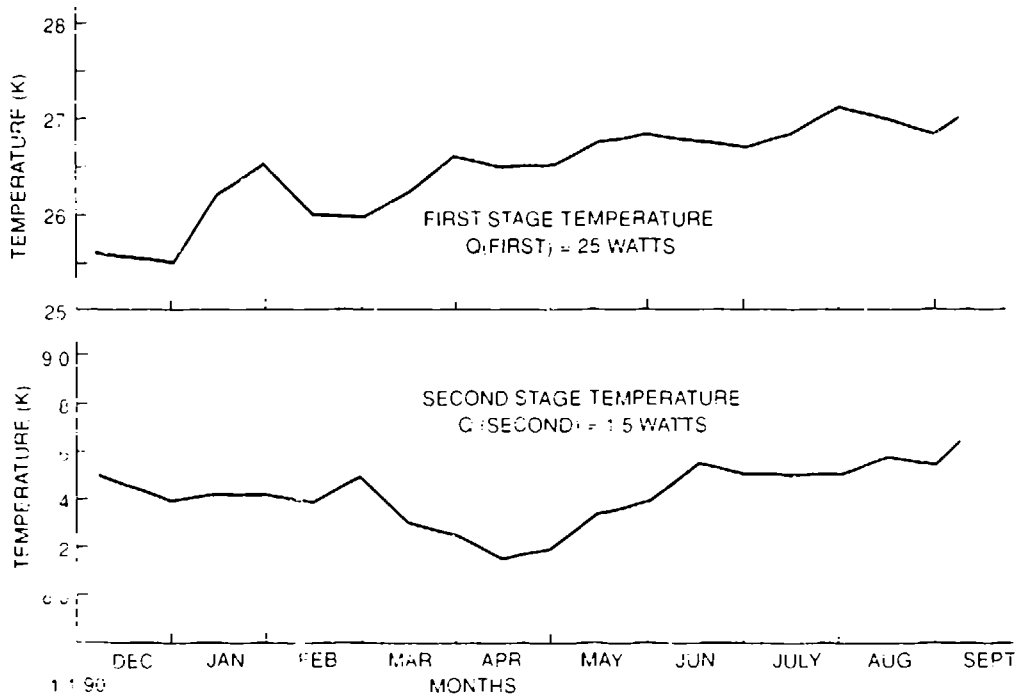


Fig. 9. Temperature tracking for the second mechanical drive GM refrigerator (continuous operating time = 6,480 h).

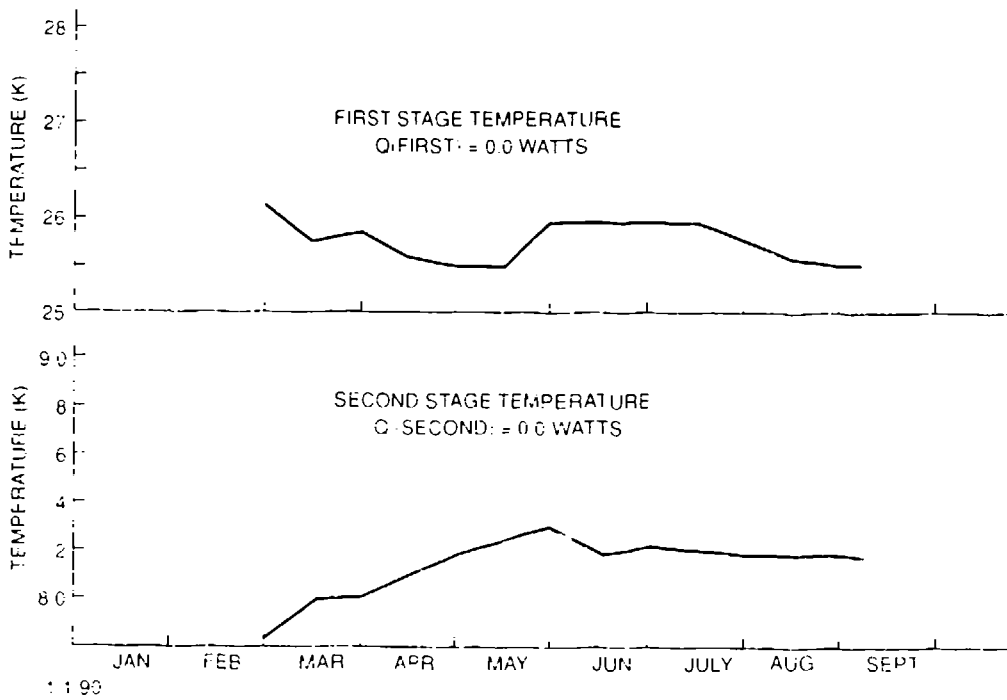


Fig. 10. Temperature tracking for the pneumatic drive GM refrigerator (continuous operating time = 4,416 h).

in performance, it was decided to disconnect the cold head from the compressor, warm it to ambient, and take a gas sample from the cold head. After the sample was taken, the cold head was pressurized and started. After reaching temperatures of 10.7 K and 42 K the refrigerator ran for an additional 5 weeks before rapid temperature rises on both the first and second stages caused the termination of the testing. Disassembly and inspection of the cold head by the manufacturer again failed to show any evidence of wear or damage to the cold head, but the gas sample taken prior to the test termination revealed high levels of CO₂ (>1000 ppm). The gas sample taken before the start of the 13.5-month run had shown no gas contamination levels greater than a few parts per million, and therefore it was concluded that the failure was due to contamination.

Over the 13.5-month testing, the refrigerator exhibited the following short- and long-term maximum temperature changes:

Short term (<24.0 h):	ΔT (first stage) = 2.0 K
	ΔT (second stage) = 0.1 K
Long term (11-month period):	ΔT (first stage) = 6.2 K
	ΔT (second stage) = 0.48 K

2. Second Mechanical Drive Refrigerator

The second mechanical refrigerator has been running for 6,480 h and continues to accumulate hours at this time. Unlike the first mechanical drive unit, several failures occurred very early in the testing, which prevented the start of the endurance testing for nearly 6 months. The failures that occurred after short operating intervals were

- Rapid temperature rise. After running for 1.3 months, there was a noticeable loss in capacity and rise in temperatures. A gas sample showed high levels of H₂O (>1000 ppm), and N₂ (>200 ppm). The refrigerator was returned to the manufacturer for contamination removal.
- Loss of gas pressure. After an additional 1.7 months of operation the unit lost pressure, forcing a shutdown. Inspection of the compressor revealed a leak in the heat exchanger between the oil cooling passages and water side of the heat exchanger. The compressor was repaired by the manufacturer and returned to GE for further testing.
- Cold head seizure. After running for an additional 2.2 months the cold head displacer seized, terminating the test. Gas samples taken this time showed high levels of CO₂ (>1000 ppm), and O₂ and N₂ (>200 ppm). The cold head was returned to the manufacturer, where inspection revealed that the scotch yoke crank had sheared from the seizure of the displacer. The cold head was repaired and returned to GE for further testing.

- Loss of gas pressure. After another month the compressor again developed a gas leak in the heat exchanger. This time the leak was between the helium cooling passages and the water side of the heat exchanger.

In December 1989 the repaired refrigerator was received from the manufacturer and endurance testing begun. The unit has been running continuously since then. The temperature tracking for this refrigerator is shown in Fig. 9. The temperature stability exhibited to date by this refrigerator has been

$$\begin{aligned} \text{Short term: } \Delta T \text{ (first stage)} &= 1.0 \text{ K} \\ \Delta T \text{ (second stage)} &= 0.20 \text{ K} \end{aligned}$$

$$\begin{aligned} \text{Long term: } \Delta T \text{ (first stage)} &= 1.5 \text{ K} \\ \Delta T \text{ (second stage)} &= 0.21 \text{ K} \end{aligned}$$

3. Pneumatic Drive Refrigerator

Endurance testing on the pneumatic refrigerator was started in February 1990, and with the exception of short periods when it was warmed to take a gas sample, the refrigerator has been running continuously for the past 6 months. To date, the refrigerator has accumulated 4,416 h of operating time with no failures.

The temperature tracking for this refrigerator is shown in Fig. 10. The temperature tracking on this refrigerator is being conducted with no thermal loads on either the first or second stages. Availability of power supplies limited the continuous operation under load. However, periodic measurements with 25 W on the first stage and 2 W on the second stage have shown a temperature history similar to the no-load tracking shown in Fig. 10.

The temperature tracking has shown that after initially achieving a no-load temperature of 26.2 K on the first stage and 7.82 K on the second stage, the refrigerator has experienced a warming of the second stage and cooling of the first stage and appears to be settling at temperatures of 25.5 K and 8.2 K. To evaluate this instability, the refrigerator was turned off after 1000 h of operation, then allowed to warm up to ambient, and a gas sample was taken from the cold head. After taking the gas sample, the cold head was recharged with helium and the endurance testing continued. The results of the gas sample were that a large amount of N_2 (> 1000 ppm) and lesser amounts of CO and CH_4 (> 50 ppm) had accumulated in the cold head after only 1000 h of operation. Based on this initial instability, the temperature changes over the past 6 months have been

$$\begin{aligned} \text{Short term: } \Delta T \text{ (first stage)} &= 0.1 \text{ K} \\ \Delta T \text{ (second stage)} &= 0.04 \text{ K} \end{aligned}$$

$$\begin{aligned} \text{Long term: } \Delta T \text{ (first stage)} &= 0.7 \text{ K} \\ \Delta T \text{ (second stage)} &= 0.48 \text{ K} \end{aligned}$$

With 25 W on the first stage and 2 W on the second stage, the resulting temperature changes over the 6-month period have been

$$\begin{aligned}\Delta T \text{ (first stage)} &= -0.6 \text{ K} \\ \Delta T \text{ (second stage)} &= +0.5 \text{ K}\end{aligned}$$

CONCLUSIONS

Based on projected future GE-MRI applications, the following conclusions regarding cryogenic refrigeration requirements were drawn:

1. Greater first- and second-stage capacities will be required. Performance equal to or better than the best performing refrigerators in Table 2 will be sought.
2. Contamination was the major cause of failure in our endurance testing. Table 3 summarizes these failures and shows that the slow accumulation of contaminants, such as CO₂, N₂, and hydrocarbons, limits long-term operation.

Table 3. Summary of contamination failures

Refrigerator	Failure Mode	Run Time (h)	Concentrations (ppm)
First mechanical drive	Temperature degradation over 3-month period	2,664	N ₂ > 400 CO ₂ > 50
	Rapid temperature rise	9,696	CO ₂ > 1000
Second mechanical drive	Rapid temperature rise	951	H ₂ O > 1000 N ₂ > 200
	Cold head seizure	1,610	CO ₂ > 1000 N ₂ > 200
Pneumatic drive	Temperature rise	1,000	N ₂ > 1000 CO ₂ > 50 CH ₄ > 50

4 K GM/JT CRYOCOOLER FOR CRYOGENIC SENSORS

Yoon-Myung Kang*, Tadashi Ogura, Satoru Uosaki, Katsumi Sakitani
Shuichi Sochi, Shuji Fujimoto*, Ken-ichi Sata*, Naoki Fukui*
DAIKIN INDUSTRIES, LTD., 1304 Kanaokacho, Sakai, Osaka 591, JAPAN
*(from November 1990) 3 Miyukigaoka, Tsukuba, Ibaraki 305, JAPAN

ABSTRACT

4 K Gifford-McMahon/Joule-Thomson cryocoolers have been developed for cooling sensors, e.g., far-infrared detectors, SIS receivers for radio astronomy and SQUID magnetometers. The cryocooler can be operated for 10,000 hours without service. The outline of the cooler configuration and application problems for cooling sensors are shown in this paper. Vibration characteristics are measured by the laser Doppler vibrometer. Temperature homogeneity of the 4 K stage is estimated by FEM analysis of thermal conduction. Biomagnetic measurements with a SQUID system, cooled by the GM/JT cryocooler, are also presented.

INTRODUCTION

DAIKIN INDUSTRIES, LTD. has been developing a variety of 4 K Gifford-McMahon (GM) cryocoolers with a Joule-Thomson (JT) cycle to provide reliable commercial coolers for industrial and laboratory applications [1], e.g., recondensing helium in the MRI (Magnetic Resonance Imaging) cryostat, cooling far-infrared detectors and SIS (Superconductor Insulator Superconductor) receivers for radio astronomy.

When cooling sensors in the vacuum cryostat with a closed cycle cryocooler (without liquid helium), mechanical and electromagnetic noise, temperature fluctuation and temperature-inhomogeneity in the cooling stage should be at an acceptable low level. The SQUID (Superconducting QUantum Interference Device) magnetometer is one of the most sensitive sensors for those perturbations. Zimmerman et al. [2] developed low-power Stirling cycle cryocoolers for cryoelectronic devices, particularly SQUID magnetometers and magnetic gradiometers. Buchanan et al. [3] developed a neuromagnetometer with a GM/JT cryocooler, and succeeded in magnetic measurements of auditory evoked fields from the brain. DAIKIN succeeded in the development of a reliable 4 K GM/JT cryocooler [4], a low vibration cryostat for optical measurements [5], and biomagnetic measurements with a SQUID-based magnetic gradiometer cooled by the GM/JT cryocooler [6]. This paper reviews our related works on the GM/JT cryocooler for cryogenic sensors.

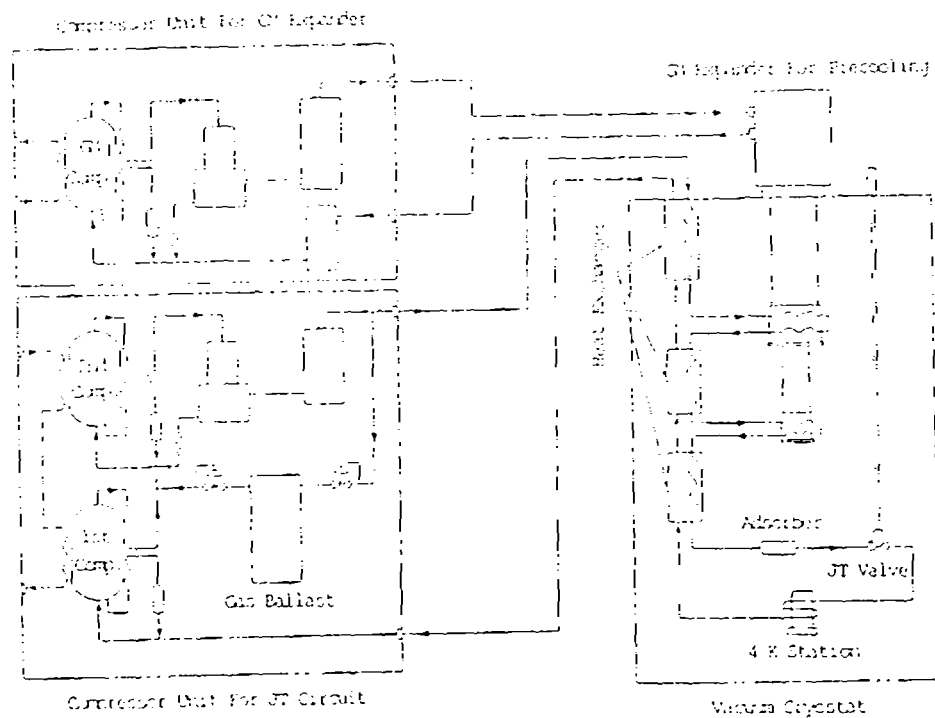


Figure 1. The flow diagram of the GM/JT cryocooler

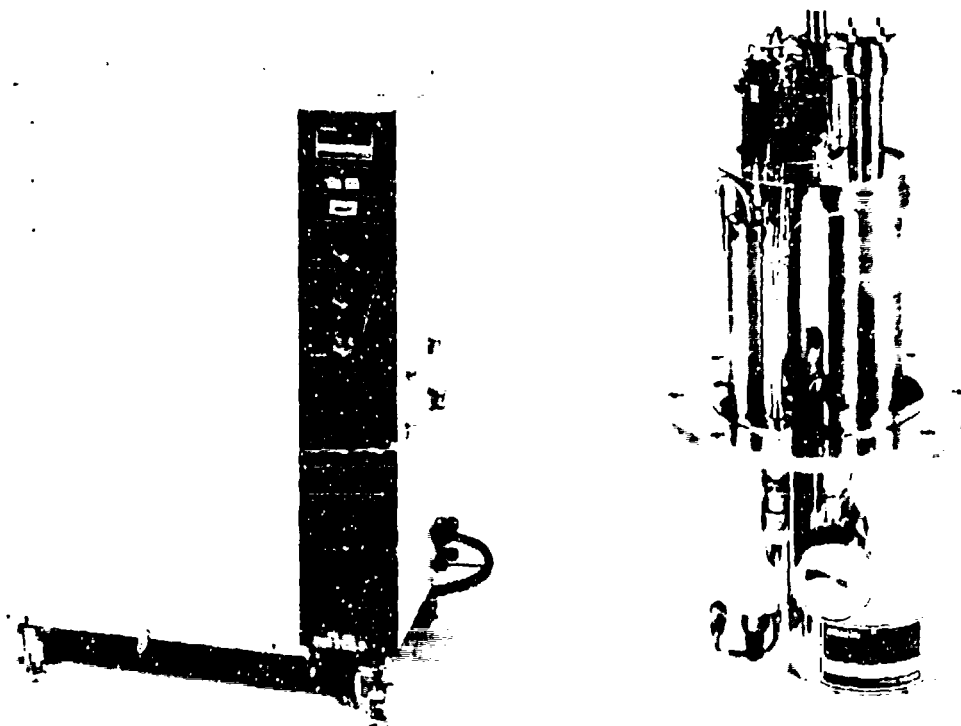


Figure 2. The basic model of the compressor and refrigerator unit

COOLER CONFIGURATION

The flow diagram of the GM/JT cryocooler is shown in figure 1. The JT circuit is separated from the GM circuit, therefore, it is easy to clean the JT circuit and there is no possibility of contamination while GM expander being serviced. The prototype attained 20,000 hours of operation without JT service and even after that test, contaminants were not detected in the cryostat section of the JT circuit [1]. Until today, Several tens of units have been operated in the field without a JT blockage problem. The basic model of the compressor and refrigerator unit is shown in figure 2 and its specifications are summarized in table 1.

Table 1. Specifications of the basic model

	50 Hz	60 Hz
Refrigeration capacity	3.0 W	3.5 W
Power Dissipation	5.1 kW	6.4 kW
Maintenance Interval	10000 hrs	
Size: Cryostat	$\phi 300 \times 740H$ mm	
Compressor Unit	$750W \times 530D \times 1000H$ mm	
Weight: Cryostat	55 kg	
Compressor Unit	230 kg	

Because the GM expander used here has a pneumatic driven mechanism [7], the valve motor can be separated from the cryostat [8]. This is advantageous for SQUID magnetometer applications.

The new fin tube is used in the JT heat exchanger, which has a fin cut in pitch to almost half of the fin height (figure 3). As shown in figure 4, the heat transfer ratio (Colburn's j factor) between fin and helium gas is about 40 to 60 % better than in the usual Collins type [9] which has a straight fin. Figure 5 shows the friction factor of the low pressure path of the heat exchanger. Although the friction factor seems to be rather large, only causes a pressure drop less than one third of the total JT flow resistance in the cryostat.

VIBRATION CHARACTERISTICS

Vibration characteristics at the 4 K cooling stage were measured by a laser Doppler vibrometer and the results are shown in figure 6. The upper graph shows the displacement amplitude of the basic model with twenty or thirty microns of vibration at 2 Hz (displacer reciprocating frequency). The middle graph shows data for the low vibration cryostat in which the cooling stage is vibration-isolated from the expander cold station. This is done by using coiled tube for the JT line and rigid supports mounted on a vacuum chamber as shown in figure 7. The cryostat weighs 135 kg. The vibration amplitude was reduced to 0.1 micron r.m.s. at 2 Hz. The lower graph shows the background level when the expander is stopped (valve motor off). At the lower frequency, the vibration amplitude is almost the same as in the middle graph.

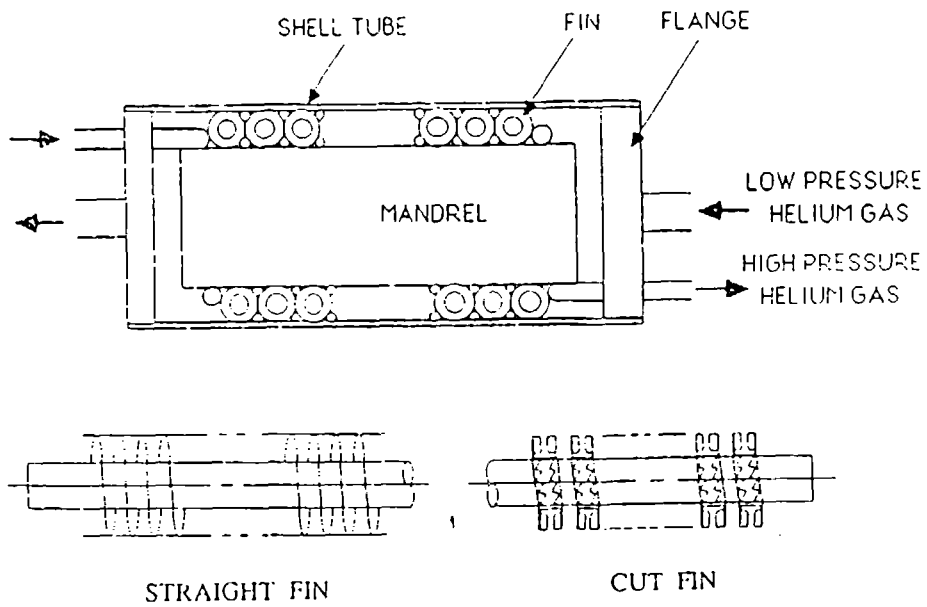


Figure 3. JT heat exchanger

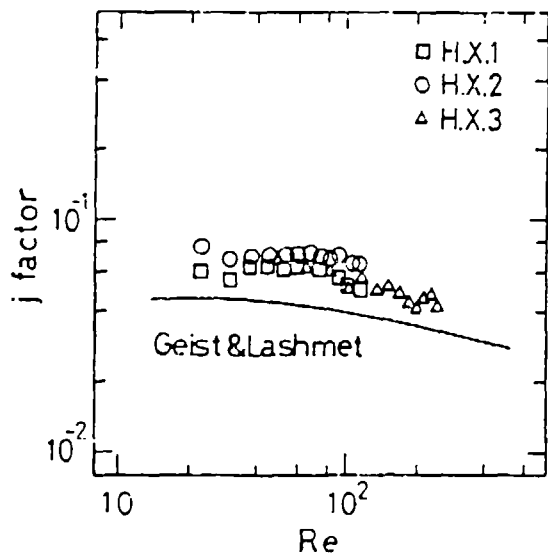


Figure 4. Heat transfer ratio

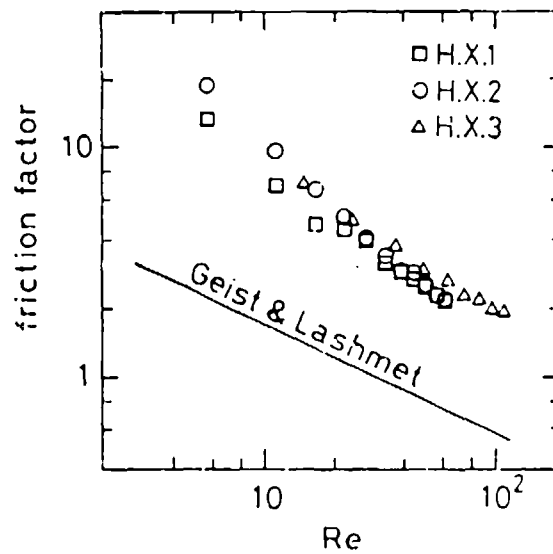


Figure 5. Friction factor

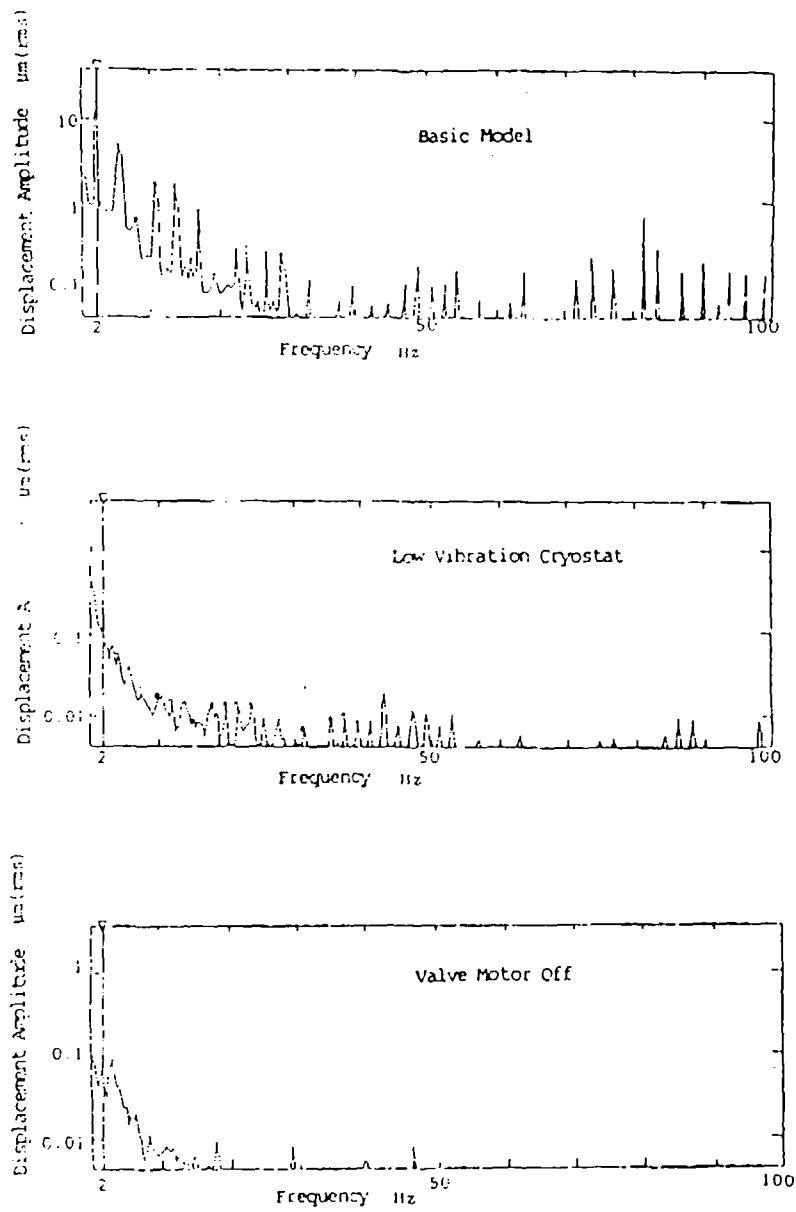


Figure 6. Vibration characteristics at the 4 K cooling stage

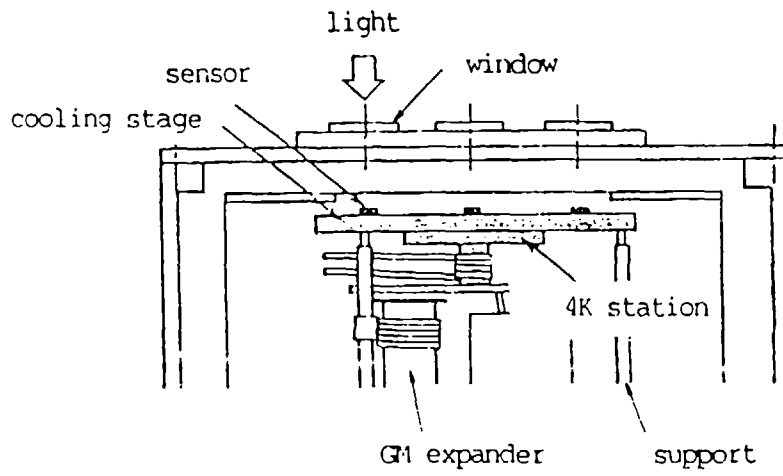


Figure 7. 4 K cooling stage of the low vibration cryostat

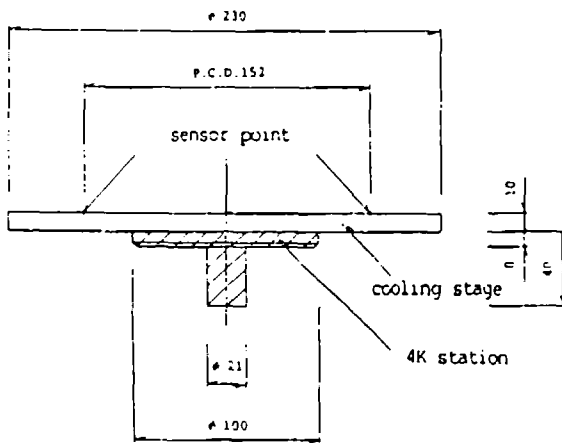


Figure 8. Model dimensions for FEM analysis

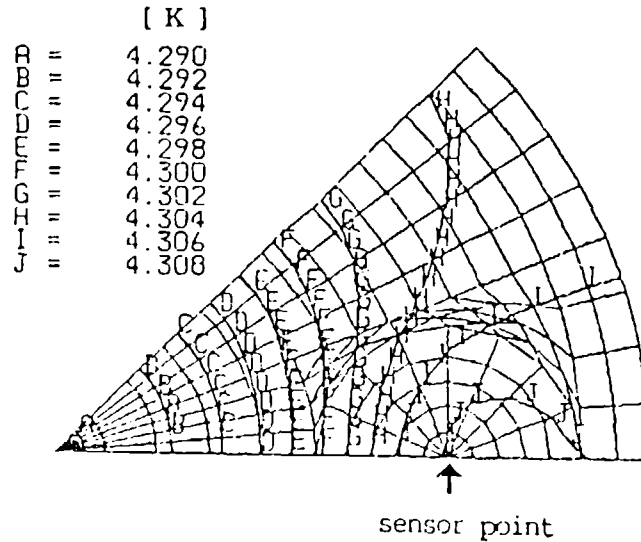


Figure 9. Calculated results of FEM analysis

TEMPERATURE HOMOGENEITY IN THE COOLING STAGE

In the optical cryostat, the radiative heat flux enters directly into the 4 K stage as shown in figure 7. In this case, temperature homogeneity in the cooling stage was estimated by the FEM (Finite Element Method) analysis of thermal conduction. The model dimensions are shown in figure 8. Oxygen free copper was used both for the 4 K station and the cooling stage and its thermal conductivity was measured at 13.5 W/cmK. The thermal resistance between the 4K station and the cooling stage was 2.0 cm² K/W, which was determined by another experiment. Boundary conditions were as follows; lower edge temperature of the 4 K station was 4.2 K, heat input through the 4 optical windows was 1.5 W, the remaining surface was adiabatic, symmetry conditions were utilized to reduce computations. Calculated results are shown in figure 9. The temperature differences in the cooling stage are within 20 mK. Temperature fluctuations might be within the same level.

BIOMAGNETIC MEASUREMENTS WITH A SQUID SYSTEM

By utilizing the above results, a SQUID system for biomagnetic measurements was constructed and magnetocardiograms (MCG) were taken. The system consists of a second order magnetic gradiometer, the DC-SQUID [10] developed at the Electrotechnical Laboratory, a flux locked loop (FLL) controller and the GM/JT cryocooler. The diameter of the gradiometer is 24 mm and its base line is 40 mm. The system was installed in a RF shield room and the valve motor of the GM expander was set outside of the RF shield. Figure 10 shows the MCG taken when the valve motor is off and figure 11 shows it when the valve motor on. Graphs on the left side shows the real time signals with a 60 Hz notch and a 100 Hz low pass filters, graphs on the right show averaged data in both figures. Vibration noise is obviously found when the valve motor is on. The main frequency of the noise is about 20 Hz which is the resonance frequency of the 4 K stage supporting system. This noise can be eliminated by digital filtering and a new system with a modified support is now in construction.

CONCLUSIONS

The GM/JT cryocooler was found to be as reliable as the GM cryocooler, i.e., the maintenance interval of the cryocooler is 10,000 hours, which is determined by the usual expander service. For applications to cryogenic sensors, the vibration amplitude of the cooling stage can be reduced to a submicron level, and temperature inhomogeneity can be within a few tens of mK in the cryostat with several optical windows. Magnetocardiograms can be taken by the SQUID system without liquid helium.

The authors are glad to acknowledge the kind discussions and technical guidance in biomagnetic measurements by Drs. H. Kado, N. Kasai and S. Kiryu. They would also like to thank Mrs. K. Nishiguchi and T. Ueda for their technical support in SQUID electronics.

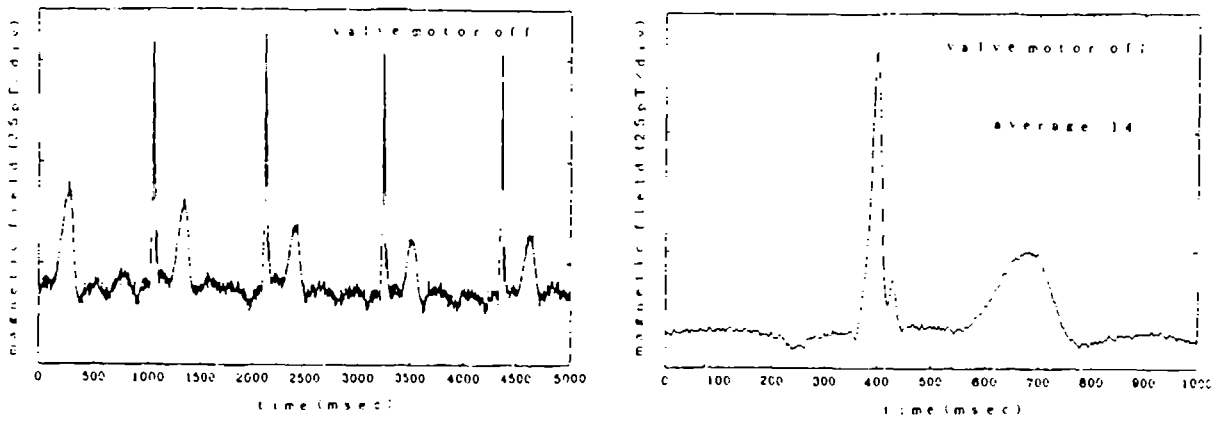


Figure 10. Magnetocardiograms with a SQUID system (valve motor off)

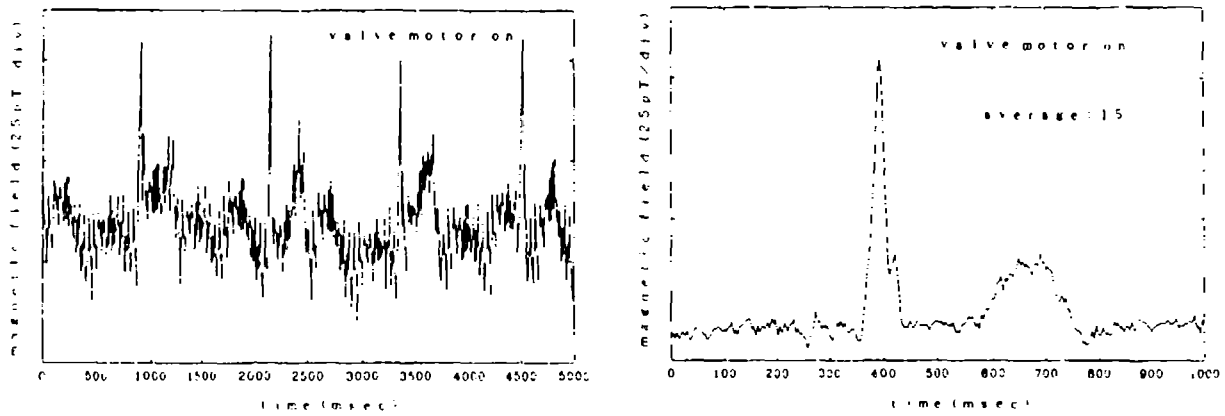


Figure 11. Magnetocardiograms with a SQUID system (valve motor on)

REFERENCES

1. Y.M.Kang, K.Sakitani, S.Taneya and K.Miura, "Development of a 4 K GM/JT Cryocooler," *Proc ICEC12*(1988)pp.582-586.
2. J.E.Zimmerman and D.B.Sullivan, "A Study of Design Principles for Refrigerators for Low-Power Cryoelectronic Devices," NBS Technical Note 1049(1982).
3. D.S.Buchanan, D.N.Paulson, G.A.Klemic and S.J.Williamson, "Development of a Hybrid Gifford-McMahon Joule-Thomson Based Neuromagnetometer CryoSQUID," *Proc. CRYOCOOLERS 5*(1988)pp.35-46.
4. S.Shinozaki, S.Taneya, K.Miura, S.Noguchi, Y.M.Kang and K.Sakitani, "Development of a Small 4 K Refrigerator(in Japanese)," *Prep. 35th Conf. Japan Soc. of Cryog. Eng.* (1986)p.163.
5. Y.M.Kang, T.Ogura, K.Miura, S.Taneya, S.Noguchi and K.Sakitani, "Development of a Small 4 K Refrigerator, part 2; a low vibration cryostat(in Japanese)," *Prep. 37th Conf. Japan Soc. of Cryog. Eng.*(1987)p.65.
6. K.Sata, N.Fukui, Y.M.Kang and H.Kado, "Cooling SQUID by GM/JT Cryocooler, part 2 (in Japanese)," *Prep. 44th Conf. Japan Soc. of Cryog. Eng.*(1990).
7. R.C.Longsworth, "A Modified Solvay-Cycle Cryogenic Refrigerator," *Adv. Cryog. Eng.*, vol.16(1971)pp.195-204.
8. R.C.Longsworth, "Interfacing small Closed-Cycle Refrigerators to Liquid Helium Cryostats," *Cryogenics*, vol.24, no.4(1984)pp.175-178.
9. J.M.Geist and P.K.Lashmet, "Miniature Joule-Thomson Refrigeration Systems," *Adv. Cryog. Eng.*, vol.5(1960)pp.324-331.
10. M.Nakanishi, M.Koyanagi, S.Kosaka, A.Shoji, M.Aoyagi and F.Shinoki, "Integrated DC-SQUID Magnetometer," *Japanese J. Appl. Phys.*, vol.26, no.7(1987)pp.1050-1055.

CHARACTERIZATION OF MINIATURE STIRLING-CYCLE CRYOCOOLERS FOR SPACE APPLICATION

R.G. Ross, Jr., D.L. Johnson, R.S. Sugimura

Jet Propulsion Laboratory
California Institute of Technology
Pasadena, California 91109

ABSTRACT

The growing demand for long-life infrared and submillimeter imaging instruments for space observational applications, together with the emergence of the multi-year-life Oxford University Stirling-cycle cooler, has led to a rapidly expanding near-term commitment to second-generation Stirling-cycle cryocoolers based on the Oxford heritage. The precision space-science instruments in need of these coolers have especially demanding requirements in the areas of lifetime and reliability, where many require continuous operation over 5 to 10-year timeframes with reliabilities of 0.95 to 0.99, and in the area of allowable generated vibration and EMI. To support the success of these near-term applications, the Jet Propulsion Laboratory (JPL) has initiated an extensive cooler characterization test and analysis program. This activity is focused at developing special sensitive performance measurement techniques for quantification of vibration, EMI, and thermal performance, and to developing carefully instrumented accelerated reliability screening tests to uncover long-time-constant degradation mechanisms.

In January of 1990, JPL took delivery of one of the first Oxford-heritage Stirling-cycle coolers manufactured by British Aerospace, and began the characterization activity with an initial emphasis on thermal and vibration performance. This paper describes the research results to date including the design and construction of JPL's special 6-degree-of-freedom force dynamometer, and special instrumentation used to measure the force spectra and reliability attributes of emerging first- and second-generation space Stirling-cycle cryocoolers.

INTRODUCTION

In recent years a growing number of space-instrument developers have proposed using long wavelength infrared and submillimeter imaging detectors to perform systematic mapping of earth and astrophysical subjects. The demand for low background noise requires that these detectors, and often portions of the electronics and optical subsystems, be cooled to cryogenic temperatures in the range of 60 to 150K.

The expense of these instruments -- often over \$100M -- together with science objectives of continuously monitoring subject changes over multi-year time spans, demands cryogenic cooling systems with lives of 5 to 10 years with reliabilities greater than 0.95. The emerging line of second-generation miniature Stirling-cycle cryocoolers, which are building on the successful Oxford University ISAMS cooler^{1,2}, are ideally suited to these applications. However, to satisfy the demanding application requirements, these emerging Stirling cryocoolers must successfully address not only the critical reliability requirement, but also a broad array of complex interface requirements that critically affect successful integration to the sensitive instrument detectors. Low vibration and EMI, and improved cooling performance at lower temperatures (55 to 60K) are particularly important parameters. Many of the space instruments baselining the use of these second-generation coolers are associated with NASA's Earth Observing System (Eos) space platforms and require that the advanced coolers be developed, qualified, and delivered between now and the mid 1990's.

Because the time available for design, fabrication and qualification is significantly less than the required operational life, the design and qualification process must rely on a thorough and accurate technical understanding of the cooler's performance-determining parameters and on sophisticated testing techniques and facilities. Examples include:

- 1) Accurate standardized thermal performance measurement techniques.
- 2) Sophisticated vibration/EMI characterization facilities and techniques.
- 3) Special non-destructive accelerated reliability screening tests for early diagnosis of life limiting failure mechanisms and eventual flight hardware acceptance testing. This task is made particularly difficult by the strong sensitivity of Stirling-coolers to manufacturing parameters such as contamination, machining and assembly tolerances, and dimensional stability.
- 4) Carefully instrumented long-duration life tests to discover, quantify and allow successful early resolution of long-time-constant failure and degradation mechanisms.

In January of 1990, JPL took delivery of one of the first Long-life 80K Stirling cryocoolers manufactured by British Aerospace (BAe)³, and began an extensive characterization activity designed to learn from and build upon the Oxford-heritage in a program to assist industry in meeting the demands of NASA's near-term space-science instruments. Research results to date are described in the areas of thermal performance characterization, vibration characterization, and reliability characterization.

THERMAL PERFORMANCE CHARACTERIZATION

Because of the demands of long-wavelength (up to 15 μ m) HgCdTe infrared detectors, important NASA Eos instruments are requiring greater than 1 watt of

cooling at temperatures as low as 55K. This level of cooling places increased emphasis on accurately understanding cooler thermal performance at the lowest achievable temperatures, and on accurately estimating and minimizing the heat load that the cryocooler must accommodate. This heat load includes both active power dissipation, from detectors for example, and the sum of all parasitic loads -- both conduction down wires and supports, and radiation from surrounds.

Because the cryocooler cold finger becomes an integral part of the instrument cryo-assembly, it is important that it be designed to minimize parasitic heat loads. Conduction down the cold finger is especially critical if redundant coolers are to be used without heat switches. Minimizing radiation transfer to the cold tip requires the incorporation of low-emittance surfaces and radiation shields into the cold finger and its interface design.

Because parasitic loads are systematically included into the design of the instrument cryo-assembly, it is important that accurate estimates of cooler-generated parasitics be available, and that cooler performance be measured and quoted for carefully defined boundary conditions. JPL's preference is that cooler performance be defined in terms of total external refrigeration load -- where external includes external parasitic loads encountered in the performance measurement setup such as radiation and instrumentation wiring; loads internal to the cryocooler, such as conduction down the cold finger, are not counted as refrigeration load.

Initial characterization of the thermal performance of JPL's BAe 80K Stirling cooler has highlighted the strong sensitivity of the measurements to thermal boundary conditions and instrumentation parasitics. Figure 1 illustrates the significant performance increase achieved at the lowest temperatures by carefully incorporating low-conductivity (Constantan) instrumentation wiring to the cold finger and thermal shields to minimize radiation parasitics transferred to the cold finger from

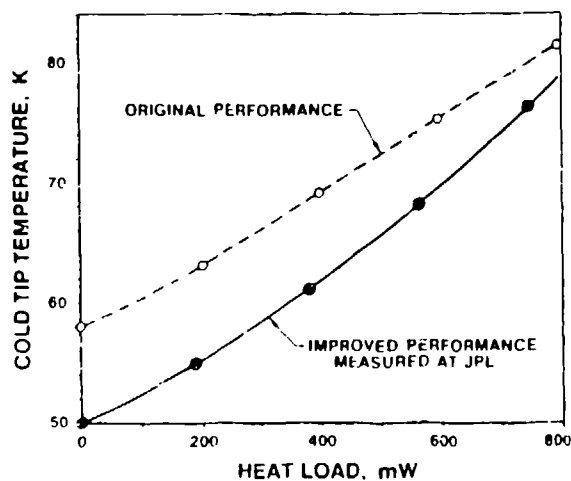


Fig. 1. Improved low-temperature performance of BAe 80K cooler resulting from minimizing cold-finger parasitics.

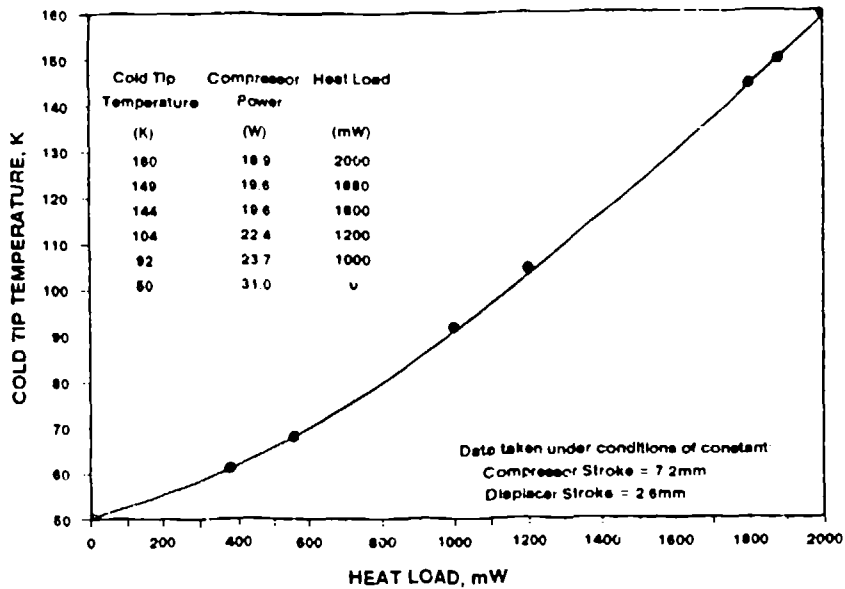


Fig. 2. Thermal and power performance of the BAe 80K cooler over the extended operating range from 50 to 160K.

its surroundings. The enhancement represents over a doubling in performance at 60K -- and more accurately reflects the true cooling performance of the cooler.

Another factor complicating the comparison of competing cooler designs is the strong dependency (shown in Fig. 2) between cooler input power and operating temperature for a fixed compressor piston stroke. Although cooler input power is the appropriate universal parameter for comparing competing coolers of different designs, the physical limitations imposed by control of piston stroke greatly complicate taking data using input power as an independent parameter. Note that for a fixed compressor stroke, the input power of this cooler drops from 31 watts to 19 watts as the maximum cold-end load increases from 0 watts at 50K to 2 watts at 160K. This reduced power required at higher temperatures can be an important consideration for some instrument designs.

VIBRATION CHARACTERIZATION

In addition to a cooler's thermal performance, cooler-generated vibration is another particularly important parameter for precision imaging instruments; it thus has been targeted as a key area for improvement in the emerging second-generation space Stirling cryocoolers.

In characterizing cooler-generated vibration it is useful to speak in terms of the peak vibratory force imparted by the cooler into its supports when rigidly mounted. This force is the reaction force to moving masses within the cooler that undergo peak accelerations during various phases of the cooler's operational cycle. The accelerations can be from controlled motion such as the reciprocating motion of

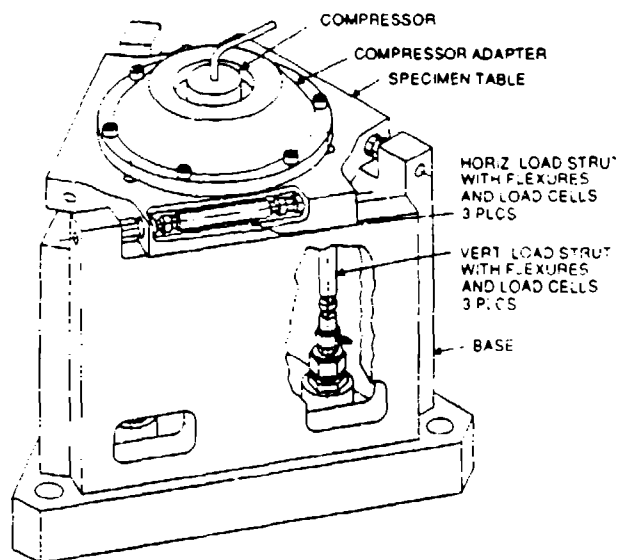


Fig. 3. JPL 6-degree-of-freedom force dynamometer.

the Stirling compressor piston and displacer, or natural vibratory resonances of the cooler's elastic structural elements.

Problems occur when the vibrating interface forces excite elastic deflections and resonances within the instrument structure and components that either adversely affect optical alignment, or generate spurious electrical signals. The latter are generated when electrical current-carrying or capacitively-coupled components undergo relative motions. Although no formally agreed upon requirements exist for acceptable vibratory force levels, a value on the order of 0.2 N (0.05 lbs) has gained acceptance as a reasonable design goal.

To help quantify and understand the force levels generated by present cooler designs, JPL has developed the 6-degree-of-freedom force dynamometer shown in Figure 3. This dynamometer has a frequency range from 10 to 500 Hz and a force sensitivity from 0.005 N (0.001 lb) to 445 N (100 lbs) full scale⁴. During operation the forces and moments generated about each of the cooler's axes are available simultaneously for real time quantitative analysis.

Research to date has centered on characterizing and understanding the vibration attributes of first-generation Stirling coolers of the Oxford type in support of achieving significant reductions in second-generation units. The overall test setup is shown in Figure 4.

Figure 5 illustrates the typical time-dependent vibration force generated by a single uncompensated BAe 80K Stirling compressor in each of three principal axes. Note that although the largest force is in the piston stroke direction (longitudinal direction), as expected, considerable force also exists in the lateral direction, normal to the piston axis, and as a moment about the piston axis. The lateral force is

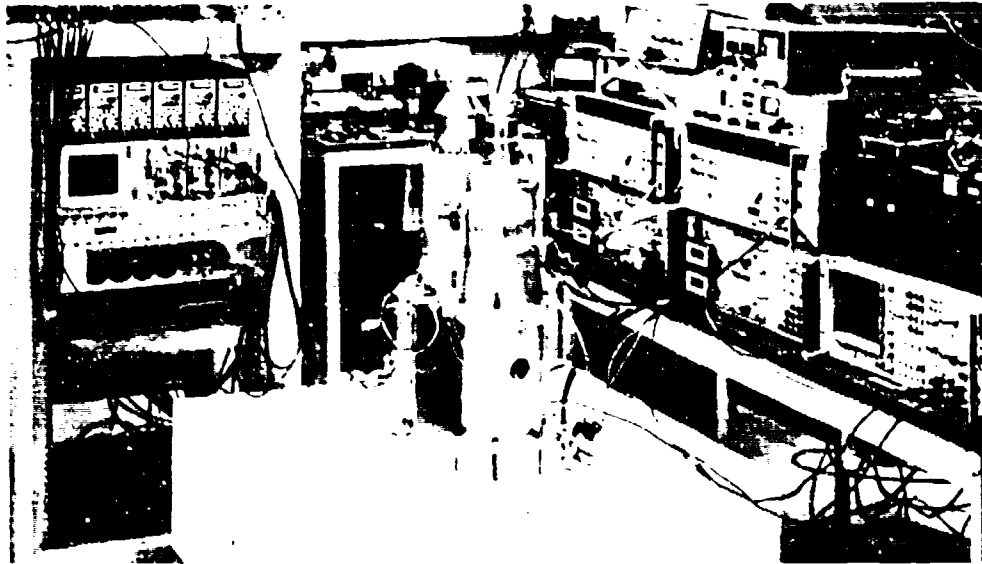


Fig. 4. Vibration characterization of back-to-back BAe 80K coolers on JPL's force dynamometer.

particularly important because it cannot be canceled by running two coolers back-to-back. Note also the high level of high frequency harmonics present in the generated forces. This high level of upper harmonics is particularly evident in the spectral analysis shown in Fig. 6 and has important implications relative to exciting possible cooler and instrument resonances far removed from the cooler's fundamental 40-Hz drive frequency.

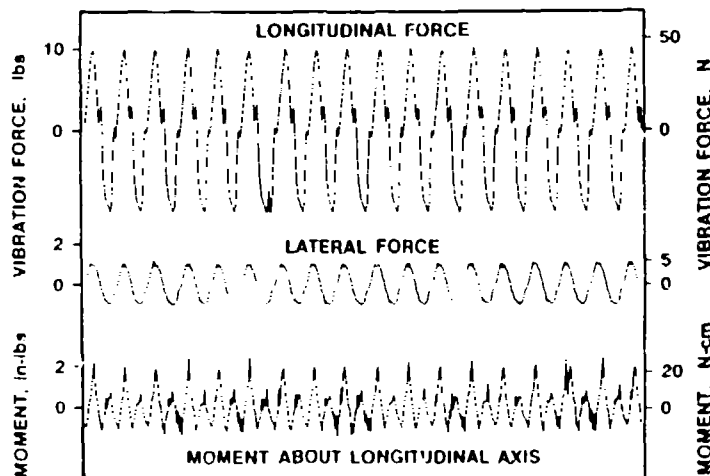


Fig. 5. Typical vibration force versus time for single BAe 80K compressor with conventional BAe lab electronics.

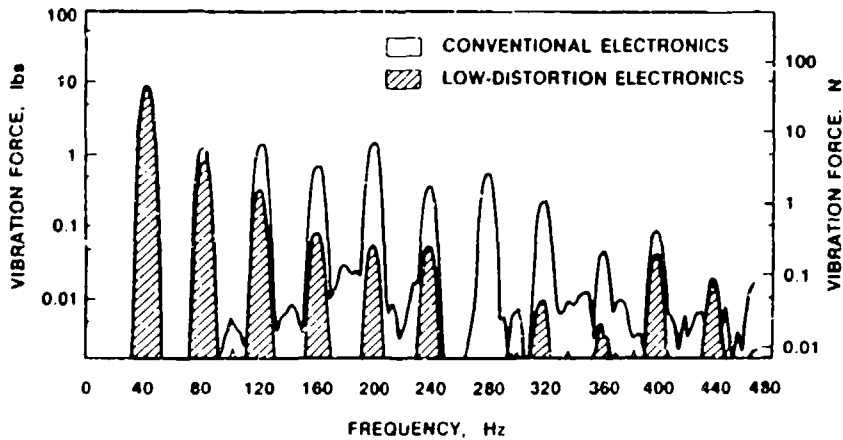


Fig. 6. Influence of electronic drive distortion on the vibration force spectrum of a single BAe 80K compressor.

During the course of the research it became evident that the harmonic purity and closed-loop control implementation within the compressor drive electronics plays an important role in the generation of upper harmonics. As a result, a very low distortion amplifier and high purity function generator were substituted for the conventional closed loop compressor drive electronics. The significant improvement achieved with the low distortion open-loop drive is illustrated in Fig. 6. Even greater reductions were achieved in the lateral direction.

With the help of a second cooler from BAe/TRW, a variety of tests have been conducted with two coolers back-to-back to access the levels of vibration cancellation achievable, and the sensitivity of the nulling to various operational parameters. In general, it was found that open-loop back-to-back nulling of the 40-Hz fundamental is relatively easy to achieve with the visibility provided by the force dynamometer; however, when this is done, the 80-Hz harmonic is nulled to a lesser extent, and little if any cancellation occurs in the upper harmonics (120 Hz and up). The poor cancellation of the upper harmonics makes the net vibration of a back-to-back compressor pair quite sensitive to the harmonic purity of the drive electronics as shown in Figs. 7, 8 and 9.

With high purity electronics (Fig. 9), significant (100X) reductions in vibration were achievable with back-to-back coolers. Lowering the levels further required simultaneous nulling at multiple frequencies using injected harmonics phase-locked to the 40-Hz drive oscillator. This complex open-loop nulling, shown in Fig. 10, resulted in most harmonics near or below the 0.2-N (0.05 lb) goal.

Tests of the vibration force of the displacers revealed vibration spectra similar in harmonic content to those generated by the compressors, but with lower levels, as expected. Because the level of vibration cancellation achievable with back-to-back displacers was less dramatic than with the compressors, the residual forces were comparable. An overview of the forces for both compressors and displacers is

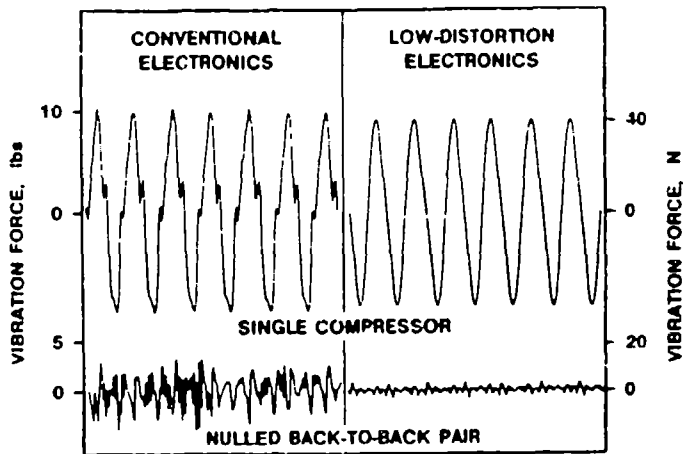


Fig. 7.
Influence of electronic drive distortion on compressor vibration levels.

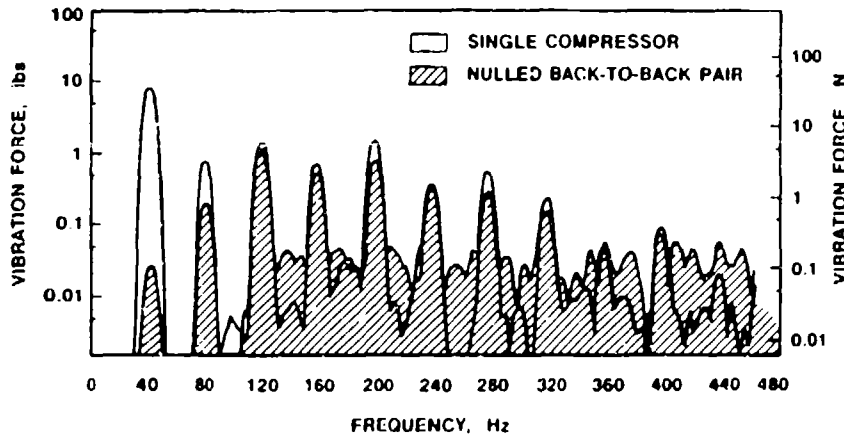


Fig. 8.
Vibration force reduction achieved with back-to-back compressors and conventional compressor drive electronics.

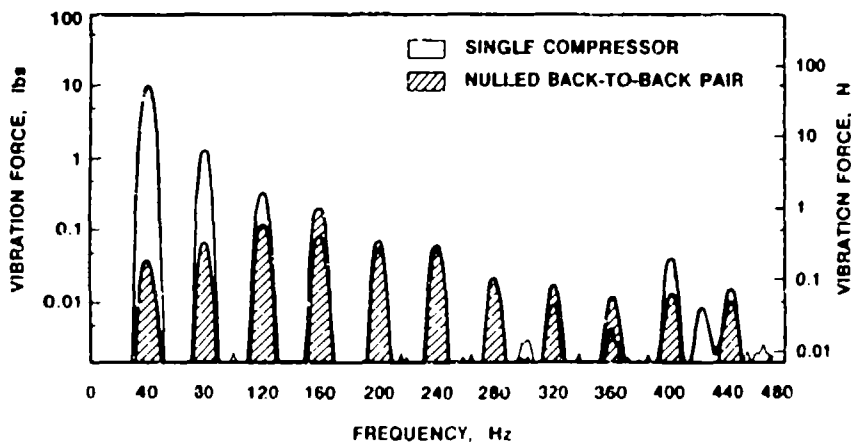


Fig. 9.
Vibration force reduction achieved with back-to-back compressors and low-distortion drive electronics.

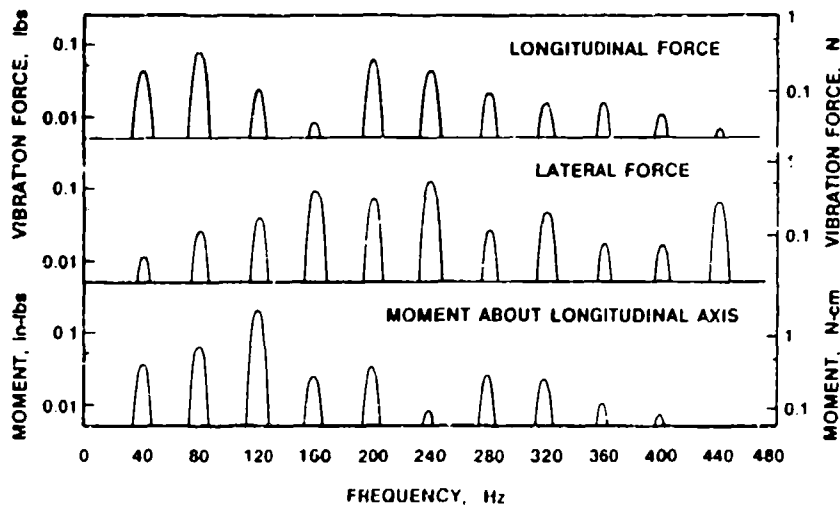


Fig. 10. Low-level residual forces achieved with back-to-back compressors and low-distortion drive electronics with 40, 120 and 160 Hz nulling.

is presented in Table 1. Note that the harmonic purity of the compressor drive electronics had a modest (2x) effect on the net vibration of back-to-back displacers.

Although the overall level of nulling of both compressors and displacers was found to be relatively insensitive to many parameters, such as the radial alignment of the back-to-back units (up to 1.5 mm)⁵, most operating parameters such as piston stroke and operating temperature had significant effects. This implies that some sort of active closed-loop nulling will be required for flight coolers.

Table 1. Summary of RMS Vibration Forces and Moments for BAe Cooler

Configuration	Longitudinal Force lbs. (N)	Lateral Force lbs. (N)	Moment about Piston axis in-lbs. (N-cm)
Single Compressor, Conventional Elect.	9.60 (43)	1.00 (4.5)	1.20 (13.5)
Dual Compressors, Low-distortion Elect.	0.09 (0.4)	0.12 (0.5)	0.20 (2.26)
Single Displacer, Conventional Elect.	0.40 (1.8)	0.80 (3.6)	0.20 (2.26)
Dual Displacers, Conventional Elect.	0.18 (0.8)	0.05 (0.2)	0.03 (0.34)
Dual Disp., Conv. Elect. w/Low-dist. Comp.	0.09 (0.4)	0.09 (0.4)	0.03 (0.34)

RELIABILITY CHARACTERIZATION

Although good efficiency and low-vibration are necessary conditions for successful space application, lifetime and reliability are probably the issues currently most responsible for limiting the use of Stirling cryocoolers in space. There is sharp contrast between the demonstrated reliability to date with Stirling coolers in space and the requirement for 5 to 10-year life with 0.95 reliability.

The historical lack of reliability in mechanical coolers stems directly from their extreme sensitivity to both gaseous and particulate contamination. Any gaseous contaminant such as water vapor or hydrocarbon gases is gettered to the cold end of the cooler where it condenses or freezes and inhibits the refrigerator function. This places rigorous constraints on the purity of initial refrigerant gases, on the degassing of internal cooler surfaces, on the use of any potential outgassing materials such as polymers, and on any degradation mechanisms that could lead to the generation of contaminant gases.

Directly tied to the problem of contamination is the problem of wear, because the lubricity or wear tolerance of most surfaces is strongly tied to the presence of lubricants and surface plasticizers -- most of which outgas contaminant gases. The result has been an unwritten rule that a long-life cryocooler must avoid rubbing surfaces. The flexure bearings and piston clearance seals incorporated into the Oxford Stirling-cooler design are examples of the application of this rule.

Unfortunately, in trade for the exclusion of rubbing surfaces, linear Stirling coolers of the Oxford type must contend with a strong sensitivity to manufacturing and assembly precision and to cooler dimensional stability. Both this assembly sensitivity as well as the sensitivity to contamination and leakage raise the possibility of modest unit-to-unit variability in life and reliability.

A second challenge, closely related to the challenge of achieving high-reliability, long-life refrigerators, is measuring their life. This is particularly difficult because there are no accepted means to accelerate the degradation mechanisms in a quantitative way, and no obvious means of measuring a cooler's reliability other than running it until failure occurs. This stresses the importance of developing means for qualifying coolers for space application, and for running acceptance tests on each flight unit. Dealing with expected unit-to-unit variability will require diligent manufacturing controls to be developed in addition to the specialized qualification tests and screening techniques for flight units.

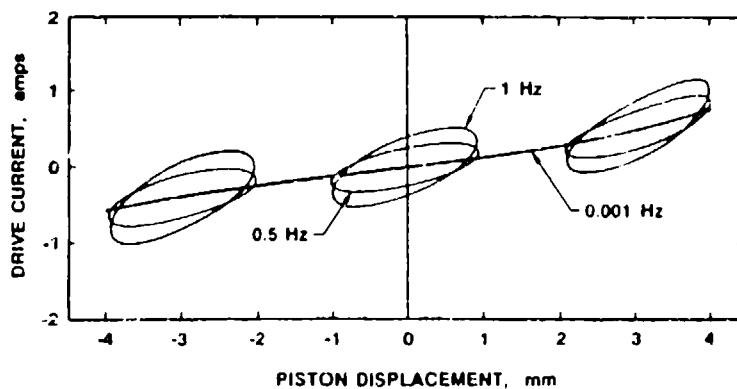


Fig. 11. Characterization and verification of piston clearance using ultra-low-frequency drive.

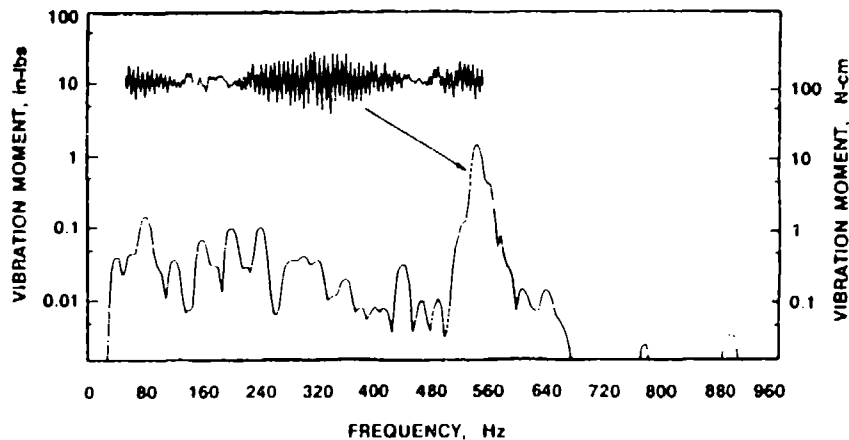


Fig. 12. Possible deleterious high-frequency resonance excited by low-level noise in cooler drive electronics.

In support of these needs, one set of reliability investigations at JPL has centered on developing non-destructive screening tests for piston and displacer clearance. One trial technique, illustrated in Fig. 11, involves driving the cooler at extremely low frequencies (0.001 to 1 Hz) and plotting the required drive current -- which is proportional to drive force -- versus piston displacement. At these low frequencies, gas pressure is extremely sensitive to piston clearance, and rubbing is immediately apparent as stiction or discontinuity in the current-displacement plot. As opposed to the standard "pluck test", which uses piston resonant decay to assess clearance during construction, this test is useful under a wide variety of post-build environmental conditions.

A second, related reliability issue is the possibility of dynamic piston contact during operation; such contact could be caused by radial oscillation of the piston excited through cross-coupling with one or more of the upper harmonics of the 40-Hz drive frequency. Unfortunately the degree of cross-coupling and the amplification level can be quite sensitive to the details of the cooler's structural mount. Figure 12 illustrates a high-level self-induced resonance in a test cooler as seen on the force dynamometer. Such resonances could severely impact the reliability of the cooler during operation and need to be attenuated to the maximum extent possible.

SUMMARY

Meeting the performance goals of near-term space-science instruments places demanding requirements on long-life space Stirling-cycle coolers. The most stringent of the requirements is 1-watt cooling at 55K with minimum levels of cooler-generated vibration and EMI; this must be achieved continuously over a 5 to 10-year timeframe with a reliability greater than 0.95. These requirements surpass the demonstrated performance of existing Stirling-cycle coolers such as the ISAM's Oxford cooler, and require that advanced second-generation coolers be developed and qualified by the mid 1990's.

An important element of the development of these advanced coolers is identifying and understanding the detailed user interface requirements of the intended applications and building on the strengths and limitations of the evolving cooler technologies. Active collaborative characterization and testing by the user community is an important step in this process.

This first phase of testing at JPL has highlighted the need for standardized thermal measurement techniques, particularly with respect to controlling parasitic heat loads on the cold finger, and has illuminated a number of issues relative to achieving acceptably low levels of cooler generated vibration. Although just beginning, reliability testing, including the development of special non-destructive accelerated reliability screening tests, is an important focus and critically needed to allow the early diagnosis and resolution of potential life-limiting failure mechanisms. This area of activity is expected to be a major JPL focus in the future.

ACKNOWLEDGEMENT

The work described in this paper was carried out by the Jet Propulsion Laboratory, California Institute of Technology, under a contract with the National Aeronautics and Space Administration. The collaborative support of British Aerospace, who provided the second cooler for back-to-back testing, and TRW, who participated in the testing are graciously acknowledged. P. Peaster and B. Jones of BAe and W. Burt and R. Orsini of TRW made important personal contributions.

Particular credit is due D. Moore of JPL who designed the 6-degree-of-freedom force dynamometer and its related fixturing and C. Larson who coordinated the instrumentation setup and calibration. Advances in the thermal performance instrumentation were principally the work of W. Petrick and W. Boulter. The financial support of JPL's Eos-AIRS instrument is graciously acknowledged.

REFERENCES

1. Werrett, S.T. et al, "Development of a Small Stirling Cycle Cooler for Space Applications", Adv. Cryo. Engin., vol. 31 (1986) 791-799.
2. Davey G. and Orłowska, A., "Miniature Stirling Cycle Cooler", Cryogenics, vol. 27 (1987) 148-151.
3. Lewis, C.A., "Long-life Stirling-cycle coolers for Applications in the 60-110K Range: Vibration Characterization of Thermal Switch Development", SAE Paper 891496, Society of Automotive Engineers, Warrendale, PA (1989).
4. Larson, C., Mauritz, A. and Moore, D., Development and Application of a Sensitive Six Axis Dynamometer, JPL Internal Report D-6611, Jet Propulsion Laboratory, Pasadena, California (1989).
5. Collaborative testing with W. Burt and R. Orsini of TRW.

THE USE OF CRYOCOOLER FOR COMPUTER COOLING

Hsien-sheng (Jason) Pei & Stephen Heng
Digital Equipment Corporation
Northborough, Massachusetts

ABSTRACT

This paper discusses the requirements for developing a cryocooler for computer cooling. For computer cooling applications, the cryocooler must perform more than the basic cooling function in order to meet the needs of today's computer market. There are more than 20 different factors that should be examined when the cryocooler is being considered, since it has a significant impact on the overall system characteristics such as: (1) physical size, (2) reliability, (3) energy, (4) cost, (5) acoustic noise, (6) vibration, (7) customer service, (8) safety, and (9) EMI/RFI. This paper provides discussions on some of these issues.

1. OVERVIEW

This paper discusses the general requirements (and challenges) that arise when utilizing cryocoolers for the cooling of modern computers. It reviews four very critical issues concerning the cryocooler: reliability, maintainability, acoustic noise, and vibration. It also emphasizes the importance of adequate specification, performance monitoring, and reliability qualification as the three key technical elements for the improvement of the cryocooler's continuous operability. Continuous operability is one of the key challenges encountered when utilizing the cryocooler for computer cooling. The definition of "failure" for the cryocooler is discussed with examples to demonstrate the need to establish limits on performance degradation. The failure modes of some cryocoolers are identified. The performance degradation characteristics of cryocoolers used in computer cooling are reviewed. The technology and methods used to monitor and correlate degradation and impending failures are discussed.

1.1 NEEDS

Recent CMOS advances have significant impact on the design of workstations. The scaling and packaging improvement of basic CMOS devices, including the merging of integer and floating-point capabilities onto a single chip, will continue to drive

the performance of computers in the 1990's. The concept of cryogenically chilled CMOS is not new; the widely accepted performance gain that can result from the application of cryogenic chilling, can benefit a wide range of commercial and technical applications. With proper process design using today's technology, the CMOS devices are also expected to be so reliable at cryogenic temperatures that it will not be factor in the overall system reliability calculation. In addition, the use of refrigeration for computer cooling also provides the opportunity to integrate the computer cooling system with the building heating/cooling system, which increases the total system availability, and reduces the total energy consumption and building system cost associated with computer cooling. ¹

In recent years, the development of low-temperature refrigerators have been spurred by the need for reliable cryocoolers for use with special sensors and for superconducting devices and systems. This need has provided the impetus for the development of new cryocoolers and the continued refinement of various components associated with the device. Some of these refrigerator developments and component improvements are highlighted in references 2 and 3. As concluded in reference 2, considerable strides have been made, but more have to be accomplished before the desirable reliability is achieved. Since some of the requirements for cryocoolers in computer application are even more demanding when compared with those applications discussed in reference 2, there is a far more critical need for the development of reliable and cost effective cryocoolers for computer cooling applications.

1.2 IMPACTS

The purpose of the cryocooler is to service its intended end function. For computer cooling, the intended end function is "chilling". However, the cryocooler must provide more than just perform the basic equipment chilling function in order to meet the needs of today's market. There are more than 20 different factors that should be examined when the cryocooler is being considered. ⁴ As in most engineering design, the optimum solution will result from a series of trade-offs. Any single factor may alter the choice of the cryocooler. When the cryocooler is used for computer cooling, it is a key element in the computer system, and has a significant impact on the overall system characteristics.

Examples:

- | | | |
|-------------|---|--|
| Physical | - | Cryocooler may occupy a significant portion of the system volume. The space required for the cryocooler may be more than that required for the power system and may exceed 50% of the system volume. |
| Reliability | - | Cryocooler will be one of the key reliability elements of the entire system and may even be the dominant reliability element. |
| Energy | - | Cryocooler will have significant impact on the energy usage of the computer systems. |
| Cost | - | Cryocooler may exceed 10% of the system hardware cost. |
| Acoustics | - | Cryocooler may be the key source of acoustic noise. |

Vibration	-	Cryocooler may be the key source of self-induced vibration which will have great impact on the integrity of system interconnections.
Customer Service	-	Cryocooler may contribute substantially to the Service cost for maintaining computer systems in the field.
Safety	-	Cryocooler safety issues and agency approval may be the gating item on meeting time-to-market of some computer systems.
EM/RFI	-	Cryocooler will be one of the sources generating conducted and radiated noise.

2. RELIABILITY

For computers, reliability is the main thrust in designing for performance. This section addresses several critical reliability related issues such as degradation and specification format. ^{4,5,6}

2.1 DEGRADATION

Excessive performance degradations have been exhibited by some cryocoolers in computer cooling applications. ⁷ In order to specify the failure rate (or life) of a cryocooler, the first item that must be defined is the term "FAILURE". For a cryocooler, failure has to be defined as the degradation condition when it fails to meet the minimum or exceeds the maximum limits of the specification. For example, the cryocooler shall be considered a "FAILURE", when:

- its power consumption is increased by $U\%$, which will have an impact on the power supply,
- its self induced vibration is increased by $V\%$, which will have an impact on the integrity of system interconnections (electric, hydraulic, pneumatic, and mechanical),
- its acoustic noise level is increased by $W\%$, which will violate the product label value on noise.

Thus, for a cryocooler, the definition of "FAILURE" cannot be "TOTALLY DEAD". The true useful life of a cryocooler is determined by the amount of degradations that can be tolerated before the system ceases to properly perform its function. This useful life has to be based on the quantitative effects of wear and on the limit set for performance degradation. The extent of the change in performance due to degradation (such as U , V , and W) cannot be generalized, since they all depend on the margins of the system design (such as redundancy) and safety factors which are built into the cryocooler specification.

To ensure system integrity and system quality, the useful life of a cryocooler is based on the maximum allowable degradation in its performance requirements as established in the specification for the cryocooler. Table 1 lists some of the parameters that will impact the performance of the cryocooler.

Table 1: Examples of Degradation in Performance.

1. increase in acoustic noise
2. reduction in flow rate (or speed, etc.)
3. increase in EMI
4. reduction in energy output
5. increase in EMP
6. change of start up torque
7. increase in the requirement of start up voltage or current
8. increase in RFI
9. increase in electric noise
10. increase in power consumption
11. increase in self induced vibration
12. leakage (air, water, electric, etc.)
13. change of temperature
14. change of pressure

Table 2 lists some of the common parts/causes contributing to one or more failure modes identified in Table 1.

Table 2: Some Common Parts/Causes for Cryocooler Failures.

	1	2	3	4	5	6	7	8	9	10	11	12	13	14
	(see Table 1 for description)													
a. electronic parts	x	x	x	x	x	x	x	x	x	x				
b. control		x	x	x	x	x	x	x	x	x				
c. bearing	x	x	x	x	x	x				x	x		x	
d. bellows		x		x	x	x				x	x		x	x
e. motor		x	x	x							x		x	
f. lubricant	x	x	x		x					x	x		x	
g. fastener	x	x			x	x				x	x			
h. adhesive	x	x			x	x				x	x			
i. vibration isolator	x	x		x			x			x	x			
j. seal		x		x								x		x
k. contamination	x	x		x	x	x				x	x		x	x
l. acoustical material	x	x		x							x			
m. valve	x	x		x	x	x				x	x	x		
n. coupling	x	x		x	x	x				x	x			
o. washer	x	x		x	x	x				x	x	x		
p. housing	x	x		x							x	x		
q. process (such as outgassing)	x	x	x	x	x	x	x	x	x	x	x	x	x	x

The extent of the change in performance degradations cannot be generalized, since they are dependent on system design redundancy and built-in safety factors. Table 3 lists examples of values that may be considered for the maximum allowable degradation of performance criteria.

Table 3: Maximum Allowable Degradation In Performance Over Product Life Time.

Performance	Maximum Degradation
1. increase in acoustic noise	2 dB
2. reduction in flow rate (or speed, etc.)	15 %
3. reduction in energy output	15 %
4. change in start up torque	20 %
5. increase in start up voltage or current	15 %
6. increase in power consumption	15 %
7. increase in self induced vibration	5 dB

2.2 CRYOCOOLER RELIABILITY

L-10 (the time during which 90% of the population can be expected to survive, 10% having failed) can be used to specify cryocooler life. The term "Reliability" denotes the probability that a specimen from a product population will continue in service at some specified time. The concept is frequently expressed in terms of "MTBF", that is the average service time accumulated by the product between successive failures of a member. It is the reciprocal of "failure rate", which is the number of failures per unit of operating time. The exact significance of this measure for the broader concept of reliability is dependent on the way in which failures in the population are distributed over time. That distribution also provides the relationship between reliability and life. Unlike ICs which tend to have a decreasing failure distributions, cryocoolers with BLDC motors can have components with every type of failure.

- increasing,
- constant,
- decreasing.

Thus, cryocoolers do not have constant rate of failure. For most cryocoolers with BLDC motors, their life characteristics are represented by Weibull functions. There are indications that for many cryocoolers, some components (such as the motor electronics or bellows, for example) might dominate failure mode for the short period (early in life), and mechanical failures would dominate after the products are in service for a long period of time. Table 4 represents an adequate format for describing or for specifying the life of cryocoolers. Only hypothetical MTFB values are used in Table 4 to demonstrate the concept of the "format".

Table 4: Reliability Specification Format.

	"Hypothetical" Steady State MTBF, in hrs				
	1st Year	2nd Year	3rd Year	4th Year	5th year
MTBF					
at 40 C	see note	1200K	1150K	850K	450K
ambient					

Note: During the first year, motor electronics' or other component's infancy is the dominate failure factor.

3. MONITORING

Predictive maintenance programs based on the periodic monitoring of critical system parameters are well known and their success is well documented. It supplies the periodic data that is necessary for the prevention of catastrophic failures, and also permits optimal scheduling of preventive maintenance. For monitoring the performance of cryocoolers, analyses of the degradation trends provide the ultimate prediction of an impending failure. This prediction process can be summarized as follows:

- monitor or detect degradation (level, in time or frequency domain),
- identify/differentiate degraded components,
- predict the remaining life by extrapolating the degradation trends to project when unacceptable performance level will be reached and therefore determine when the machine must be serviced.

3.1 AVAILABILITY

For the computer cooling function, the availability of certain machinery is so critical to production and profitability that it is not sufficient to only have monthly or even weekly monitoring. In such instances, it is essential to maintain continuous, on-line monitoring. Furthermore, for computer cooling, it will not be economically practical to implement frequent standard maintenance practices (which are common to other industries - such as warming up the refrigerator at least once a week for decontamination of the vacuum cold trap) to reduce degradation. The following techniques are examples used in the control and monitoring of computers, in which the intended goal is to attain higher availability: ^{8,9}

- component redundancy,
- preventive maintenance,
- predictive maintenance system.

References 8 and 9 both describe examples of control and monitoring systems for computers cooled with chilled water. The cooling systems include a spare pump and chiller. Each of which operates automatically if any of the regular pumps or the chiller fails. In these computers, module temperature, freon gas temperature, water flow rate, water leakage, quantity of water and water temperature are monitored and switches to the standby units if a serious malfunction occurs in the chiller or pumps. The cooling system has two failure levels - the first level is the warning level and it implies a non-fatal failure, that is failures of components with redundant parts, so the cooling system can continue to operate. The second failure level is the shutdown level, which requires the cooling system to stop immediately. These information on the failure levels are all displayed on the maintenance panel and reported to the service processor.

3.2 DATA BASE

The prediction of machinery life is generally handled by establishing limits based on previous experience. For predictive maintenance systems, a good data base for decision making is as important (if not more) as the hardware for data collection and signal processing (both in time and frequency domain). An example of the importance of good data base is given by reference 10, which describes the technical base for an EKG Multiphase Information System (EMPI) with a qualitative diagnostic rate of 85 to 90% and a differential diagnostic rate of 70 to 90% (that can differentiate 8 common heart diseases). Two key reasons contribute to the success of EMPI over the conventional EKG heart machine - one reason being its capability to utilize the power spectrum, phase shift, coherence function, impulse response, cross correlation and amplitude histogram to analyze the EKG wave forms, and the other reason is that it has an enormous clinical data base (collected over the past 10 years) to generate reliable indicators.

Although a cryocooler is not as complicated as the human heart, a good data base is also a prerequisite for any successful cryocooler monitoring system. Failures of cryocoolers are often very difficult to generalize. The time taken for a cryocooler to progress from fault initiation to catastrophic failure varies greatly with the type of cryocoolers, the type of applications, etc. Some cryocoolers degrade slowly over time while others may seem to fail quickly without any advance warning. To minimize the cost of cryocooler failures and to maximize the availability of critical equipment, a good data base is essential for the identification of faults and degradations in a cryocooler.

4. ACOUSTIC NOISE AND VIBRATION

For computer cooling, the cryocooler will be the major source of acoustic noise and self-induced vibration. Recent developments in semiconductors and superconductors have opened up the potential for extensive application of cryocoolers in the computer industry. However, as in other applications, the inherent vibration and the acoustic noise associated with some cryocoolers may preclude their use for computer cooling.¹¹

¹¹ For certain types of cryocoolers, the acoustic noise emitted by these devices may be the limitation to their potential cooling applications. ¹² This section reviews the acoustical requirements and the acoustic measurement methodology for cryocoolers used in computer cooling in general.

4.1 REQUIREMENTS

Since the cryocooler will often be the key source of acoustic noise, the EEC-directive 89/392 of 14 June 1989 on the approximation of the laws of Member States relating to machinery (so-called "machinery safety directive") is only the minimum requirement for cryocoolers that will be sold in the huge EC 92 market. In addition to all the regulatory requirements, it has been increasingly evident that the acoustical quality of computers has become a very important element of decision making which the consumer applies when purchasing equipment. Cryocoolers will have to be designed for more stringent requirements as established by the various computer companies in order to meet their special market needs. The task of lowering the noise generated by cryocoolers is assuming increasing importance, for both commercial and regulatory needs. References 13 and 14 provide some insights on the directions and trends.

4.2 MEASUREMENT

The measurement of cryocooler acoustic noise requires extremely careful control of a multiple of variables (including the cryocooler operating conditions and test system configuration) in order to obtain useful results. During the past decade, the trade associations representing the U.S. and the European computer industries have reached an agreement on the measurement methods for their products. These measurement methods have been standardized nationally and internationally. Whenever possible, acoustical measurements should be integrated into the cryocooler general performance measurement procedures in order to produce the most useful data. American National Standard Institute standard S12.10 (Method for Measurement and Designation of Noise Emitted by Computer and Business Equipment) has been integrated into several refrigerator performance measurement and rating standards. Examples are ANSI/ASHRAE 127P for Air Conditioner, and ANSI/ASHRAE 128P for Spot Cooler. Reference 15 provides a summary of many useful acoustical standards.

5. SPECIFICATION AND QUALIFICATION

The importance of an adequate specification and qualification plan cannot be over-emphasized for cryocoolers that will be used in mass produced products for the consumer market. It is the link between:

- performance requirements,
- procurement for life cycle total cost,
- acceptance test (proto-type, pre-production, production, etc.),

- vendor process control and ongoing quality conformance,
- etc.

The structures of a complete specification and a detailed qualification plan are very comprehensive and are beyond the scope of this paper. However, this paper will address four general topics: general specification, process requirement (which will be an integral part of the specification requirement), performance qualification and process qualification.

5.1 GENERAL SPECIFICATION

Specifications of cryocoolers shall include both "performance" requirements and "process" requirements as follows:

i mechanical requirements such as:

- material and finish,
- cable and connector,
- fans,
- seal,
- bellow,
- bearing,
- O-ring,
- filter,
- refrigerator,
- heat exchanger,
- motor,
- vibration isolation,
- configuration and dimension.

ii electrical requirements such as:

- voltage range,
- power requirement,
- motor characteristics,
- motor protection,
- transient line voltage protection,
- electro magnetic compatability,
- low voltage start up and start up current,
- current ripple,
- control.

- iii performance requirements such as:
 - thermodynamics,
 - life and reliability (wear out, steady state MTBF for motor electronics, shelf, etc.),
 - acoustic noise,
 - self-induced vibration,
 - quality,
 - maintainability.
- iv environmental requirements such as:
 - temperature,
 - humidity,
 - shock and vibration,
 - altitude.
- v safety requirements such as:
 - agency approval,
 - material certification,
 - regulatory requirements (OSHA, EPA, etc.).
- vi manufacturing requirements such as:
 - material and construction,
 - process and capability,
 - special test and examination.

5.2 PROCESS REQUIREMENT

For the cryocooler, the goal is to incorporate product consistency requirements in the purchase specifications. This implies that "target value", "real engineering tolerance" and "process capability index (C_{pk})" are integral parts of the purchase specification. The requirements imply process control centering around the target value and continued improvement since C_{pk} (as defined in equation 1) shall grow over time (see Table 5). The target value is an "optimal" or "ideal" value and specification limits indicate "acceptable" tolerance. A capable process, maintained in a state of statistical process control, will deliver on-target performance.

$$C_{pk} = \frac{2 * \text{smaller}\{(USL - \bar{X}), (\bar{X} - LSL)\}}{6 * \sigma} \quad (1)$$

where,

\bar{X} = mean of distribution,
 USL = upper specification limit,
 LSL = lower specification limit,
 σ = standard deviation.

Table 5: C_{pk} Growth.

Time in Product Life	C_{pk} Required
Minimum Requirement For Qualification	1.00 or better
Initial Production	1.33 or better
Steady-state, Volume Production	1.50 or better
Mature Process	2.00 or better

For normal distribution, the relationship between C_{pk} values and the % defective is given in Table 6.

Table 6: C_{pk} and Defects.

C_{pk} Values	% Defective
1.00	0.27%
1.33	0.0064%
1.50	0.00068%
2.00	Hardly Any

5.3 PERFORMANCE QUALIFICATION

One important task of any cryocooler development program is to develop test plans and methodology to provide meaningful assurance that performance targets of cryocoolers will be met. The structure of a proper qualification plan is comprehensive and should be a subject in itself. It is beyond the scope of this paper. This paper will only discuss the flow chart for performance qualification and the procedures of process qualification.

For performance qualification, the greatest emphasis should be placed on the cryocooler's parts test/analysis in the early design stages (conception, proto-type and pre-production). Figure 1 shows the minimum requirement for performance qualification with degradation considerations incorporated.

NOTE :

1. PASS = meet specification requirement,
2. <- = flow before reliability test,
3. <<- = flow after reliability test,
4. before (and after) reliability test, the ordering (with the exception of environmental test) in the flow chart is arbitrary and it is often decided by the availability and schedule of the laboratories for qualification test,
5. for the reliability demonstration, MIL STD 781C is used to establish the sample size and test time required for the qualification.

5.4 PROCESS QUALIFICATION

Before the part is qualified, the vendor processes' capability to consistently manufacture parts that meet the purchase specification, have to be demonstrated and qualified. This is to assure that the parts are capable of problem-free installations while minimizing inventory, in-house staging, testing and trouble shooting, along with minimizing field assembly, test and repair. In order to be qualified, the cryocooler manufacturer has to provide manufacturing plans for review and approval. As minimum requirements, the manufacturing plans shall include:

- a. Manufacturing process flow documentation,
- b. Material acquisition and control which include,
 - Purchasing plans,
 - Receiving,
 - Incoming Inspection,
 - Material storage,
 - Supplier management,
 - Material certification,
- c. Process design/capability study,
- d. Process control and audit,
- e. In-process non-conforming material control,
- f. Test equipment, diagnostic plans, calibration and preventive maintenance,
- g. Product qualification, feedback, failure analysis, ECO and documentation control.

6. CONCLUSION

The objective of this article is to provide the cryocooler industry with some requirements for developing cryocoolers for computer cooling. Specific issues on reliability, performance monitoring and acoustic noise were discussed. The importance of the specification and qualification plan was emphasized.

7. REFERENCE

1. Pei, H., "Computer Cooling and Energy Challenge", Proceedings of CLIMA 2000, (1985).
2. Timmerhaus, K. D., "State-Of-The-Art Of Miniature Cryocooler Technology", Proceedings of the Seventh Intersociety Cryogenic Symposium, (1989).
3. Fast, R.W., Editor, "Advances in Cryogenic Engineering", vol. 33, (1988).
4. Pei, H., "Reliability of Motor-Driven Components Used in Electronic Packaging", IEEE Spring Seminar, (April 1987).
5. Pei, H. and J. Tsao, "Predictive Maintenance of Motor-Driven Components Used in Electronic Packaging", Proceedings of IMMDC, (1989).
6. Pei, H. and S. Heng, "Cooling Components Used in VAX 9000 Family of Computers", Proceedings of IEPS, (1990).
7. Novotny, S., "Performance Evaluation of a Gifford-McMahon Refrigerator for Cryogenically Cooled Computer Applications", Proceedings of I-THERM II, (1990).
8. Simons, R.E., "Thermal Sensing and Control for a Large Scale Digital Computer", Proceedings of SEMI-THERM 1, (1984).
9. Watari, T., et.al., "Cooling Technology for the SX Supercomputer", NEC Res. & Develop., no. 88, (January 1988).
10. Feng, G., "Theory and Practice of EKG and EEG Computer Analysis", Scientific Press of China, (1986).
11. Hofer, T., "Concepts For Thermoacoustic Refrigeration and a Practical Device", Proceedings of International Cryocooler Conference, (1988).
12. Minta, M. and J. Stolz, "Vibration Spectra of a G-M Cryocooler With Various Power Supplies", Proceedings of International Cryocooler Conference, (1988).
13. Commins, D., "Europe 92 and Acoustics", Proceedings of INTER-NOISE, (1990).
14. Jacques, J., "Noise Labelling. An Overview of the Concept and Its Practical Implementation.", Proceedings of INTER-NOISE, (1990).
15. Wujek, J., "Summary of National/International Standards and Regulations, Acoustical Noise of Computers and Business Equipment", 2nd Edition, CEBMA, (May 1987).

PERFORMANCE OF A PROTOTYPE, 5 YEAR LIFETIME, STIRLING CYCLE REFRIGERATOR FOR SPACE APPLICATIONS

C. Keung, P.J. Patt, M. Starr, and R. McFarlane
Philips Laboratories, North American Philips Corporation,
345 Scarborough Road, Briarcliff Manor, New York 10566

Abstract

A second-generation, linear, Stirling-cycle refrigerator for space applications, with cooling capacity of 5 Watts at 65°K, was recently completed. The refrigerator, designed for 3-5 year life, uses closed loop controlled moving magnet linear motors for the compressor and expander. The moving elements are contactless, being supported by active magnetic bearings with clearance seal of 20 microns. Fiber-optic sensors detect the radial position of the shafts and provide a control signal for the magnetic bearings. The frequency, phase, stroke and offset of the compressor and expander are controlled by signals from the high bandwidth LVDTs. The vibration generated by compressor and expander is cancelled by an active counterbalance which also uses a moving magnet linear motor and magnetic bearings. The driving signal for the counterbalance is derived from the compressor and expander LVDTs which have wide bandwidth for suppression of harmonic vibrations. The efficiency of the three active members is enhanced by a magnetic spring in the expander and gas springs in the compressor and counterbalance. The magnetic bearing stiffness was significantly increased from the first generation refrigerator to accommodate shuttle launch vibrations.

1. INTRODUCTION

1.1 BACKGROUND

In 1982, Philips Laboratories completed the design and fabrication of a laboratory-grade, Stirling-cycle refrigerator (cooler) for NASA to prove the feasibility of long-life, frictionless operation producing 5 Watts of cooling at 65K in a 20°C ambient. The refrigerator, called the Engineering Model, extended the relatively short maintenance-free life of mechanical refrigeration systems by essentially eliminating wear. This was accomplished by electromagnetically suspending the moving parts of the refrigerator, thereby eliminating contact and the associated wear, and permitting the use of clearance seals rather than contact seals. There were no lubricants and no outgassing materials in the working volume of the refrigerator, thus no degradation in cooling performance due to contamination of the working fluid. The Engineering Model also improved flexibility

of operation by using direct electronically controlled linear drives for the moving elements, thereby allowing adjustment of amplitude and frequency. A life test of the Engineering Model was completed in 1989. The system operated for 5 years with no refrigerator failure and no change in performance over 500 start/stop cycles, and the electromagnetic suspension (magnetic bearings) operated successfully for 7 years. Feasibility and life were thus demonstrated.

1.2 FLIGHT PROTOTYPE

In this paper we describe the performance of a flight-worthy prototype cooler designed and constructed to provide 5 Watts of cooling at 65K and, in addition, to withstand launch and operate in a zero G environment. The design of the prototype cooler has been described in earlier papers [1,2]. However, some changes in the drive electronics have subsequently been made. Most notably, "synchronous" switching amplifiers have been replaced with commercial, highly efficient (90%) wide bandwidth switching amplifiers.

In Section 2 of this paper we will briefly describe the overall system design and design requirements. In Section 3, a summary of bearing analysis and performance will be presented. In Section 4, the basic thermodynamic design specifications and performance measurements are provided. Finally, in Section 5, the mechanical vibration and displacement measurements are given.

2. SYSTEM DESIGN AND DESIGN REQUIREMENTS

2.1 SYSTEM DESIGN REQUIREMENTS

The Prototype Model is similar in design concept to the Engineering Model. Linear moving-magnet motors drive a compressor and an expander, suspended by frictionless magnetic bearings. However, much of the design and the components are different in order that the system meet the requirements of launch survival and long unattended life.

The system is designed for remote as well as local operation, using a two-command sequence. In the standby mode the active elements are suspended but motionless. In the operate mode, the active elements are reciprocated and cold is produced. The major design requirements were:

- Cooling Capacity 5 Watts @ 65K initially with a 20°C rejection temperature, and 5K degradation over system lifetime.
- Life 3 years minimum, 5 year goal with 1,000 on/off cycles
- Ambient Temperature 20 ± 15°C
- Launch Load 3g at dc, 5.4 g at 7 Hz
- Cold End Stability Less than 10⁻⁵ inch lateral motion, less than 10⁻³ inch axial motion

- Power Consumption 250 Watts operating, 50 Watts standby
- Weight 200 lbs, excluding electronic module.

In addition, the refrigerator must reach stable operation in less than 5 hours after start-up, and the short-term temperature change of the cold end under stable operating conditions must be within 0.1K over a 24 hour period. The system must also be operable in any orientation in an Earth environment, in zero G, and on any type of spacecraft without deterioration of performance.

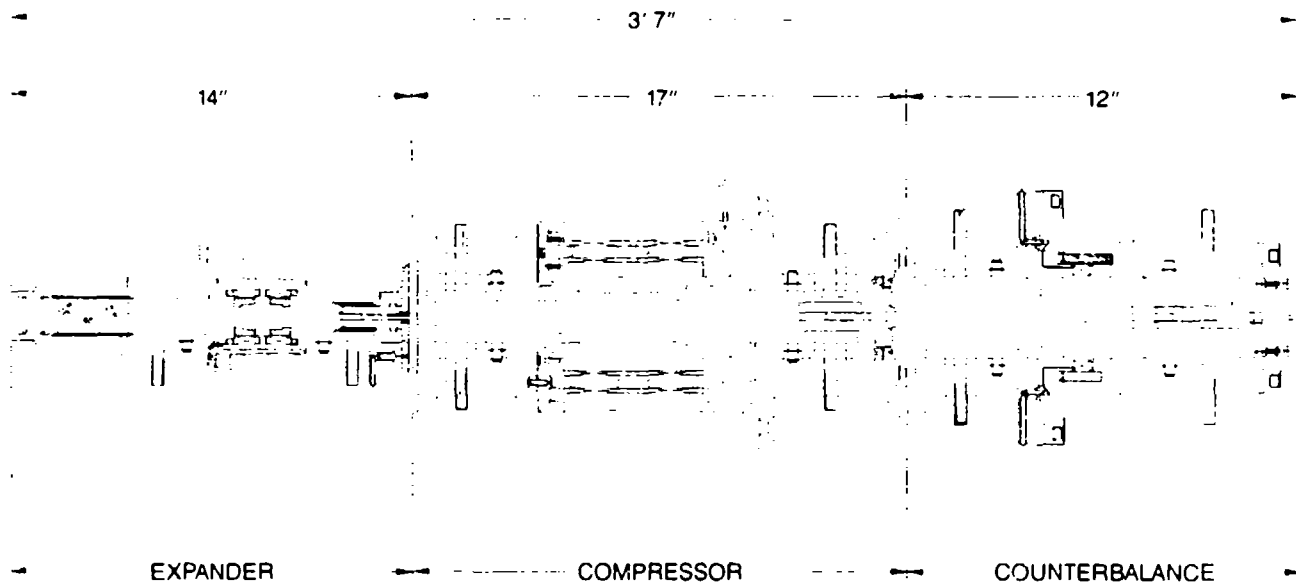


Figure 2-1. Philips/NASA Stirling Refrigerator.

2.2 DESIGN CONFIGURATION

The refrigerator is comprised of a compressor, a single stage expander, and a counterbalance (Figure 2-1). The expander section contains the displacer with a built-in regenerator and the cold and warm side heat exchangers. The compressor contains the compressor piston and piston linear motor. The counterbalance contains the countermass, which is part of the motor armature, and the two gas springs designed to resonate the countermass at the refrigerator reciprocating frequency. All the gas seals are clearance type provided by the magnetic bearing construction. The piston (compressor) and the countermass are reciprocated with a moving magnetic linear motor (no flexing leads). The displacer is reciprocated with an integrated magnetic spring/motor [3]. A photograph of the completed cooler is given in Figure 2-2.

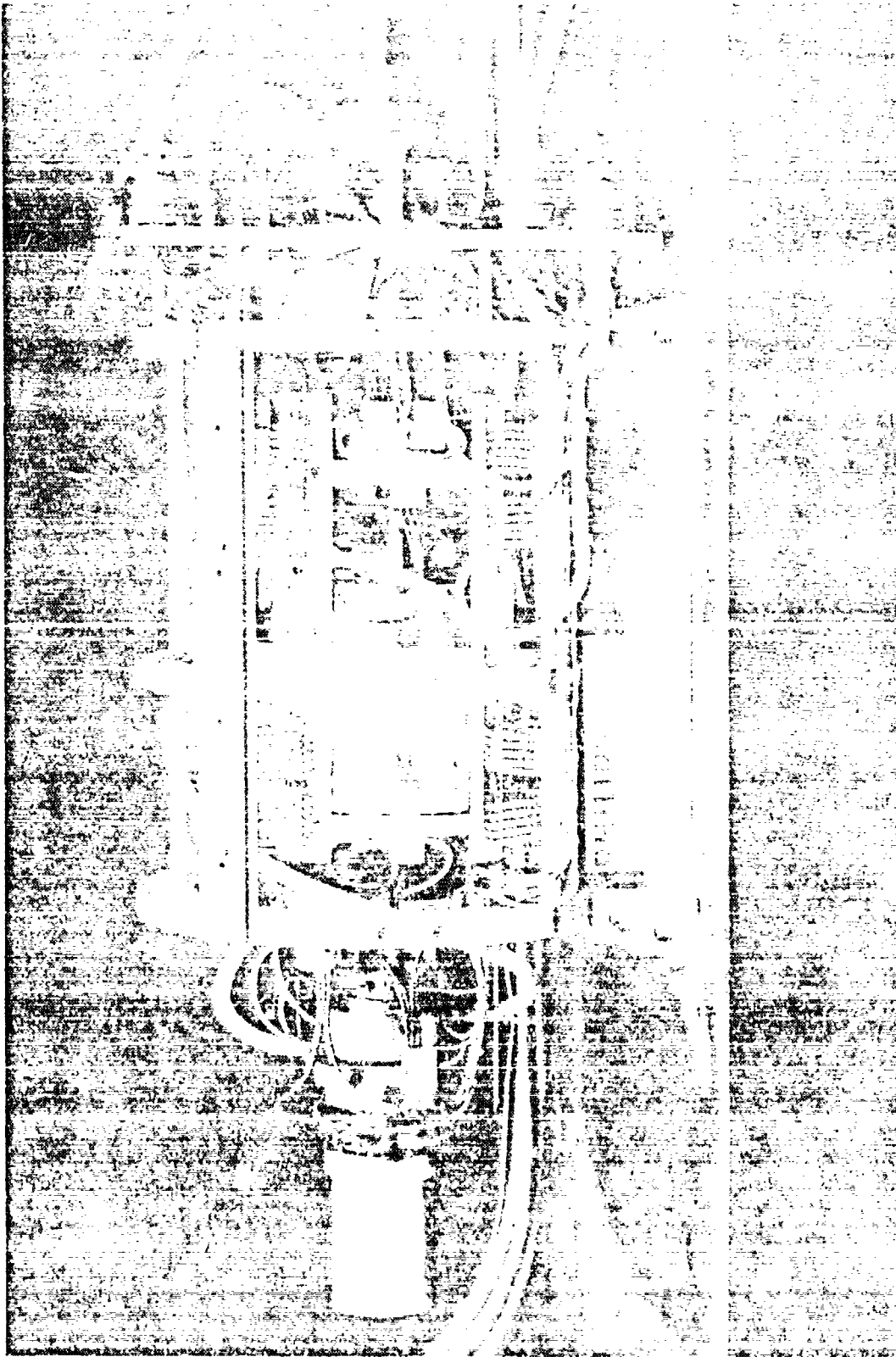


Figure 2-2. Photograph of Prototype Model Cooler.

3. BEARING ANALYSIS

Significant improvements in bearing system performance were needed to meet launch requirements. The control system methodology was based on a classical single-input-single-output approach. Significant improvements in bearing stiffness were achieved primarily through the use of an optical sensor that was flush with the internal bore thus providing high position sensitivity, higher gas damping, and stiffer housings and shafts.

The general design of the linear magnetic bearing actuator is identical to the more popular, conventional active radial magnetic bearing. There are, however, two areas of notable difference. First, significant development was needed to hermetically seal the bearings into the cooler housing. For the Prototype Cooler, this requirement led to the use of "solid" bearings and precluded the use of laminated actuator structures. This resulted in bearings that have eddy currents well within the bearing control loop. As a result, a careful understanding of the frequency dependent behavior of the bearings is essential to a proper modeling and design of the bearing system.

The other significant difference in the behavior of linear magnetic bearings comes from mechanical system considerations. Because these bearings are also used as clearance seals, there is a very narrow gap between the housing and the shafts. Gas damping plays a significant role in shaft dynamics and hence magnetic bearing performance. The gas damping provided by the clearance seals plays a larger role than mass (inertia) in shaft dynamics in the launch and operating frequencies. This is the most important difference between these magnetic bearings and those readily available for conventional rotating systems.

A classical free-body analysis of the bearing system was performed. "Squeeze film" gas damping relationship given by Hays [4] for the finite bearing case ($D/L > 0.1$) were used to predict gas damping forces. Hays' data for the case of one-half of a journal bearing were extended to full journal bearing. Results will be presented for two values of gas damping that should bound the analysis. Simple half-pole eddy current relationships were used to model the frequency dependence of the bearings.

An experimental model was specially fabricated to breadboard the control electronics and test the fiber optic sensors and bearings. The model was designed to emulate the displacer in the prototype cooler.

Even though the test displacer was operated in air, the gas damping is nearly exactly the same as in the cooler. The shaft dynamics, however, were different. Also, the optical sensors had better signal-to-noise ratio in the test displacer. Thus, the high frequency behavior of the test shaft was not identical to that of the cooler. As such, a somewhat different compensation circuit was used that could not be used in the cooler - primarily because of very low gain and phase margins. Nevertheless, the system on the test bench was stable and produced a very high stiffness bearing. The pure lag compensator employed in the test fixture, while providing superb low frequency stiffness, added no phase lead at high frequencies. This resulted in only a marginally stable system, and thus could not be used in the cooler.

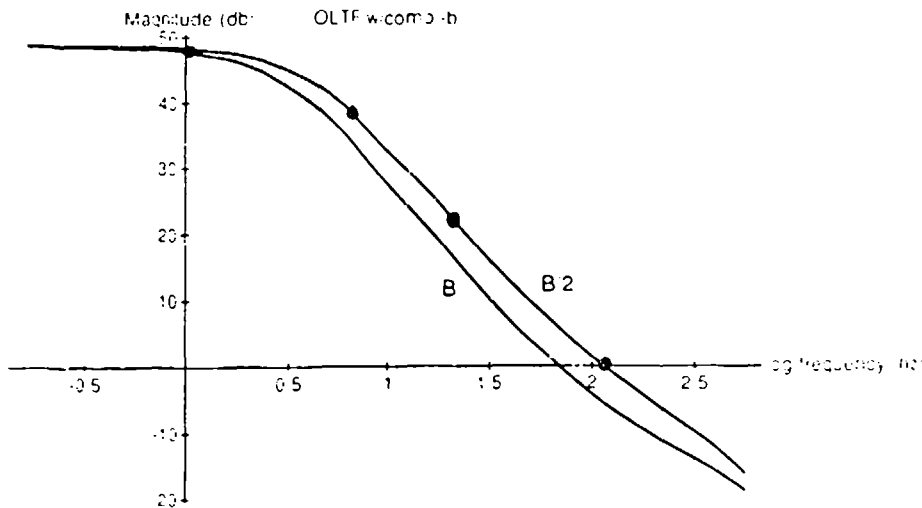


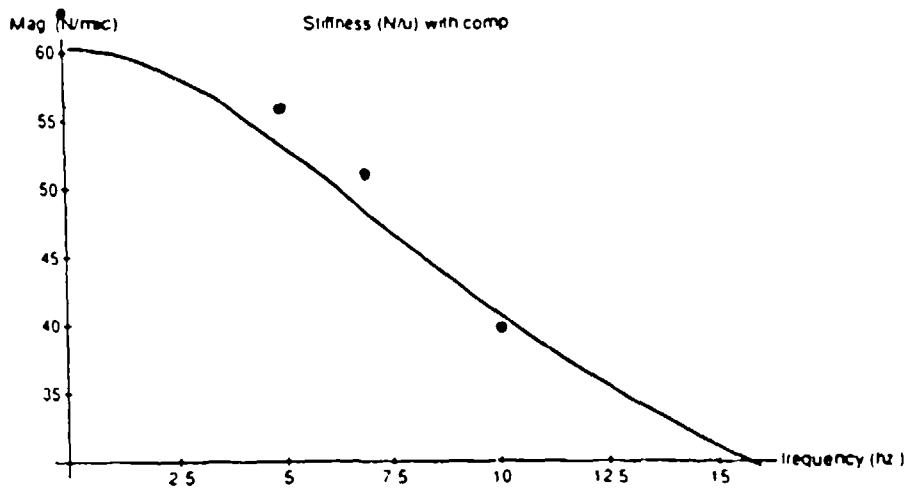
Figure 3-1. Measured and predicted behavior of the open-loop transfer function (OLTF) of displacer bearing in the cooler for two different values of the gas damping factor, B.

Figures 3-1 and 3-2 compares the predicted total effective stiffness and the measured stiffness data. As can be seen, the agreement is quite good. Note in particular the poor "high frequency" stiffness of the loop. This is because the compensator is "rolling off" along with the mass dynamics. Thus, high frequency (40 Hz) disturbances are not really rejected by the bearing control loop and nearly all the stiffness at these high frequencies comes from the gas damping and inertial terms.

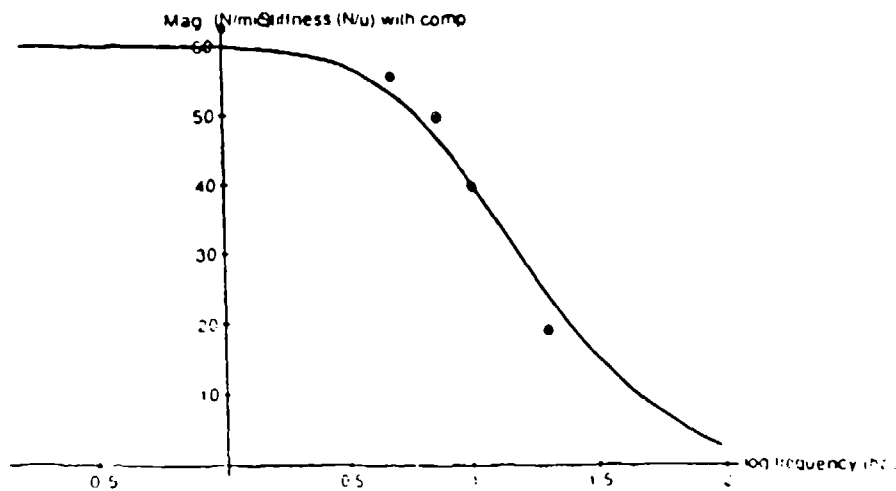
An analysis of the piston and displacer bearings indicated that there was most likely a node, a frequency at which the stiffness was a minimum, at about 50-60 Hz (Figure 3-3). We could not alter the low-frequency stiffness characteristics very much because of the launch requirements and we were limited at high frequencies by eddy currents and system dynamics.

Originally, a synchronous driver (2) was planned for the displacer and piston motors. However, for the available voltage, duty cycle, and motor characteristics, a current spectrum resulted in which the third and fifth harmonics were nearly 15 dB higher than the fundamental operating frequency. Also, we found that the relative magnitude of these harmonics would change with varying duty cycle as the system cooled down.

Thus, the synchronous driver was replaced with a commercially available, conventional high efficiency wide bandwidth drive (> 90%). The resultant piston motor current spectrum at full design conditions is given in Figure 3-4. The reduction in high frequency currents were significant and we were able to bring the system to full desired design conditions with acceptable shaft displacements.



Detail of low frequency behavior on linear frequency scale.



Dynamic behavior of the stiffness of a spacer test bearing over a wider frequency range (log frequency scale)

Figure 3-2. Comparison between measured and predicted behavior of displacer stiffness in bearing test fixture. (Gas damping value $B = 4000 \text{ Ns/m}$).

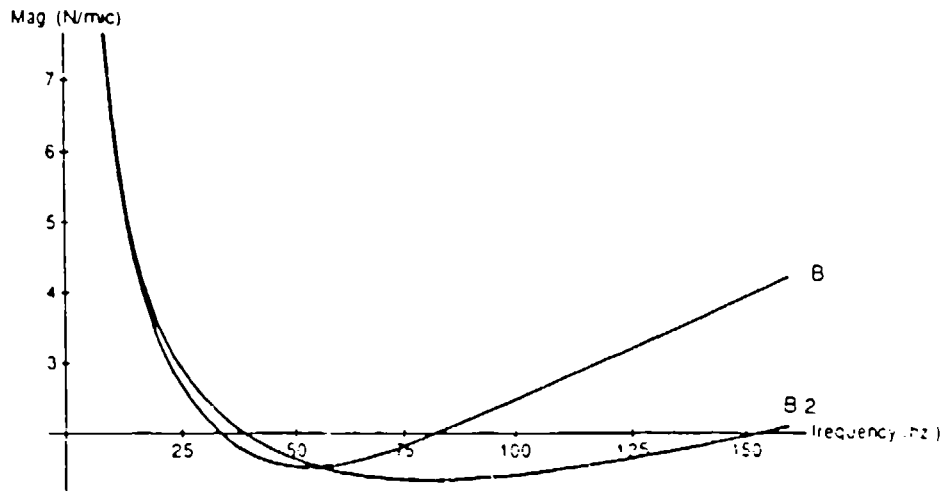


Figure 3-3. Effective displacer bearing stiffness as a function of frequency for two values of damping coefficient, B.

Table 3-1 summarizes the bearing characteristics at DC and at the 7 Hz (mount) launch frequency. The bearings are indeed stiff enough to meet the launch requirements. The data was based on measurements on the open-loop-transfer function as a function of frequency. This was done because we had not facilities to shake the entire cooler and measure displacements.

Table 3-1. Measured Open-Loop Transfer Function at Specific Frequencies and Calculated Bearing Stiffness.

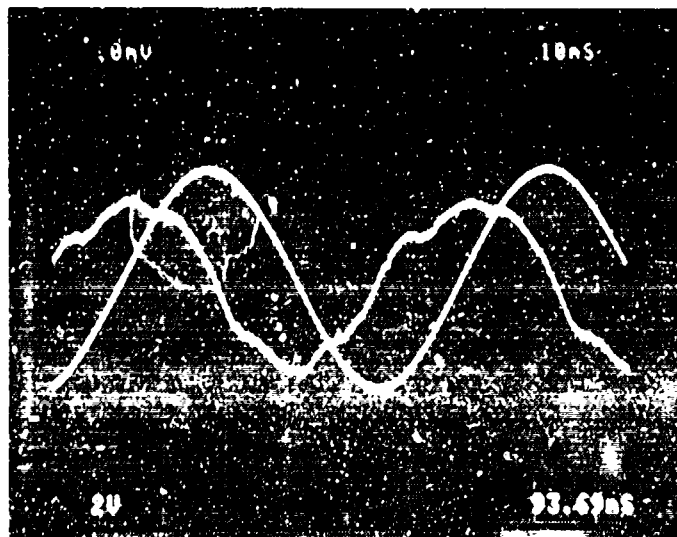
	Measured dc		Measured 7 Hz		Required K_{req} (N/u)*
	OLTF (dB)	K_e (N/u)	OLTF (dB)	K_e (N/u)	
Displacer (Rear)	47	20	39	9	8
Piston (Rear)	50	110	34	60	20
Counterbalance			37	25-50	24

(* Based on a 50% radial displacement and a 8 G load applied at 7 Hz.)

(a) Piston position and piston current.

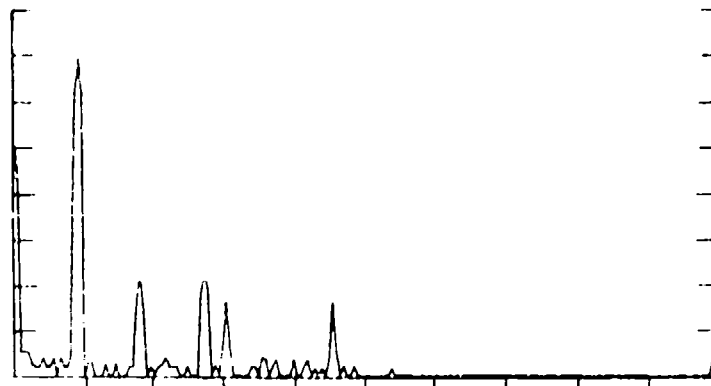
x - 3.6 mm/div.

I - 10 A/div.



(b) Piston motion spectrum.

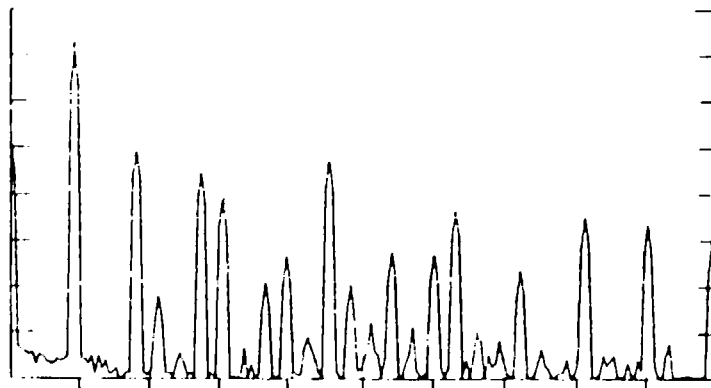
3.6 mm/V



PHS SPECT A : 8.048V 18.10 10.0000 P: 10V
 SPAN: 0.00000 - 200.00000 SEC: 20.000V FS: 20.0000V 1048

(c) Piston current spectrum.

10 A/10 mV

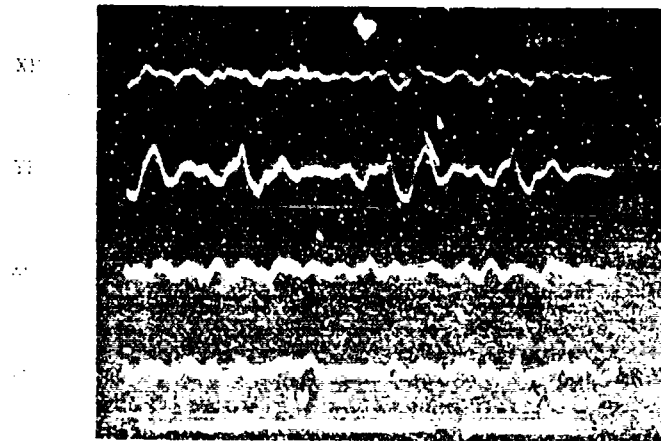


PHS SPECT A : 40.128V 18.10 10.16 P: 10V
 SPAN: 0.00000 - 200.00000 SEC: 20.000V FS: 20.0000V 1048

Figure 3.4. Spectral behavior of piston.

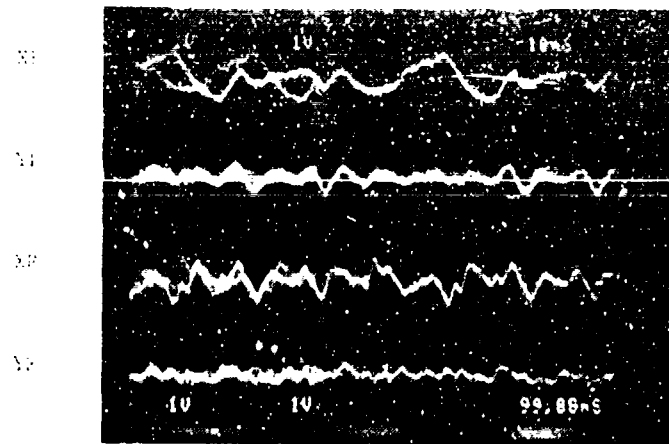
(a) Piston bearing displacements.

3.8 microns/div.



(b) Displacer bearing displacements.

3.8 microns/div.



(c) C'balance bearing displacements.

3.8 microns/div.

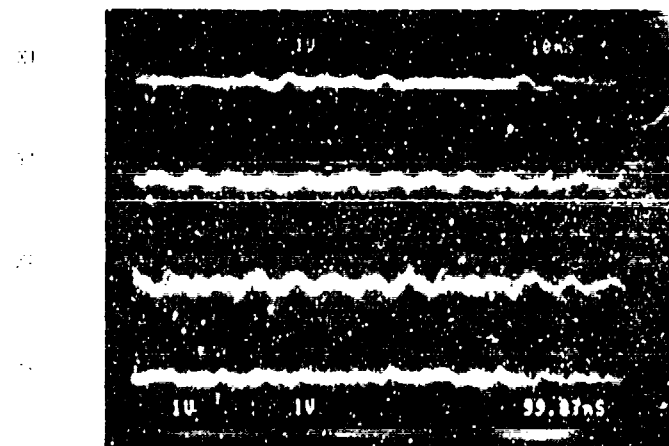


Figure 3-5. Bearing displacement errors.

RADIAL MOTION

Radial displacements of the shafts can be monitored at the buffered outputs of each of the bearing circuits. The radial bearing circuits are calibrated for a ± 5 volt deviation corresponding to the mechanical limits of travel (in all cases: ± 19 micron clearance seal annular gap), yielding an approximate resolution of 4 microns per volt.

Scope photographs of all 12 bearing displacements at the design operating point are included in Figure 3-5. It is interesting to note that the peak bearing excursions vary during cooldown, as the changes in gas temperature and thermodynamic loading affect the harmonic current content of the motor drive currents. Once the system has attained resonance at the operating point, the radial errors are reduced and stable.

4. THERMODYNAMIC DESIGN SPECIFICATION AND PERFORMANCE

The Philips Stirling Computer Program was used to design the refrigerator for minimum input power. The computer results included physical dimensions of the expansion and compression spaces, operating parameters such as charge pressure and speed, and regenerator size and material. Practical considerations of weight, reliability, and complexity of fabrication were then applied to perturb the theoretically optimized design. Throughout the design process, practical consideration and thermodynamic performance were iterated to achieve the optimal, physically-realizable refrigerator. The thermodynamic parameters are summarized in Table 4-1.

The cold production and thermodynamic input power were also calculated by the Philips Stirling Computer Program. The analysis is included: the effects of regenerator losses, flow losses, heat leakage through the regenerator matrix and walls, imperfect heat transfer between the gas and the heat exchanger wall, annulus losses, losses due to shuttle heat transfer and seal leakage. All these effects are considered in characterization of the thermodynamic parameters. The result of the optimization is a design in which the sum of these losses is minimized.

TABLE 4-1. Summary of Thermodynamic and Dynamic Design Parameters.

No. of expansion stages	1
Working gas	helium
Displacer diameter	3.155 cm
Piston diameter	4.445 cm
Max. displacer amplitude	0.33 cm
Max. piston amplitude	0.9 cm
Regenerator	
Type wire	mesh
Material	phosphor bronze
Wire diameter	53 μ m

Fill factor	0.36
Cross-sectional area	7.31 cm ²
Length	6.0 cm
Cold-end Heat Exchanger:	
Type	slit
No. of slits	40
Slit width	0.0305 cm
Slit depth	0.2 cm
Slit length	2.0 cm
Ambient Heat Exchanger:	
Type	slit
No. of slits	20
Slit width	0.07 cm
Slit depth	0.22 cm
Slit length	7.0 cm
Clearance Seals	19 μm (0.00075 in) gap
TOTAL SYSTEM WEIGHT	185 lbs.
(Excluding vacuum dewar and cooling jacket plus electronics.)	

The total input power is the sum of the thermodynamic input power to the Stirling cycle and the electromechanical inefficiency of the motors. Based on thermodynamic analyses, confirmed by measurement on refrigerators fabricated in the past, a small adjustment of the optimized operating parameters does not significantly affect the Stirling efficiency, but would seriously compromise the motor efficiency. The refrigerator consists of three damped oscillatory spring-mass systems actuated by linear motors. The conditions for minimum power input operation of these systems are a first-order function of the refrigerator operating parameters such as cycle speed, spring stiffness, and mean pressure. Of these three systems, the piston input power is about 80% of the total input power; thus, it is important that the piston be operated under minimum power conditions.

After the Prototype Model was assembled, one could optimize the Stirling performance by hunting for the minimum thermodynamic input power by perturbing the operating parameters while maintaining 65K and a 5 watt load. The operating conditions were optimized to achieve the minimum power operation of the piston; this resulted in better than predicted efficiency.

Minimum power operation of the piston was accomplished by first setting the refrigerator to run under the design parameters until it reached 65K. Then, the phase between the first harmonics of the piston motor current and the piston position waveform was measured. Adjustments to the cycle speed and mean pressure were made to obtain a 90° phase. This ensured the piston was operating under the minimum power condition. The piston and displacer strokes were subsequently adjusted to obtain 5 watts of cooling. To minimize excessive heat load above 5 watts due to ambient radiation heating of the cold end, two radiation shields were installed inside the vacuum dewar. The shields were made from multilayers of insulated mylar sheets with highly reflective metallization

coatings. The outer shield lined the inside walls of the vacuum dewar and the inner shield surrounded the cold end.

Table 4-2 shows the design operating parameters and final optimized values. The close agreement between the two sets of values validates the accuracy of the engineering analyses in this program. Also shown are the operating parameters of the refrigerator under a reduced head load of 2 watts at 65K.

TABLE 4-2. Refrigerator Design and Optimized Operating Parameters.

		Design (predicted)	Optimized (measured)	<u>2 Watts</u>
Cold End Temperature	K	65	65	65
Heat Sink Temperature	K	293	293	293
Cooling Capacity	W	5	5	2
Speed	Hz	18.3	18.0	18.0
Mean Pressure	psia	263	290	290
Displacer Amplitude	mm	2.3	2.6	2.6
Piston Amplitude	mm	7.3	6.67	5.2
Phase (disp./piston)	degrees	60	63.5	63.5
Motor Input, Piston	W	136	125	85
Motor Input, Displacer	W	3	1.6	1.5
Motor Input, Counterbalance	W	10	11.5	9

4.2 ELECTRICAL POWER

The total electrical power input requirements of the cooler in both the STANDBY and RUN modes of operation were assessed; the power requirements of the support electronics were measured as well.

Axial motor power was determined by simultaneously acquiring (in one acquisition) the real-time voltage and current waveforms with the digital scope. A software routine scaled and multiplied the stored waveform data (VI). The mean value (over 1 cycle) of the resulting power waveform was then summed into a cumulative average power reading.

The STANDBY power for the bearing pole piece actuators (in a 1g environment) was estimated using a nominal bias current of 100 mA per coil, with dissipation for each coil based on resistance losses. The RUN power estimate for the pole piece actuators was based on the difference of the measured 28V power input to the bearing driver circuits when the system was running. This assumes that the current drivers are 100% efficient and hence is a conservative estimate. Cooler instrumentation requires an insignificant amount of power.

The power input requirements of each of the electronic subsystems were measured in both the STANDBY and RUN modes. They are presented in Tables 4-3 and 4-4. No attempt was made to minimize the electronic power supply requirements.

TABLE 4-3. Electrical Power - System in STANDBY MODE.

- Breakdown of dc Power Requirements:

dc Subsystem	Power (W)
Bearing Rack	47.2
LVDT & Instrumentation	13.0
Computer Rack	13.5
Axial Drivers (3)	1.05
Piston Driver	2.2
Displacer Driver	2.5
C'balance Driver	7.8

Total	87.5W

- Power Delivered to Cooler:

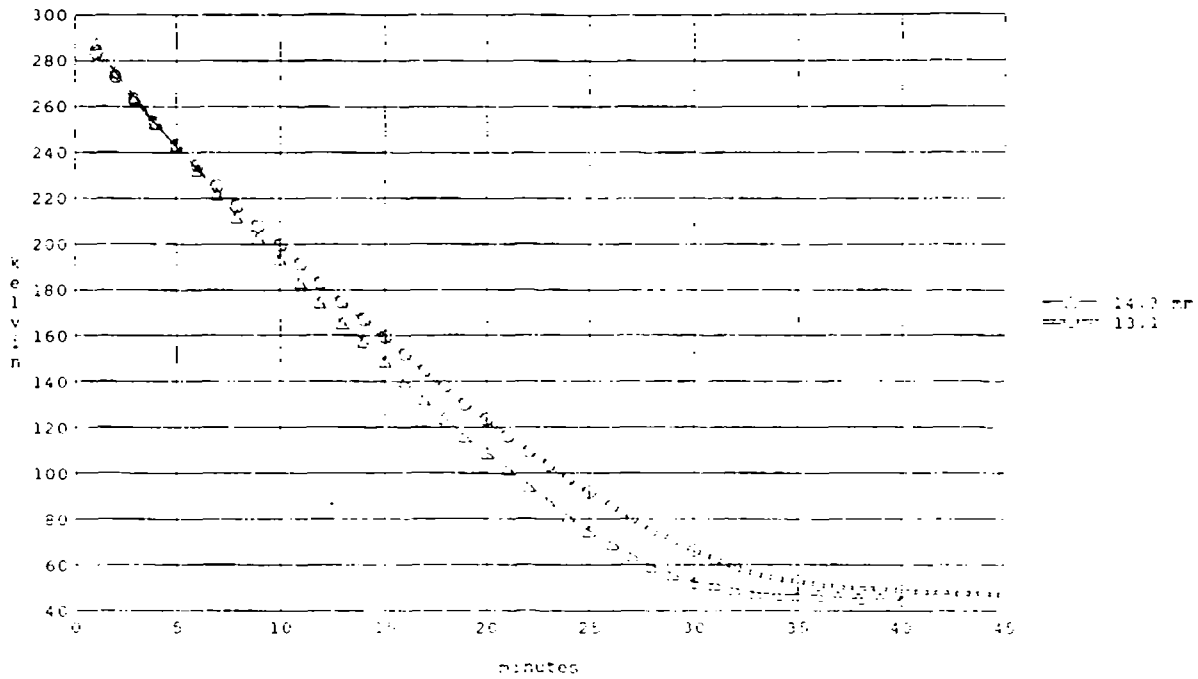
Radial Sensors	11.5
Displacer Radial	2.5
Piston Radial	0.84
C'balance Radial	0.21
Displacer Axial	0.35
Piston Axial	0.02
C'balance Axial	0.1

Total Power Delivered	15.5 W

TABLE 4-4. Electrical Power - System in RUN MODE.

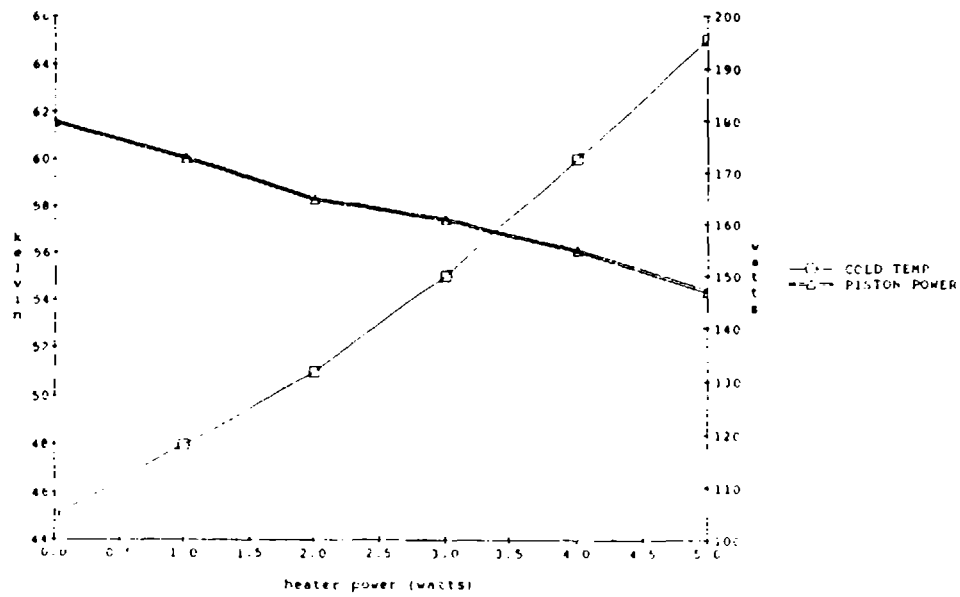
- Breakdown of dc Power Requirements:

dc Subsystem	Power (W)
Bearing Rack	57.8
LVDT & Instrumentation	21.75
Computer Rack	19.3
Axial Drivers (3)	1.35
Piston Driver	151.2
Displacer Driver	3.92
C'balance Driver	24.9



- 1) 18 Hz, 63° phase, piston stroke = 14.3 mm, displacer stroke = 5 mm.
- 2) 18 Hz, 63° phase, piston stroke = 13.1 mm, displacer stroke = 5 mm.

Figure 1-1. Cooldown curve - no heat load.



18 Hz, 63°, p = 14.8 mm stroke, d = 5.2 mm stroke.

Figure 4-2. Piston motor power required to produce cooling at 65K.

Total	280.3 W
• Power Delivered to Cooler:	
All bearings	10.8
Radial Sensors	11.5
Displacer Axial	1.6
Piston Axial	25.0
C'balance Axial	11.5
Total Power Delivered	160.4 W

4.3 COOLDOWN CHARACTERISTICS

The remote control computer was used to log the cold end temperature at one minute intervals during cooldown from room temperature. Two tests were performed, using the design stroke and an increased stroke (Fig. 4-1). No heat load was applied at the cold finger. These cooldown curves may be utilized as a benchmark to gauge any deterioration in cooler performance. With the design operating strokes, the refrigerator reached 65K in 30 minutes.

4.4 ADDITIONAL TESTING

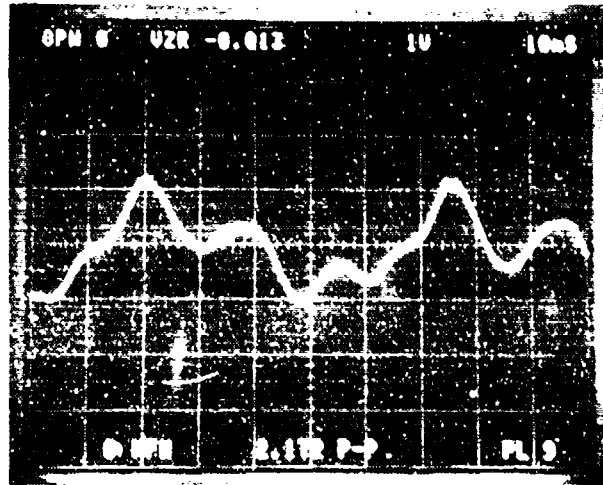
Cooling performance at various heat loads was investigated. For these tests, the heater power was varied while all other parameters remained unchanged. Final temperature and cooler input power was measured once steady operation was established (Fig. 4-2). Note that this test was performed without the inner radiation shield around the cold end, thus reflects performance with the additional radiation heat load above the heater power.

5. VIBRATION MEASUREMENTS

Axial accelerations of the cooler housing were measured at the ends of the housing, and radial accelerations were measured at three points along the length of the housing with the accelerometer. Power spectra of this data are shown in Figures 5-1 to 5-3.

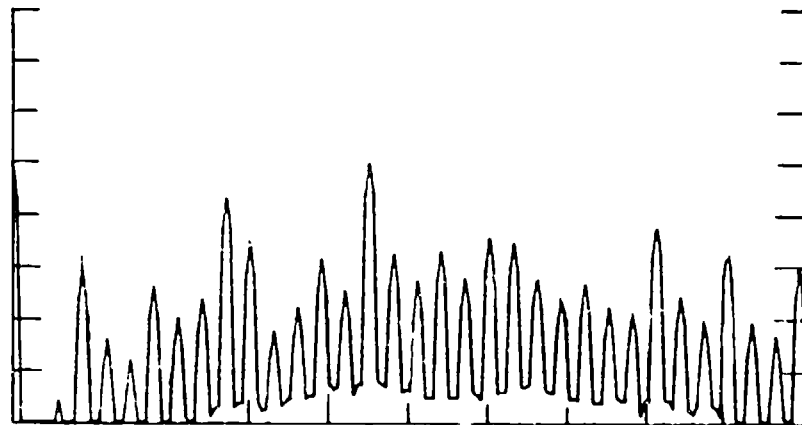
Axial and radial displacement measurements were made at the extreme edges of the cold finger insulating dewar, where we would expect to find worst-case excursions. To minimize extraneous vibrations, the instrument was securely anchored to the same rigid surface as was the mounting cradle of the cooler. Photographs of the displacement waveforms appear in the performance data. A power spectrum of the axial displacement is included for correlation with the axial acceleration data. The results are shown in Figures 5-1 to 5-3.

a) Cold end axial displacement.



600 micro inches/Div.

b) Axial acceleration spectrum.



1 m/s²/volt

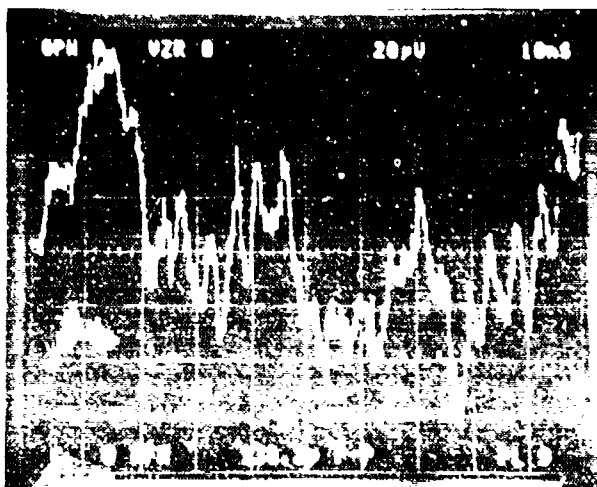
PWR SPECT A 30.94BV 18. HZ N. 16 P. 1HZ
SPAN 0.000HZ -200.00HZ S: 204BV 1 S: 20.0043V 104BV

Sheet 1 of 2

Figure 5-1. Displacement and acceleration at cold end. (Cont'd.)

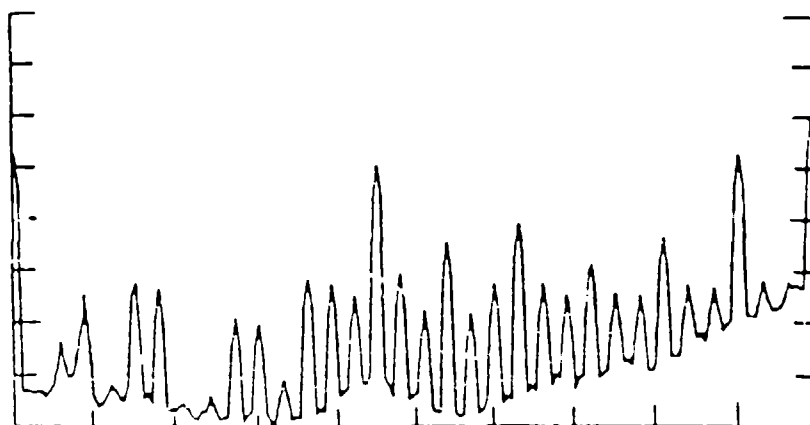
c) Cold end radial displacement.

20 micro inches/Div.



d) Radial acceleration spectrum.
(at cold end)

1 m/s²/ volt



PKR SPECT A : - 47.648V 18.42 N: 32 P: 1HZ
SPAN: 0.000HZ - 200.000HZ SW: 10dBV FS: 10.0048V 10dBV

Sheet 2 of 2

Figure 5-1. Displacement and acceleration at cold end.

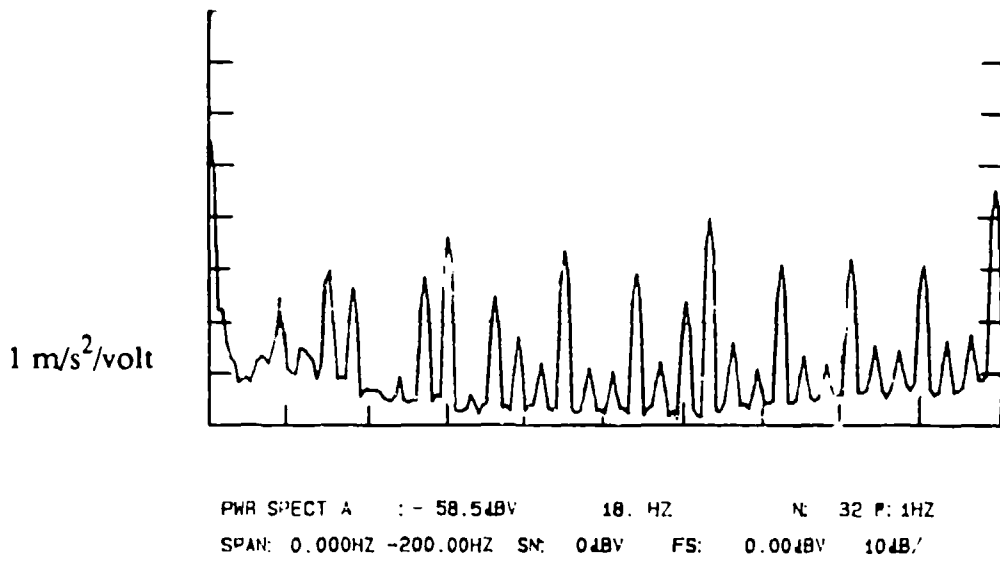


Figure 5-2. Radial displacement spectrum at piston housing.

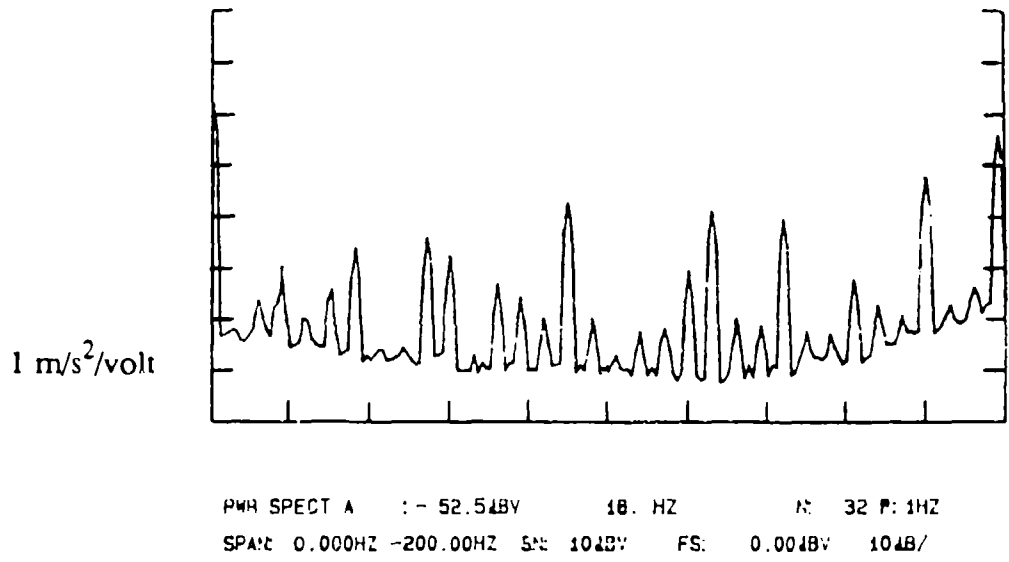


Figure 5-3. Radial acceleration spectrum at counterbalance end.

6. FUTURE WORK

The Prototype Model refrigerator is a free piston and free displacer Stirling machine with the flexibility in varying the operating parameters built into the control electronics. Parameters such as frequency, amplitude and relative phase angle of the piston and displacer motions can be changed while the cooler is running. With these features, detail parametric testing of the performance of the Prototype Model can be easily carried out. Further parametric testings will be performed at NASA-Goddard Space Flight Center. The long-life cryocooler technology developed under this program has been transferred to the Cryogenic Products group at Magnavox Electro-Optical Systems, a corporate affiliate. Recent development [5] programs include multi-stage linear magnetic cryocoolers for cooling of electronics such as high-temperature superconductors and central processing units of high-speed computers.

7. SUMMARY

Technology developed for a long-life cryocooler has been demonstrated. A magnetically suspended, linearly driven Stirling refrigerator was successfully tested for 5-year continuous operation with no mechanical wear and failures and no degradation in cooling performance.

The system performance results of the Prototype Model refrigerator met or exceeded the specified goals of the program. Table 7-1 summarizes the major specifications and the actual performance of the Prototype Model refrigerator.

TABLE 7-1. Prototype Model Refrigerator.
Specified Goal and Actual Performance.

Cold end temperature - 5 Watt load	65K	65K
Operating Power (Refrigerator only)	≤ 250 W	160 W
Standby Power (Refrigerator only)	≤ 50 W	16 W
Time to Reach Stable Operation	≤ 5 hours	< 30 minutes
Radial Movement of cold end (Operating) - Inches	10^{-5}	1.4×10^{-4} p-p
Axial Movement of cold end (Operating) - Inches	10^{-3}	1.3×10^{-3} p-p
Weight (Refrigerator only)	200 lb	185 lb

ACKNOWLEDGMENTS

The work summarized in this paper was supported by the NASA-Goddard Space Flight Center, under Contract Number NAS5-26688. The contributions of L. Bourdillon, R. Bronnes, R. Carminucci, R. Eggleston, R. Figueroa, E. Harkins, M. Hartmann, J. Hejduk, E. Lindale, A. Shaik, J. Sanchez, and R. Sweet towards the design and fabrication of the refrigerator are acknowledged.

REFERENCES

1. Knox, L.; Patt, P.; Maresca, R.; "Design of a Flight Qualified Long-Life Cryocooler," Proceedings of the Third Cryocooler Conf., Boulder, Colorado, 1984, NBS Special Publication 698 (May 1985).
2. McFarlane, R.; Keung, C.; Shaik, A.; Starr, M.; "Long-Life Stirling Cryocooler for Space Applications," Proceeding of the 5th International Cryocooler Conf., Monterey, CA, August 18-19, 1988.
3. Patt, P., "Design and Testing of a Co-Axial Linear Magnetic Spring with Integral Linear Motor," IEEE Transactions on Magnetics, 21(5):1759-1761.
4. Hays, D.F.; "Squeeze Films: A Finite Journal Bearing with a Fluctuating Load", Journal of Basic Engineering, Transactions of ASME, pp. 519-588, 83D, Dec. 1961.
5. Lehrfeld, D., et al.; "Design of a Prototype Long-Life Stirling Cycle Refrigerator for Satellite Systems", Ninth DARPA S3 Symposium, Monterey, CA, October 1983.

Session II — Pulse Tube and Sorption Coolers

Chairperson: Kathy McDermott, NIST

Co-Chairperson: Steve Castles, NASA/GSFC

SYSTEM DESIGN ANALYSIS OF PULSE-TUBE CRYOCOOLER

B.J. Huang, L.T. Lee, and C.W. Lu
Department of Mechanical Engineering
National Taiwan University, Taipei, Taiwan 10764

ABSTRACT

We performed a system design analysis of pulse tube cryocoolers. The analysis basically followed Colangelos' approach¹¹ but considered the pressure drop across the regenerator. In addition, laminar or turbulent heat transfer in the pulse tube was considered. A system analysis was then carried out to predict the performance of pulse tube refrigerators. It was unnecessary for us to determine the pressure-time wave form in the pulse tube experimentally.¹¹ It was found that the performance of a pulse-tube cryocooler depends on six operating parameters: charging pressure P_h , discharging pressure P_l , charging gas temperature T_{g0} , heat sink temperature T_h , cold-end temperature T_c , and pulse rate f . The analytical result was found to agree fairly well with the test data, verifying the analysis and also indicating that the convective heat transfer between the gas and the tube wall or regenerator matrix during flowing periods may be a controlling mechanism in the performance of basic pulse-tube (BPT) refrigerators. A system analysis also showed that at higher cold-end temperatures, the performance of BPT refrigerators does not significantly differ for various designs of regenerators and pulse tubes.

INTRODUCTION

The system modeling and performance analysis of a valved pulse tube refrigerator or basic pulse tube refrigerator (BPT) has been studied by several researchers. Gifford and Longworth¹ first introduced a simple gas-piston model to perform a thermodynamic analysis by assuming an isentropic process in the pulse tube. They showed that the ideal or minimum cold end temperature achievable in a BPT refrigerator at an absolute zero heat pumping condition is affected by the ratio of the volumes of pulse tube to gas heat exchanger, V_{pt}/V_h , and the ratio of gas specific heats γ . A similar thermodynamic analysis using a multiple step, isentropic process concept was carried out by Narayankhedkar and Mani.² They pointed out that performance is also affected by the pressure ratio P_h/P_l .

Instead of assuming an isentropic process, Rauh³ assumed a polytropic process in the BPT refrigerator and carried out a similar thermodynamic analysis. Shnide⁴ further employed thermodynamic analysis in conjunction with the solutions obtained from a system of gas dynamic differential equations to predict the cold-end temperature achievable at zero heat pumping condition. The previous thermodynamic analysis¹⁻⁴ will yield large errors because the regenerator performance was assumed to be perfect and the actual process in BPT refrigerators is neither isentropic nor polytropic.

From a heat transfer viewpoint, the transient performance of a BPT refrigerator can be determined by solving a set of governing equations based on conservations of mass, momentum, and energy for the regenerator and pulse tube. However, the solution procedures are so complicated that a numerical technique could be a problem. A mainframe or super computer may be required in the analysis. A detailed heat transfer model that is capable of predicting instantaneous performance of a BPT refrigerator is thus not presently available.

Storch and Radebaugh⁵ developed an enthalpy flow analysis using time-averaged properties over one cycle for valveless orifice pulse tube refrigerators. A valveless orifice pulse tube (OPT) refrigerator is quite different from a valved pulse tube refrigerator without receiver (BPT) not only in design but also in working principle.⁶ For OPT refrigerators, the refrigeration effect is produced mainly by the adiabatic expansion of gas in the pulse tube due to flow through the orifice, in addition to the surface heat pumping effect, which is the controlling mechanism in the performance of BPT refrigerators. The enthalpy flow model developed by Storch and Radebaugh^{5,6} is not only subject to large error (3 to 5 times greater than experimental values⁶) in the performance prediction of OPT refrigerators, but is also not applicable to the analysis of BPT refrigerators due to different working principles.

Longworth⁷ assumed that conductive heat transfer between gas and pulse-tube wall during the quiescent periods is the controlling mechanism, and he derived an element-by-element gas heat conduction model to analyze the heat pumping effect and predict the wall temperature. The disagreement between experiments and analysis may have resulted from Longworth's ignoring convective heat transfer between the gas and the pulse-tube wall or regenerator matrix during flowing periods and assuming a perfect regenerator.

More recently, Richardson^{8,9} modified Longworth's analysis⁷ for BPT refrigerators by considering the maximum value of the gas charging period, and he reached the prediction of an optimum pulse rate, which was verified qualitatively by experiments. However, this study was mostly experimental and no system modeling or performance analysis was done.

In fact, the convective heat transfer rate between the gas and the tube wall or regenerator matrix is several orders higher than the conduction heat transfer

in gas. Therefore, unless the quiescent period is much longer than the flowing period, the convective heat transfer rate may in turn be a controlling process in the performance of BPT refrigerators.

Rea¹⁰ and Colangelo *et al.*¹¹ developed a simplified heat transfer model for the performance analysis of BPT refrigerators. Their model basically assumed that the convective heat transfer between the gas and the pulse-tube wall or regenerator matrix during flowing periods is a controlling mechanism. Their analysis started with the derivation of mass and energy equations of the gas and the pulse tube wall or regenerator matrix. Since the numerical solutions of the governing equations are quite complicated, Colangelo *et al.*¹¹ divided the pulse tube process into charging (pressurization) and discharging (depressurization) periods and then defined half-cycle mean properties of each period. By neglecting the pressure drop across the regenerator and assuming a sawtooth pressure-time wave form, the governing equations were then simplified a great deal and became solvable by using numerical techniques. Through half-cycle averaging, a system of ordinary differential equations finally resulted and the numerical analysis could be carried out. Rea and Colangelo *et al.* showed that the analytical result agrees very well with the experimental data.

The analytical model of BPT refrigerators developed by Colangelo *et al.*¹¹ takes into account the heat and mass transfer processes in the regenerator and the pulse tube and, thus, is closer to the practical situation. However, the pressure drop due to gas flow through the regenerator was ignored in the modeling. This implies that the modeling was incomplete due to the lack of a momentum equation. It is a fact that the pressure-time wave form remains unknown in Colangelos *et al.* model.¹¹ And, the system of equations can be solved only after this pressure wave form has been determined experimentally. The analysis is thus semi-empirical and cannot be used to predict the performance of BPT refrigerators theoretically.

Our study basically follows Colangelos' approach but considers the pressure drop due to gas flow through the regenerator. A system analysis procedure is then established, and the system performance is theoretically predicted. Furthermore, the empirical correlation of convective heat transfer in the pulse tube, which covers laminar and turbulent flow regions, is used in our study.

SYSTEM MODELING

BASIC ASSUMPTIONS

In our model of BPT refrigerators (Fig. 1), Rea¹⁰ and Colangelos *et al.*'s¹¹ assumptions are followed, such as 1-D approximation, ignoring of pressure variation within the pulse tube, equilibrium temperature between matrix and fluid in the regenerator, etc. Additional assumptions other than those of Rea and Colangelos *et al.*^{10,11} are made as follows:

REGENERATOR

Following the approach of Rea and Colangelos *et al.*,¹¹ and ignoring gas conduction heat transfer during quiescent periods, the governing equations of regenerator for matrix temperature θ and gas mass flowrate m are, in dimensionless form,

$$\frac{dm}{dw} = \frac{1}{\theta} \quad (1)$$

$$\frac{d\theta}{dw} = \frac{C_R - [(\gamma - 1)/\gamma]m^{1-n}}{m^{2-n}} \quad (2)$$

where $\theta = T/T_0$; $m = \tilde{m}/\tilde{m}_0$; $w = (V_R r_p / T_0 \tilde{m}_0 R)(x/L_R)$;

$$C_R = \frac{\gamma - 1}{\gamma} \left(\frac{K A_T L_R}{V_R} \right) \frac{C_{1R}}{2 \tilde{m}_0 r_p}; \quad C_{1R} \equiv [\tilde{m}(\tilde{T}_{gc} - \tilde{T}_{ge})]_R = \text{constant}, \quad (3)$$

where K is a constant defined in the convective heat transfer coefficient correlation; $\tilde{h} = Km^n$, where $n = 0.59$ for packed regenerator,¹¹ which is taken from the correlation obtained by Rea and Smith;¹² $Nu = 0.71 Pr^{1/3} Re^{0.59}$, where the Reynolds number Re is based on the hydraulic diameter. The symbol tilde denotes the averaged property taken within the time period $\Delta t = \psi \zeta$, i.e., flowing periods. The relations between the half-cycle averaging and flowing averaging properties, \bar{z} and \tilde{z} , are as follows:

$$\tilde{z} \equiv \frac{1}{\Delta t} \int_0^{\Delta t = \psi \zeta} z dt; \quad (4)$$

$$\bar{z} \equiv \frac{1}{\zeta/2} \int_0^{\zeta/2} z dt = \frac{\Delta t}{\zeta/2} \tilde{z} = 2\psi \tilde{z}. \quad (5)$$

The boundary conditions for Eqs. (1) and (2) are: (i) at $w = 0$, $\theta = 1$, $m = 1$; (ii) at $w = w_R = V_R r_p / \tilde{m}_0 R T_0$, $\theta = \tilde{T}_i / T_0$, $m = \tilde{m}_i / \tilde{m}_c$.

To account for the pressure drop across the regenerator, the following empirical relation can be used for packed regenerators:¹³

$$\Delta P = 4f_o \frac{L_R}{d_p} \frac{\bar{Q}U^2}{2} \quad (6)$$

where f_o is the friction coefficient defined as

$$f_o = \begin{cases} 114 Re_d^{-0.742}, & Re_d \leq 210; \\ 6.85 Re_d^{-0.216}, & Re_d > 210. \end{cases} \quad (7)$$

where Re_d is the Reynolds number defined based on particle size d_p and pore velocity u , i.e., $Re_d = \bar{q} u d_p / \mu_g$.

If the pulse rate f is not too high, a quasi-steady assumption can hold¹⁴ and Eq. (6) can be used to correlate the mass flowrate ($\dot{m} = \bar{q} u A_c$) with the pressure drop ΔP which, in the charging period, is defined as,

$$\Delta P(t) = P_h - P_o(t) = \begin{cases} P_h - r_p t, & \text{for } t \leq \psi \zeta \\ 0, & \text{for } t > \psi \zeta \end{cases} \quad (8)$$

For regenerators made from wire screen, a similar correlation can be used.¹⁵

PULSE TUBE

Similarly, the governing equations of a pulse tube for tube wall temperature θ and gas mass flow rate m are

$$\frac{dm}{dw} = \left(1 - \frac{\phi C_{1pt}}{m\theta} \right) \frac{1}{\theta} \quad (9)$$

$$\frac{d\theta}{dw} = \frac{C_{pt}[1 + (\phi/\theta)] - [(\gamma - 1)/\gamma]m}{m^2} \quad (10)$$

$$C_{pt} = \frac{\gamma - 1}{\gamma} \left(\frac{h_{pt} A_{pt} L_{pt}}{V_{pt}} \right) \frac{C_{1pt}}{2\bar{m}_h r_p}; \quad C_{1pt} = [\bar{m}(T_{gc} - T_{ge})]_{pt} = \text{constant} \quad (11)$$

$$\phi = 2 \left(\frac{\gamma}{\gamma - 1} \right) \left(\frac{V_{pt}}{h_{pt} A_{pt} L_{pt}} \right) \frac{P_{ave}}{\Delta t} \frac{1}{T_h} \quad (12)$$

where $P_{ave} = (P_h + P_l)/2$; $\Delta t = \psi \zeta$; $\theta = T/T_h$; $m = \bar{m}/\bar{m}_h$; h_{pt} is the convective heat transfer coefficient between gas and tube wall, which can be obtained from Nusselt correlation¹⁶ for turbulent flow; $Nu = h_{pt} d_{pt} / k_g = 0.036 Re^{0.6} Pr^{1/3} (d_{pt}/L_{pt})^{0.055}$, where the Reynolds number is defined based on the pulse tube inside diameter. For laminar flow, $Nu = 4.36$ is used.

The boundary conditions for Eqs. (9) and (10) are: (i) at $w=0$, $\theta=1$, $m=1$;
(ii) at $w = w_{pt} = V_{pt}/T_h \tilde{m}_h R r_p$, $\theta = T_c/T_h$, $m = \tilde{m}_c/\tilde{m}_h$.

SYSTEM ANALYSIS

BASIC ASSUMPTIONS

In the system analysis of BPT refrigerators, several assumptions are made:

1. The cooling jacket is designed very well so that the inner jacket wall temperature T_w , the pulse tube wall temperature at the junction $w=0$, T_h , and the coolant flow temperature T_m (i.e. heat sink temperature) are approximately the same, i.e. $T_h \approx T_w \approx T_m \equiv T_h$.
2. The volume of the cold end is small, and the temperatures at the junctions of the regenerator, the cold-end heat exchanger, and the pulse tube wall are in thermal equilibrium, i.e. $T_0 \approx T_c \approx T_L$. The mass flowrate at inlet and outlet of the cold-end heat exchanger are approximately the same, i.e. $\dot{m}_0 \approx \dot{m}_c$.
3. The efficiency of the regenerator is very high so that the matrix temperature T_i is approximately equal to the gas temperature at the entrance T_{gt} , i.e., $T_i \approx T_{gt}$.
4. The flowing periods will not exceed the half cycle period, i.e., $\psi \leq 0.5$.

With the previous assumptions, the normalized variables defined in the previous dimensionless governing equations can be determined and system analysis can be performed.

INPUT PARAMETERS AND ANALYTICAL PROCEDURES

By solving the governing equations of the regenerator and the pulse tube one after the other and applying the boundary conditions, a system performance analysis can be carried out with some parameters remaining to be inputs. The analytical procedure represented by an information-flow diagram is as shown in Fig. 3. It should be noted that the instantaneous mass flowrate through the regenerator $\dot{m}_r(t)$ is calculated first, and then the average mass flowrate at flowing period \bar{m}_r is determined and matched with the solution from the governing equations of the regenerator and pulse tube. During the solution processes, C_R and C_{pt} are determined by matching the boundary conditions in the regenerator and the pulse tube.

It was found that there are six input parameters for the performance of BPT refrigerators: P_h , P_L , T_L , T_{gt} , T_m , and f . For a design of BPT refrigerator, the performance is then determined if these six input parameters related to the operating conditions were given. The performance of BPT refrigerators can be represented by the heat rejection rate Q_h , the cooling load

Q_L , and COP. It can be shown that

$$Q_h = \psi C_p C_{1pt}; \quad (13)$$

$$Q_L = Q_h - Q_R = \frac{1}{\xi} \oint_0^{\xi} [(\dot{m} C_p T_g)_h - (\dot{m} C_p T_g)_R] dt = \psi C_p (C_{1pt} - C_{1R}); \quad (14)$$

$$W = \frac{1}{2} \frac{\bar{m}_i}{\bar{q}} (P_h - P_L) = \frac{1}{2} \frac{\bar{m}_i}{\bar{q}} (P_h - P_L) \frac{\Delta t}{\xi/2} = \psi \frac{\bar{m}_i}{\bar{q}} (P_h - P_L); \quad (15)$$

$$COP = \frac{Q_L}{W} = \frac{\bar{q} C_p (C_{1pt} - C_{1R})}{\bar{m}_i (P_h - P_L)}. \quad (16)$$

EXPERIMENTAL VERIFICATION

The present system analysis was carried out for the BPT refrigerator used by Colangelos et al. in their experiment.¹¹ The design specifications, operating conditions and system performance are listed in Table 1. The predicted cooling capacity (8.0 W) agrees fairly well with the experimental result (9.0 W), about an 11% deviation. The deviation may result mainly from having ignored gas heat conduction during quiescent periods and the quasi-steady assumption of the gas flow rate vs. the pressure drop across the regenerator, the errors of heat transfer and the frictional factor correlations of the regenerator used, and the experimental errors. The agreement between the experimental data and the present analysis also indicates that the convective heat transfer between gas and tube wall or regenerator matrix could be a controlling mechanism of the surface heat pumping effect in the performance of BPT refrigerators. We expect that the accuracy of the present analysis could be improved if more accurate empirical correlations for the heat transfer coefficient and friction factor were used and the gas conduction heat transfer mode during quiescent periods was considered.

PERFORMANCE OF PULSE-TUBE CRYOCOOLERS

A system performance analysis was carried out for the BPT refrigerator presented in Table 1. Figure 4 shows that at a fixed cold-end temperature T_L , the COP increases first with the charging pressure P_h , then reaches a maximum value and then decreases. This is due to the transition of convective heat transfer in the pulse tube from laminar to turbulent. Since the mass flow rate in the pulse tube increases with charging pressure, the curve at the left side of the optimum COP point represents the laminar flow region. In laminar flow operation, COP will increase monotonically with the charging pressure P_h . This coincides with many field experiences that a BPT refrigerator will perform better if laminar flow is maintained in the pulse tube.^{1,7,11}

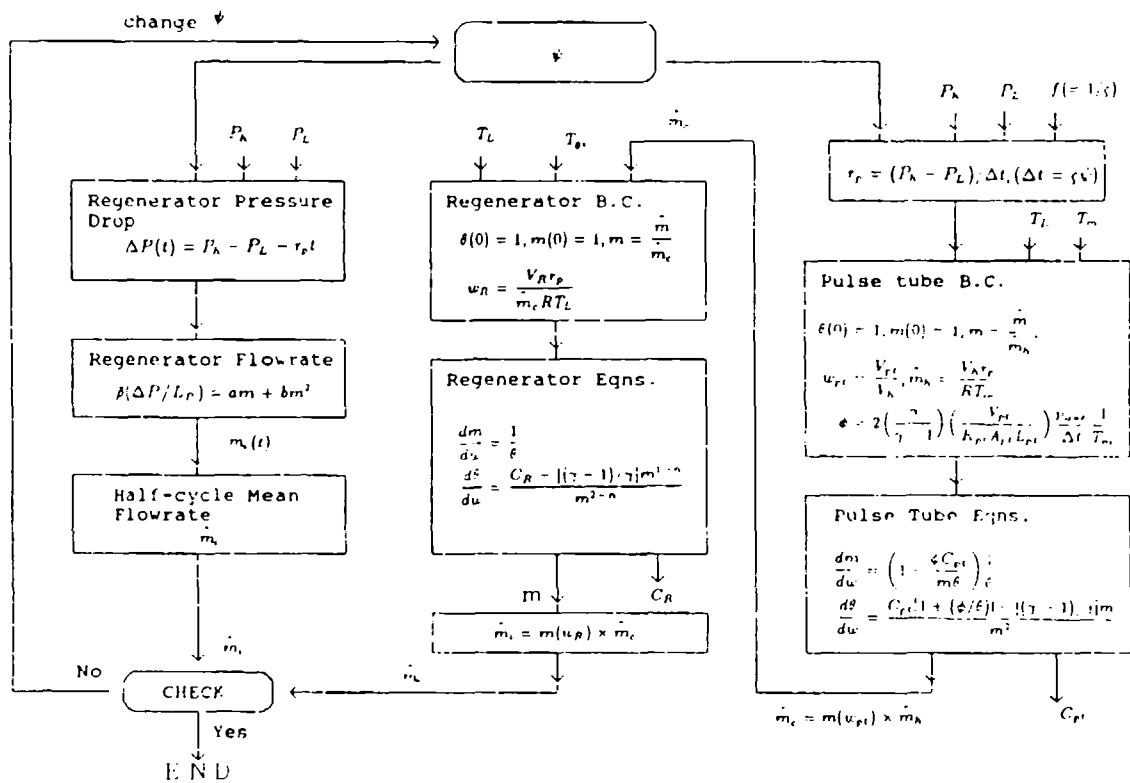


Fig. 3. Information-flow diagram of system analysis for BPT refrigerators.

Table 1. Comparison of experimental and analytical cooling capacities.

Design Specifications		
Pulse Tube:	stainless steel	
$d_{pt} = 15.06$ mm	$L_{pt} = 304.8$ mm	thickness = 0.40
Regenerator:	packed lead spheres	
$d_p = 1.27$ mm	$L_R = 304.8$ mm	$\epsilon = 0.388$
$D_R = 24.38$ mm		
Gas Heat Exchanger:		
$D_{hx} = 15.06$ mm	$V_h = 1.1 \times 10^{-5}$ m ³	
Operating Conditions		
$T_h = 278.5$ K	$T_l = 208.9$ K	$T_{kt} = 298.0$ K
$P_h = 5.1$ atm abs	$P_l = 1.7$ atm abs	$f = 158$ rpm
Cooling Capacity		
Measured:	$Q_l = 9.0$ W	
Predicted:	$Q_l = 8.0$ W	

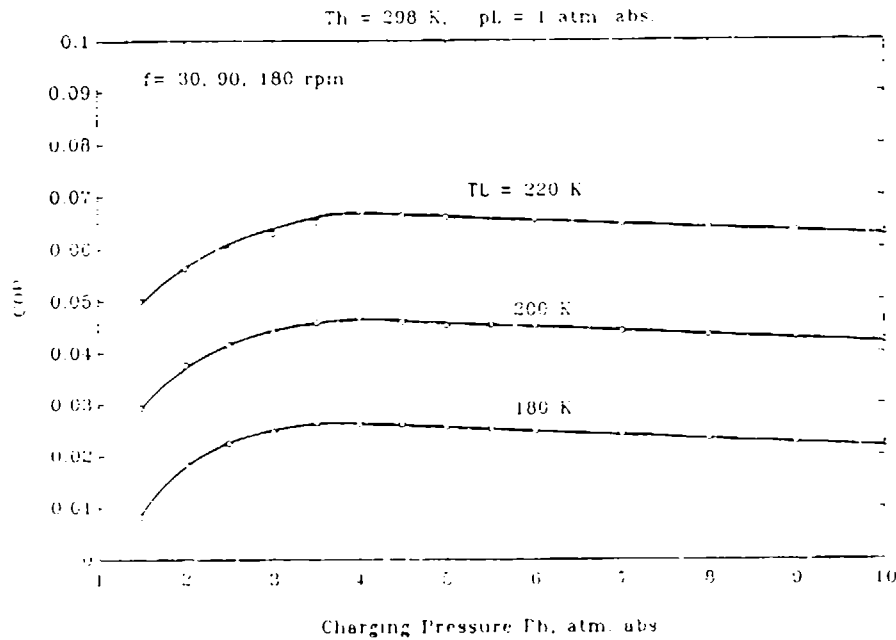


Fig. 4. Variation of COP with charging pressure P_h .

Figure 4 also shows that COP does not vary with the pulse rate. The reason is that, as long as the flowing period does not exceed the half-cycle period, i.e. $\psi \leq 0.5$, and the gas conduction heat transfer during quiescent periods is ignored, the pressure-time wave form and the heat transfer rate will remain unchanged at a fixed charging pressure. Figure 5 shows that the cooling load Q_L increases with the cold-end temperature T_L and pulse rate f .

The present system analysis can also be used to investigate the effect of regenerator and pulse-tube designs on system performance. Figure 6 is a result simulated for the same BPT refrigerator but with regenerator design changed by using different diameters for the lead spheres. At higher cold-end temperature, changing regenerator particle size d_p will not change the performance significantly. However, at the lower cold-end temperature, the regenerator design will significantly affect performance, especially the cold-end temperature at zero cooling load. The dashed line shown in Fig. 6 is the result for the BPT refrigerator design shown in Table 1 but with the pulse tube length increased by 1.5 times and the lead sphere diameter of the regenerator reduced by 4 times. The results show that the cold-end temperature at zero cooling load drops significantly. Figure 6 indicates that at the higher cold-end temperature, the system performance will not be significantly different for various BPT refrigerator designs.

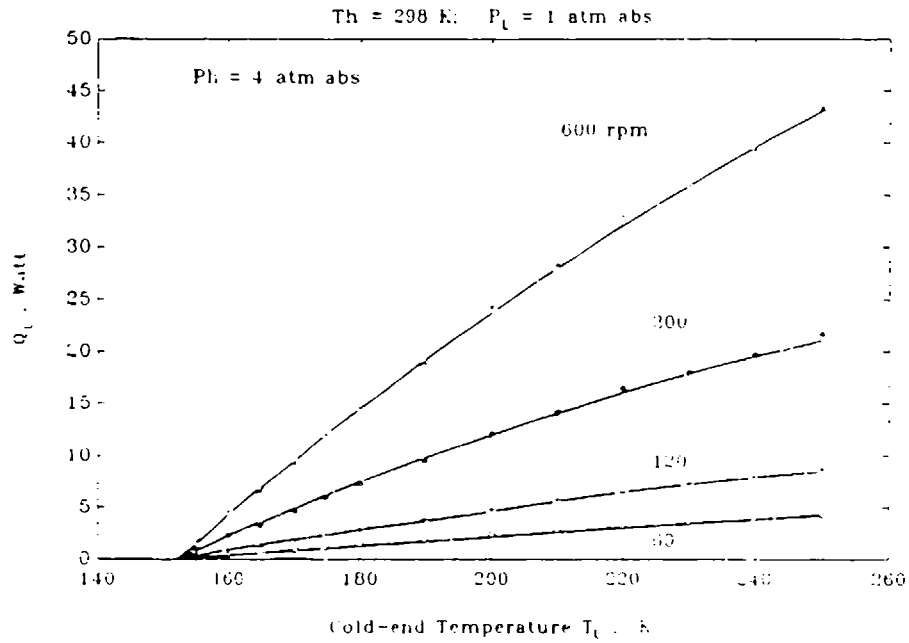


Fig. 5. Variation of cooling load Q_L with charging pressure P_h and pulse rate f .

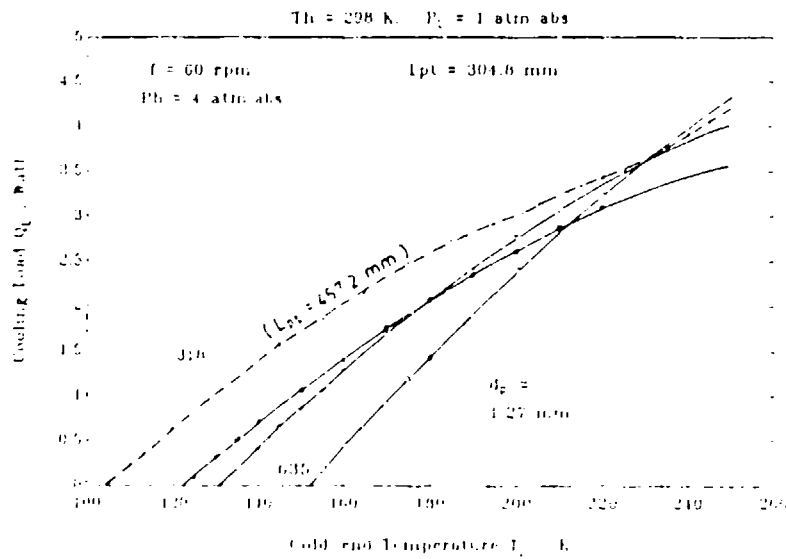


Fig. 6. Variation of cooling load Q_L with regenerator and pulse tube designs.

CONCLUSIONS

The system performance analysis developed in the present study can be used to predict the performance of BPT refrigerators without the need for determining the pressure-time wave form in the pulse tube experimentally as required by Colangelo *et al.*¹¹ Thus, the analysis is simple and can be carried out even on a personal computer. The analytical results obtained in the present study also indicate that the convective heat transfer between the gas and the tube wall or regenerator matrix during flowing periods may be a controlling mechanism in the performance of BPT refrigerators. However, the accuracy of the analysis may become lower if the gas heat conduction during the quiescent periods dominates, which may depend on the design and operating conditions. We believe that the surface heat pumping effect of BPT refrigerators consists of the heat transfer processes during quiescent (gas conduction) and flowing (gas convection) periods. The relative importance of both heat transfer modes will depend on the design and operating conditions. The system analysis including both kinds of heat transfer modes will definitely improve the accuracy. This remains for further studies.

ACKNOWLEDGMENT

The present study was supported by the National Science Council of the Republic of China, Taiwan, through Grant No. NSC78-0401-E002-27.

NOMENCLATURE

- A_T = surface area per unit length of regenerator;
 A_{pt} = surface area per unit length of pulse tube;
 d_p = particle diameter of regenerator;
 d_{pt} = inside diameter of pulse tube;
 k_g = thermal conductivity of gas;
 D_R = inside diameter of regenerator;
 L_{pt} = length of pulse tube;
 L_R = length of regenerator;
 R = gas constant;
 T = temperature of pulse-tube wall or regenerator matrix;
 V_R = gross volume of regenerator;
 $\bar{\rho}$ = mean gas density;
 μ_R = gas viscosity;

Subscripts:

- c = compression
- e = expansion
- g = gas
- $0, i, h, c$ = locations

Superscripts:

- = half-cycle average
- = time average over flowing periods

REFERENCES

1. W.F. Gifford and R.C. Longworth, "Pulse-tube refrigeration," *Trans ASME J. Eng. for Ind.*, Vol. 63, (1964) p. 264-268.
2. K.G. Narayankhedkar and V.D. Mane, "Investigation of pulse tube refrigerator," *Trans ASME J. Eng. for Ind.*, Vol. 95 (1973) p. 373-378.
3. M. Rauh, "Kalteerze U Gung Durch Pulsationsrohre," *Kaltetechnik*, Vol. 19 (1967) p. 62-65.
4. I.M. Shnide, "Thermodynamic characteristics of refrigerating machines using the pulse tube," *Proc Int Inst Refrg Commission III*, (1969) p. 59-67.
5. P.J. Storch and R. Radebaugh, "Development and experimental test of an analytical model of the orifice pulse tube refrigerator," *Adv Cryo Eng*, Vol. 33, p. 851-859, Plenum Press, New York (1988).
6. R. Radebaugh, "A review of pulse tube refrigeration," *Adv Cryo Eng*, Vol. 35, p. 1191-1205, Plenum Press, New York (1988).
7. R.C. Longworth, "An analytical and experimental investigation of pulse tube refrigeration," *PhD Thesis*, Syracuse University, U.S.A. (1966).
8. R.N. Richardson, "Pulse tube refrigerator – an alternative cryocooler?" *Cryogenics*, Vol. 26 (1986) p. 331-340.
9. R.N. Richardson, "Valved pulse tube refrigerator development," *Cryogenics*, Vol. 29 (1989) p. 850-853.
10. S.N. Rea, "A study of thermal regenerators subjected to rapid pressure and flow cycling," *PhD Thesis*, Department of Mechanical Engineering, MIT, USA (1966).

11. J.W. Colangelo, E.E. Fitzpatrick, S.N. Rea and J.L. Smith, Jr., "An analysis of the performance of the pulse tube refrigerator," *Adv Cryo Eng*, Vol. 13, p. 494-504, Plenum Press, New York (1967).
12. S.N. Rea and J.L. Smith, Jr., "The influence of pressure cycling on thermal regenerators," *ASME J. Eng. Ind.*, August (1967) p. 563-569.
13. Teruo Takahashi, Yasuharu Akagi and Katsuki Ueyama, "A new correlation for pressure drop pf packed column," *J. Chem. Eng. Japan*, Vol. 12 (1979) p. 341-346.
14. P.D. Roach and K.J. Bell, "Analysis of pressure drop and heat transfer data from the reversing flow test facility," Report No. ANL/MCT-88-2, Argonne National Laboratory, Argonne, Illinois 60439, U.S.A. (1989).
15. H. Miyabe, S. Takahashi and K. Hamaguchi, "An approach to the design of Stirling engine regenerator matrix using wire gauzes," *Proc. 17th IECEC* (1982) p. 1839-1844.
16. W. Nusselt, "Der Wärmeaustausch zwischen Wand und Wasser im Rohr," *Forsch. Geb. Ingenieurwes*, Vol. 2, (1931) p. 309.

PULSE TUBE COOLER MODELING

G.M. Harpole and C.K. Chan
TRW Space & Technology Group
Redondo Beach, California 90278

ABSTRACT

A pulse tube refrigerator model was developed by combining detailed component models. The component models are based on local conservation of mass, momentum, and energy. The system model predicts pressure, mass flow rate, heat flow, and enthalpy flow at all the interfaces between components as functions of time as well as overall system performance parameters, heat loads, and compressor work. The numerical methods were selected for rapid convergence and simultaneous solution of the component models at all interfaces.

A sensitivity study with this model demonstrates the strong dependence of system performance on the orifice valve setting. There is an optimum valve coefficient that gives peak performance. The sensitivity study also showed that performance can be significantly improved if the regenerator pressure losses are reduced (by increasing the regenerator permeability, by increasing the cross-sectional flow area, by decreasing the length, by decreasing the compressor frequency, or by increasing the mean pressure).

SYSTEM CONFIGURATION

The one-stage pulse tube refrigerator configuration including an orifice and reservoir (see Fig. 1) studied here was first reported by Mikulin¹ and further developed by Radebaugh². This refrigerator consists of a compressor, heat exchangers, and passive components connected in series. In sequence, these are: the compressor, the aftercooler (heat exchanger), the regenerator (heat exchanger), the cold end heat exchanger, the pulse tube, the hot end heat exchanger, the orifice, and the reservoir. The pulse tube and the reservoir are empty volumes. The heat exchangers are typically packed fine mesh screens. Helium is the working fluid. From the compressor through the cold end, the pulse tube refrigerator is similar to a Stirling refrigerator. However, in a Stirling refrigerator there is a displacer piston instead of the components from the pulse tube through the reservoir. These components have the same function as a second piston. The pulse tube cooler is a variant of the Stirling refrigerator.

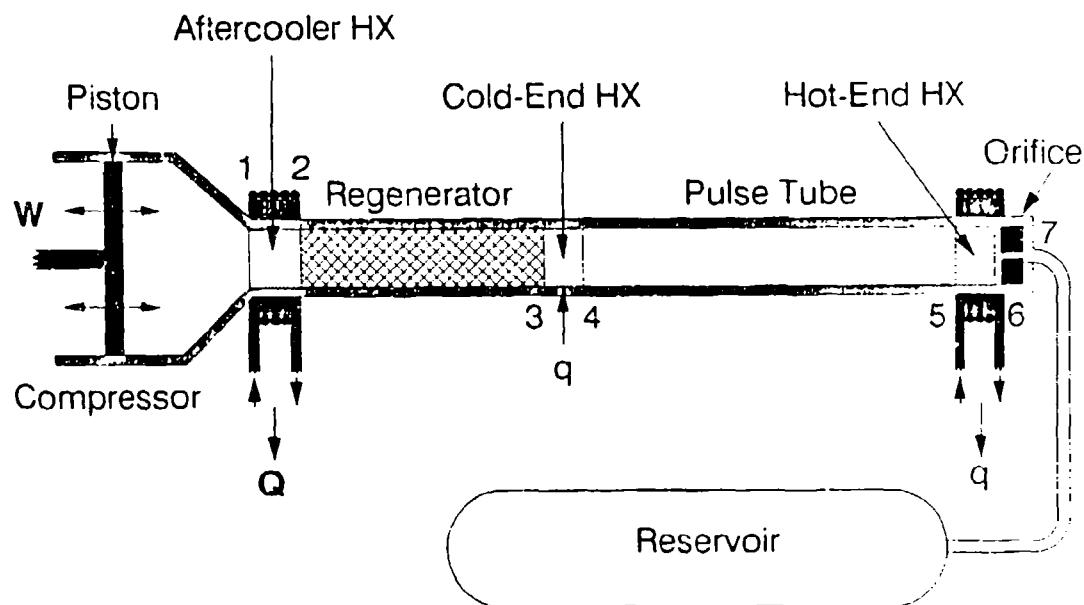


Figure 1. Pulse tube cooler configuration.

SYSTEM MODEL APPROACH

ASSUMPTIONS

The purpose of the present model is to simulate the "periodic steady state" after the hardware cooldown. During the "periodic steady state" the hardware temperatures are constants, and the gas states and heat exchange are predicted as functions of time. In the calculation, the gas usually equilibrates to a cyclically repeating condition in just a few compressor cycles.

The present pulse tube refrigerator model uses simplifications that take advantage of the characteristically efficient heat exchangers in practical devices. The number of transfer units (N_{tu}) for typical regenerators is on the order of 100. The gas temperature approaches the heat exchanger temperature as $\exp(-N_{tu})$. The model assumes for all heat exchangers (aftercooler, regenerator, cold end, and hot end) that the gas temperature is the same as the heat exchanger solid temperature. For the regenerator, this temperature is a linear function of position

$$T = T_a + (T_c - T_a) \frac{x}{L}$$

where T_a is the aftercooler temperature, T_c is the cold end temperature, L is the regenerator length, and x is the axial position within the regenerator. This linear regenerator temperature has been verified for

Stirling refrigerators³. These temperature assumptions imply zero enthalpy flow averaged over a cycle at both of the regenerator boundaries. The gas temperatures are used only in mass and momentum conservation equations to solve for pressure drops. All other heat exchanger solid temperatures are assumed time and space independent. Heat rejection from the heat exchangers is determined from the non-symmetrical gas temperature at the interfaces with the pulse tube or the compressor components.

The reservoir is assumed isothermal. This assumption is in keeping with the low flow rates through the orifice and typical system configurations. The reservoir pressure variations are small, so the system impact of assuming an isothermal reservoir as opposed to say an adiabatic reservoir is minimal.

Both an adiabatic compressor model and an isothermal compressor model are implemented. The compressor volume is considered well mixed. The gas temperature and pressure are both predicted as functions of time, but the entire compressor volume is represented by one temperature and one pressure. When gas enters the compressor from the aftercooler it has the aftercooler temperature, while the gas exits at the compressor mixed gas temperature.

Conversely, the pulse tube is assumed to have segregated gas elements. There is no direct thermal diffusion between adjacent gas elements. However, the gas elements can transfer heat with the wall (solid) elements. Thus, heat can be transferred indirectly between gas elements by temporary storage of heat in a wall element that both gas elements pass. This wall heat transfer can optionally be shut off by setting the wall Nusselt number to zero. The pressure within the empty pulse tube is dependent on time, but is assumed independent of position (e. i., no pressure drop in the pulse tube). The gas temperature is computed as a function of both time and position in the pulse tube. As gas elements enter the pulse tube from the heat exchanger at either end, they are assumed to be at that heat exchanger temperature. As gas elements leave the pulse tube, they exchange enthalpy in proportion to the difference between the gas exit temperature and the heat exchanger solid temperature.

SYSTEM NUMERICAL APPROACH

The flow behavior in each of the components is strongly coupled to the others. The equations governing the flow in each component are highly non-linear. However, shooting methods such as Runge-Kutta have been found ineffective. Therefore, the numerical method selected uses linearization and solves for the flow in all components simultaneously. The numerical approach subdivides the compressor cycle into many time steps and satisfies equations for conservation of mass, momentum, and energy in each component (and at many node points within some components) at the current time step before proceeding to the next time step.

The present model consists of component models and a method to solve those component models simultaneously. First, the component models (which consist of all the conservation equations) are linearized. Linearization necessitates iteration at each time step, but it also results in rapid convergence within just a few iterations. This linearization is not an approximation, but merely a numerical method to converge on the solution to true non-linear equations (it is analogous to the Newton-Raphson method). Second, the component models produce the coefficients for a set of linear relations between the pressures and mass flow rates at the boundaries of the components. Most components have two boundaries with their neighbors, and their models produce coefficients for two linear relations of the pressures and flow rates at the boundaries. The compressor and the reservoir each have one boundary and their models each produce coefficients for one such relation. An elimination procedure is then used to solve simultaneously for the pressures and mass flow rates at all the interfaces between components.

The gas temperatures are inputs (taken from the hardware temperatures) for all components except the (adiabatic) compressor and the pulse tube. These two components are isolated with heat exchangers at each boundary. Thus, their gas temperatures can be viewed simply as functions of the pressures and mass flows, not as additional primary variables. The compressor and pulse tube component models solve for these gas temperatures as a separate step between iterations. The pressure and mass flow rate at each node point subdivision of each heat exchanger are also computed in a separate step between iterations.

COMPONENT MODELS

COMPRESSOR

The instantaneous mass of gas in the compressor is

$$m = \frac{pV}{RT}$$

Conservation of mass is expressed by taking the time derivative of the above expression.

$$-\frac{\dot{m}}{m} = \frac{1}{p} \frac{\partial p}{\partial t} + \frac{1}{V} \frac{\partial V}{\partial t} - \frac{1}{T} \frac{\partial T}{\partial t}$$

The initial negative is due to the sign convention of \dot{m} being the mass flow rate out of the compressor. The last term is zero for an isothermal compressor. For an isothermal compressor, the gas temperature remains at the initial input value, and no energy conservation equation is needed.

The adiabatic compressor requires a different energy conservation equation depending on whether the flow is in or out of the compressor. The adiabatic compressor is actually only adiabatic when the mass flow is out of the compressor

$$\frac{1}{T} \frac{\partial T}{\partial t} = \frac{k}{p} \frac{\partial p}{\partial t} \quad \dot{m} > 0$$

where $k = (\gamma - 1)/\gamma$. When gas enters the compressor from the aftercooler it is at the T_0 aftercooler temperature, and it mixes with the other compressor gas. Mixing gas of two different temperatures is not adiabatic. The energy conservation equation in this case is

$$\frac{1}{T} \frac{\partial T}{\partial t} = \left(1 - \frac{T}{T_0}\right) \frac{1}{V} \frac{\partial V}{\partial t} + \left(1 - \frac{T}{\gamma T_0}\right) \frac{1}{p} \frac{\partial p}{\partial t} \quad \dot{m} < 0$$

HEAT EXCHANGERS

The temperature of the heat exchanger surfaces is a (time independent) function of x -- linear for the regenerator and constant for the other heat exchangers. The gas temperature is assumed to equilibrate rapidly to the local heat exchanger temperature. This known heat exchanger temperature takes the place of an energy conservation equation. Local conservation of mass and momentum are solved by a finite difference method to compute pressure and mass flow rate as functions of x (downstream axial position) at each time step.

The gas temperature is a function of position but not a function of time. Thus, the equation for local conservation of mass is

$$\frac{\partial \dot{m}}{\partial x} = - \left(\frac{\epsilon A}{RT} \right) \frac{\partial p}{\partial t}$$

where ϵ is the porosity of the heat exchanger packing and A is the total flow area upstream of the packing, so that ϵA is the flow area within the packing.

The equation for local conservation of momentum is

$$\frac{\partial p}{\partial x} = - \frac{RT\mu\dot{m}}{AKp} - \frac{C_1 RT \dot{m} |\dot{m}|}{A^2 K^2 p} - \frac{1}{A\epsilon} \frac{\partial \dot{m}}{\partial t} - \frac{R}{(A\epsilon)^2} \frac{\partial}{\partial x} \left(\frac{T\dot{m}^2}{p} \right)$$

where K is the permeability of the heat exchanger packing and C_1 is the second permeability coefficient. The terms contributing to the pressure drop (right hand side of the equation) in order are: the viscous drag, the form drag, transient momentum storage, and inertia. The mass and momentum conservation equations are linearized and solved by the Keller

Box method* to produce the coefficients of a pair of linear relations between the pressures and mass flow rates at the component boundaries.

For packed screens, the permeability is well correlated by the Kozeny equation⁵

$$K = \frac{d^2}{122} \frac{\epsilon^3}{(1-\epsilon)^2}$$

where d is the wire diameter. For packed screens⁶, $C_1 = 0.074$.

PULSE TUBE

The pulse tube is assumed to have the same pressure at all points. This spatial independence of pressure takes the place of a momentum conservation relation. Local conservation of mass and energy are solved using a Lagrangian approach. A set of gas elements are defined with fixed, equal gas masses. The gas element positions, volumes, and temperatures are tracked with time.

The temperatures of the gas elements change with compression or expansion, with heat exchange to the pulse tube walls, and when entering a heat exchanger at either end of the tube. At the beginning of each time step, the pressure changes, and temperatures of all gas elements within the pulse tube are adjusted for adiabatic compression or expansion, $T=T_0(p/p_0)^{(\gamma-1)/\gamma}$. The gas elements move in the tube both because of the mass flow rates at the ends and because of gas element volume changes (due to pressure and temperature changes). The tube wall is divided into solid elements with equal thermal mass. As the gas elements move past the solid elements, there is heat exchange. The Nusselt number (a user input) is used to determine the heat transfer coefficient, $h = Nu k/D$. The heat exchange is proportional to this Nusselt number, to the temperature difference between the gas element and the solid element, and to the residence time for the gas element being next to the solid element. This wall heat transfer can be shut off (i.e., adiabatic wall assumption) by inputting a zero Nusselt number. When a gas element enters a heat exchanger at either end of the pulse tube, it exchanges heat to equilibrate to the heat exchanger temperature. Gas elements leave the heat exchangers to re-enter the pulse tube at the heat exchanger temperature.

ORIFICE OR VALVE

The orifice component model assumes that the mass flow rate at the right and left ends are equal (no temporary storage of mass, as in the other components). Thus, only a pressure drop relation is needed. The choices of a circular tube orifice (specified length and diameter) or a valve (specified valve coefficient, C_v) are implemented.

In the case of a tube, the pressure loss is the sum of viscous losses and (entrance and exit) dynamic losses

$$P_6^2 - P_7^2 = \frac{4RT \mu L fRe \dot{m}}{AD^2} + \frac{K RT \dot{m} |\dot{m}|}{A^2}$$

where L is the tube length, D is the tube diameter, A is the tube flow area, K is the dynamic loss coefficient, μ is the gas viscosity, and fRe is the friction factor times Reynolds number. The orifice is between component interfaces 6 and 7 -- hence the subscripts on pressure.

The valve coefficient, C_v , is a dimensional quantity which is defined by valve manufacturers with an odd mix of units. With all other quantities in SI units (kg, s, m, Pa, kmol, K), the pressure drop relation for a valve is

$$P_6^2 - P_7^2 = \frac{3 \times 10^{13} T \dot{m} |\dot{m}|}{C_v^2 M}$$

where M is the gas molecular weight.

SYSTEM MODEL RESULTS

The present pulse tube system model has been used for sensitivity studies, to identify key parameters, and to determine performance potential. The model presented in this paper has a number of idealizations that do not perfectly match hardware for which we currently have data. In general, the model predicts the pressure quite well, but not the cooling power. However, this model is being upgraded.

SENSITIVITY STUDY

A pulse tube system with a compressor of 3 cc swept volume was selected as a baseline for our study. The aftercooler, regenerator, and cold end fit in a 8.64 mm ID tube. The aftercooler has 15 150-mesh/inch copper screens. The regenerator has 620 250-mesh/inch stainless steel screens. The cold end has 22 150-mesh/inch copper screens. The pulse tube is a 48 mm long, 5 mm diameter tube. The hot end has 14 150-mesh/inch copper screens. The reservoir is 52 cc. Some other parameters for this baseline case are given in Table 1.

Pressure and mass flow rate histories for the baseline case are shown in Figs. 2 and 3. These solutions are for component interfaces 1 (between the compressor and aftercooler), 4 (between the cold end and

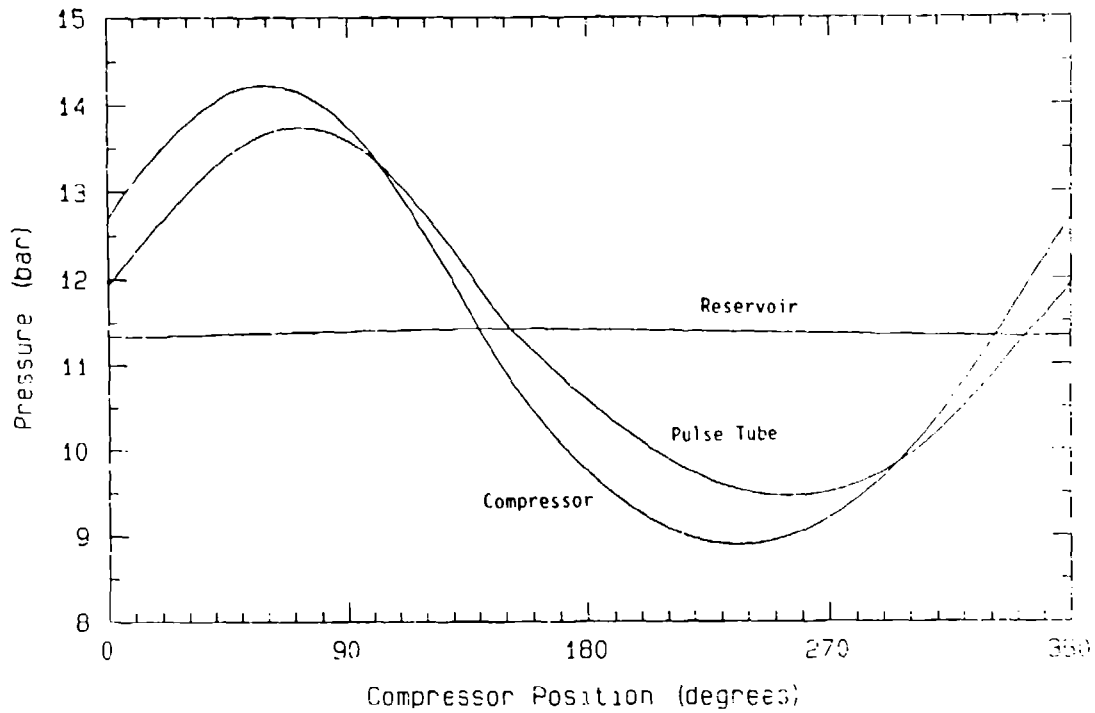


Figure 2. Pressure history in the compressor, pulse tube, and reservoir.

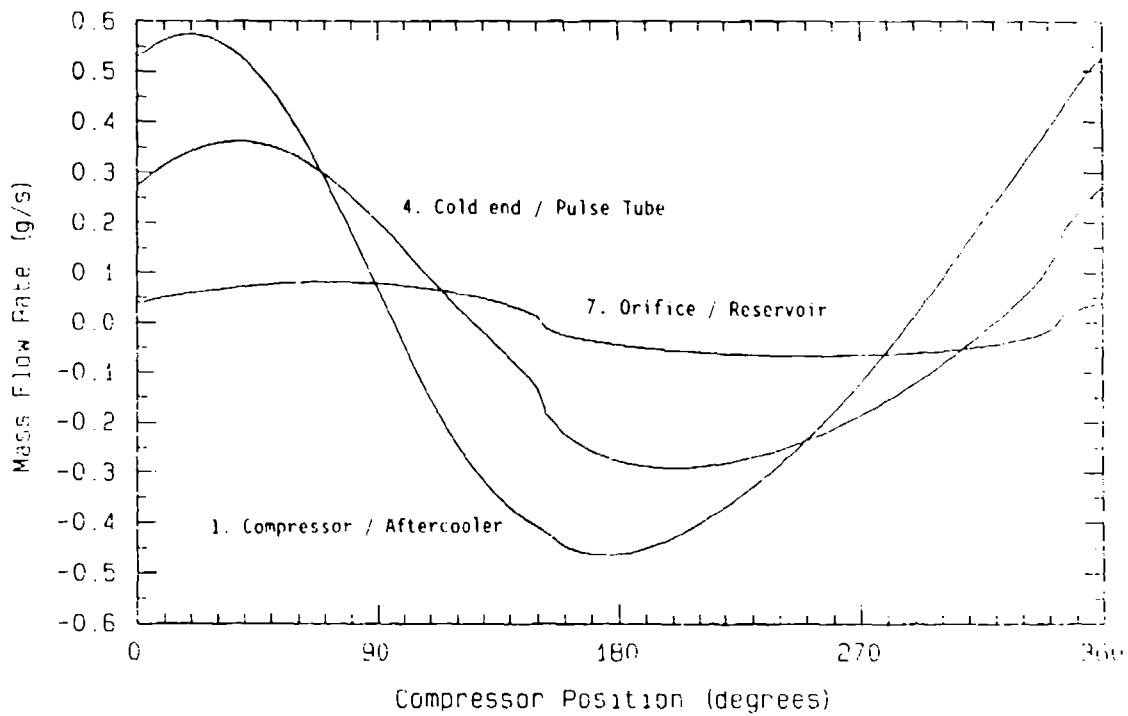


Figure 3. Mass flow rate history at interface numbers 1, 4, and 7.

Table 1. Varied Parameters and Baseline Values.

<u>Parameter</u>	<u>Baseline Value</u>
Frequency	40 Hz
Swept volume	3 cc
Porosity	0.65
Permeability	2.33E-11 m ²
C _v of orifice	0.005
Pulse tube length	4.76 cm
Regenerator length	3.67 cm
Regenerator flow area	0.586 cm ²
Mean pressure	11.36 bar
Cold end temperature	100 K
Hot end temperature	300 K

pulse tube), and 7 (between the orifice and reservoir). The abscissa in these figures was converted from time to compressor position. The solutions shown here are for the fourth compressor cycle. Four cycles is sufficient, because the pressures and mass flow rates are seen to repeat at the 0° and 360° points, and because the component work and heat rejection values converge. The pressure histories (Fig. 2) are seen to deviate from sinusoidal by being more peaked at high pressures and broader at low pressures.

The mass flow rate histories (Fig. 3) are more non-sinusoidal than the pressures. The mass flow rate history through the orifice has a kink at zero mass flow. There is a mass flow rate squared proportionality for the pressure drop through valve type orifices. Thus, as the pressure difference across the orifice approaches zero, the rate of change of mass flow rate is infinite. The finite time step size (each compressor cycle was subdivided into 120 time steps for this example) with the infinite slope at zero mass flow results in a small kink.

A sensitivity study was conducted to determine the impact of many of the pulse tube cooler design and operating parameters to the system performance (parameters varied are listed in Tables 1 and 2). In most cases, only one variable at a time was altered from the baseline case. However, when porosity was varied, permeability was also varied. The compressor mean volume was always 4.58 cc minus half the swept volume.

The sensitivity study results (fraction of Carnot efficiency, compressor work, cold end heat rejection, and ratio of dynamic pressure to mean pressure in the compressor) are shown in Table 2. The largest predicted efficiencies (0.52 times Carnot efficiency) were achieved by increasing the regenerator permeability (cases 7 and 8). Most other predicted significant improvements in the specific performance are also directly related to reducing the pressure drop in the regenerator. These include: lower frequency (case 2), smaller regenerator length

Table 2. Sensitivity Study Results.

Case	Varied Parameter	Value	η_c	Work (W)	Cooling (W)	P_3/P_0
1	None (baseline)	--	0.356	27.6	4.9	0.234
2	Frequency	20 Hz	0.439	14.4	3.1	0.176
3	Frequency	80 Hz	0.193	55.8	5.4	0.275
4	Swept volume	2 cc	0.386	12.3	2.4	0.150
5	Swept volume	4 cc	0.323	50.8	8.2	0.324
6	Porosity	0.4	0.070	53.6	1.9	0.537
	Permeability	1.85E-12 m ²				
7	Porosity	0.8	0.510	18.6	4.7	0.192
	Permeability	1.33E-10 m ²				
8	Porosity	0.63	0.515	20.5	5.3	0.205
	Permeability	1.33E-10 m ²				
9	C_v for orifice	0.001	0.185	13.0	1.2	0.238
10	C_v for orifice	0.002	0.279	17.1	2.4	0.239
11	C_v for orifice	0.01	0.335	34.5	5.8	0.209
12	C_v for orifice	0.02	0.162	31.0	3.5	0.162
13	Pulse tube length	2.38 cm	0.386	30.2	5.8	0.257
14	Pulse tube length	9.52 cm	0.294	24.5	3.6	0.202
15	Regenerator length	1.84 cm	0.458	28.6	6.6	0.250
16	Regenerator length	7.34 cm	0.201	29.3	2.9	0.228
17	Regen. flow area	0.293 cm ²	0.267	41.3	5.5	0.320
18	Regen. flow area	1.172 cm ²	0.409	16.8	3.4	0.168
19	Mean pressure	5.68 bar	0.262	17.1	2.2	0.269
20	Mean pressure	22.72 bar	0.431	47.6	10.2	0.397
21	Cold temperature	70 K	0.385	28.1	3.3	0.199
22	Cold temperature	130 K	0.310	26.6	6.3	0.264
23	Hot temperature	250 K	0.332	25.1	5.6	0.253

(case 15), increased regenerator flow area (case 18), and increased mean pressure (case 21).

The valve coefficient, C_v , of the orifice has a large impact on the specific performance. There is an optimum C_v for each system that gives a peak efficiency, and both smaller and larger C_v values result in smaller specific performance values. The valve coefficient of the baseline case is near optimum. The valve coefficient is varied in cases 9 through 12, resulting in smaller specific performance than for the baseline case.

Increasing the compressor swept volume increases both the cold end cooling and the compressor work nearly proportionally, so that the efficiency variation is small. Increasing the compressor frequency also increases both the cooling and the work, but then the efficiency decreases due to increased regenerator pressure losses.

ACKNOWLEDGMENT

This work was supported by NASA Ames under contract NAS2-13009.

REFERENCES

1. E.I. Mikulin, A.A. Tarasov, and M.P. Shkrebyonock, "Low temperature expansion pulse tubes," Adv. Cryogenic Engn., 29, 629 (1984).
2. R. Radabaugh, J. Zimmermann, D.R. Smith, and B. Louie, "A comparison of three types of pulse tube refrigerators: New methods for reaching 60 K," Adv. Cryogenic Engn., 31, 779 (1986).
3. I. Urieli and D.M. Berchowitz, Stirling Cycle Engine Analysis, Adam Hilger Ltd, Bristol (1984).
4. H.B. Keller, "Accurate difference methods for nonlinear two-point boundary value problems," SIAM J. Numer. Anal., 11, 305-320 (1974).
5. J.E. Eninger, "Capillary flow through heat-pipe wicks," Radiative Transfer and Thermal Control, Progress in Astronautics and Aeronautics, 49, 435-459 (1976).
6. G.S. Beavers and E.M. Sparrow, "Non-Darcy flow through fibrous media," J. Appl. Mech., 36, 711-714 (1969).

ACTIVATED CARBON TEST ASSEMBLY

Ben P. M. Helvensteijn and Ali Kashani
Sterling Federal Systems, Inc.
Palo Alto, CA 94303

Randall A. Wilcox
Trans-Bay Electronics, Inc.
Richmond, CA 94804

ABSTRACT

A cryostat has been assembled in order to establish the helium adsorption characteristics of several commercially available activated carbons. The apparatus is designed to allow studies of both static and transient behavior. Static pressures are measured with room temperature instrumentation applying thermo-molecular pressure difference corrections. Transient pressure data are established using cryogenic pressure gauges. This paper discusses the apparatus and results obtained in preliminary tests. One sample of activated carbon has been tested at temperatures between 4.2 K and 30 K for pressures ranging from 0.1 kPa up to 300 kPa.

INTRODUCTION

The amount of helium adsorbed by activated carbon depends strongly on both the temperature and pressure. Large amounts of helium may be adsorbed at low temperatures (mostly below 30 K) and over a wide range in pressure (even below 1 Pa = 7.5 mTorr). Activated carbon is applied in various types of low temperature refrigerators for its ability to adsorb and desorb large amounts of helium reversibly. Typically, carbon forms the getter for a gas/vacuum heat switch^{1,2}. In more advanced systems the carbon affects evaporative cooling^{3,4}. The efficiency of carbon controlled heat switches and pumps may be improved significantly by precise knowledge of the temperature - pressure - adsorption relations of the incorporated carbon.

Low temperature helium adsorption data has been collected by Vazquez et al. and others^{5,6}, however, the carbons used for these publications are not so readily available. Because of the variation in adsorption qualities of nonidentical carbons (e.g. between the two sets of Vazquez data) one may not assume the specifications of one source to be

valid in general, particularly if the margins for operation are tight. The dilemma presented by availability, variability and need for efficient adsorption pumps^{2,4} has lead us to study carbons which are easy to come by. Ironically the first results published here are on a carbon sample for which future production is uncertain. This choice is related to the unusually high surface area ($2000 \text{ m}^2/\text{g}$) suggesting a great potential for helium adsorption. Experiments on mass-produced carbons are not yet completed and so will be published elsewhere.

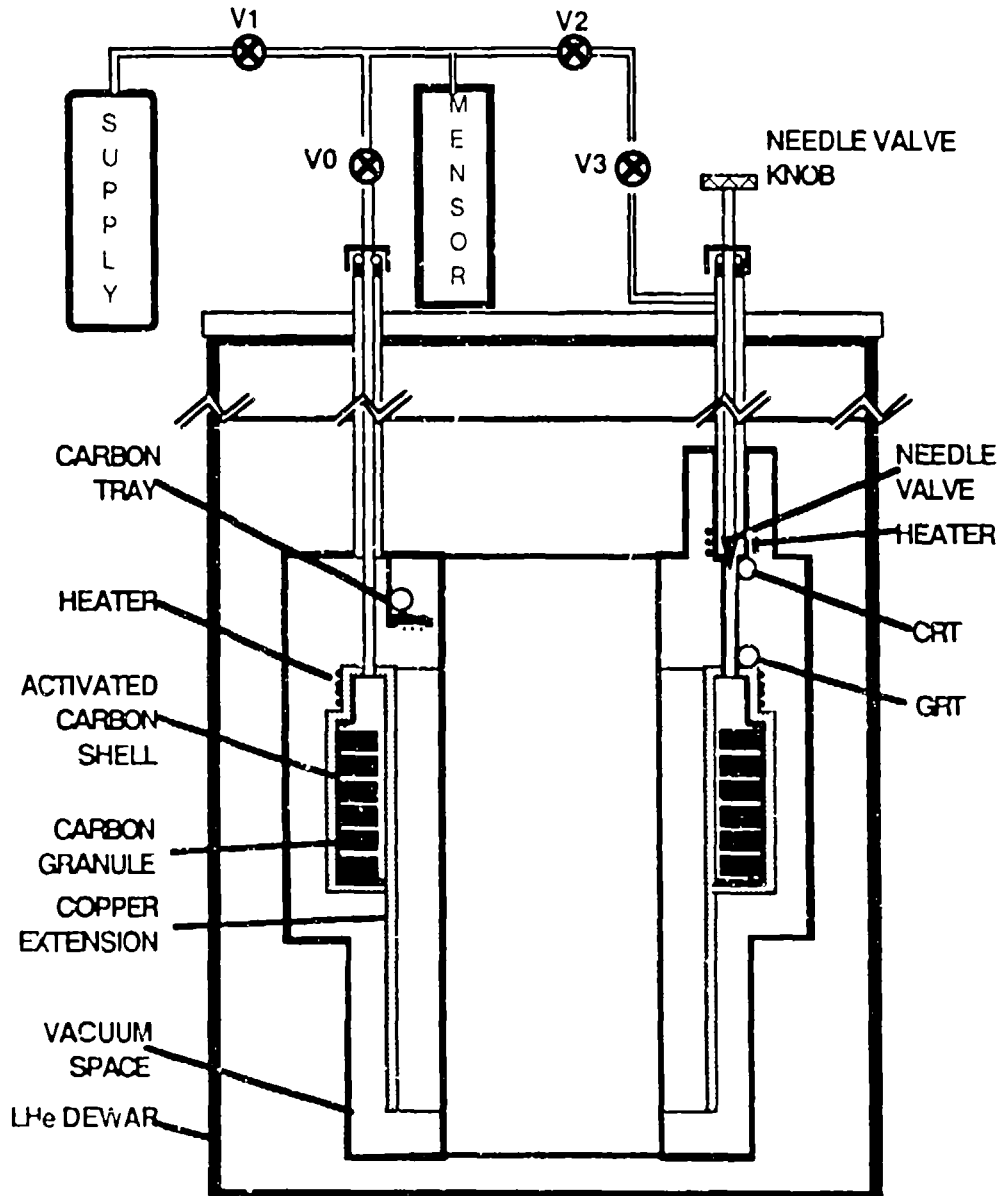


Fig. 1 Sketch of the Activated Carbon Test Assembly.

APPARATUS

The main component of the activated carbon test assembly (ACTA) is the annular carbon shell (ACS) depicted in figure 1. The container is constructed as an annular space in order to attain the desired wall area to bond the carbon to, without compromising on container volume (39 cm^3). The ACS contains 3.5 g of cylindrical carbon granules*, roughly 4 mm tall and 3 mm in diameter. The granules are bonded with a thin layer of stycast 2850 FT to the container wall. A manganin wire heater is varnished to the ACS as well as a germanium resistance thermometer (GRT). The pressure inside the ACS may be measured through a 1.5 mm inner diameter tube by an external gauge# (as shown) or by means of a cryogenic pressure sensor (CPS, not shown). The pressure data contained in this paper are measured with an external Mensor gauge (model 100) fitted with a 1.4 MPa (200 psi) pressure module. Modules for different pressure ranges are available. The gauge volume (including the space between the valves V0, V1 and V2) equals 37 cm^3 . A second port to the ACS is provided by the needle valve to supply the helium when the CPS is in place. In the present experiments the needle valve is closed (average leakrate over three days $< 10^{-6}$ std.cc/s). The needle valve port is supplied with a separate heater and carbon resistance thermometer (CRT) so that its temperature may be kept in check with the ACS temperature.

The ACS is surrounded by an annular vacuum can. The pressure inside the vacuum can is controlled by means of a small carbon tray. When the carbon tray is heated up, the vacuum is broken, thermally shorting the ACS to the liquid helium bath. The ACS is made out of copper and its inner wall is extended downwards increasing the cooldown heat exchange area. The spacing between the ACS facing walls of the vacuum can and the ACS is roughly 0.5 mm. This close fit allows the rapid cooldown needed in transient studies. To date no transient data have been recorded using ACTA since this requires a CPS in place.

Not shown in figure 1 is the data acquisition (HP), wiring and some additional plumbing. For graphics and minor computations a MacIntosh computer has been used with Abelbeck Software.

PROCEDURE

After leaktesting, the cryostat is prepared for an experiment by purging the ACS at room temperature repeatedly with nitrogen gas and at a later stage with helium gas. In between pressurizing and before cooldown inside the dewar, the ACS is thoroughly evacuated using a turbo pump. Once the dewar is filled with liquid helium and the cryostat is cold, the activated carbon is given a first charge of helium gas. The amount admitted is derived from the change in tank pressure before and after

passing gas through valve V0. The pressure gauge is pumped out after which the charge in the ACS is allowed to also enter the pressure gauge.

Being charged with helium, the cryostat is ready for testing. The ACS is heated up while monitoring the progression in temperature and pressure readings. Near predetermined pressure values the heating rate is slowed down. The pressure and temperature data are recorded during the slow passage of a setpoint. No significant difference in data values ($< 0.1\%$) has been observed between this mode of measurement and complete steady state. When the pressure and/or temperature range of interest has been traversed, the heaters on the ACS and needle valve are turned off, the carbon tray heater being turned on. Due to the drop in temperature, the activated carbon pumps the remaining helium out of the Mensor back into the ACS. The completion of one set of data at a particular charge of helium to the ACS is succeeded by a repetitive series of additional charges of helium to the system and more data collection.

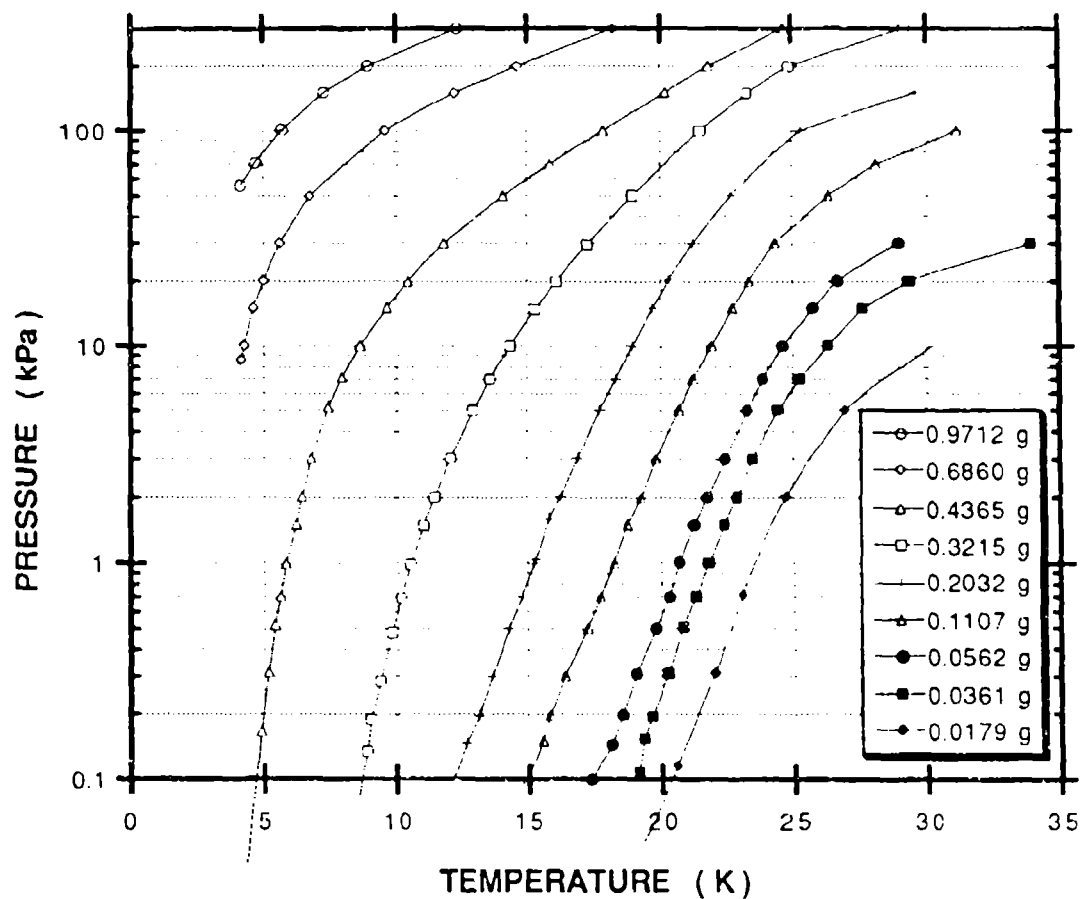


Fig. 2 Pressure Data as a Function of Temperature.
at Various Helium Charges.

RESULTS AND DISCUSSION

The temperature and pressure data gathered at various charges of helium to the system are plotted in figure 2. The index shows the total mass of helium in the system for each curve. In the initial run the system has been charged with 0.4365 g of helium; a measured amount of helium (0.4186 g) has been extracted between the first and second run. Given the selection of experiment setpoints, the data are easily converted into adsorption diagrams at constant pressure (figure 3). In addition the variation of helium adsorption during each test is shown in figure 4. The adsorption is computed by subtracting the mass of helium in the gas phase in the ACS as well as in gauge volume from the total charge. To this purpose merely the ideal gas law has been applied. No corrections are made for thermo-molecular pressure differences over the tube connecting the ACS and the Mensor. Also ignored is the volume of the tube.

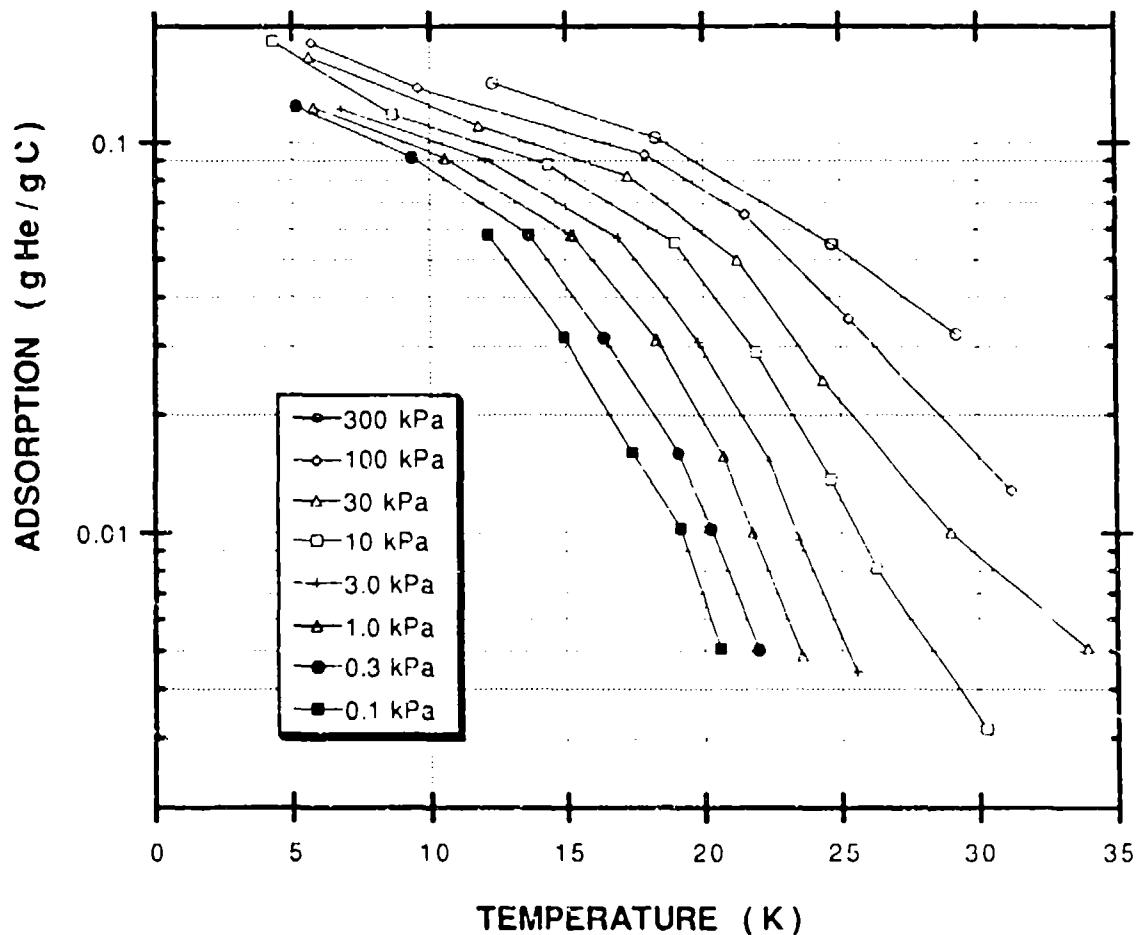


Fig. 3 Isobars of Helium Adsorption.

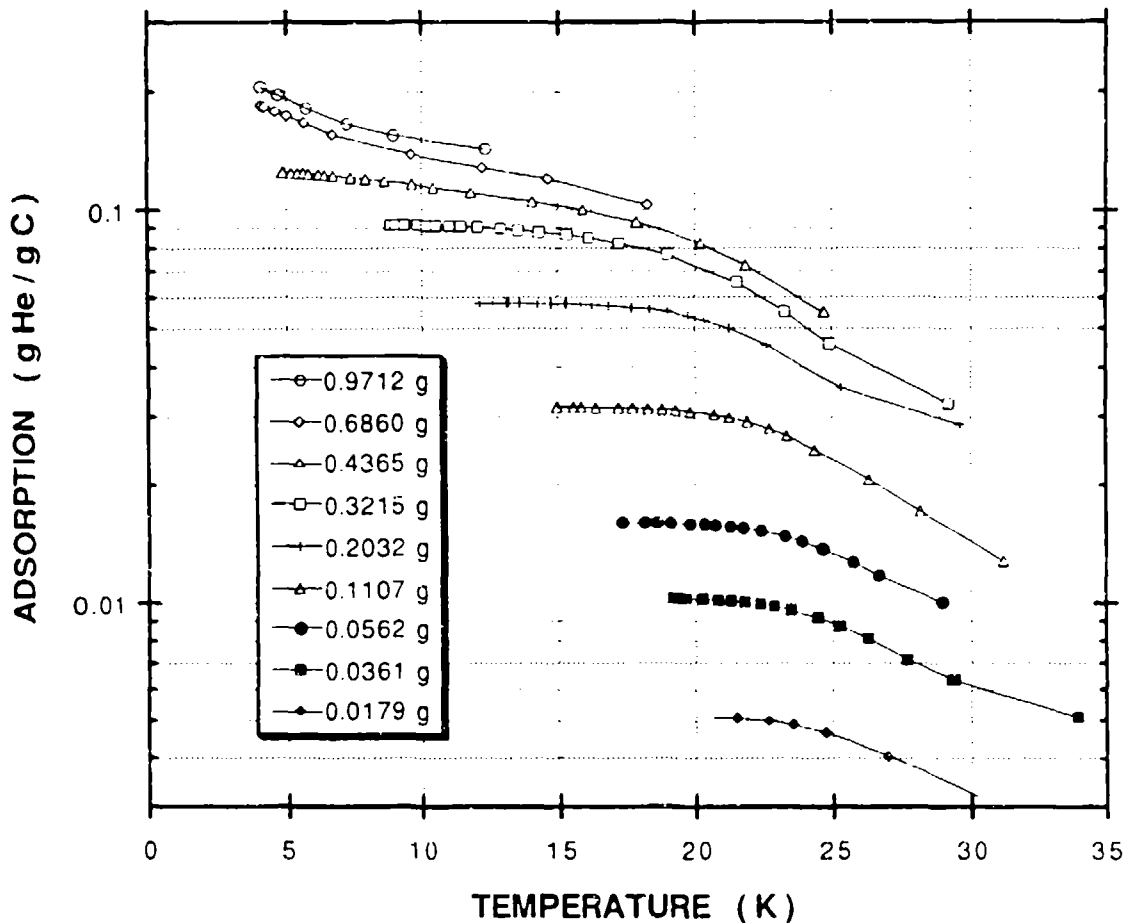


Fig.4 Adsorption at Various Charges of Helium.

The data in figure 2 clearly demonstrate the well known feature of activated carbon to enable one to control the helium gas pressure over a wide range merely by regulating the temperature of the carbon. The pressure-temperature relation is of importance in the design of heat switches. Supplementary data at low pressures is to be taken in the near future. Computations are in progress to compute the appropriate pressure setpoints taking into account the thermo-molecular pressure ratios.

Near 20 K the results on the adsorption of the given sample of carbon presented in figure 3 are found to be quite similar to the data provided by Vazquez et al. on their sample of Saran. However, at high pressures, around 10 K and below, the APD sample appears to be a superior helium adsorber. Figure 4 shows that near 5K and at high helium charges, the adsorption increases as the temperature is lowered, which suggests multi-layer condensation onto the carbon. Whether the adsorption increase is an artifact caused by our approximations has not yet been resolved.

At low pressures the present data indicate a lesser ability for the APD than the Saran to adsorb helium. This may be the result of our failure to include thermo-molecular effects in the data conversion. The effect this correction is expected to have on the data is to alter the pressure index labels on the curves to lower values.

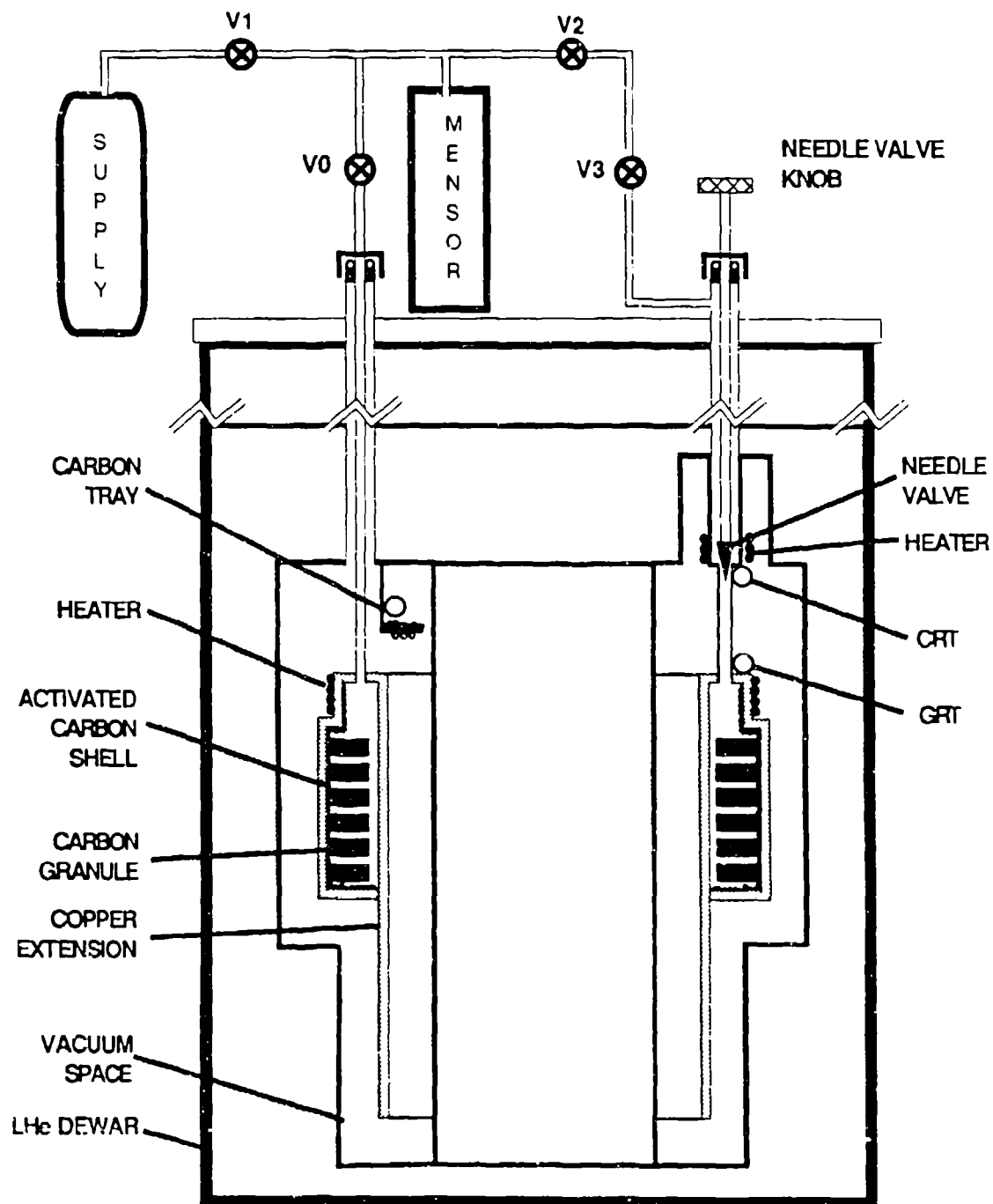
CONCLUSIONS AND FUTURE WORK

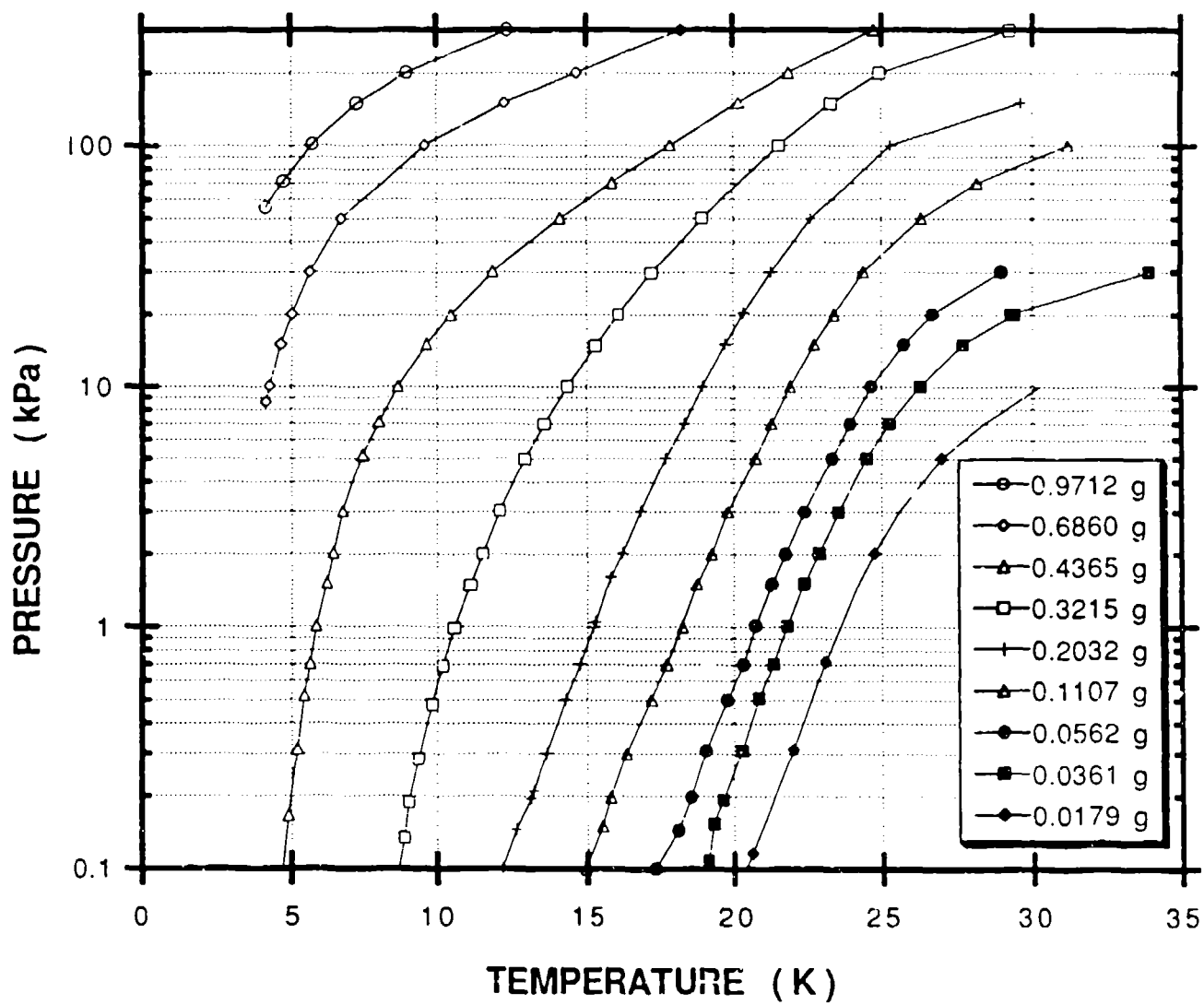
The experiments have demonstrated the capability of the apparatus to provide us the desired data-base on various activated carbons. The data obtained thus far need to be analyzed more precisely to exclude the possibility of errors due to inappropriate approximations. The tested sample of carbon appears to be an excellent adsorber of helium.

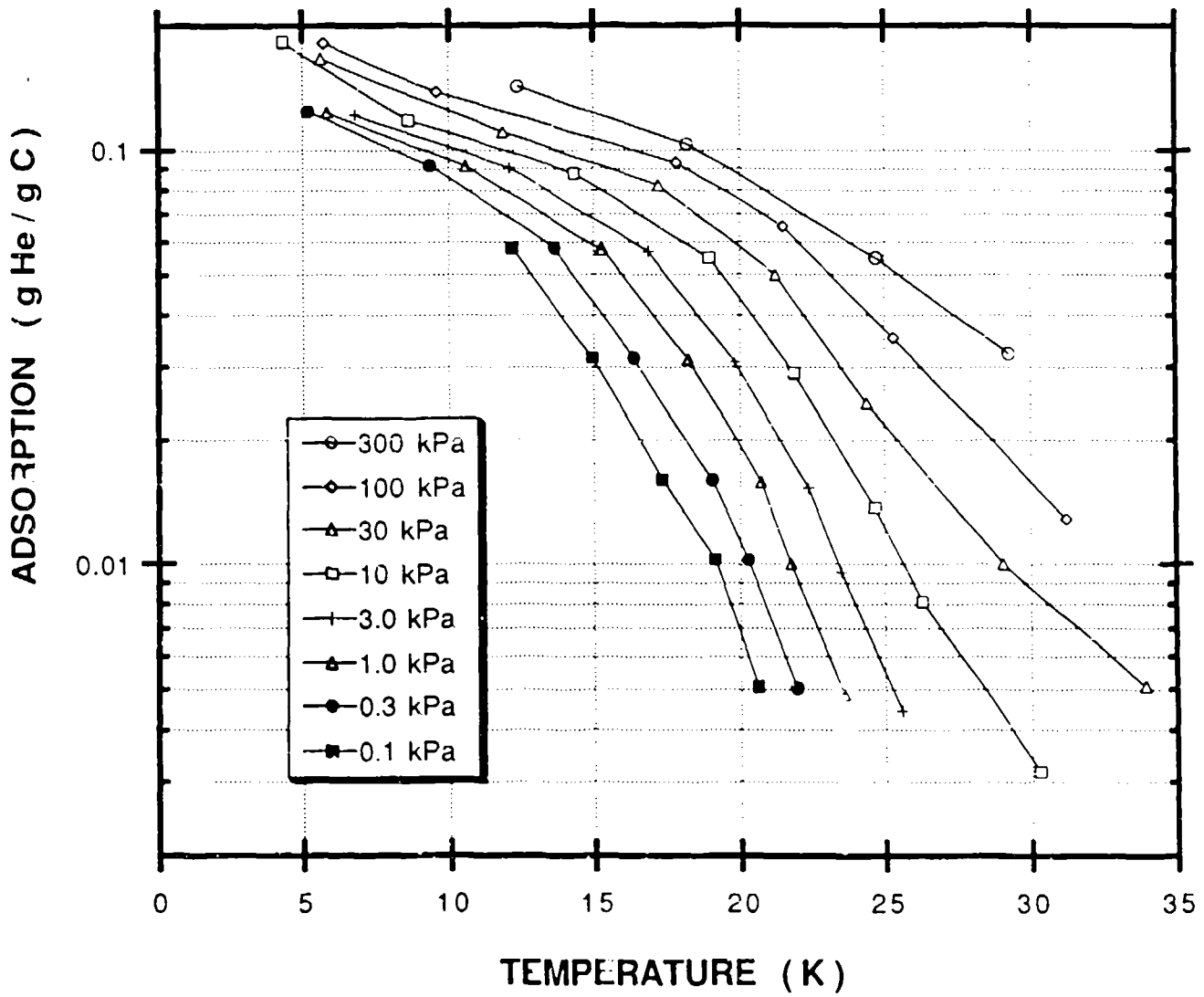
This work is to continue and expand in three ways. Data will be gathered over a wider range of pressures; a variety of carbon samples is to be tested and lastly: adsorption of ^3He and ^3He - ^4He mixtures will be compared to that of the presently studied, more common isotope ^4He .

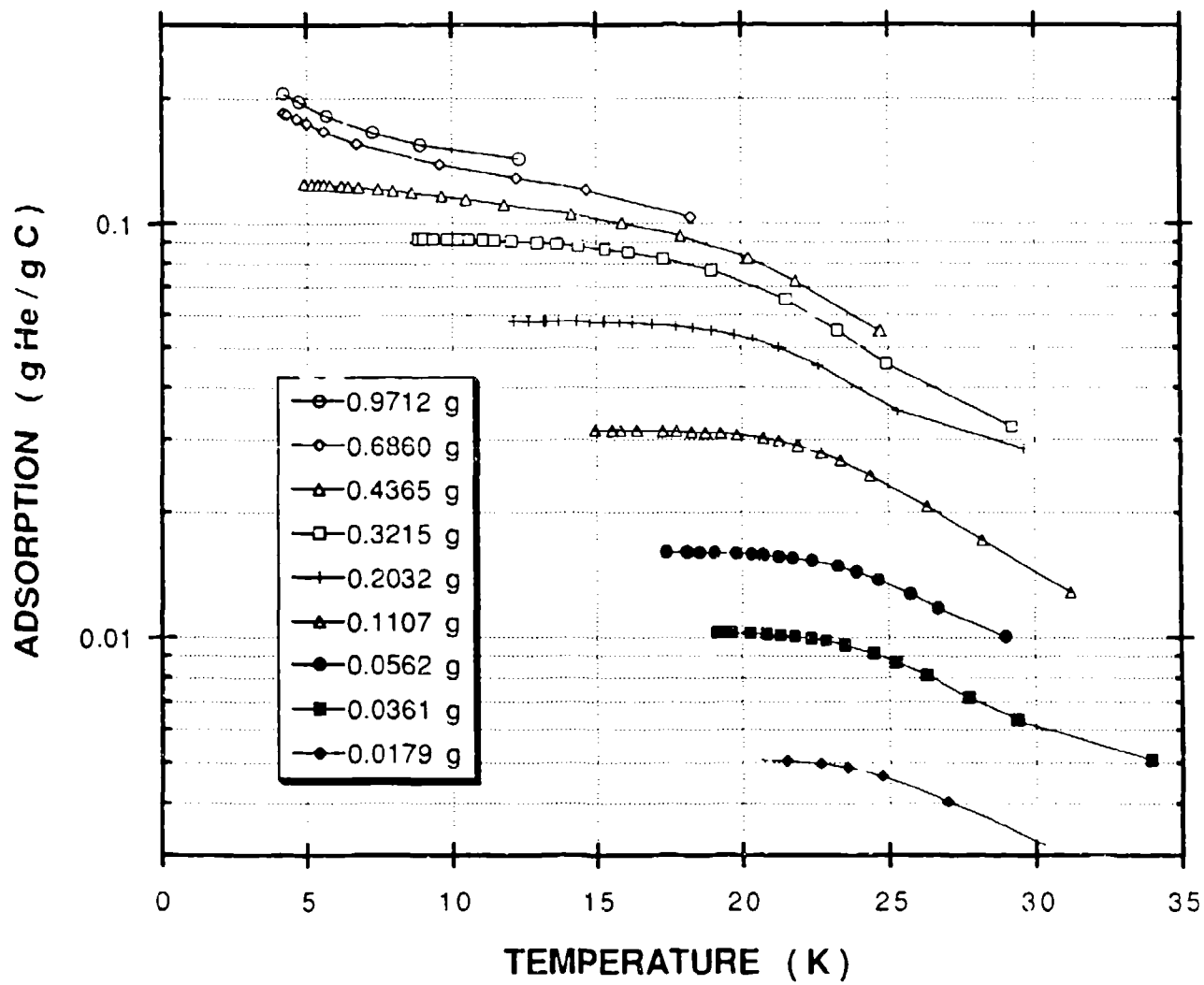
REFERENCES

- * Courtesy APD Cryogenics Inc., Allentown, PA 18103, USA
- # Mensor, Model 100
- 1 Chan, C.K.; "Gas Adsorption/Adsorption Heat Switch", Jet Propulsion Laboratory, Pasadena, CA, (July 1987).
- 2 Helvensteijn, B.P.M., Kashani A.; "Conceptual Design of a 0.1 W Magnetic Refrigerator for Operation between 10 K and 2 K", *Advances in Cryogenic Engineering*, Vol. 35, Plenum Press, New York (1988), p. 1115-1123.
- 3 Roach, P.R., Gray, K.E.; "Low-Cost, Compact Dilution Refrigerator: Operation from 200 to 20 mK", *Advances in Cryogenic Engineering*, Vol. 33, Plenum Press, New York (1988), p. 707-712.
- 4 Roach P.R., Helvensteijn, B.P.M.; "A Continuously-Operating Dilution Refrigerator for Space Applications", ICCS ,1990, Plymouth, MA.
- 5 Vazquez, I., Russell, M.P., Smith, D.R., Radebaugh, R.: "Helium Adsorption on Activated Carbons at Temperatures between 4 and 76 K", *Advances in Cryogenic Engineering*, Vol. 33, Plenum Press, New York (1988), p. 1013-1021.
- 6 Roubeau, P., Nigohossian, Avenel, O.: "Adsorption de l'Helium 4 par le Charbon Actif", *Colloque International: "Vide et Froid"*, Grenoble, 2-5 Decembre, 1969; p.22-33.









DEVELOPMENT OF A HIGH DENSITY ACTIVATED CARBON-CARBON COMPOSITE FOR CRYOGENIC APPLICATIONS

Gilbert Brassell, James Lieberman, and Josephine Curtis
R&D Material Science Division
NFT, Incorporated
409 Corporate Circle, Denver, Colorado 80401

ABSTRACT

NFT has developed a method for molding structural activated carbon-carbon composites (ACCs) which can be manufactured into many shapes to be used in getters and cryopumps. An effort is underway to improve the ACC for use in adsorption compressors for use with Joule-Thompson refrigerators. The material currently has a surface area of between 400 and 500 m²/g, a compressive strength of 20 to 150 psi, and a density of 0.1 to 0.5 g/cm³. The initial objective is to raise the surface area to 1000 m²/g and the density to 1 g/cm³, a level which is believed necessary for use in adsorption compressors. Preliminary studies have shown that high densities and anisotropic thermal conductivity behavior can be achieved by tailoring the materials and processes. During the past year, fiber to binder ratios, and different binders have been investigated, in addition to metallic salt pretreatment of starting materials. The molding, curing and activation methods also were studied.

The current results show that CO₂ activation under a partial blanketing gas of nitrogen gives the best results. Chemical treatments of precursor material has, so far, been inconclusive. Further study is being conducted in that area.

INTRODUCTION

The use of activated carbon for adsorption of gases in cryogenic applications such as cryopumps is common-place. Another cryogenic application now under extensive study is

adsorption compressors for use with Joule-Thompson refrigerators. These compressors have no moving parts and require only heat input for their operation. Their efficiency can be improved with higher surface areas per unit volume in the adsorber and with lower void volumes. A new application which has received some attention recently is the use of adsorbers as a matrix for regenerative heat exchangers in the 4-20 K temperature range. These adsorbers would also require high surface-to-volume ratios. The optimum geometry for the adsorber would be in the form of plates in order to eliminate void volume.

For use in a regenerator, the adsorber should have a good thermal conductivity in the direction perpendicular to the gas flow, but a low thermal conductivity in the direction parallel to the gas flow.

Commercially available activated carbon which is used in these applications is granular and exhibits a density in the range of 0.5 to 1.0 g/cm³ and a surface area of about 1000 m²/g. However, since the carbon is used in the form of a packed bed, a certain amount of void space between the particles lowers the overall surface area per unit volume of the system. Thus, the adsorber efficiency is lowered. Also, the granulated carbon has a tendency to produce contamination problems due to dusting (friable) characteristics.

NFT has developed a structural activated carbon-carbon composite (ACC) for use in cryogen containment systems. This composite material which consists of a carbon bonded carbon fiber exhibits a surface area of between 400 and 500 m²/g, a compressive strength of 20 to 150 psi, and a density of 0.1 to 0.5 g/cm³. The material can be fabricated in a large array of sizes and shapes. Preliminary studies have shown that high densities, high surface areas and anisotropic thermal conductivity behavior can be achieved by tailoring the materials and processes.

EXPERIMENTAL

Fabrication of the activated carbon composite can be separated into three different steps: 1) fiber preparation, 2) composite molding and 3) carbonization/activation. A flow diagram of this process is presented in Figure 1. The effects of fiber activation techniques and process variables on composite density, porosity, compressive strength, surface area and thermal conductivity were studied. Process variables investigated included fiber length, fiber-to-resin ratio, binder type, composite compression and curing of

composite block, and composite carbonization/activation profile.

FIBER PREPARATION

These studies used rayon, polyacrylonitrile and cotton fibers as precursor materials for producing carbon fibers. Original work was conducted using carbonized rayon fiber. Because of availability and price, cotton fiber was later substituted. The carbonized cotton fiber retained most of the positive characteristics needed for its intended purpose, i.e. as a starting material for carbonized composite media for high efficiency particulate filters. Further investigation was conducted on the cotton based material to optimize it for use in getter applications. Studies of the cotton based activated carbon composites (ACCs) showed a distinct predominance of average pore sizes in the 17 to 18 A diameter range. Other samples had average pore size distributions centering at 7.5 A. The material's pore size distribution resulted in an ability to adsorb gases at cryogenic temperatures.

The carbon fiber used to fabricate composites was obtained by subjecting the fiber precursor to temperatures up to 800°C in an argon, nitrogen, argon/carbon dioxide, or N_2/CO_2 atmosphere to prevent degradation. The carbon fiber was then sized to the desired length by processing through a Wiley mill.

COMPOSITE MOLDING/CURING

Composite molding consisted of preparing a mixture of carbon fibers and powdered phenolic resin in a dilute water slurry and using pulp/vacuum molding techniques to form a solid cake of the desired configuration. The wet cake was cured/dried at 100-150°C for 3-12 hrs which allowed the resin to flow and create a bonding web between the carbon fibers resulting in a rigid structure. High density samples were produced by compressing the wet cake and then curing the cake in a compressed state.

Preferred fiber orientation in the final composite is achieved during the vacuum molding process. Fibers tend to align randomly in planes normal to the applied force of vacuum. Because of this preferential orientation, the material has different conductivities normal and parallel to the vacuum mandrel or plate. It is thought that anisotropic thermal conductivity behavior can be achieved by introducing highly conductive flake or fibrous materials into the

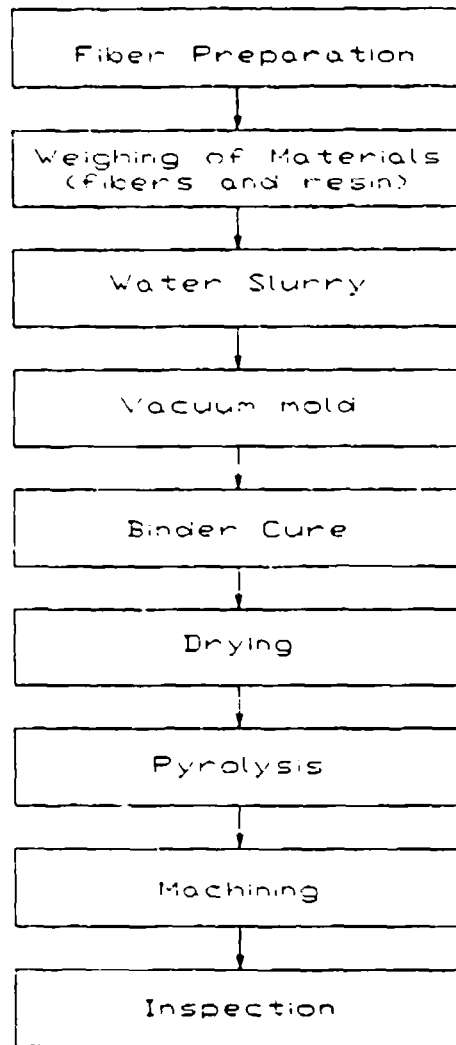


Figure 1. Process flow chart for producing fibrous carbon-carbon composites

composite during molding. The final composite would have high thermal conductivity in the plane parallel to the vacuum source and be thermally insulative in the direction perpendicular to the vacuum source. Towards this end, graphite flakes and metallic particles were added to the water slurry prior to the molding of several composite samples.

Two naturally occurring organic binders were tried as substitutes for the phenolic resin. These were cornstarch and powdered tapioca. Although composites were successfully fabricated with these binders, preliminary studies of dusting characteristics and surface area were unfavorable. Future experimentation may overcome these problems.

COMPOSITE CARBONIZATION

The carbonization cycle consisted of subjecting the composite to a temperature in excess of 700°C in an inert atmosphere to prevent oxygen-induced degradation. This operation resulted in transformation of the phenolic resin to carbon with the resin shrinking and losing about 50% of its original weight.

COMPOSITE SURFACE ACTIVATION

The surface area of carbon bonded carbon fiber composites carbonized as described above is quite low (<10 m²/g). However, high surface area values were obtained by exposing the composite to a controlled oxidizing atmosphere.

Experiments were conducted in which carbonized rayon fiber, commercially available cotton fiber and final composite structures were exposed to different amounts of argon, nitrogen and carbon dioxide while at temperatures in excess of 700°C. The results of these experiments are discussed below.

COMPOSITE PROPERTIES

The composite properties of interest include: density, porosity, compressive strength, dusting characteristics, hygroscopy, surface area and thermal conductivity. The density and porosity values were determined by using volume and weight relationships. Compressive strength values reported were measured using an Instron Tensile testing machine. Dusting characteristics of the material were determined by testing to Mil. Std. 1246A and found to have a

contamination level of <500; the specified limit is <750. The affinity for water was determined by placing weighed samples of the activated carbon composite and samples of a commercially available activated charcoal (0.635 cm size) in a humidity chamber for 24 hours. The samples were then re-weighed and percent of weight gain was calculated. The surface area measurements were conducted using a Digisorb Model 1600 BET analyzer utilizing nitrogen as the adsorbent.

DISCUSSION OF RESULTS

FIBER PREPARATION

The carbon fiber used was obtained by subjecting a fiber precursor to temperatures up to 800°C in a inert or slightly oxidizing atmosphere. The carbon fiber was milled to produce different sizes of fiber. Rayon precursor studies were conducted using fibers milled to 0.0635 cm ("long" fiber) and 0.0127 cm ("short" fiber). The long fiber exhibited a surface area of 0.75 m²/g and the short fiber exhibited a surface area of 1.19 m²/g. Composites made with smaller size fiber have higher apparent density, lower porosity, greater compressive strength and higher surface area per unit mass.

EFFECTS OF FIBER LENGTH

The effect of fiber length on composite properties of interest was studied by fabricating composite specimens with long carbonized rayon fiber (0.0635 cm), short carbonized rayon fiber (0.0127 cm), and a 50/50 mixture of the two lengths of carbonized rayon fiber. The resin content was held constant at 30% and the composite specimens were all subjected to 700°C for three hours and 3% carbon dioxide in an argon carrier gas.

The effect of fiber length on density, compressive strength and surface area is shown in Figures II, III and IV. The composite density appears to be directly proportional to the fiber length with the long fiber resulting in a composite density of 0.14 g/cm³ (93% porosity) and the short fiber resulting in an increase of composite density to 0.33 g/cm³ (84% porosity).

The most significant fiber-length-induced change in properties is that of compressive strength. The compressive strength increased from 0.38 MPa for the long fiber composite

to 2.03 MPa for the short fiber material, representing a change of more than 500%. This behavior is significant since the dusting characteristics of the fibrous composite are directly related to strength and structural stability.

The composite disks fabricated exhibited a surface area of 310 m²/g and 380 m²/g for the long and short fibers respectively. This change is attributed to the inherently larger surface area per unit volume of the small fiber due to the larger number of fibers.

EFFECTS OF RESIN CONTENT

The effect of resin content on the composite properties was evaluated by fabricating disks with 30, 35, 40, and 50 weight percent resin and the remaining material being long carbonized rayon fiber (0.0635 cm). This resin system will lose about 50 to 60% of its original weight when pyrolyzed at temperatures in excess of 700°C. The effects of resin content on density, strength and surface area are plotted in

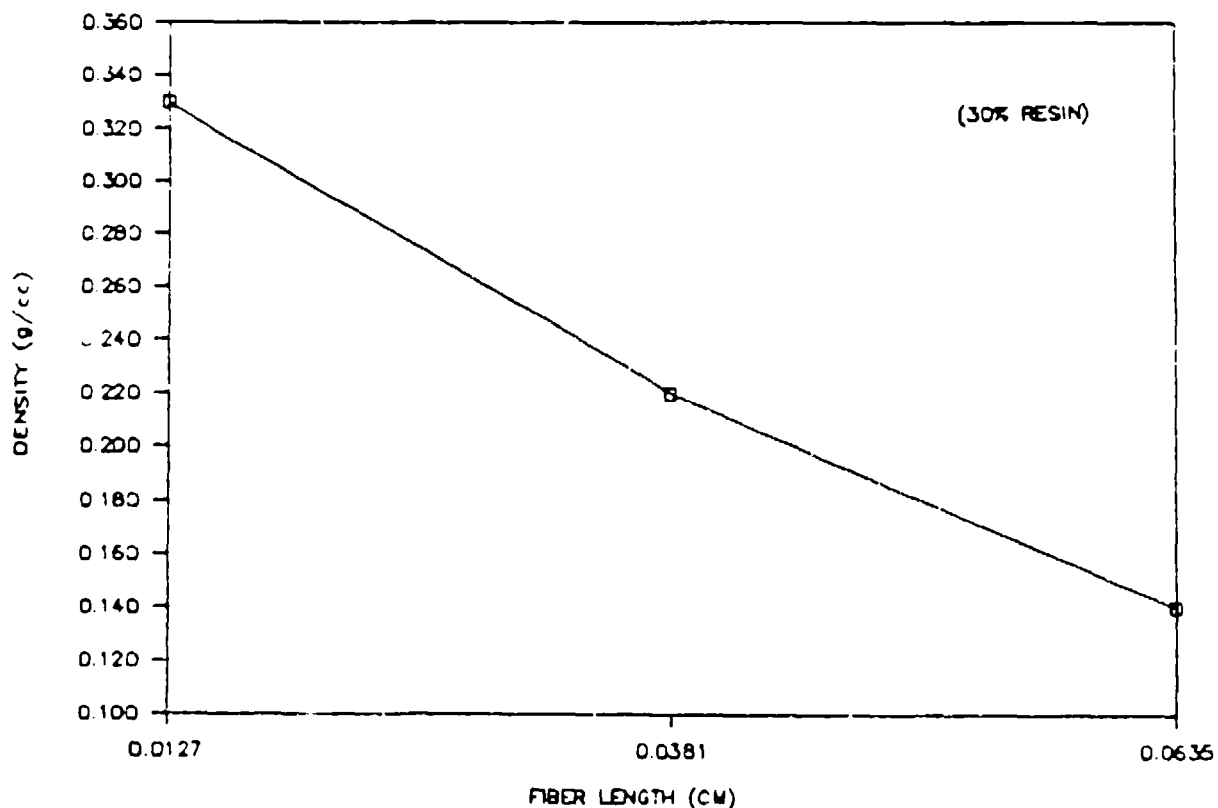


Figure II. Effect of carbonized rayon fiber length on composite density.

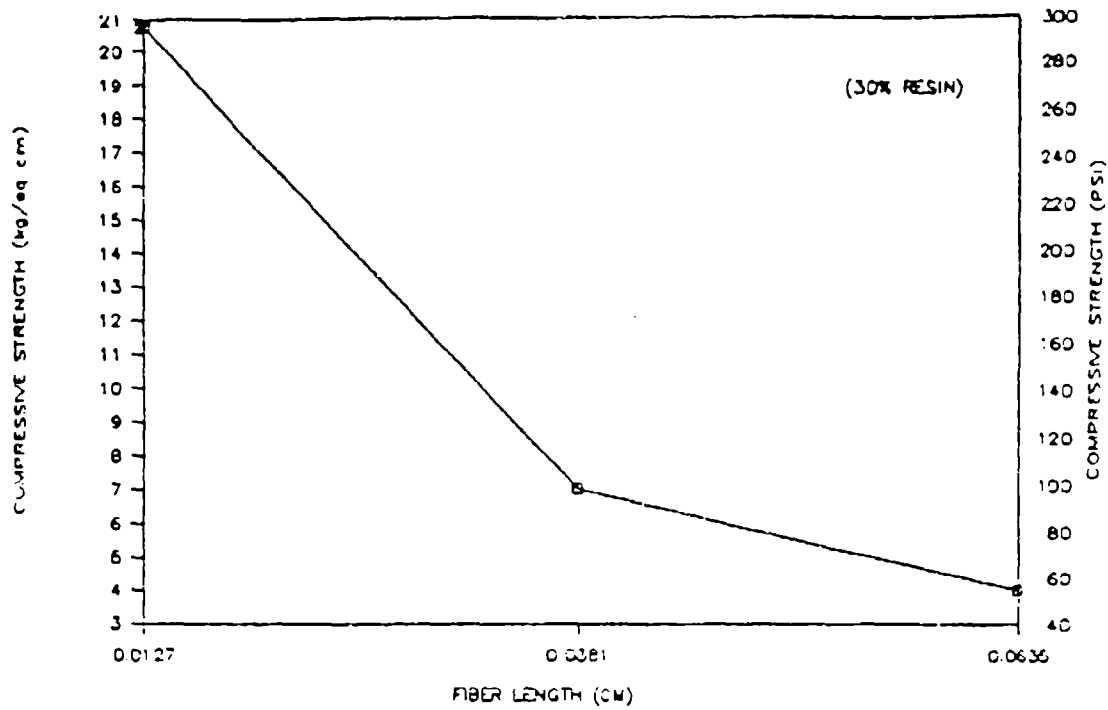


Figure III. Effect of carbonized rayon fiber length on composite compressive strength.

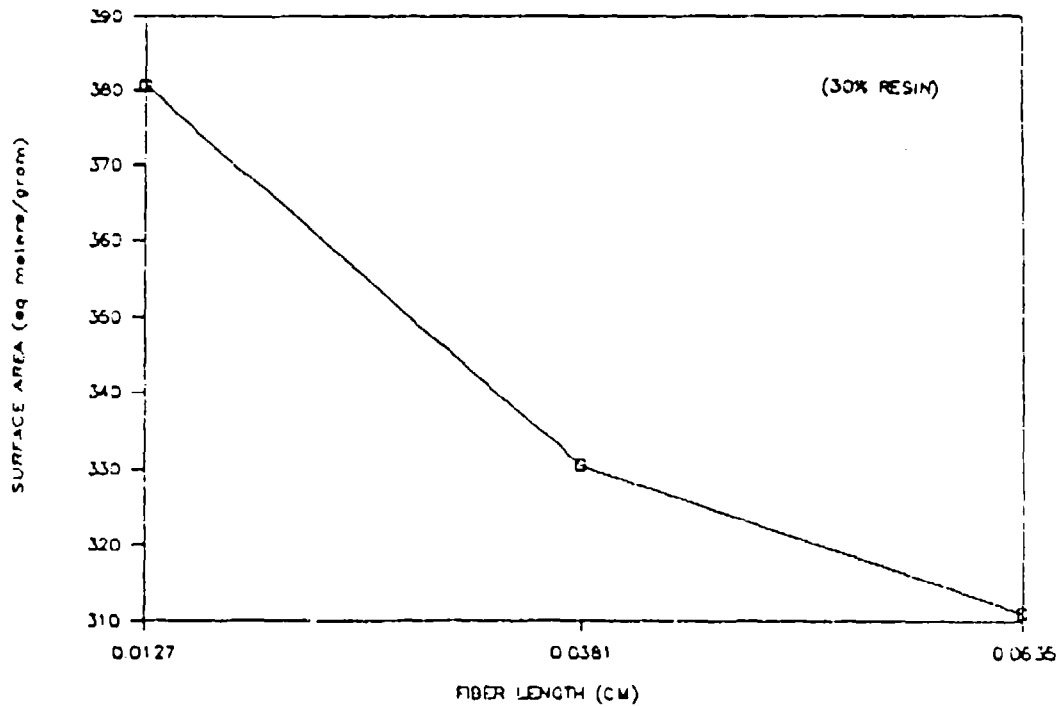


Figure IV. Effect of carbonized rayon fiber length on composite surface area.

Figures V, VI, and VII. As expected, the density and compressive strength of the composite increase with resin content while the total porosity decreases.

The effects of resin content on surface area is significant in that the surface area of the disk increased from 310 m²/g to 460 m²/g when the resin content was increased from 30% to 50%. This behavior indicates that the phenolic resin used in this process can be more easily activated than the fibrous carbon material.

EFFECTS OF MOLDING PROCESS

Preliminary studies on fabrication of a composite exhibiting anisotropic thermal conductivities were conducted using graphite flakes and metallic powders. However these studies were inconclusive and will require additional experimentation.

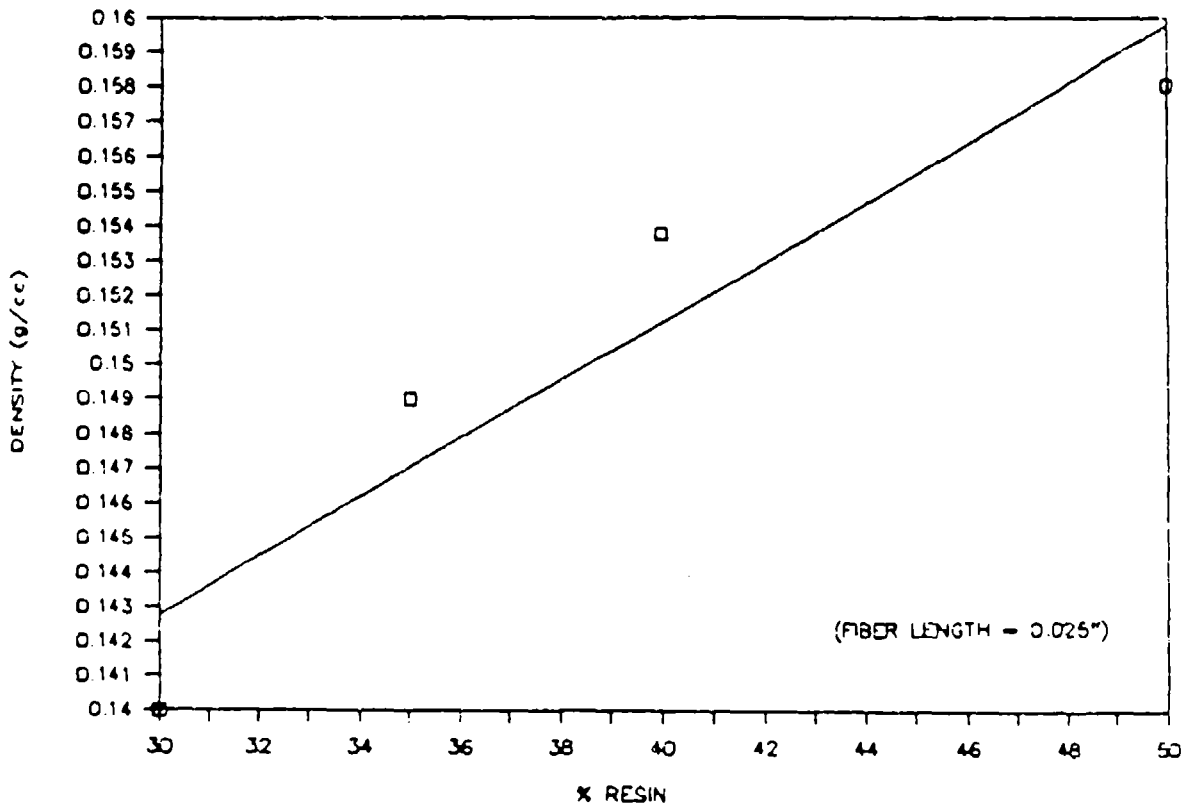


Figure V. Effect of resin content on composite density.

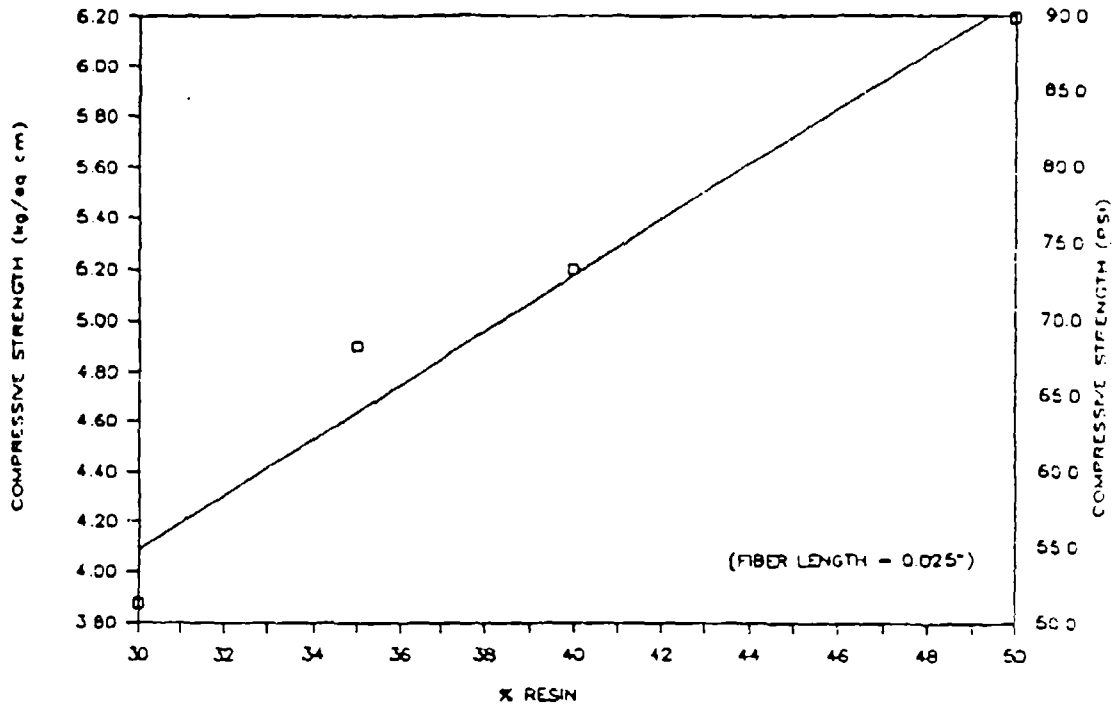


Figure VI. Effect of resin content on composite compressive strength.

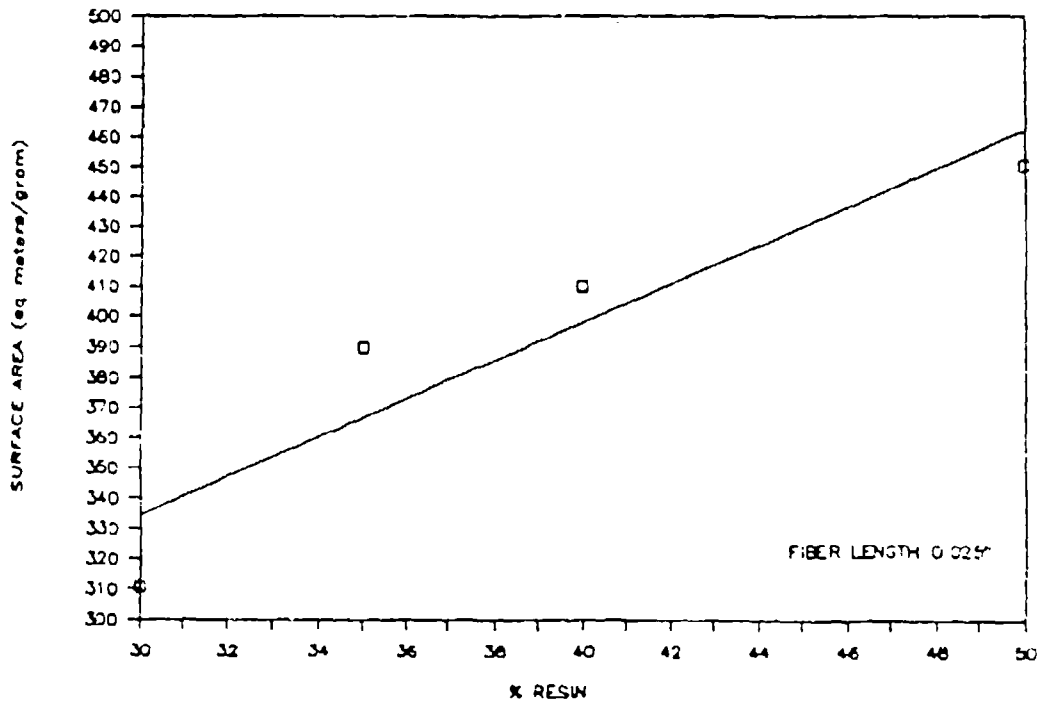


Figure VII. Effect of resin content on composite surface area.

EFFECTS OF COMPACTION DURING CURING

High density carbon-carbon composites can be achieved by mechanical compaction of the composite after pulp/vacuum molding and prior to curing/drying. Since the molding technique is not changed, benefits relating to fiber orientation such as anisotropic thermal conductivity are related. Recent experiments have achieved densities as high as 0.7 g/cm^3 .

COMPOSITE CARBONIZATION/ACTIVATION

As described in the experimental section, the activation techniques used in this study consisted of exposing the starting fiber and carbon composite to a controlled oxidizing atmosphere at a temperature of 700°C . Experiments were designed to determine the optimum conditions (temperature, time and $\% \text{CO}_2$) for activation of the composite structures. In the first experiment, composite specimens were fabricated using carbon fibers obtained from a rayon precursor. The surface area of the fiber used was $0.75 \text{ m}^2/\text{g}$. The composite specimens were fabricated with resin contents of 30% and 50% and a fiber length of 0.0635 cm. The activating operation was performed at 700°C for a period of 3, 6, and 9 hours in an atmosphere of 3% CO_2 in argon. The surface area values, which are reported in Table I, increased from $310 \text{ m}^2/\text{g}$ to $807 \text{ m}^2/\text{g}$ for composites having 30% resin and exposed for 3 hours and 9 hours respectively.

Scanning Electron Microscopy (SEM) photomicrographs of several specimens were obtained which revealed the macrostructure of the composite as well as the rough, crater-like surface formed during the activation cycle.

The composite specimens containing 50% resin and activated in the same run exhibited surface area values of $450 \text{ m}^2/\text{g}$ and $911 \text{ m}^2/\text{g}$ when exposed for 3 hours and 9 hours respectively. The results of this experiment reveal that the composites fabricated with 50% resin exhibit larger surface area values. This is an indication that the phenolic resin is more easily activated than the carbon fiber.

Also, higher surface area values were obtained by increasing the exposure time from 3 hours to 16 hours. However, the increase in surface area does not appear to be a linear function of exposure time.

A second experiment consisted of exposing samples of carbon fiber obtained from rayon and untreated rayon fiber

Table I. Surface Activation Parameters

Fiber Length (cm)	%Resin (%)	Temp. (°C)	%CO ₂ (%)	Time (hrs)	Surface Area (m ² /g)
0.0635	30	700	3	3	310
0.0635	30	700	3	6	510
0.0635	30	700	3	9	807
0.0635	50	700	3	3	450
0.0635	50	700	3	6	600
0.0635	50	700	3	9	911

to 700°C and 3% CO₂ for 9 hours. The surface area of the previously carbonized fiber increased from 1.19 m²/g to 621 m²/g while the surface area of the rayon fiber carbonized and activated simultaneously increased from <1 m²/g to 775 m²/g. Thus, it appears that higher surface area values are obtained when the rayon precursor is carbonized and activated simultaneously.

A third experiment conducted consisted of fabricating a composite specimen using high surface area fiber (775 m²/g) and 30% resin. The composite was exposed to 700°C and 3% CO₂ for 9 hours. The surface area exhibited by this composite was 822 m²/g, and increase of about 6% over the composite fabricated with low surface area fiber. It appears that the phenolic resin flows and forms a coating which covers some of the high surface area of the starting fiber material.

Several chemical treatments of precursor material (rayon and cotton fiber) prior to carbonization have been tried, but the results have, so far, been inconclusive. Further study is being conducted in that area.

Although activation of the carbon fiber prior to composite molding will increase the surface area of the final composite, it may also decrease fiber strength. Also, activation of the carbon fiber prior to composite molding, using current activation techniques, has less effect on final surface area than activation of the composite during final carbonization. Thus, greater increases in composite surface area are currently achieved by activation during the final carbonization rather than by activation of the carbon fiber.

The surface area currently achieved by the carbon bonded carbon fiber composites made with fiber originating from a cotton precursor and carbonized in an atmosphere of nitrogen and carbon dioxide while at temperatures in excess of 700°C is between 400 and 500 m²/g (as compared to <10 m²/g for composites carbonized in a nitrogen-only atmosphere). The highest surface areas achieved using a cotton fiber precursor were with a 50% N₂/50% CO₂ carbonization atmosphere. Higher surface areas might be achieved with higher oxygen concentrations, but it becomes harder to prevent serious degradation or combustion of the composite under such conditions.

CONCLUSIONS

The activated carbon-carbon composite media developed possess high surface area, high density, structural strength, low dusting characteristics and a low affinity for water.

The activated carbon composite potentially can be used in cryogenic applications such as adsorption compressors, getters, dewars, liquid transfer lines, anti-slosh containers, superconductor housings, liquid transfer in space, and liquid cryogen containment.

ACKNOWLEDGMENTS

The authors wish to thank Pascal Hinnen, Marville R&D Center; Alice Mason, Solar Energy Research Institute; and Roland Manning, Ball Aerospace Corporation for their assistance in testing and analyzing the materials. This work was partially supported through a NASA SBIR Phase I award.

REFERENCES

1. D.H. Sedgley, and A.G. Tobin, Grumman Corporation; T.H. Batzer, and W.R. Call, Lawrence Livermore National Laboratory, "Characterization of Charcoals for Helium Cryopumping in Fusion Devices," (August 1987).
2. S.A. Stern, and F.S. DiPaolo, "The Adsorption of Atmospheric Gases on Molecular Sieves at Low Pressures and Temperatures. The Effect of Preadsorbed Water,"

Journal of Vacuum Science and Technology, vol. 4 , no. 6 (1967).

3. S.S. Barton, J.A. Holland, and D.F. Quinn, "The Development of Adsorbent Carbon for the Storage of Compressed Natural Gas," Department of Chemistry and Chemical Engineering Royal Military College of Canada, Kingston, Ontario, (May 1985).

RELIABILITY AND LIFE OF SORBENT MATERIALS FOR SORPTION COOLERS

G. Mon, L.C. Wen, J. J. Wu, S. Bard, and A. Garnica
Jet Propulsion Laboratory (JPL)
California Institute of Technology
Pasadena, California 91109

ABSTRACT

The ongoing research effort at JPL to understand and confirm the reliability of praseodymium-cerium-oxide and Saran carbon sorbents for use in long-life 65 K spacecraft cryocoolers is described. At the system level, a laboratory PCO/O₂ compressor system that began operation in March 1989 has now logged a total of 12,000 hours of operation with no signs of degradation. Similarly, a Saran carbon/krypton compressor system has logged a total of 2000 hours. At the component level, a detailed investigation is underway to measure any possible chemical interactions between the sorbents, sorbates, and container materials, and any possible physical changes that might alter the heat and mass transfer properties of the compressor. A specially fabricated sorbent/sorbate test cell is used to precisely measure the pressure response to programmed temperature cycling, and both gravimetric and volumetric techniques are used to periodically monitor sorption isotherms as the materials undergo life testing.

INTRODUCTION

Reliability physics investigations are an important element of an ongoing research effort at JPL to develop and demonstrate 65 K sorption cooler technology as a viable low-vibration alternative to long-life mechanical Stirling coolers. The goal of the reliability physics program is to establish the technology base required to design sorption coolers that can operate reliably in space for 10 years or more. Developing a detailed understanding of the important failure mechanisms governing cooler life will enable identification of operating constraints, design enhancements and other means of eliminating the failure mechanisms.

Sorption coolers have the potential for long life due to the use of solid-state sorption compressors in place of moving mechanical parts. Achieving and demonstrating this long-life potential requires a thorough test and evaluation program at both the materials and component level to understand the fundamental reliability physics of the sorbent materials themselves, and at the cryocooler compressor level to understand any system-level synergisms that might adversely affect long-term sorbent performance. The status, progress and plans of this sorbent test and evaluation program are the subject of this paper. Reference 1 describes related work being performed at JPL in the area of reliability of high-temperature sorption compressor components such as electrical heaters and sorbent container materials.

The overall design of the 65 K sorption cooler system is briefly reviewed in the following section. Next, the sorption compressor system-level performance testing and life testing is described, followed by a discussion of the sorbent characterization and reliability testing. Finally, conclusions regarding the prospects for achieving ten-year life for sorption coolers are discussed.

65 K SORPTION COOLER SYSTEM DESIGN

The basic principle behind sorption refrigeration is the temperature-dependent physical or chemical sorption of a gas by a solid micro-porous sorbent material such as charcoal. As the sorbent is sequentially heated and cooled, the gas is alternately exhausted from the sorbent at high pressure, or resorbed at low pressure, respectively. In a sorption refrigerator, the sorbent material is contained in a number of compressor canisters that are alternately heated and cooled over a temperature cycling range on the order of 300°C. The range of operating temperatures varies for different sorbent/gas systems, but is typically between approximately room temperature and 600°C.² By ganging multiple compressor elements together with check valves, a steady stream of refrigerant gas can be provided to a conventional Joule-Thomson (J-T) refrigeration expansion stage.

To achieve reasonable efficiencies with sorption coolers below 100 K requires the cascading of multiple J-T sorption stages. The three-stage sorption cooler system shown in Fig. 1 is used to achieve temperatures between 65 and 90 K.² The system consists of a 65 to 90 K praseodymium-cerium-oxide/oxygen ($\text{Pr}_{0.92}\text{Ce}_{0.08}\text{O}_x$, or "PCO/ O_2 ") chemisorption lower stage, a 120 to 140 K Saran carbon/krypton (C/Kr) physisorption intermediate stage, and a 165 to 200 K Saran carbon/xenon (C/Xe) physisorption upper stage.

To further improve efficiency, the waste heat rejected by the hot compressors can be used to raise the temperature of the cold compressors by

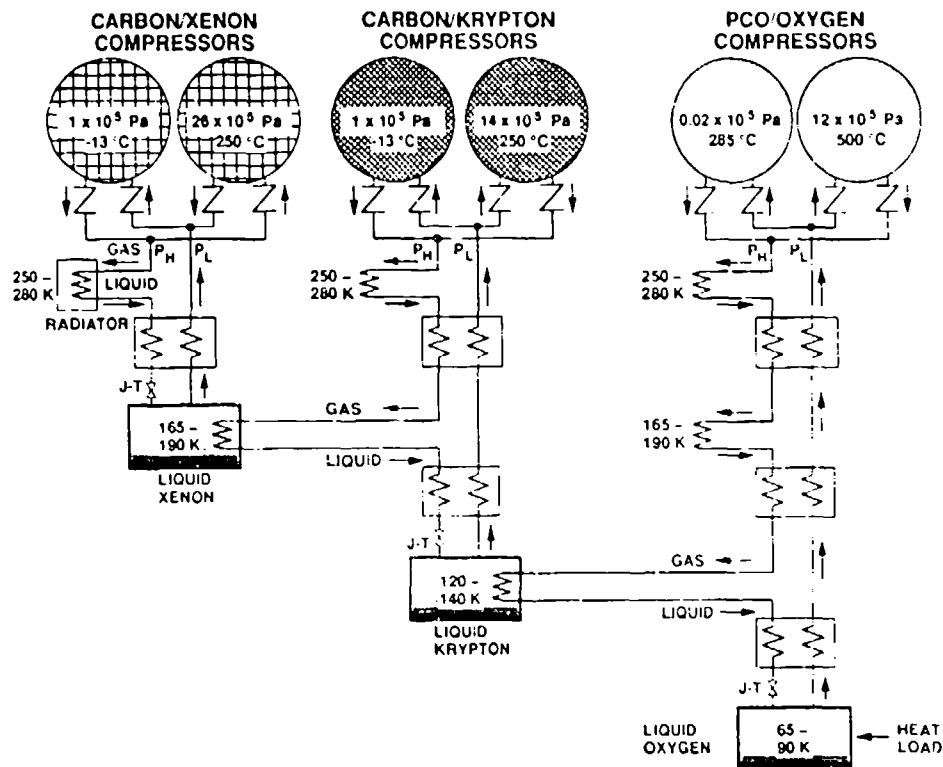


Figure 1. Three-stage 65 to 90 K sorption cryocooler.

incorporating various heat regeneration techniques.^{2,3} By using these heat regeneration techniques, the projected efficiencies and weights of 65 K sorption coolers are comparable to that for long-life Stirling coolers.²

SYSTEM-LEVEL SORPTION COMPRESSOR TESTING

The two main goals of the system-level sorption compressor tests are to: (1) understand performance characteristics of sorption compressor systems by quantifying performance sensitivity to critical operating parameters, and (2) identify long-term degradation trends or failure mechanisms for sorbents, as well as for sorbent container materials, heaters, check valves, and solenoid valves operating together and interacting in an integrated system.

To perform the system-level sorption compressor tests, two laboratory breadboard systems have been constructed. Originally, the laboratory systems operated in tandem as an integrated two-stage sorption cooler, consisting of an 80 K PCO/O₂ refrigeration stage precooled by a 140 K C/Kr stage,^{3,4} as shown in Fig. 2. Instead of an upper C/Xe stage, a 200 K thermoelectric cooler was used



Figure 2. JPL laboratory breadboard two-stage sorption cryocooler.

to precool the C/Kr stage. Compressor heat regeneration techniques were not used, and the compressor designs utilized gas-gap thermal switches to control the heat flows. The integrated system successfully demonstrated 1/3 W of cooling at 80 K, and operated at temperatures as low as 72 K.³

Subsequent to the above feasibility tests, the system was reconfigured and upgraded for independent continuous life testing of the two PCO/O₂ compressors in March 1989, and the four C/Kr compressors in December 1989. The upgrades included the incorporation of various fail-safe hardware mechanisms and control software to enable continuous unattended operation. The vacuum dewar was also eliminated and the cryogenic J-T valves were replaced by room-temperature throttling valves.

For the performance characterization phase, the PCO/O₂ compressor system was operated with various heater input powers, cycle times, compressor maximum and minimum temperatures, and flow rates. Varying these parameters caused the equilibrium levels of the high and low system pressures to change. The characterization test results are summarized in Fig. 3, which relates the gas flow rate to the system pressure difference that was produced. The flow rate was set by adjusting the throttling valve. Note that for any given heater power level, increasing the flow rate causes a reduction in the pressure difference. For any given flow rate and high and low operating pressures, the projected J-T cooling power and refrigeration temperature can be easily computed.³ Thus, the compressor system performance data can be related directly to projected refrigerator performance.

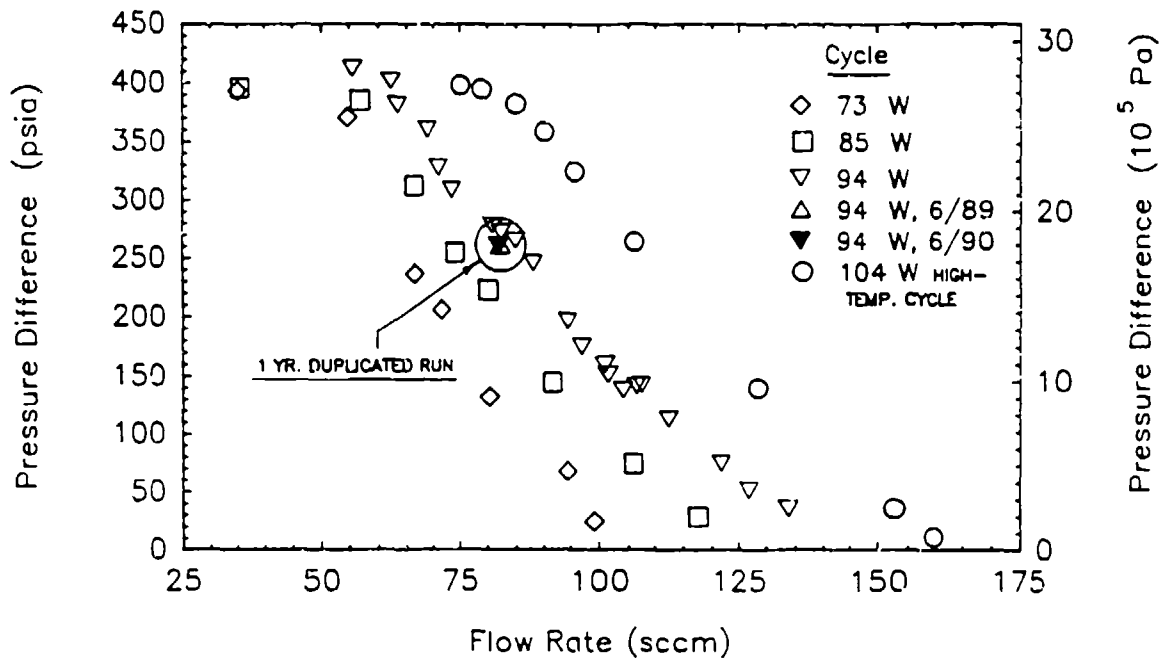


Figure 3. Comparison of laboratory PCO/O₂ system pressure difference vs. flow rate relationship after 1 year of operation.

Also shown in Fig. 3 are data for the nominal life test conditions repeated after one year of operation for the PCO/O₂ compressors. The data indicates that the identical pressures and flow rates were produced. The nominal test conditions are a high and low pressure of 275 psia and 6 psia, a high and low temperature of 923 K and 545 K, a heater input power of 100 W, and a cycle time of 26 minutes.

Figure 4 shows temperature and pressure cycle data for one of the PCO/O₂ compressors operating under the nominal test conditions described above. As in Fig. 3, the superimposed cycles clearly indicate no significant change in performance (i.e. identical temperatures and pressures) after one year of operation.

As of September 10, 1990, each PCO/O₂ compressor has accrued over 12,000 hours and 26,500 cycles without any signs of degradation. Note that the test compressors nominally operate at maximum pressures and temperatures that are about 100 psia and 150 K greater than the 65 K flight cooler design conditions. Thus, the life testing subjects the laboratory compressors to significantly greater stress conditions than expected for flight compressors.

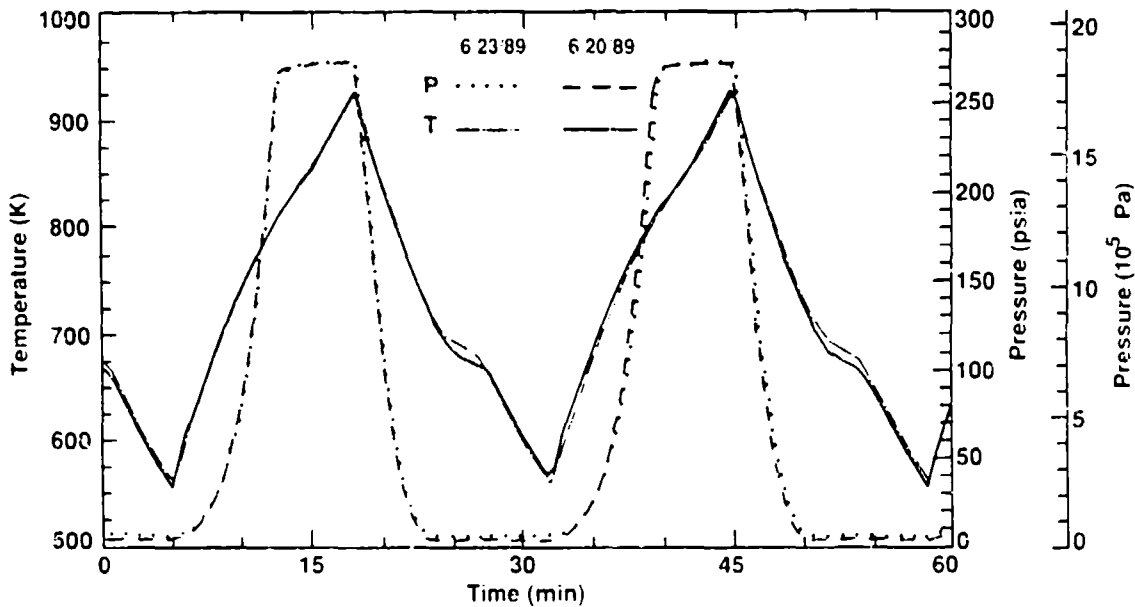


Figure 4. Comparison of laboratory PCO/O₂ compressor temperature and pressure cycles after 1 year of continuous operation.

The C/Kr compressors are presently in the performance characterization test phase. Curves similar to those in Fig. 3 are being generated for various heater input powers, cycle times, and compressor temperature and pressure levels.

One of the compressors in the C/Kr system developed a leak through the Inconel container wall after about 800 hours of testing. Chemical analysis revealed the leak to have been caused by corrosion due to the presence of hydrogen chloride (HCl). The presence of HCl is due to the incomplete pyrolysis of the polyvinylidene chloride (PVDC), which is the starting material in the production of Saran carbon. Elemental analysis of the Saran carbon samples used in the compressors indicated 2.1 to 2.6% residual chlorine present in the original samples. Prior to initial operation of the system in 1988, the Saran carbon in three of the four compressors was reprocessed by dehydrochlorination with a 700°C bakeout for four days and a subsequent 900°C bakeout for two additional days, with a dry nitrogen purge. Elemental analysis of the reprocessed samples indicated the level of chlorine to be reduced to 0.13%, which is an order of magnitude less than the original chlorine content.

However, the Saran carbon in the fourth compressor was never reprocessed, and thus still contained over 2% chlorine. Therefore, development of a leak caused by HCl corrosion in that compressor was not surprising. The faulty

compressor has since been removed from the system. However, the plumbing lines in the rest of the system have not been cleaned to remove any residual chlorine that may still be present. Nevertheless, the remaining three compressors continue to operate successfully and have accrued over 2000 hours of operation as of September 30, 1990.

It is important to note that the Saran carbon presently being produced at JPL is processed at 1000°C, with a resulting final chlorine content of less than 0.02%.⁵ This is two orders of magnitude lower than the chlorine content of the Saran carbon originally used in the C/Kr laboratory compressor system. Further separate testing of the new JPL-produced Saran carbon samples is planned to verify that no significant quantity of chlorine is evolved when the samples are cycled between the expected flight compressor temperatures, and to verify that no significant corrosion is caused by any evolved trace quantities of chlorine. In conjunction with continued life testing of the remaining laboratory C/Kr compressors, which contain Saran carbon with about 0.13% chlorine, these separate tests with the JPL Saran carbon should help to completely resolve the HCl corrosion issue.

Although no performance degradation of the PCO/O₂ and C/Kr compressor systems has been detected, one of each compressor type will be removed, disassembled, and analyzed in depth to study any changes that may indicate internal degradation or design weaknesses that need to be corrected for a flight design. In addition, a high-precision mass spectrometer (UTI ISS-25A Intelligent Sampling System) facility has been established to periodically analyze gas samples from the remaining PCO/O₂ and C/Kr compressors. This mass spectrometer is particularly suited to analyze trace quantities of contaminant gases in oxygen.

SORBENT CHARACTERIZATION AND RELIABILITY TESTING

The primary goals of the sorbent characterization and reliability testing are to: (1) understand critical sorption, kinetic, pressure drop and mass flow performance characteristics of sorbent beds and materials, (2) to understand parameters controlling sorbent reliability, and (3) to develop test methods to demonstrate 5 to 10 year life. The approach includes developing small sorbent test cells to be used for cycling PCO/O₂, C/Kr and C/Xe sorbent beds, and developing techniques to measure selected sorption isotherms in order to evaluate possible changes in sorption capability after prolonged cycling.

SORBENT RELIABILITY TESTING

While the ongoing compressor system testing provides useful sorbent degradation information, and the 12,000 hours of accrued PCO/O₂ compressor life without degradation is encouraging, the slow cycle time of about 30 minutes makes prediction of long-term behavior very difficult. Therefore, a separate accelerated sorbent life-test program was planned in which several small sorbent reliability test cell (SRTC) canisters filled with PCO and carbon sorbents are subjected to repeated temperature and pressure cycling. By continuously monitoring temperature, pressure, and concentration data, any signs of degradation should become evident. If performance degradation occurs, understanding its cause may identify operating constraints or enable a remedy to be incorporated into the design.

Degraded performance may be due to reduced sorption capability, corrosion reactions that may occur between the sorbent and the compressor wall and/or heater sheath, other chemical reactions, or a change in the heat and/or mass transfer characteristics of the compressor. For example, if after repeated cycling a gap forms between the sorbent and container wall, the heat and mass transfer characteristics may be altered. Cycling may also cause the sorbent to break up into smaller particles, thus reducing the effective thermal conductivity and possibly changing the mass transfer characteristics of the sorbent bed. To study these effects, the canisters are constructed from the actual Inconel alloy flight compressor wall materials, and have been instrumented to monitor radial temperature gradients. The SRTC design can accommodate various heating configurations. The current samples are being heated from the outside wall with a tube furnace, while future samples may include a central embedded heater, thus simulating the heat transfer processes of various candidate compressor configurations. The SRTC will also allow study of sorbent kinetics, mass transfer and pressure drop characteristics, by analyzing the effect of varying cycle time on sorption and pressurization-depressurization.

The SRTC apparatus with its associated plumbing, plenum chambers, and transducers, shown in Fig. 5, was designed to allow precise measurements of the gas mass introduced into the cell by monitoring pressures and temperatures at various locations. Testing consists of several phases, and is focused initially on the PCO/O₂ system.

The first phase consisted of purposely oxidizing the container in order to form an oxide scale on the inner walls of the SRTC. After assuring that the system was leak-tight by performing a thorough helium leak check, the SRTC was filled with 13.1×10^2 kPa (190 psia) of oxygen and maintained at a temperature of 550°C for 760 hours. Oxidation did cause a measurable decrease in pressure over

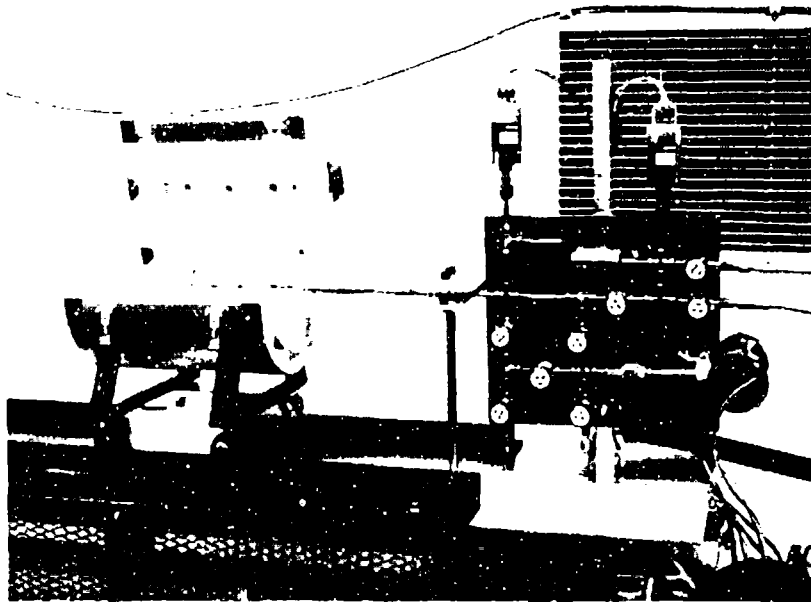


Figure 5. Sorbent Reliability Test Cell (SRTC) apparatus.

time, but the oxygen mass loss of 12 mg was found to follow a highly predictable function of pressure, temperature and exposure time. This predictability is critical because it is important to be able to ascribe any mass loss during the SRTC life test phase to either degradation or simply oxide formation. It is also important so that any predicted mass loss due to oxidation in a flight compressor system can be accommodated by pre-oxidizing the compressor metallic elements and by carrying a small quantity of excess oxygen to replace any lost during the mission.

The next phase consisted of filling and packing the SRTC with PCO to a density of 4.2 g/cm^3 using a specially fabricated press fixture. The sorbent cell was then reinstalled into the SRTC test apparatus and a known mass of oxygen was introduced. Next, the cell temperature was cycled between 280°C and 550°C by passing a constant temperature tube furnace back-and-forth over the SRTC. The sorption-desorption driven by the thermal cycling caused a pressure rise from $0.021 \times 10^2 \text{ kPa}$ (0.3 psia) to $11.5 \times 10^2 \text{ kPa}$ (167 psia).

Figure 6 shows pressure, concentration, and internal and case temperature data for two cycles. The time lag between the internal and case temperatures is due to the relatively poor thermal conductivity of PCO. Note the change in slope of the temperature profiles during the heating phase. This occurs when the PCO becomes mostly depleted of oxygen, after which the energy required to desorb additional oxygen is reduced, allowing the temperature to rise more rapidly. The preliminary temperature/pressure cycling phase has now been completed.

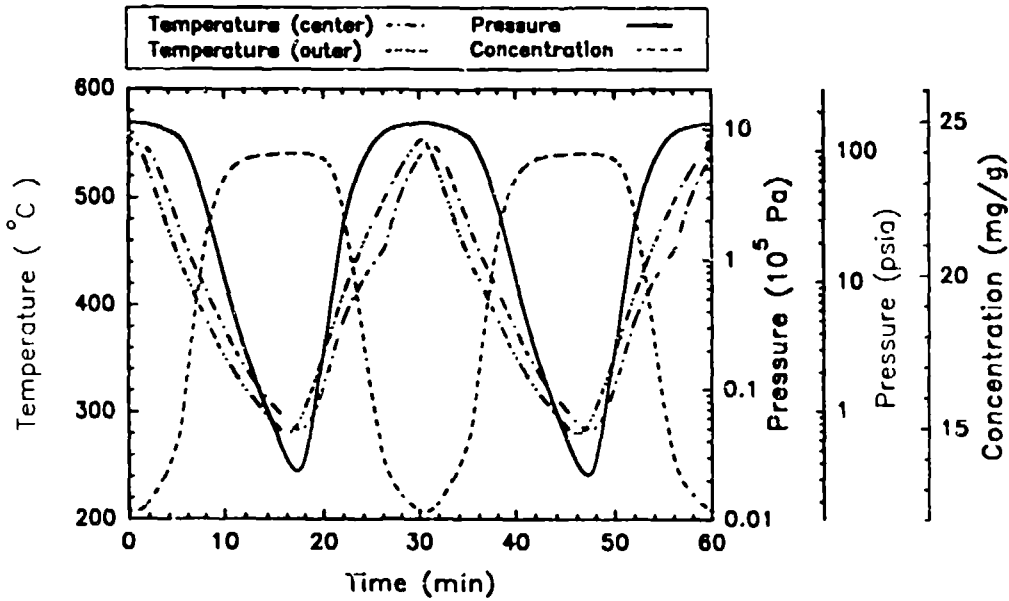


Figure 6. SRTC PCO/O₂ temperature, pressure and concentration data for two cycles.

The current test phase is focused on measuring selected equilibrium isotherms at various temperatures, pressures, and oxygen loadings, and comparing the results with transient isotherm measurements in order to fully characterize transient effects.

Prior to the final life-test phase, a separate SRTC experiment will be performed to characterize oxygen permeation capability through the PCO bed. If the pressure drop through the sorbent bed is too great, it may not be possible to maintain a low pressure of 0.021×10^2 kPa (0.3 psia) while introducing the desired flow rate of oxygen to the cell. If this is indeed the case, it may be difficult to obtain a refrigeration temperature of 65 K for a sorption cooler with a similar PCO bed geometry and packing density. If pressure drop proves to be a problem with the initial SRTC, subsequent testing with various sorbent packing densities and oxygen flow distribution hole geometries is planned.

Note that packing density affects not only oxygen permeation and pressure drop, but also void volume. Minimizing void volume by increasing the packing density is important in order to improve the volumetric efficiency of sorption compressors.⁶ However, increasing the packing density also increases the pressure drop through the sorbent bed. The SRTC experiments are designed to improve understanding of these trade-offs.

After the isotherm and permeation experiments are completed, the life test phase will be initiated. The SRTC will be thermal/pressure cycled and continuously monitored over an extended period and analyzed for any significant deviations from initial benchmark cycles similar to those in Fig. 6. If degraded performance is noted, its cause will be identified by conducting various diagnostic tests, including comparisons to the initial characterization test data, analyzing the gases in the SRTC with the mass spectrometer described above, and comparing sorption isotherms of pristine and aged PCO using the high-temperature and high-pressure Cahn microbalance described below in a later section.

After the life-test phase for the first SRTC unit is initiated, a second unit (which is already built) will be assembled and tested using Saran carbon.

SORBENT CHARACTERIZATION TESTING

A high-temperature, high-pressure Cahn C-1100 Recording MicroBalance facility has been established to measure sorption capability of potential sorbate/sorbent systems. The Cahn microbalance, shown in Fig. 7, is a beam balance that gravimetrically measures the amount of gas physisorbed or chemisorbed by a known quantity of sorbent.

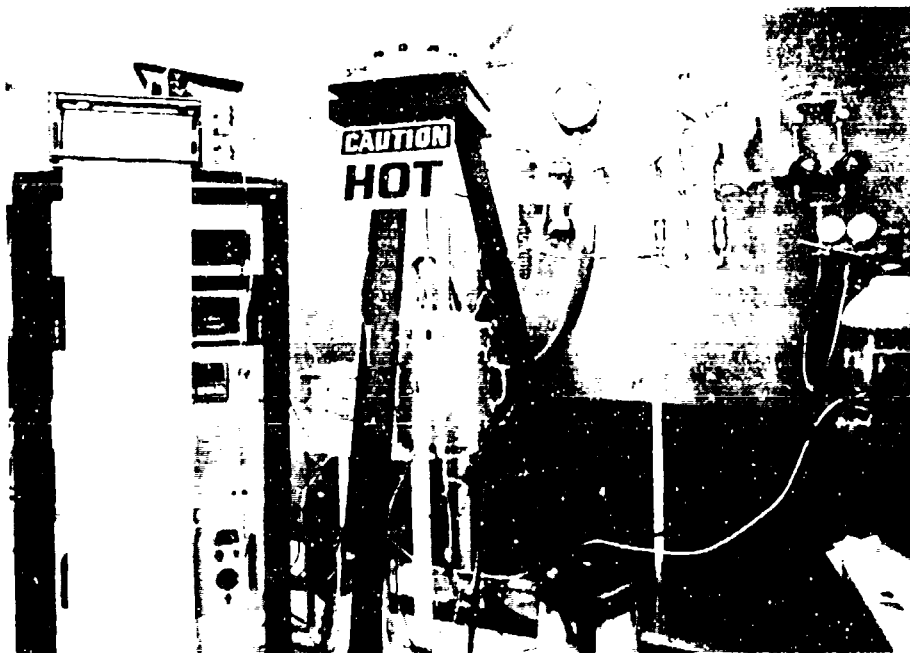


Figure 7. High-temperature and high-pressure Cahn microbalance facility for gravimetric sorption isotherm characterization.

The initial phase of testing is focused on the PCO/O₂ system to enable the results to be used in conjunction with the SRTC experiments described above. To further understand the effect of sorbent packing density on sorption-desorption capability, isotherm kinetics, and low-pressure oxygen permeation through the sorbent bed, several Cahn microbalance experiments with various sample packing densities and flow distribution hole geometries are planned.

Future experiments are planned to measure selected isotherm points for JPL Saran carbon/nitrogen. The results will be compared to independent volumetric adsorption isotherm measurements at the National Institute of Standards and Technology (NIST) using sorbent samples from the identical lot.⁷ These comparisons are expected to give further confidence in the gravimetric technique.

CONCLUSIONS

The ongoing research effort at JPL to understand and confirm the reliability of praseodymium-cerium-oxide and Saran carbon sorbents for use in long-life 65 K cryocoolers has been described. Various test facilities have been established and collection of detailed data needed to design reliable long-life sorption coolers is underway.

At the system level, a laboratory PCO/O₂ compressor system has now accrued over 12,000 hours of continuous operation with no signs of degradation. Similarly a Saran C/Kr compressor system has logged a total of 2000 hours.

At the component level, a specially fabricated sorbent/sorbate test cell is being used to perform accelerated life testing of the sorbent materials. The initial characterization phase is currently underway to precisely measure the pressure response to programmed temperature cycling, and to understand the critical sorption, kinetic, pressure drop and mass flow performance characteristics of the PCO/O₂ bed. Separate Cahn microbalance experiments are also underway to characterize sorption-desorption capability and sensitivity to sorbent packing density and flow distribution geometry.

Combined with the initial results of separate tests of high-temperature compressor components such as heaters and container materials,¹ the sorbent system-level and component-level test results described here are highly encouraging in terms of demonstrating ten-year life capability for sorption cryocoolers.

ACKNOWLEDGEMENTS

This research described in this paper was carried out by the Jet Propulsion Laboratory (JPL), California Institute of Technology under contract with the National Aeronautics and Space Administration. The work was sponsored in part by the Strategic Defense Initiative Organization and managed by the Air Force Space Technology Center. A portion of the work was sponsored by the NASA Civilian Space Technology Initiative program, managed under NASA Code R. The authors would like to thank Lt. Col. Hilmer Swenson, Capt. Bill Wyche, Jill Ludwigson, Lt. Col. Tom Davis, and Lt. Stephen Dunn and for their continued support of this effort. The technical contributions of Dr. Ron Ross, Jr., Andre Yavrouian, and Russ Sugimura are also greatly appreciated. The authors would also like to express their appreciation to Bill Boulter, Scott Leland, Larry Chen, and Frank Loya for their valuable testing, hardware fabrication and instrumentation support.

REFERENCES

1. L.C. Wen, G. Mon, R. Sugimura, and R. Ross, Jr., "Reliability of High-Temperature Metallic Components in Sorption Cryocoolers," Interagency Meeting on Cryogenics, Plymouth MA, (October 24, 1990).
2. S. Bard, J.A. Jones, R.W. Hughes, D. Moore, N. Sherman, P. Sywulka, L. Wade, and R. Bowman, "Comparison of Regenerative 65 K Sorption Cooler Systems," Interagency Meeting on Cryogenics, Plymouth MA, (October 24, 1990).
3. S. Bard, J.A. Jones, and H.R. Schember, "A Two-Stage 80 K/140 K Sorption Cryocooler," Proc. ICEC-12, Butterworth, Guilford, U.K., (1988), p. 626-631.
4. H.R. Schember, "Development of an Adsorption Compressor for Use in Cryogenic Refrigeration," Paper No. AIAA-89-0076, 27th Aerospace Sciences Meeting, Reno, Nevada, (January 9-12, 1989).
5. A. Yavrouian, and H.R. Schember, "Saran Carbon Sorbent Development for Sorption Cryocooler Use," JPL Report D-7368, (May 1990).
6. S. Bard, "Improving Adsorption Cryocoolers by Multi-stage Compression and Reducing Void Volume," Cryogenics, vol. 26, (Aug/Sept 1986), p. 450-458.
7. R. Radebaugh, I. Vazquez, and J. Light, National Institute of Standards and Technology (NIST), personal communication, (June 1990).

Session IIIA — Space Coolers I

Chairperson: Lee S. ... ASA/GSFC

Co-Chairperson: Joe Smith, MIT

Session IIIB — Regenerator Technology

Chairperson: Joseph Walters, DTRC

Co-Chairperson: Ralph Longworth, APD Cryogenics Inc.

IS THE V-GROOVE RADIATIVE COOLER OPTIMIZED?

Peter Kittel
Technology Development Branch
NASA, Ames Research Center, Moffett Field, California

ABSTRACT

A probabilistic approach to radiative heat transfer is applied to the V-groove radiative cooler. This approach allows an exact formulation of the relationship between the parasitic heat transfer and the rejected heat. An approximate method for finding effective emissivity, ϵ_0 , of the V as a function of the angle of, ϕ , of the V is developed. From these results, it is shown that from thermodynamic considerations the V-groove radiator is not optimized.

INTRODUCTION

The V-groove radiator has been developed as a high performance cryogenic radiator for spacecraft^{1,2}. The radiator is claimed to offer significant advantages over conventional radiators. These advantages include an increased cooling capacity and the ability to reach lower temperatures. Using a simple model, this paper analyzes the radiative heat transfer of the V-groove radiator and concludes that the radiator is not optimized.

A sketch of a V-groove radiator is shown in figure 1. The parasitic heat loads on the radiator cold plate are intercepted by an arrangement of lightweight, low emissivity, highly specular, reflective radiation shields. These shields are arranged to create V-groove cavities with an included angle of 1.5° . The shields intercept parasitic loads and radiate out through the mouths of the V-grooves. In effect each opening acts like a radiator in a multi-stage radiator. There is also radiative heat transfer between neighboring shields.

To analyze the performance of the V-grooves we will use a simplified model of a single V-groove. As shown in fig. 2, we will model the V-groove as a right pyramid with three hot sides, T_h , and one cold side, T_c . The angle between the cold side and the opposite hot side is ϕ . The base is open and has dimensions l and w . The height of the sides is h .

ANALYTIC MODEL

Radiative heat transfer involves the emission and absorption of photons. If the photons are confined to a chamber with low emissivity walls, then the photons have only a small probability of being absorbed when they strike a wall. The probability is ϵ , where ϵ is

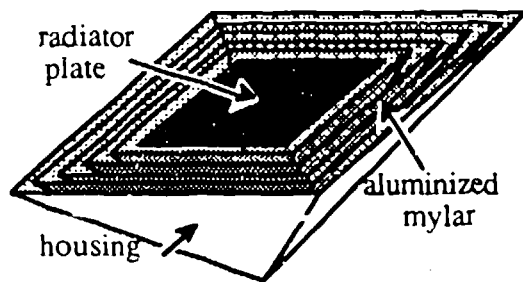


Fig. 1: Sketch of a V-groove radiator showing the principal components

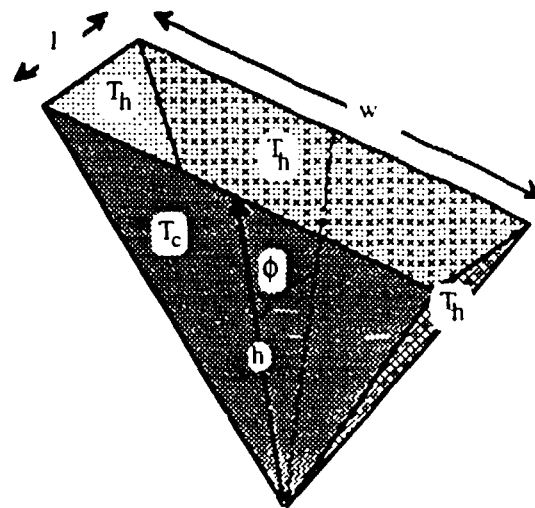


Fig. 2: Model of single V-groove showing dimensions

the emissivity. In the limit of $\epsilon \rightarrow 0$, A photon will make a large number ($\sim 1/\epsilon$) collisions before it is absorbed. This results in near uniform density of photons within the chamber and the probability of a photon being absorbed by a surface of area A is proportional to ϵA . I.e., the probability of a photon being absorbed by A is independent of where the photon was emitted.

HEAT BALANCE WITHOUT END EFFECTS

We can apply this approach to our model of the V-groove. As first approximation, end effects will be ignored. I.e., all photons are confined to the V-groove and none are allowed to leave the opening. This is the same as covering the opening with a perfect reflector with $\epsilon_0=0$. Each surface emits heat:

$$Q_x = \sigma \epsilon_x A_x T_x^4 \quad (1)$$

A fraction, f_x , is absorbed by each surface; where

$$f_x = \epsilon_x A_x / (\epsilon_c A_c + \epsilon_h A_h + \epsilon_0 A_0). \quad (2)$$

In the case at hand, both the hot and cold surfaces have the same emissivities ($\epsilon \equiv \epsilon_c = \epsilon_h$).

Thus

$$f_x = \epsilon_x A_x / \epsilon A \quad (3)$$

and

$$Q_x = f_x \sigma \epsilon A T_x^4. \quad (4)$$

where $f_x = \epsilon_x A_x / \epsilon A = f_x \epsilon_c A_c / \epsilon A$, $A = A_c + A_h$, $A_t = A + A_0$, $\epsilon_c = (\epsilon A + \epsilon_0 A_0) / A_t$. When $\epsilon_0 = 0$, $f_x = f_x$. From fig. 3 we see that heat emitted by the cold surface and the incident heat on the cold surface are, respectively

$$Q_{cc} = f_c \sigma \epsilon A T_c^4 \quad (5)$$

$$Q_{ci} = f_c \sigma \epsilon A (f_h T_h^4 + f_c T_c^4). \quad (6)$$

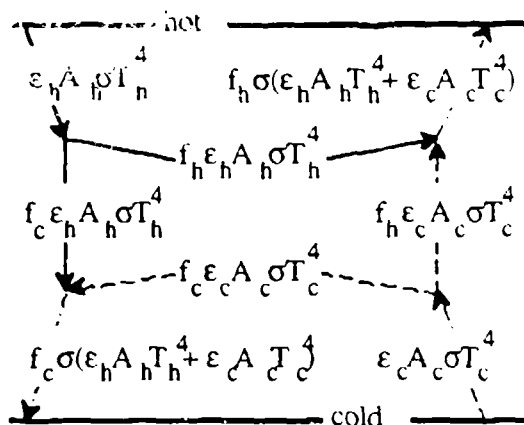


Fig. 3: Diagram of radiative heat flow in the V-groove when end effects are ignored.

Combining these results in net heat load on the cold surface of

$$Q_c = f_c f_h \epsilon \sigma A (T_h^4 - T_c^4) \quad (7)$$

By conservation of energy

$$Q_h = -Q_c \quad (8)$$

On a per unit area basis, only f_c of the heat flux, q , within the gap is absorbed by the the cold surface. Thus $Q_{ci} = f_c \epsilon A q$ and

$$\dot{q} = \sigma (f_h T_h^4 + f_c T_c^4) \quad (9)$$

HEAT BALANCE WITH END EFFECTS

In this section the effect of having an open end will be looked at. In the previous discussion the gap was closed off with a perfect reflector. From (9), the heat incident on this reflector is $Q_o = A_o q$. If the reflector were removed, one might be tempted to think that Q_o is the heat radiated from the system. This is not so. The flow of heat out of the gap is not balanced by an equal flow into the gap. (We are assuming that the radiator is radiating to deep space and that the heat radiated from space is negligible.) This results in q being reduced. Instead the gap acts as if it had an emissivity of ϵ_o and only a fraction these photons are radiated. Thus $Q_o = \epsilon_o A_o q = f_o \epsilon A q$,

The effect of the open gap on the heat flows is shown in fig. 4. The net heat load on the cold surface is now

$$Q_c = f_c f_h \epsilon \sigma A [(1-f_o)T_h^4 - (1+f_o f_r)T_c^4] \quad (10)$$

where $f_r = f_c/f_h$. The heat radiated out is

$$Q_o = f_o \epsilon \sigma A (f_h T_h^4 + f_c T_c^4) \quad (11)$$

and by conservation of energy

$$Q_h = - (Q_c + Q_o) \quad (12)$$

Equations (10) and (11) can be rewritten as

$$Q_c = \epsilon \sigma A_n [\delta_h T_h^4 - \delta_c T_c^4] \quad (10a)$$

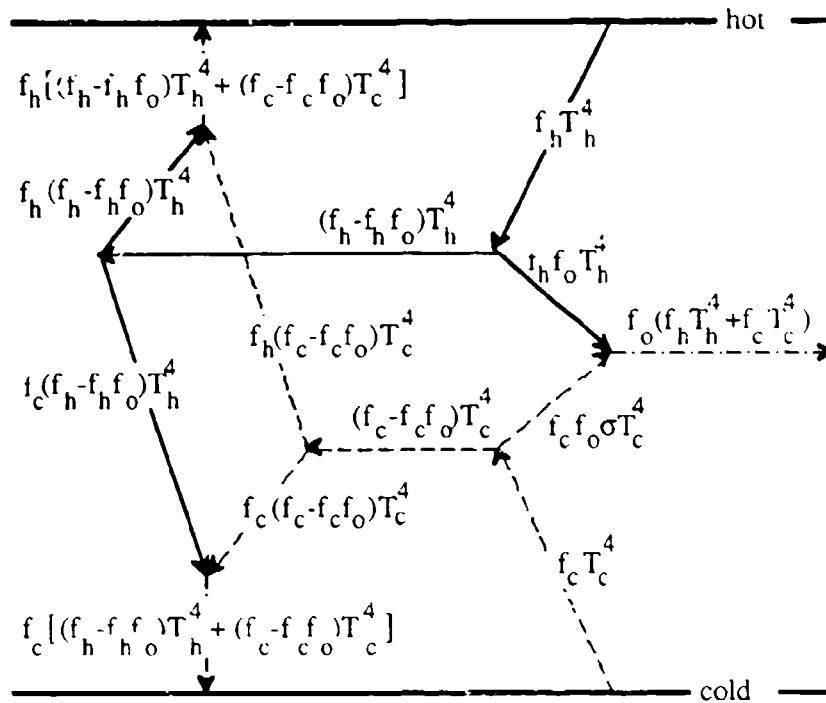


Fig. 4: Heat flow in the V-groove diagram with end effects. Each of the flows has been divided by $\epsilon\sigma A$ for simplicity.

and
$$Q_o = \epsilon_o \sigma A_n (\gamma_h T_h^4 + \gamma_c T_c^4) \quad (11a)$$

where $A_n = hw$, $\delta_c = f_c f_h (1 + f_o f_r) A / A_n$, $\delta_h = f_c f_h (1 - f_o) A / A_n$, $\gamma_c = f_c A_c / A_n$, $\gamma_h = f_h A_o / A_n$. Writing (10a) and (11a) in this form emphasizes the dependance of Q_c on ϵ and Q_o on ϵ_o . The coefficients γ_c and γ_h depend only on the geometry of the radiator. While δ_c and δ_h are functions of ϵ_o and of the geometry.

The quantity ϵ_o is also function of the geometry. To study its dependance on ϕ , we will look at the case when $h=w$. This is a reasonable assumption in that the radiators that have been built have had $h=w$ and ϵ_o is not a strong function of h/w . It is not easy to calculate ϵ_o . Two methods of estimating it are compared in fig. 5. The first is Gouffe's method developed for axisymmetric cavities³. The second method is to estimate the number of times that an incoming photon beam must be reflected before it escapes the radiator. The beam is attenuated by $(1-\epsilon)$ on each reflection. Integrating over all angles of

incidence yields
$$\epsilon_o \approx 1 - \int_0^{\pi/2} (1-\epsilon)^n \sin\theta \, d\theta \quad (13)$$

where
$$n = \begin{cases} (\pi - 2\theta)/\phi - 1 & ; \quad \theta < \pi/2 - \phi \\ 1 & ; \quad \theta > \pi/2 - \phi \end{cases} \quad (14)$$

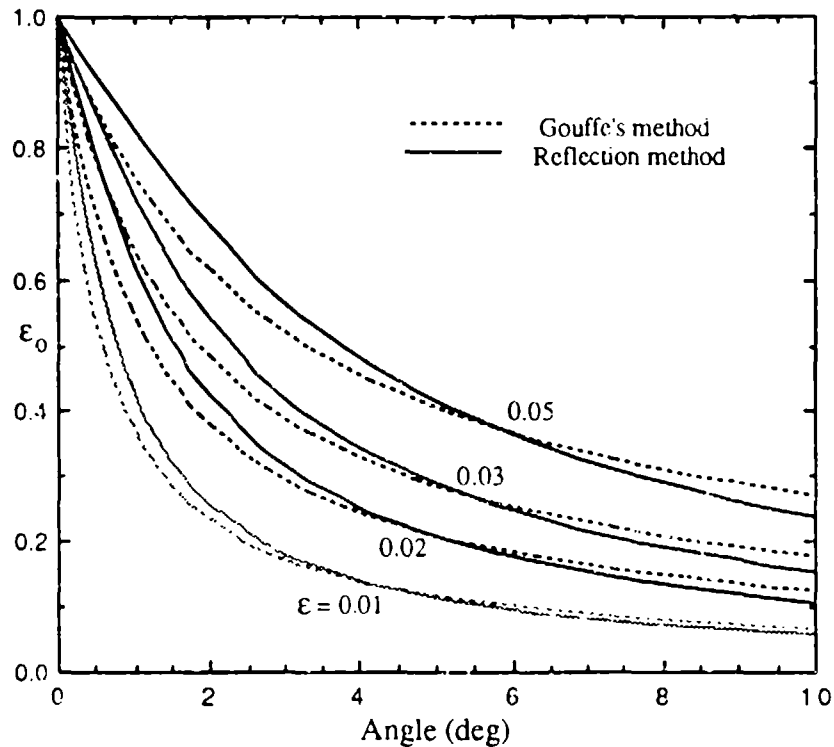


Fig. 5: The emissivity, ϵ_0 , of the V-groove as a function of gap angle, ϕ , for various values of ϵ calculated using two different methods.

DISCUSSION

In designing a radiator one would like to minimize Q_c while maximizing Q_0 for a given nominal radiator size, A_n . This is accomplished by minimizing δ_h while maximizing δ_c , $\epsilon_0\gamma_c$, and $\epsilon_0\gamma_h$. These quantities are shown as functions of ϕ in fig. 6. This figure shows that $\epsilon_0\gamma_c$ and $\epsilon_0\gamma_h$, and thus Q_0 , can be increased by about 50% by increasing the angle between the V-groove from 1.5° to 3-4°. This increase comes in spite of ϵ_0 decreasing by about 50%. It is a result of A_0 increasing and of the changing view factors. More importantly, increasing ϕ also increases δ_c by about 10% and decreases δ_h by 50%. This decreases Q_c . Thus increasing the angle of the V-groove from 1.5° to 3-4° will significantly improve the radiators performance.

Another useful comparison is between the V-groove and a conventional multistage radiator with the same dimensions. Such a radiator is sketched in fig. 7. If both of the radiating surfaces are of equal area and have an emissivity of near 1, then

$$Q_0 = \sigma A_n \sin^2 \frac{\phi}{2} (T_h^4 + T_c^4) \quad (15)$$

Comparing (15) and (11a) shows that for all but the very smallest angles $Q_0 \gg Q_c$. This is a

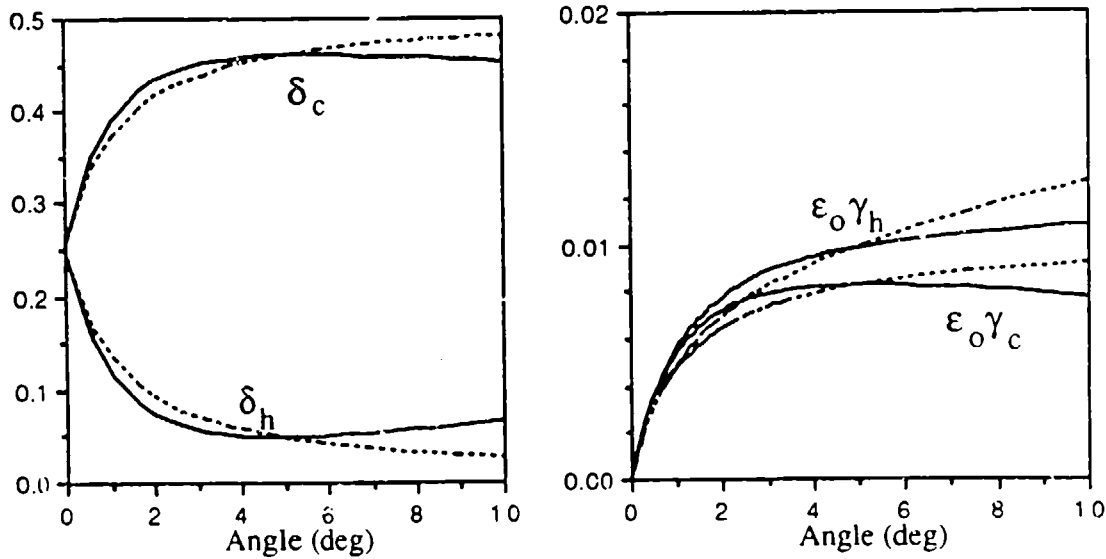


Fig. 6: Plot of δ_c , δ_h , $\epsilon_0 \gamma_c$, and $\epsilon_0 \gamma_h$ as a function of ϕ . The solid line uses the reflection method and the dashed line Gouffe's method of determining ϵ_0 . They all use $\epsilon=0.02$.

result of the low emissivity of the V-groove (fig. 5). For small angles $\gamma_h = \sin(\phi/2)$. So to a good approximation:

$$Q_b \approx (1/\epsilon_0)Q_0. \quad (16)$$

This suggests that the V-groove radiator performance only approaches the multistage performance as $\phi \rightarrow 0$. Furthermore, the gap between the hot and cold plates of the multistage radiator could be filled with multilayer insulation reducing Q_c . Thus, $Q_c < Q_c$.

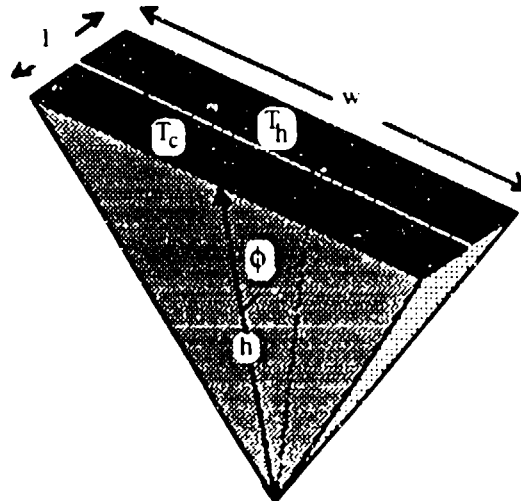


Fig. 7: Sketch of one section of a multistage radiator. The two black surfaces radiate to deep space

CONCLUSION

The individual V-grooves in a V-groove radiator have a peak thermal performance (maximal heat radiated and minimal interstage heat transfer) for V's in the 3-4° range. However, the overall thermal performance of a V-groove radiator is inferior to a conventional multistage radiator. The performance of the two are the same in the limit of $\phi \rightarrow 0$.

These conclusions are based on an analysis that only considered the radiative heat transfer. When other considerations are included (such as mass) the system optimization may come to a different conclusion.

NOMENCLATURE

A	surface area	<u>subscripts</u>	
f, f	fraction absorbed/emitted	c	cold surface
h	edge of V-groove	ϵ	emitted by cold surface
l	length of gap	ci	incident on cold surface
Q, Q	heat flow	e	effective
q	heat flux in gap	h	hot surface
w	width of V-groove	n	nominal
ϵ	emissivity	o	opening
σ	Stefan-Boltzmann constant $= 5.67 \times 10^{-8} \text{ W m}^{-2} \text{ K}^{-4}$	t	total
ϕ	angle between surfaces	x	generalized surface

REFERENCES

1. S. Bard, "Advanced Passive Radiator for Spaceborne Cryogenic Cooling," *J. Spacecraft* vol.21 (1984) p.150.
2. S. Bard, "Development of a High-Performance Cryogenic Radiator with V-Groove Radiation Shields," *J. Spacecraft* vol.24 (1987) p.193.
3. A.J. LaRocca, "Artificial Sources," in: *Infrared Handbook*, W.L. Wolf and G.J. Zissis, ed., Environmental Research Inst. of Michigan (1978) p2-2.

LONG-LIFETIME STORED CRYOGEN SYSTEMS USING REFRIGERATORS TO REDUCE PARASITIC HEAT INPUT

Richard A. Hopkins, Jeffrey H. Lee, Rodney L. Oonk,
Chris D. Miller, and Stephen J. Nieczkoski

Ball Aerospace
Electro-Optics/Cryogenics Division
P.O. Box 1062
Boulder, Colorado 80306

ABSTRACT

The use of active refrigerators instead of or in combination with stored cryogens in spaceborne, long-lifetime cryogenic instrument systems has been recognized for some time as being inevitable. The successful development of multi-year lifetime, space-compatible refrigerator technology has allowed this vision to become a reality. Three NASA development contracts which involve 5-year lifetime, hybrid stored cryogen/refrigerator systems are in the preliminary design stage. These are (1) the X-Ray Spectrometer (XRS), an Advanced X-Ray Astrophysics Facility instrument, (2) the Spectroscopy of the Atmosphere Using Far Infrared Emission (SAFIRE) instrument to be flown on the Earth Observing System platform, and (3) the Near-Infrared Camera and Multi-Object Spectrometer (NICMOS), a second-generation Hubble Space Telescope instrument. Within the given mass and envelope constraints, the cryogen lifetimes of these systems are increased a factor of 2 to 10 with proper use of refrigerators that are either space qualified or in an advanced stage of development. The XRS design uses single-stage, split Stirling-cycle coolers with a superfluid helium dewar. The SAFIRE also uses a superfluid helium dewar, but with both single-stage and two-stage, split Stirling-cycle coolers. The NICMOS uses thermoelectric coolers with a two-stage, solid nitrogen/carbon dioxide dewar. We discuss the predicted lifetime improvements provided for these systems by refrigerators, the thermal performance trades leading to the chosen system designs, the dewar/refrigerator interface issues, and the performance loss in the event of refrigerator failures.

INTRODUCTION

Several long-lifetime, spaceborne dewars have been developed and flown in support of orbiting instrument systems, as typified by the superfluid helium dewar for the Cosmic Background Explorer (COBE)¹. These systems have achieved cryogen lifetimes of about 1 year by using state-of-the-art insulation, tank support and low-conductance cabling technology. Their lifetimes have also been enhanced by use of very cold vacuum shell temperatures (140 K in the case of the COBE)² and extensive use of vapor cooling, which can provide more than a factor of 10 lifetime improvement for a helium system.

New cryogenic systems are being planned with the requirement for 5-year operating lifetime in orbit. For most of these systems the mass and envelope constraints and the inability to achieve a cold vacuum shell within the thermal environment mandate use of refrigerators, either in hybrid combination with stored cryogens or alone. There are reasons why a pure refrigerator approach may be unsatisfactory for a given application, including:

- (1) For a very low operating temperature requirement, say 4 K, space-compatible refrigerator technology is simply not mature enough; this will change with time.
- (2) The vibration of a mechanical refrigerator can produce unacceptable microphonic disturbances in the detector readout or jitter in the optical system. In some cases these problems can be overcome by remote mounting and vibration isolation of the refrigerators.
- (3) The temperature stability provided by a large cryogen reservoir may be needed.
- (4) The power available may be insufficient to operate the necessary refrigerators.

The cryogen loss rate from a dewar can potentially be lowered considerably by coupling the dewar to a refrigerator. Therefore, for an extended-lifetime mission the cryogen system overall mass and envelope might be considerably reduced by a hybrid stored cryogen/refrigerator approach. This of course requires more power consumption than a purely passive approach. The most effective use of refrigerator(s) and the interfacing between the dewar and refrigerator(s) depend on many things. Most important are the cryogen (its storage temperature and vapor cooling potential), the heat lift profile and configuration of the refrigerator(s), the power dissipation (level and temperature) produced by the instrument inside the dewar, and the allowable vibration level. To be effective, the refrigerator must lift heat from a spot inside the dewar where the levels of heat flow are very small compared to heat flows outside the dewar. System-level requirements and interactions must be considered in choosing, or designing, a refrigerator for a certain application. A given refrigerator might be quite suitable for one application, but unacceptable for another.

Several space science missions are being planned which will use hybrid stored cryogen/refrigerator systems for sensor cooling. The designs and predicted performance of three of these are the topic of this paper. They are: (1) the X-Ray Spectrometer (XRS) of the Advanced X-Ray Astrophysics Facility (AXAF), (2) the Spectroscopy of the Atmosphere Using Far Infrared Emission (SAFIRE) instrument to be flown on the Earth Observing System (EOS), and (3) the Near-Infrared Camera and Multi-Object Spectrometer (NICMOS), a second-generation Hubble Space Telescope (HST) instrument. Characteristics of these cryogenic systems are given in Table 1. The XRS cryogenic subsystem (CSS), the SAFIRE instrument and the NICMOS instrument are in the preliminary design phase at Ball Aerospace under contract to the NASA.

The high-performance dewar technology developed and proven on previous programs is essential to achieving 5-year lifetimes for these hybrid systems within the mass, power and envelope constraints. Sophisticated

Table 1
CHARACTERISTICS OF THE CRYOGENIC
SYSTEMS FOR XRS, SAFIRE AND NICMOS

SYSTEM	TYPE OF CRYOGEN	TANK SIZE (liters)	VACUUM SHELL TEMPERATURE (K)	TYPE(S) OF REFRIGERATOR	RESERVOIR TEMPERATURE (K)
XRS	He II	490	250	1-stage split Stirling	1.3
SAFIRE	He II	124	300	1-stage and 2-stage split Stirling	1.9
NICMOS	N ₂ /CO ₂	71/25	270	Thermoelectric	58/130

computer modeling tools to predict dewar performance for these types of systems have been developed and carefully verified by ground test and flight performance data³. These analytic tools are equally applicable to hybrid systems and help provide the confidence needed for their development.

Refrigerator reliability is a concern for a 5-year mission. Appropriate levels of redundancy must be considered to control performance risks. The dewar and dewar/refrigerator interface should be designed to minimize the impact of a failed cooler, so that one failure does not end the mission. Although significant advances in mechanical cooler technology have occurred during the last decade, a space-compatible mechanical cooler does not yet have a demonstrated lifetime over 3 years. Abbreviated testing to prove extended lifetime is unreliable. The most successful mechanical cooler that is space qualified to date was developed at the Oxford University and uses the linear, split Stirling-cycle approach⁴. This single-stage machine provides about 0.8 W cooling at a temperature of 80 K, depending on the compressor temperature. In addition a two-stage version has been built more recently using the same technology that provides about 0.3 W at 30 K⁶. The XRS and SAFIRE programs plan to use mechanical coolers derived from the Oxford technology. The NICMOS program is baselining solid-state thermoelectric coolers.

These three systems are separately discussed in the following sections. They all use multilayer insulation and tension strap tank support systems similar to those proven by the COBE dewar and previous flight dewars developed by Ball Aerospace. The vapor-cooled and actively-cooled shields inside the dewars are supported from and cool the tank support straps. Heat flows through all conduction and radiation paths into the dewar are reduced by vapor cooling. State-of-the-art miniature cables minimize the heat leak through the hundreds of wires that penetrate the dewars for housekeeping sensors, mechanisms control and science instrument readout. Emphasis in the following sections is on the overall architecture of the hybrid approach, the trades from which it resulted,

the main issues regarding dewar/refrigerator interfacing, the nominal performance, the improvement in cryogen lifetime provided by the refrigerator(s), and the impact of refrigerator failures.

Because the dewars contain complex and sensitive instruments, many aspects of performance must be considered with regard to refrigerator interfacing and operation⁶. These include:

- Vibration control
- Electromagnetic interference control
- Efficiency of the thermal link
- Alignment and assembly
- Mechanical flexibility in the thermal link
- Thermally disconnecting a failed refrigerator (on the ground or on orbit)
- Removing a refrigerator with minimal disturbance to the dewar
- Operating in multiple gravity orientations for testing

All these aspects have been considered in the designs of the systems discussed below.

AXAF X-RAY SPECTROMETER (XRS)

The XRS is one of the instruments to be flown aboard the AXAF scheduled for launch in 1998. The instrument will measure incident energy over the spectral range of 0.3 to 10 keV with a resolution of 10 eV using bolometers at a temperature of 0.1 K. The bolometers are cooled by an adiabatic demagnetization refrigerator (ADR)⁷.

Table 2 summarizes the requirements which drive the XRS/CSS design. Detailed analyses have been performed to arrive at the current design, which meets or exceeds all requirements.

BASELINE DESIGN

Figure 1 depicts the dewar baseline design. A 490-liter superfluid helium tank provides the heat sink for the ADR. Both the ADR and the detectors are part of the removable cryogenic assembly (RCA), which is bolted to the forward end of the cryogen tank. Once installed in the dewar, the RCA is accessible through the removable aperture assembly at the forward end of the dewar. Surrounding the cryogen tank are four vapor-cooled shields (VCSs) which make effective use of the helium vent gas to intercept heat at various levels within the insulation system. The outermost VCS is also cooled by single-stage, split Stirling-cycle mechanical refrigerators through a flexible cold finger attachment to the aluminum shield.

There are four of these refrigerators, based on the Oxford design, which are mounted as in-line pairs for momentum compensation to the vacuum shell forward girth ring. The displacer cold tips are contained in a separate vacuum space. This allows replacement without disturbing the dewar vacuum and prevents condensation of water from the dewar outer insulation blanket on the cooler cold tip. The compressor pairs are mounted on separate pallets which are shock mounted to the forward girth ring to minimize vibration transmission to the dewar and RCA. Heat is

Table 2
XRS/CSS OPERATING REQUIREMENTS

ITEM	REQUIREMENT	PREDICTED VALUE
Bath Temperature	<1.5 K Orbital Operation <1.9 K Ground Operation	1.29 K <1.6 K
Bath Temperature Stability	0.05 K over mission duration	0.04 K worst case
Cryogen Lifetime	4.5 years with 10 percent analysis margin	>5 years
Dewar Lockup	6 days without power	9 days
Vibration at RCA	<0.001 g	factor of 6 margin
Power Consumption	<185 W Total	<184 W
Main Shell Temperature	>243 K Operational >233 K Hold (limited by mechanical coolers)	>249 K >240 K

rejected from the coolers by a combination of radiation to the AXAF cold shroud and conduction to the dewar main shell, which is also cooled by radiation to the cold shroud.

A single cold finger provides the interface between a pair of displacers and the outer VCS. Very thin, flexible copper strips separated by indium foil spacers are used to connect a pair of displacer cold tips to an interface block. This arrangement provides adequate thermal conductance while preventing side loading on the cold tip from exceeding several ounces. The outer VCS is connected to the interface block with a copper rod. A combined thermal conductance of about 600 mW/K is needed in the flexible link and copper rod. Thin-walled fiberglass tubes separate the displacer chamber from the dewar vacuum. Snubbers mounted on the displacer housings limit the motion of the cold tips during ground handling and launch.

SYSTEM TRADES

The development of mechanical refrigerators for space application has been tracked during the XRS/CSS design development. At present, a refrigerator that could provide the required 1.5 K ADR heat-sink temperature has not been developed, mandating the use of superfluid helium. Only the split Stirling-cycle cooler based on Oxford technology is currently considered mature enough for the XRS schedule. Still, uncertainty exists regarding the operational lifetime of these coolers. This

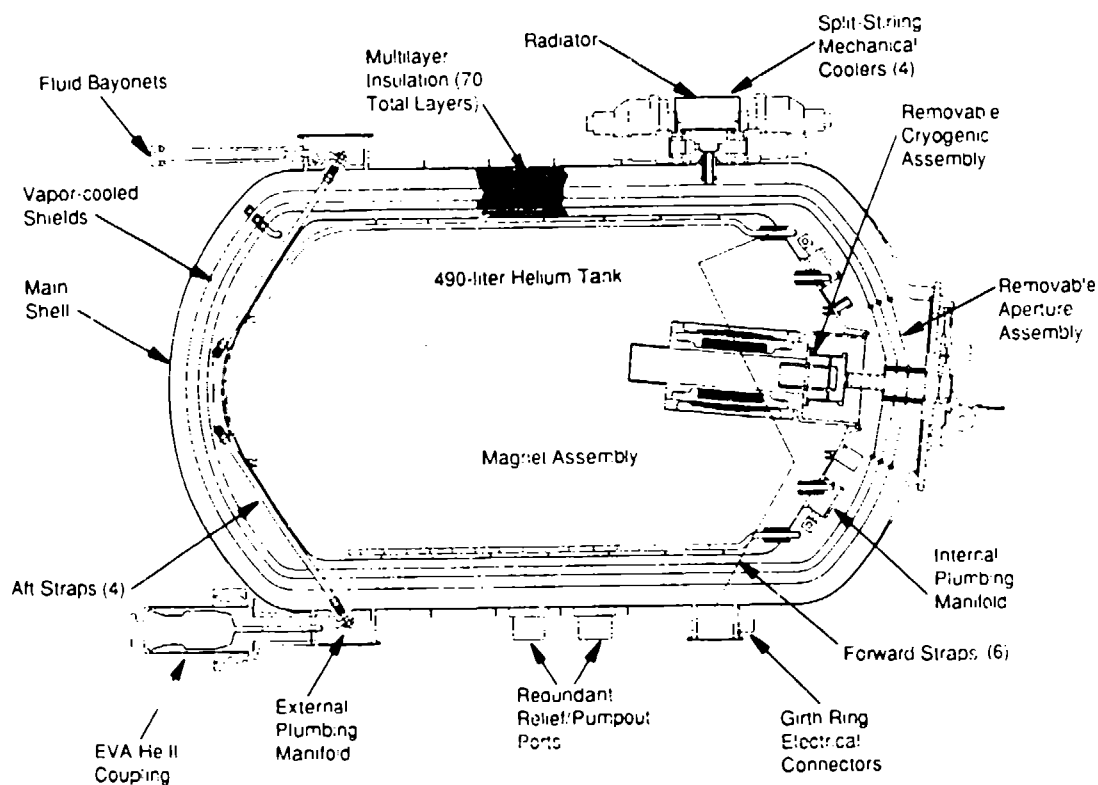


Fig. 1. IRS cryogenic subsystem design layout.

must be folded into the risk assessment of achieving the mission lifetime goal, and choices for operating the coolers must be made accordingly.

The current baseline uses four coolers. With all four coolers operating the power they consume (160 W) just meets the available budget, and the predicted helium lifetime is 6.5 years. However, because the 5-year lifetime requirement can be met by operating only a single cooler pair, the prudent choice is to reserve a pair of coolers, thereby increasing the probability of meeting the requirement. This is the focus of the current trade study, identifying and possibly developing other cooler options based on the same technology which will maximize lifetime without introducing further risk to the science or cost to the system. An example is the two-stage, Stirling-cycle cooler which is currently in development for use in the SAFIRE instrument and has been investigated as an option for the XRS. Such a cooler has the potential to nearly double the helium lifetime for the XRS/CSS when used in combination with a single-stage cooler pair. However, the power budget would preclude the redundancy of either the single-stage or two-stage coolers. The failure of a two-stage cooler is much more detrimental to the helium lifetime, and the result is an increased risk in achieving a 5-year lifetime. The final selection as to the size and quantity of coolers

will be based on continued risk, lifetime and cost considerations.

System Modeling and Performance

A 24-node thermal network model of the XRS/CSS is used to predict helium lifetime, ground hold capability and transient response to operations. Six nodes are used to model the mechanical coolers interface with the dewar. Cooling at the displacer cold tip is modeled as a negative heat flow using linear interpolation tables of measured performance which characterize the cooling capacity based on cold tip temperature, compressor mount temperature, and input power.

The XRS/CSS relies heavily on both vapor cooling (passive) and mechanical cooling (active) to meet the required 5-year orbital lifetime within both mass and envelope constraints. Vapor cooling alone increases the helium lifetime by a factor of 25. Another factor of 2 is provided by a single pair of coolers using just half the allocated power. Table 3 shows lifetimes for the baseline dewar design with the various degrees of cooling. It is easy to see how important the mechanical coolers are to the success of the XRS mission. Therefore, evaluating the effects of cooler failure is very critical to the dewar design and the cooler operating strategy.

The baseline dewar design uses four mechanical coolers operated in momentum-compensated pairs to meet vibration requirements of the system. Only a single pair of coolers will be operated initially to attain the highest level of redundancy in the system. The two operating coolers remove about 1.8 W of heat from the outer VCS at a temperature of 80 K. The non-operating cooler pair adds a parasitic heat load of about 0.2 W to the outer VCS, depending on the means chosen for thermal disconnect. The failure of any single cooler is assumed to result in the loss of a pair because of the vibration requirement. In the event the first

Table 3
XRS/CSS LIFETIME IMPROVEMENT ACHIEVED WITH VAPOR
COOLING AND ACTIVE COOLING

DEGREE OF DEWAR COOLING	HELIUM LIFETIME (YEARS)
None	0.083
Vapor cooling only	2.2
Vapor cooling plus 2 coolers at 80 W power	5.6
Vapor cooling plus 4 coolers at 160 W power	6.5

cooler pair fails, it will be switched off and the reserve pair will be switched on. This operational strategy was chosen because it requires a minimum 2.5-year lifetime from each cooler pair to meet the 5-year helium lifetime requirement. Operating all four coolers from the start would require at least a 4-year lifetime from one pair of coolers. The nominal predicted helium lifetime is 5.1 years using the reserve cooler operational strategy and assuming the first cooler pair fails 2 years after launch and the reserve pair operates for another 3 years.

If all four coolers fail at launch, lifetime is reduced to about 2 years. However, in this event the helium reservoir temperature still meets the temperature requirement of <1.5 K so that instrument operation can continue. The use of an active thermal switch can reduce the heat load to the dewar resulting from a non-operating cooler. Two types of switches are candidates for use in connecting the mechanical coolers to the dewar. One type involves metal-to-metal contact making use of differential expansion between materials, and the other employs gaseous conduction across a narrow gap. Both would require further development work for application to the XRS/CSS. A trade study is underway to weigh benefits and risks of incorporating active thermal switches in the design. Preliminary thermal modeling results indicate that a thermal switch with a closed conductance of 500 mW/K and a switching ratio of 1000 can increase the helium lifetime 7 percent.

The compressors operate about 20 K warmer than the vacuum shell, or 270 K on the average. Lifetime is increased by lower vacuum shell temperature because parasitic heating into the dewar is decreased and by lower mechanical cooler temperature because the coolers become more efficient. The combined effect results in 0.7 percent lifetime change for each degree Kelvin temperature change. It is therefore important to operate both items as cold as possible. However, temperatures of the two are interdependent, and the minimum temperature of the mechanical coolers is limited by its allowable range for operation and startup.

It is necessary that the helium be in the superfluid state to ensure proper function of the porous plug phase separator when the vent valve is opened on orbit. The lock-up capability is defined as the time it takes for the superfluid helium reservoir temperature to rise to the lambda point following the final prelaunch toloff and pumpdown. Power is not available to the CSS during this period, which is nominally 5 days prior to launch and 1 day following. The predicted capability is 9 days without powering the mechanical coolers. It can be extended to about 5 months by powering one pair.

EOS SPECTROSCOPY OF THE ATMOSPHERE USING FAR INFRARED EMISSION (SAFIRE)

The SAFIRE instrument is one of a suite of instruments proposed for the second NASA Eos polar orbiting platform. By obtaining Earth limb emission data in both the mid-infrared (6 to 17 μm) and far-infrared (25 to 35, 62 to 125 μm) spectral regions, SAFIRE will provide information on diurnal and temporal variations of observed gases that is necessary for the understanding of issues regarding middle atmospheric ozone chemistry. SAFIRE must cool its far-infrared detectors to 3 to 4 K, which

is well below the 55 to 80 K required by some of the other Eos instruments. The SAFIRE mid-infrared module will use mechanical coolers to cool its detectors to 80 K. The far-infrared module, called the Cold Optics and Detectors Module (CODM), will use the hybrid cryogenic system described in this section.

Table 4 summarizes some of the allocated system budgets. The CODM performance requirements shown in Table 5 are derived from the mission and system requirements.

BASELINE DESIGN

Figure 2 shows the baseline design of the SAFIRE CODM cryogenic subsystem. A 124-liter cylindrical tank containing superfluid helium at about 1.9 K provides cooling for the focal plane assembly. The helium tank is surrounded by four shields. The innermost shield is vapor cooled, and the other three shields are actively cooled by split Stirling-cycle mechanical coolers as well as vapor cooled. During normal operation, the use of vapor cooling on the actively-cooled shields has little benefit. However, in the event of any mechanical cooler failure, the rise in helium boiloff will make the vapor cooling benefit significant. The outer actively-cooled shield (OACS) and the middle actively-cooled shield (MACS) are each cooled by a single-stage, split Stirling-cycle mechanical cooler⁴ while the inner actively-cooled shield (IACS) is cooled by a two-stage, split Stirling-cycle cooler⁶.

Table 4
SAFIRE SYSTEM REQUIREMENTS

ITEM	REQUIREMENT
Instrument Envelope	Double standard size payload assembly plate on Eos platform
Mass	375 kg, current estimate
Power	426 W, current estimate
Image Stability	≤3 arcsec scan mirror jitter
Total boresight error	≤19 arcsec (preliminary)
Launch Vehicle	Titan 4

Table 5
SAFIRE CODM DERIVED REQUIREMENTS AND CONSTRAINTS

ITEM	REQUIREMENT
CODM envelope	74 cm x 74 cm x 135 cm
Mass	113 kg (current estimate)
Power	216 W (current estimate)
Lifetime	≥5 years
Vacuum shell temperature	>243 K (limited by mechanical coolers)
Focal plane assembly temperature	3 to 4 K
Cold optics subsystem temperature	≤30 K
Cold preamplifiers temperature	≤80 K
Focal plane assembly temperature stability	<40 mK/hr
CODM alignment (inter-module)	≤0.15 mm (displacement) ≤10 arcsec (tilt)
Component alignment within COS	≤0.2 mm (displacement) ≤20 arcsec (tilt)
CODM operating mode (ground)	In any orientations

The design of the mechanical cooler interfaces to the dewar have taken into consideration those issues mentioned in the previous sections. All of the components of the split Stirling-cycle coolers are mounted to the forward girth ring. The two compressors and two displacers of the single-stage coolers are mounted in line to provide momentum compensation. For the two-stage mechanical cooler, only the two compressor units are mounted in line. The level of vibration from the uncompensated two-stage displacer can be transmitted to the dewar without violating the alignment requirements. Heat is conducted from the dewar shields to the displacer cold tips via a cold finger using a combination of flexible, high-purity copper strips and a copper rod. System analysis is currently in progress to assess the impact of using active thermal switches and redundant mechanical coolers.

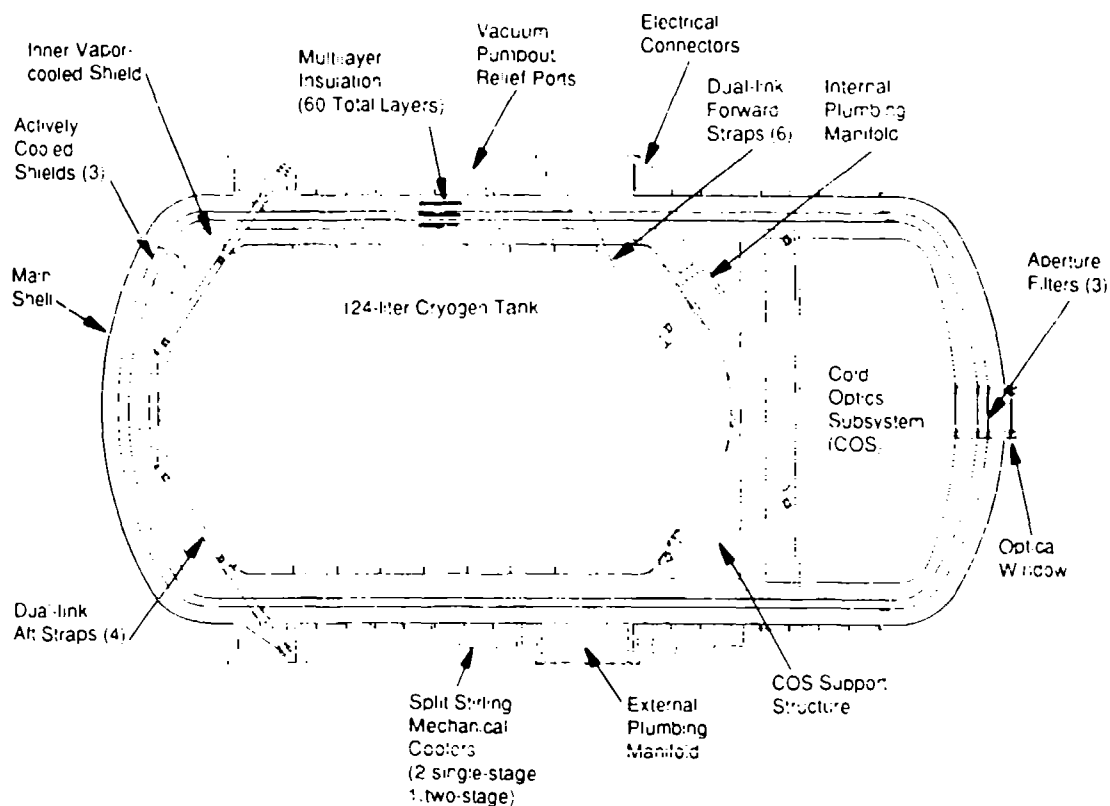


Fig. 2. SAFIRE cold optics and detectors module layout.

SYSTEM TRADES

Various design options were considered to optimize the cryogenic subsystem performance. The required far-infrared detector operating temperature of 3 to 4 K can be provided by either using superfluid helium in a stored cryogen system or using a closed-cycle system with mechanical coolers providing the pre-cooling stage for a Joule-Thomson (J-T) expander. A base temperature of 3.5 K was demonstrated with laboratory components of the closed-cycle J-T system⁶. However, the superfluid helium stored cryogen system was selected as the baseline for several reasons. The maturity of the J-T system is questionable for the SAFIRE schedule. Ample experience was gained during the development and flight of previous superfluid helium dewars. A 5-year superfluid helium dewar is achievable by using mechanical coolers to extract heat from the dewar radiation shields, thus reducing the heat load to the superfluid helium. The hybrid mechanical cooler/superfluid helium system also requires about half the power consumption of the closed-cycle J-T system. However, the hybrid helium system does occupy a larger volume and weighs about 30 kg more than the J-T system. A hybrid supercritical helium/J-T system can also provide detector cooling to about 3 to 4 K.

However, this system would be even less mass and volume efficient than with superfluid helium.

Another trade study was made to determine the optimum cooling configuration of the dewar MACS and OACS using the single-stage mechanical coolers. Two cases were analyzed and compared with the baseline configuration. Results show that placing both the single-stage coolers at either the MACS or the OACS gives 12 to 15 percent lower helium lifetime than the baseline design. A final trade study was performed to evaluate the benefit of using helium vapor cooling on all of the actively-cooled shields. During normal operation, the cooling capacities of the three mechanical coolers overwhelm the small amount of enthalpy available from the low helium vent rate; therefore, only 2 percent gain in lifetime is obtained with the vapor cooling. However, vapor cooling the actively-cooled shields can reduce helium boiloff by 5 to 50 percent in the event of mechanical cooler failures.

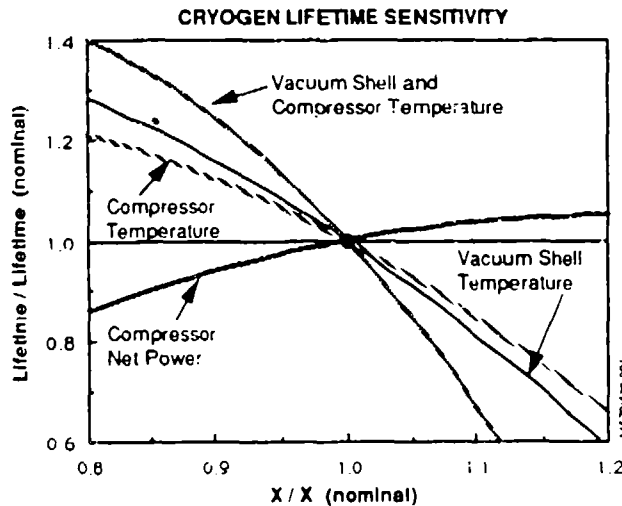
SYSTEM PERFORMANCE

The dewar thermal/math model predicts a lifetime of about 7 years for the 124-liter hybrid superfluid helium system. Dewar vacuum shell temperature of 300 K and mechanical cooler compressors temperature of 310 K are assumed in the analysis. The nominal operating temperatures and cooling capacities required from the mechanical coolers are 0.3 W at 30 K for the two-stage cooler and 0.66 W at 77 K and 1.8 W at 145 K for the single-stage coolers. Reliable operation of the mechanical coolers is critical to meeting the 5-year mission requirement. The baselined hybrid approach provides ten times greater lifetime than a passive stored helium approach within the mass and envelop constraints.

Figure 3 shows the sensitivity of cryogen lifetime to changes in dewar vacuum shell temperature and mechanical cooler compressor temperature. Lifetime increases by about 0.6 percent for every degree Kelvin decrease in dewar vacuum shell temperature and about 0.9 percent if both the vacuum shell and compressors temperature decrease by one degree Kelvin. Note that for the range of single-stage cooler input power shown in the figure, lifetime changes by at most 15 percent.

Preliminary analysis of mechanical cooler failure shows that dewar lifetime is least affected by a failure of the cooler on the OACS, while the failure of the two-stage cooler on the IACS affects dewar lifetime dramatically. This is because the amount of parasitic heat load to the superfluid helium is largely controlled by the temperature of the IACS. In addition to the lifetime loss resulting from mechanical cooler failure, the increased temperature of the helium reservoir detectors, and cold optics could degrade the instrument function. Also, if the helium goes to the normal state, the porous plug phase separator used for normal operation would not function. These issues are being investigated. One part of the solution may be to provide an alternate venting system to use for extreme failure conditions.

Analysis with the dewar thermal/math model shows that use of an ideal thermal switch (i.e., zero thermal conductance and infinite switching ratio)



NOMINAL VALUES

Lifetime = 7 years
 T(Vacuum Shell) = 300 K
 T(Single-stage Cooler Compressors) = 300 K
 Single-stage Cooler Compressor Net Power = 20 W

Fig. 3 Sensitivity of cryogen lifetime to main drivers.

would reduce the boil-off rate about 5 percent if the OACS cooler fails, 25 percent if the MACS cooler fails, and 100 percent if the IACS cooler fails.

The effect of mechanical coolers residual vibration on dewar performance was evaluated assuming a worst case where the dewar resonant frequency coincides with the mechanical cooler drive frequency of 40 Hz. Results indicate that the CODM can withstand an excitation force of about 2 lb from the mechanical coolers without exceeding the line-of-sight jitter and displacement error requirement specifications of 20 arcsec and 0.2 mm, respectively. Measurements to be presented at this conference by the NASA Jet Propulsion Laboratory indicate that this residual vibration level is achievable.

HST NEAR-INFRARED CAMERA AND MULTI-OBJECT SPECTROMETER (NICMOS)

NICMOS is a multi-purpose, second-generation HST instrument capable of performing imaging and spectroscopy in the 1 to 3 μm wavelength region. It is unique in that it is the only HST instrument that is cryogenically cooled and operates in the near infrared.

Table 6 summarizes the science-driven performance requirements for the NICMOS cryogenic subsystem. Also shown are the baseline design values for each of the performance requirements. The interface and constraint requirements are derived from four sources: (1) the NICMOS instrument, including the other subsystems, (2) the HST, (3) the Space Transportation System (STS), and (4) integration and testing. Table 7 summarizes the requirements derived from the NICMOS instrument and HST. The interfaces and constraints set by the STS and integration and test activities cover the areas of launch loads, safety, venting in the payload bay and ground operations. NICMOS must meet the safety requirements imposed by

Table 6
NICMOS SCIENCE-DRIVEN PERFORMANCE REQUIREMENTS

ITEM	REQUIREMENT	BASELINE VALUE
Detector temperature	≤62 K	58 K
Detector temperature stability	≤200 mK short term ±2 K over duration of mission	Meets
Cold stop temperature	≤180 K	130 K
Lifetime	≥5 years	6 years

the STS, including that the cryogenic subsystem can be left unattended for at least five days prior to launch and deployment.

BASELINE DESIGN

Figure 4 shows the baseline design of the NICMOS cryogenic subsystem. The 58 K solid N₂ stage of 71 liters surrounds the cold optics bench containing the six detector arrays. The 130 K, 25-liter annular CO₂ tank uses passively-cooled domes on each end to completely enshroud the N₂ stage. Surrounding the CO₂ stage are two actively-cooled shields. These shields are each cooled by a pair of thermoelectric coolers (TECs). The solid-state TECs use the Peltier effect to produce cooling using the 25 to 30 W of power available to the cryogenic subsystem. The TECs are attached to radiators located on the outboard panels of the NICMOS enclosure and connected to the shields via permanently attached flexible cold fingers. They share a common vacuum with the dewar via low-conductivity titanium tubes, which minimize heat flow between the cold radiators and the temperature-controlled vacuum shell. The vacuum shell mounts to the NICMOS main optical bench.

Figure 5 shows the arrangement of TEC cooling. (For clarity, only one of each pair of inner and outer TEC/radiator combinations is shown.) The TEC-cooled shields substantially reduce the heat load on the CO₂ stage. Since the cooling capacity of the TECs increases with temperature, the temperatures of the TEC-cooled shields are not very sensitive to variations in parasitic heat loads.

SYSTEM TRADES

A mechanical cooler approach can provide the required operating temperatures, but the only technology considered mature enough at this time to choose for multi-year, on-orbit use is the linear, split Stirling-cycle approach. However, to reduce the vibration to an acceptable level would require operating them in compensated pairs, requiring about 80 W of power per pair. The 30 W power budget does not permit this. Therefore,

Table 7
NICMOS INTERFACE AND CONSTRAINT REQUIREMENTS

ITEM	REQUIREMENT
Mass	164 kg
Input power available	30 W during operation, 25 W during hold
Maximum vibration	Cannot cause an HST pointing error >0.0007 arcsec
Thermal	270 \pm 1 K vacuum shell temperature 255 K HST radiative sink temperature (operation) 232 K HST radiative sink temperature (hold)
Focal plane dissipation power	1 mW during operation, zero during hold

the only type of refrigerator that meets reliability, vibration, and power constraints is a TEC. Unfortunately, a system using only TECs and radiators cannot provide the required 62 K operating temperature. On the other hand, a pure stored cryogen system was found to be too heavy. It was thus determined that the only approach that could provide the operating temperature within mass, vibration, and power constraints is a hybrid system using stored cryogens with TECs and radiators.

SYSTEM MODELING AND PERFORMANCE

The NICMOS dewar lifetime is calculated using a 28-node thermal network model. This model sizes the N_2 and CO_2 tanks to yield equal cryogen lifetimes, with total dewar mass constrained by the 164 kg budget.

The thermal environment viewed by the TEC radiators is warmer during the operate mode than during the hold mode. This results in warmer TEC shield temperatures and a higher CO_2 depletion rate during the operate mode. The N_2 depletion rate is nearly independent of the TEC shield temperatures because nearly all heat transfer paths to the N_2 tank (supports, plumbing, etc.) come from the CO_2 tank. Table 8 shows the predicted net heat leaks, sublimation rates, cryogen masses and on-orbit lifetime. Timelined average shield temperatures are shown in Figure 5.

A modified version of the dewar thermal model was used to determine the lifetime attainable by a dewar without the TEC cooled shields. Holding the overall dewar mass budget at 164 kg, the predicted lifetime is only 3.0 years. Similar results were recently obtained during demonstration testing at Ball Aerospace. In these tests, TECs were used to cool a shield installed in the annulus of a dewar containing Freon-14. The dewar boil-off rate increased by a factor of two when the TECs were removed.

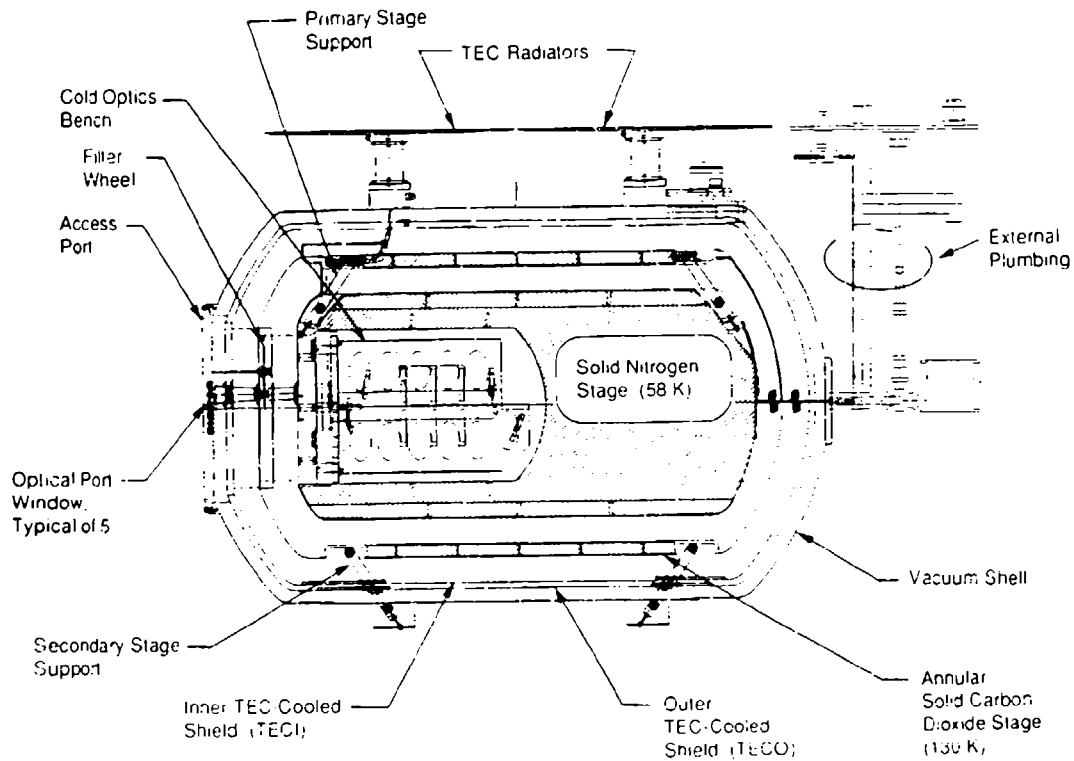


Fig. 4. NICMOS cryogenic subsystem design layout

Fig. 5 Thermoelectric cooling arrangement for NICMOS.

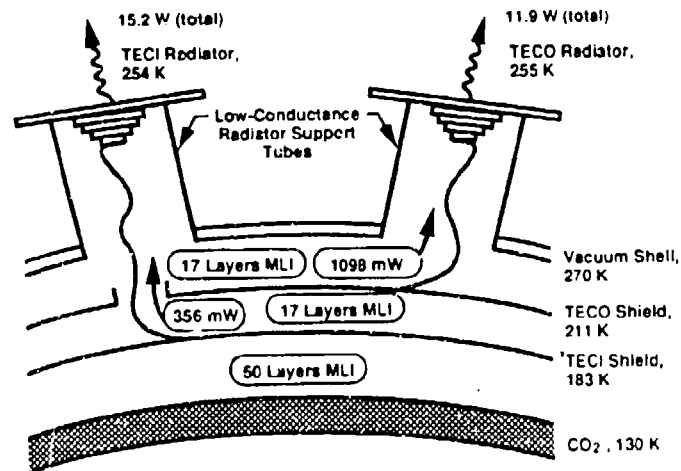


Table 8
NICMOS BASELINE CRYOGENIC PERFORMANCE

ITEM	OPERATE (20% of life)	HOLD (80% of life)
Primary stage heat leak	82.6 mW	81.9 mW
N ₂ sublimation rate	29.1 g/day	28.9 g/day
Secondary stage heat leak	150 mW	110 mW
CO ₂ sublimation rate	21.2 g/day	15.6 g/day
Average sublimation rates	N ₂ : 28.9 g/day CO ₂ : 16.7 g/day	
Fully-loaded cryogen mass	N ₂ : 63.9 kg CO ₂ : 36.9 kg	
On-orbit lifetime	6.0 years	

TECs are inherently very reliable due to their solid-state construction and the absence of moving parts. The use of redundant cooling elements shows promise for further improving TEC reliability⁸. The lifetime impact of a single TEC failure is lessened by using two identical TECs to cool each shield. Still, the potential exists for an on-orbit failure of one or more TECs, resulting in a shortened instrument lifetime.

Performance trades showed that for credible TEC failures, thermal disconnects provided little system performance benefit. For failure of a single TEC on either shield, the heat leak across the failed device is about 400 to 800 mW. The shield temperature will rise as a result, but the non-linear cooling performance of the remaining TEC limits this temperature rise to about 10 to 20 K. If both TECs on either shield fail, the lifetime impact is greater, but is softened because the TEC radiator temperatures are relatively low compared to the dewar vacuum shell temperature. For a complete failure of all four TECs, thermal disconnects offer no performance benefit. This is because the uncooled shields are, on average, warmer than the TEC radiators. Therefore, leaving the failed TECs attached actually cools the shields.

Figure 6 shows the lifetime impact of single and multiple TEC failures as a function of time after launch. The analysis assumed that a failed TEC provides no cooling and that input power to the remaining TECs is unchanged. The failure scenario with the least lifetime impact is a failure of a single TEC on the outermost shield. The failure of all four TECs at launch results in a lifetime reduction of 46 percent. While this lifetime reduction is severe, many of the science objectives could still be met since detector temperatures will rise less than 1 K.

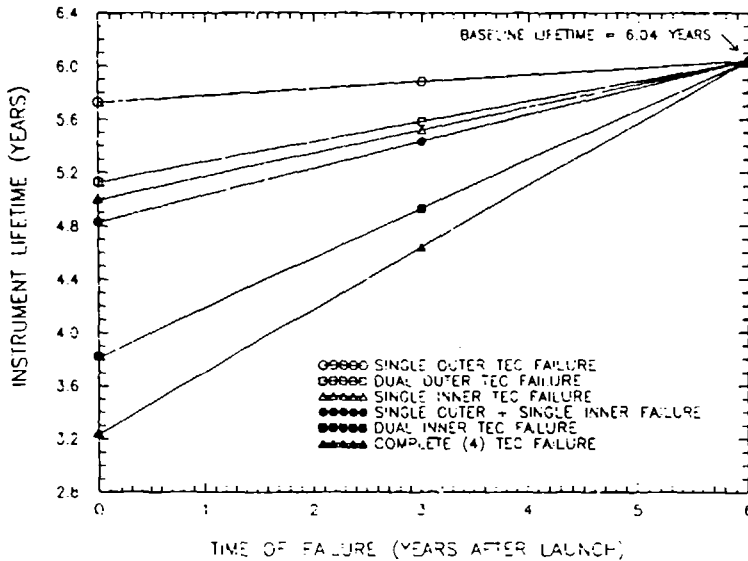


Fig. 6 Lifetime impact of TEC failures.

CONCLUSIONS

Three hybrid cryogenic systems are being developed that combine proven cryogen storage technologies with refrigerators to achieve on-orbit lifetimes over 5 years. The lifetime increase provided by use of refrigerators for these systems ranges from a factor of 2 to a factor of 10. Interfacing between the dewar and refrigerators is critical and involves a variety of issues that must be carefully considered. Most of these issues, such as the replacement of refrigerators with minimal disturbance of the dewar, vibration isolation, thermal efficiency and mechanical flexibility of the connection, are important to all three systems discussed. The greatest risk in achieving the predicted lifetimes for these systems is premature failure of the refrigerators. Therefore, consideration of the mission impact from refrigerator failures and implementation of redundancy is a critical aspect of the design process.

ACKNOWLEDGEMENTS

The systems discussed in this paper are under development at Ball Aerospace/Electro-Optics and Cryogenics Division. The NASA Goddard Spaceflight Center is funding development of the cryogenic subsystem for the XRS under contract NAS5-31251. The NASA Langley Research Center is funding development of the SAFIRE instrument under contract NAS1-19129. The SAFIRE development is an international program with partners from France, Italy, and the United Kingdom. The NASA Goddard Spaceflight Center is funding development of the NICMOS instrument through the University of Arizona under contract NAS5-30008.

REFERENCES

1. R.A. Hopkins and S.H. Castles, "Design of the Superfluid Helium Dewar for the Cosmic Background Explorer," Proceedings of SPIE, Vol. 509 (1984).
2. R.A. Hopkins and M.G. Ryschkewitsch, "Measured Ground Performance and Predicted Orbital Performance of the Superfluid Helium Dewar for the Cosmic Background Explorer," Proceedings of SPIE, Vol. 619 (1986).
3. R.A. Hopkins, S.J. Nieczkoski, and S.M. Volz, "Performance Predictions for Spaceborne, Long-lifetime Helium Dewars Containing Large-aperture Telescopes," to be published, presented at 1990 SPIE International Symposium on Optical and Optoelectronic Applied Science and Engineering, San Diego.
4. G. Davey and A. Orłowska, "Miniature Stirling Cycle Cooler," Cryogenics, Vol. 27 (1987).
5. A.H. Orłowska, T.W. Bradshaw, and J. Hieatt, "Closed Cycle Coolers for Temperatures Below 30 K," Cryogenics, Vol. 30, March (1990).
6. R.G. Ross, "Requirements for Long-life Mechanical Cryocoolers for Space Application," Cryogenics, Vol. 30, March (1990).
7. A.T. Serlemitsos, B.A. Warner, and M. SanSebastian, "Spaceworthy ADR: Recent Developments," to be published, presented at 1990 SPIE International Symposium on Optical and Optoelectronic Applied Science and Engineering, San Diego.
8. D.A. Johnson, "Improvements in Reliability of Thermoelectric Coolers through Redundant Element Design," Proceedings of SPIE, Vol. 1044 (1989).

EFFECT OF VOID VOLUME IN REGENERATOR

Yoichi Matsubara
Atomic Energy Research Institute
Nihon University
Chiba, 274 Japan

Yu Hiresaki
Cryogenic Division
Suzuki Shokan Co., Ltd.
Saitama, 350 Japan

ABSTRACT

The fundamental study of the regenerator performance taking account of the void volume by means of numerical calculation is described. It leads that the definition of the efficiency for the regenerator is very complex due to the gas in the void volume. The approach using the ineffectiveness at the cold end of the regenerator is proposed to evaluate the performance of the regenerator and is discussed with the results of numerical calculation.

INTRODUCTION

The performance of regenerative heat exchangers has been discussed in many papers by means of the regenerator efficiency.¹⁻³ D. Daney and R. Radabaugh considered the effect of void volume assuming constant pressure, constant flow-rate and incompressible gas.⁴ In this study, we extend the consideration to the variable operating conditions which should be satisfied for understanding an actual regenerator performance for the temperature range is above 20K, where the working helium gas could be assumed as the ideal gas.

The regenerator efficiency is defined as the ratio of the actual heat transfer rate to the maximum possible heat transfer rate. The performance of a regenerator with void volume usually can not be defined

as an unique expression even for the ideal gas, mainly because that mass-flow rate of working gas is not constant in the regenerator.

The total mass of gas within the void volume varies during each half cycle, unless the heat capacity of the regenerative material is infinite. Therefore, considering the equation of continuity for gas, the mass-flow rate in the regenerator should not be uniform along the flow. When the pressure is constant, the mass-flow increases with increasing gas temperature within the void volume at the same position. As a result, the mass-flow rate of the exhaust gas at the cold end is always greater than that of the inlet gas at the warm end of the regenerator. Similarly, the exhaust gas at the warm end is less than the inlet gas at the cold end during the another half cycle. The fact of the variable mass-flow rate induces difficulty of the definition of the regenerator efficiency.

Temperature profile of the gas and the matrix in the regenerator has been carried out by the numerical method. Effects of void volume will be discussed by means of usual regenerator efficiency and also by means of the efficiency taking account of cooling capacity and expander work at the cold end.

BASIC EQUATION

The energy equation of fluid flow is written as

$$\frac{\partial}{\partial t}(\rho U) + \frac{1}{A} \frac{\partial}{\partial X}(\dot{m}H) = -q + \frac{\dot{m} \partial P}{\rho A \partial X} \quad (1)$$

where ρ is density, U is the internal energy, \dot{m} is the mass-flow rate, H is the enthalpy, A is the cross-section area and P is the gas pressure.⁵ Assuming an ideal gas for the working fluid and ignoring pressure drop, we can obtain next equation from the equation (1)

$$C_v \frac{\partial}{\partial t}(\rho AT) + C_p \frac{\partial}{\partial X}(\dot{m}T) = \frac{Q}{L} \quad (Q = -ALq) \quad (2)$$

Where C_p and C_v are specific heat at constant pressure and specific heat at constant volume respectively. T is temperature, L is total length of the regenerator and Q is total heat flow to the gas.

The heat flow Q is transferred from the matrix with temperature of T_s through the surface with area of S as follows.

$$Q = hS(T_s - T) \quad (3)$$

Temperature of the matrix with specific heat C_s and total volume V_s is defined by following equation.

$$Q = -C_s V_s \frac{\partial T}{\partial t} \quad (4)$$

Where, the axial heat conduction and radial temperature distribution of the matrix are ignored.

We can obtain temperature profile of the gas and the matrix by these equations along with the equation of continuity for the gas as follows.

$$A \frac{\partial \rho}{\partial t} + \frac{\partial \dot{m}}{\partial x} = 0 \quad (5)$$

In the case of constant pressure, the first term of the energy equation (1) is vanished, because the internal energy of the void volume does not change. Therefore the effect of the void volume appeared only on the equation of continuity. As a result, mass-flow rate varies along axial direction of regenerator.

Numerical calculation have been done using these five equations by means of finite difference. The accuracy of results is mostly depend on numbers of dividing pitch N_x for the variable x . N_x is chosen fixed number 600 because of time limitation of our computer system, although the results still have numerical error of several per cent.

DEFINITION OF THE EFFICIENCIES

The performance of regenerator is discussed on the model shown in Figure 1 in this paper. In the first half cycle, the cold gas flows into the left cold end with enthalpy $(mH)_{c1}$ and flows out from the right warm end with enthalpy $(mH)_{h1}$. The hot gas flows opposite direction during another half cycle.

Boundary conditions of the mass-flow rate at cold end \dot{m}_c and the pressure P as follows,

$$\dot{m}_c = \frac{\pi}{2} \dot{m}_m \sin\left(\frac{\pi t}{\tau_0}\right) \quad (6-A)$$

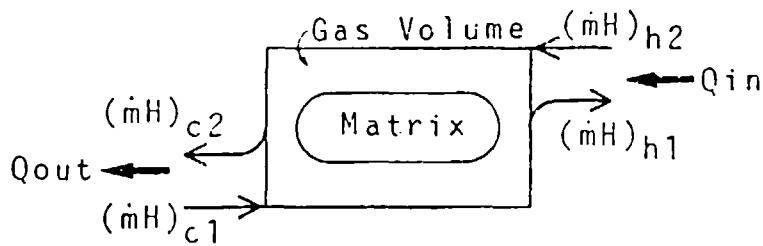


Fig. 1. Enthalpy flow of regenerator

$$P = P_m \left[1 + P_0 \sin\left(\frac{\pi t}{\tau_0}\right) \right] \quad (6-B)$$

for the case of sinusoidal variation. Where P_m is the mean pressure, P_0 is the amplitude for pressure and τ_0 is the half period of the cycle. \dot{m}_m corresponds to the mean value of the mass-flow rate. The pressure P describes the pressure of the gas in the regenerator for our case where the pressure drop is ignored.

In order to reduce parameters of the equations, it is convenient to use well known three parameters as follows.

$$\Lambda = \frac{hS}{\dot{m}_m C_p} \quad , \quad \Gamma = \frac{\dot{m}_m C_p \tau_0}{V_s C_s} \quad , \quad \Phi = \frac{V_g \bar{\rho} C_v}{V_s C_s} \quad (7)$$

Φ is proportional to the value of void volume and defined by using the density of gas at the mean temperature of hot and cold end in our case.

Following three similar type of efficiencies η_a , η_b , η_c and another type one η_x will be discussed later with results of the calculation.

$$\eta_a = \frac{(\dot{m}H)_{h1} - (\dot{m}H)_{c1}}{\dot{m}_m \tau_0 C_p (T_h - T_c)} \quad (8-A)$$

$$\eta_b = \frac{(\dot{m}H)_{h1} - (\dot{m}H)_{c1}}{(\dot{m}H)_{h2} - (\dot{m}H)_{c1}} = \frac{(\dot{m}H)_{h2} - (\dot{m}H)_{c2}}{(\dot{m}H)_{h2} - (\dot{m}H)_{c1}} \quad (8-B)$$

$$\eta_c = 1 - \frac{Q_{out}}{\dot{m}_m \tau_0 C_p (T_h - T_c)} \quad (8-C)$$

$$\eta_x = 1 - \frac{Q_{out}}{W_{exp}} \quad (8-D)$$

The first three formulas are defined as the usual definition of the efficiency for the regenerator, that is the ratio of the actual heat transfer rate to the maximum possible heat transfer rate. Where Q_{out} is the thermal loss at the cold end which corresponds to the excess enthalpy flow to the cold end in a cycle.

η_x is defined by the inefficiency which is the ratio of Q_{out} to the ideal expander work W_{exp} at the cold end. W_{exp} can be evaluate by pressure-volume integral. Therefor, η_x is a sort of the cycle efficiency.

$$\Lambda = 200 \quad \Gamma = 0.6 \quad T_h = 300K \quad T_c = 80K$$

$$\dot{m}_m = 1 \text{ g/sec} \quad f = 1 \text{ Hz}$$

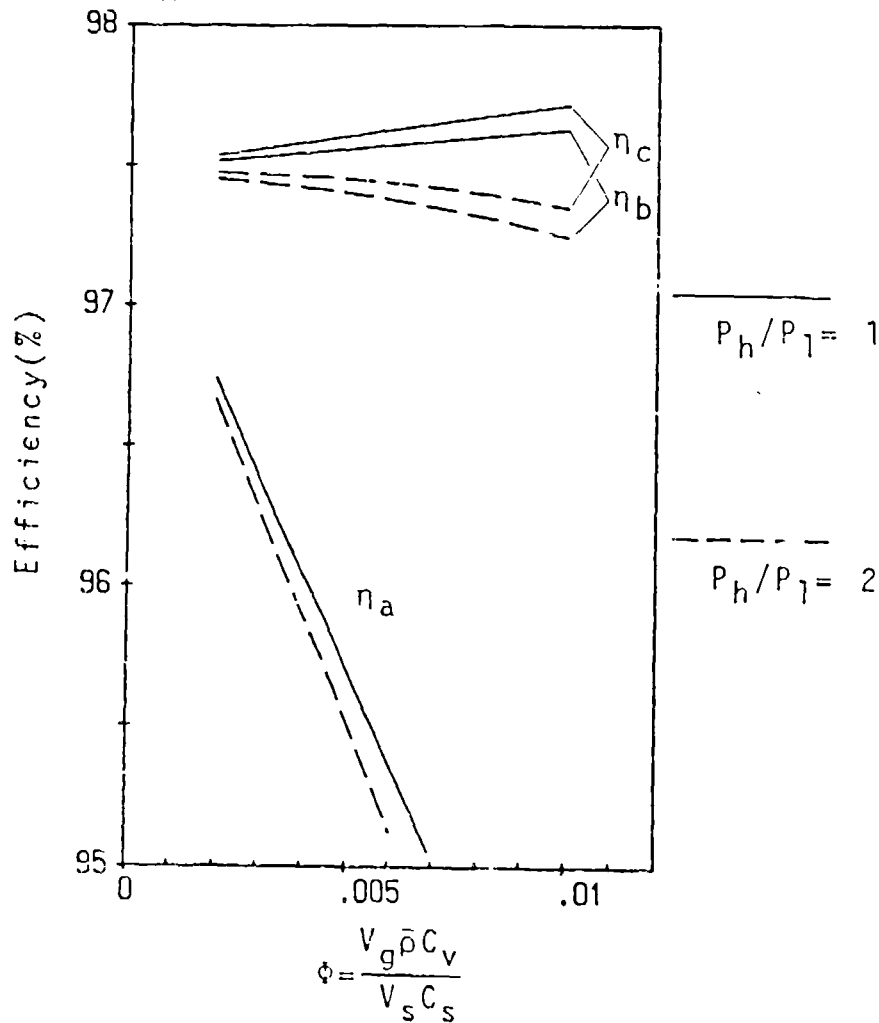


Fig. 2. Comparison of efficiencies defined by equation(8)

RESULTS AND DISCUSSION

Figure 2 shows a results of regenerator efficiencies as a function of ϕ for the case of $\Lambda=200$ and $\Gamma=0.6$. Solid lines show the case of the constant pressure and dashed line shows that of the sinusoidal pressure change with the pressure ratio of 2. η_b and η_c for the case of constant pressure increase with increasing void volume, which tendency has been predicted by D.Daney and R.Radabaugh.⁴ On the other hand, dashed line decrease with increasing void volume. In any case, it is found that the pressure change gives lower efficiency compare to the case of constant pressure with void volume, and that the efficiencies decrease with increasing void volume.

Figure 3 shows the effect of the pressure ratio with different fixed parameters. The efficiency decrease with increasing the pressure ratio. Changing value of the heat capacity ratio Γ moves the curve of the efficiency against pressure ratio mostly parallel. On the other hand, the effect of the pressure ratio on the efficiency is decreased by decreasing the void volume which is proportional to ϕ .

There is a cross point of the efficiency at the pressure ratio of about 1.7 in this particular case. This means if we use the pressure ratio below the cross point, the efficiency increases with increasing void volume.

The effect of the flow patterns which are shown in Figure 4 are summarized also in the figure along with the result from Hausen's equation which assumes constant pressure, constant mass-flow rate and no void volume. Both results are obtained by the sinusoidal pressure change with pressure ratio of 2. The efficiency of the trapezoidal mass-flow is better than of the sinusoidal mass-flow.

For the actual cryocooler, the ratio of the heat loss of the regenerator to the maximum possible cooling capacity of the cold end is useful for analysis and design. The efficiency defined as formula 8-D represents this ratio. Considering η_x , if the pressure is constant the expander work should be vanished, therefore the efficiency η_x does not mean anymore.

When the pressure and the mass-flow rate vary sinusoidally in phase, P-V diagram at the cold end is shown in Figure 5-b. The results of the

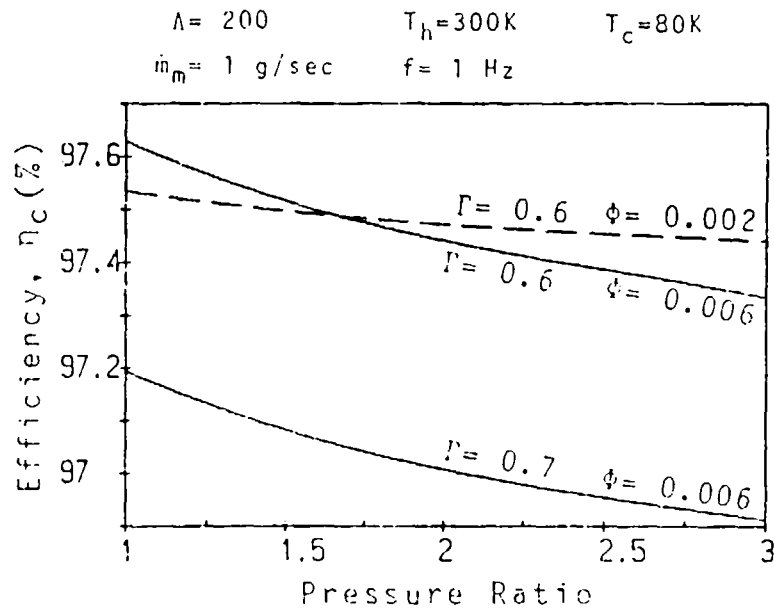


Fig. 3. Effect of the pressure ratio

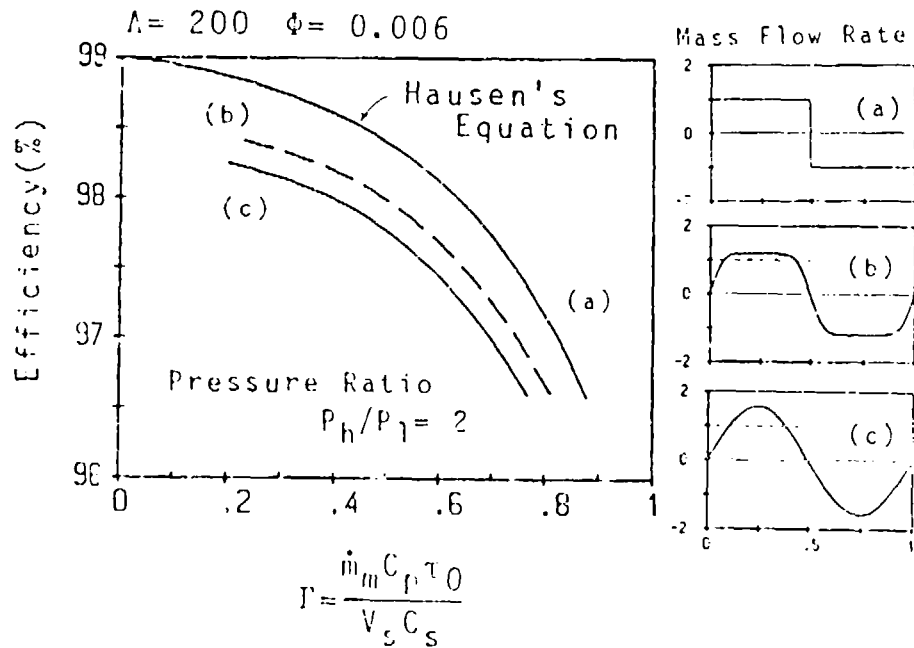


Fig. 4. Effect of the pattern of mass flow rate

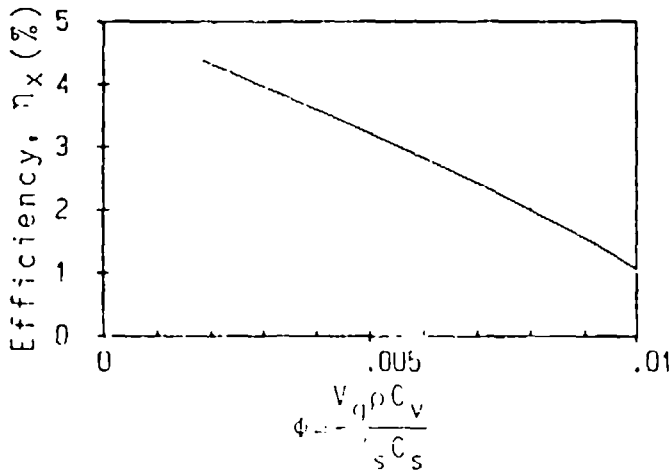
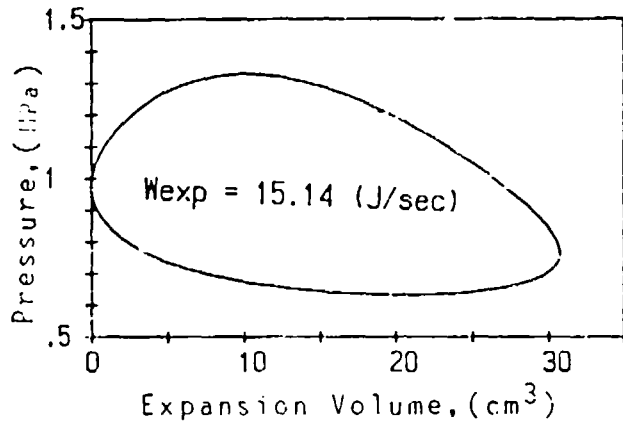
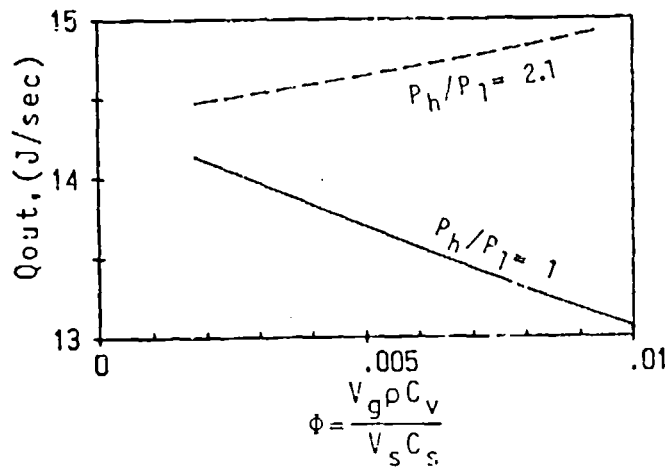


Fig. 5. Relation of the regenerator loss and the expansion work

net heat Q_{out} carried into the cold end by gas are shown in Figure 5-a and also the efficiency η_x is shown Figure 5-c. Although the results are obtained on the particular conditions, the efficiency η_x is decreasing with increasing void volume, which seems to agree with the experimental results.

CONCLUSIONS

The numerical calculation for the gas and the matrix of the regenerator has been carried out assuming the ideal gas and the constant specific heat of the matrix, and ignoring the pressure drop, but considering the void volume.

The fundamental study for the regenerator performance shows that the definition of the regenerator efficiency is very complex due to the effect of the void volume in the regenerator.

An approach using the ineffectiveness at the cold end of the regenerator is proposed, which introduces the efficiency η_c for the simple case and η_x as a cycle efficiency for a cryocooler.

The void volume may act as the heat transport media which induces the regenerator loss except the condition of the very low operating pressure ratio.

The approach mentioned in this paper could be applied to the non ideal gas and the actual matrix materials.

The difference of shape and the peak value of instantaneous mass-flow rate gives a significant change of the regenerator efficiency.

REFERENCES

- 1.H.Hausen, *Wärmeübertragung im Gegenstrom, Gleichstrom und Kreuzstrom*, Springer-Verlag, (1950)p.358
- 2.W.M.Kays and A.L.London, *Compact Heat Exchangers*, McGraw-Hill, (1955)p.44
- 3.R.F.Barron, *Cryogenic Systems*, p.276
- 4.D.E.Baney and R.Radebaugh, *Non-ideal regenerator performance-the*

effect of void volume fluid heat capacity, Cryogenics, vol.24,
(1984)p.499

5.R.B.Bird,W.E.Stewart and E.Lightfood, Transport Phenomena, John Wiley
& Sons, (1960)p.313

MEASUREMENT OF REGENERATOR PERFORMANCE IN A PULSE TUBE REFRIGERATOR*

Wayne Rawlins and K. D. Timmerhaus
University of Colorado
Department of Chemical Engineering
Boulder, Colorado

Ray Radebaugh
Chemical Engineering Science Division
National Institute of Standards and Technology
Boulder, Colorado

ABSTRACT

An apparatus has been constructed to measure the performance of regenerators in pulse tube refrigerators operating at pressures oscillating at frequencies between 5 and 30 Hz. The apparatus measures the ineffectiveness of a regenerator using either the liquid nitrogen boil-off method or the instantaneous enthalpy flow method. The latter method relies on measurements of the instantaneous mass flow rate, temperature, and pressure at both ends of the regenerator. This method required the design and use of devices able to measure temperature and mass flow rate at high speeds. The ineffectiveness of a regenerator in a pulse tube refrigerator has been evaluated using both methods.

INTRODUCTION

A regenerator is one of the primary components of an orifice pulse tube refrigerator and has a major effect on refrigerator performance. Regenerative heat exchangers have several advantages over recuperative heat exchangers in that they are compact and simple to construct and have high efficiencies and long lifetimes. An apparatus has been designed (see Fig. 1) and constructed to experimentally evaluate this performance.¹ Mass

*Research sponsored by NASA/Ames Research. Contribution of NIST, not subject to copyright.

flow rate in a pulse tube refrigerator is higher than that in a Stirling refrigerator; thus, the former requires better regenerator performance.² A single stage orifice pulse tube can achieve useful refrigeration and reasonable efficiencies at 77 K.^{3,4} This study examines the performance of a regenerator with the warm end at 300 K and the cold end at 77 K.

THEORY

Regenerator performance is generally specified in terms of regenerator effectiveness. This is defined as the dimensionless ratio of the actual heat transfer rate in the regenerator to the maximum possible

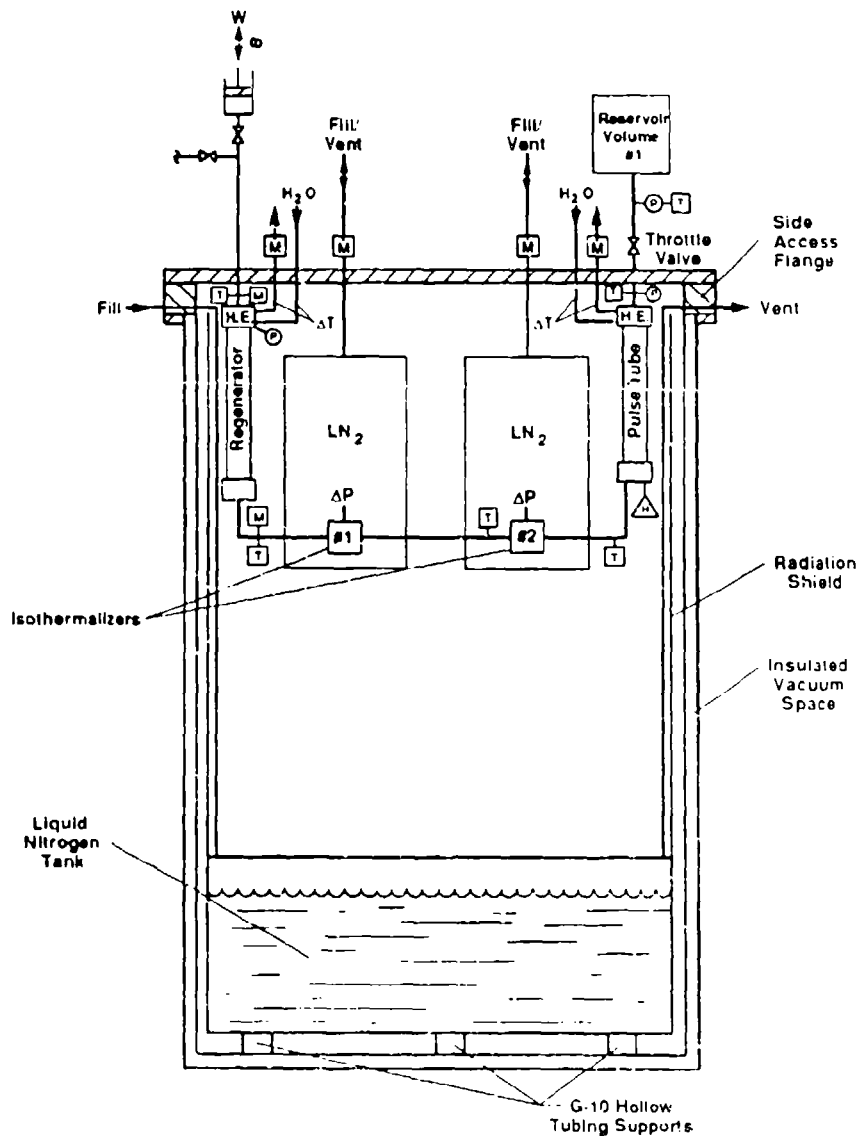


Fig. 1. Schematic of the apparatus designed to evaluate regenerator performance.

heat transfer rate^{5,6}, that is,

$$e = \frac{\dot{Q}_{act}}{\dot{Q}_{max}} = \frac{\text{actual heat transfer rate}}{\text{maximum possible heat transfer rate}} \quad (1)$$

To determine the effectiveness of a regenerator it is more convenient to define a regenerator ineffectiveness term given by^{1,6}

$$\lambda = 1 - e = \frac{\dot{Q}_{max} - \dot{Q}_{act}}{\dot{Q}_{max}} \quad (2)$$

If it is assumed that the heat capacities of the gas for the hot and cold periods of the regenerator operation are equal, the numerator of Eq. (2) becomes

$$\dot{Q}_{max} - \dot{Q}_{act} = \dot{m}C_p(\bar{T}_{h,o} - T_{c,i}), \quad (3)$$

where \dot{m} is the mass flow rate of the gas in the regenerator, C_p is the gas heat capacity, $T_{c,i}$ is the temperature of the cold gas entering the regenerator from the cold end, and $\bar{T}_{h,o}$ is the average temperature of the hot gas leaving the cold end of the regenerator. In terms of the specific enthalpy of the gas in the regenerator, h_r , Eq. (3) becomes

$$\dot{Q}_{max} - \dot{Q}_{act} = \dot{m}h_r(\bar{T}_{h,o}) - \dot{m}h_r(T_{c,i}). \quad (4)$$

This difference is the enthalpy flow through the regenerator and is equal to the heat load at the cold end of the refrigerator due to the regenerator ineffectiveness. Therefore,

$$\lambda = \frac{\dot{Q}_{reg}}{\dot{Q}_{max}}, \quad (5)$$

where \dot{Q}_{reg} represents this heat load. An energy balance for any differential section of the regenerator shows that the enthalpy flow is constant throughout the entire length of the regenerator, as long as there are no radiative or convective losses to the outside environment.

The heat load, or enthalpy flow, for an oscillatory system must be integrated over one full period; therefore, the ineffectiveness becomes

$$\lambda = \frac{\oint \dot{m}h_r dt}{\int_0^{P_c} \dot{m}_r h(T_U) dt - \int_{P_h}^{P_c} \dot{m}_c h(T_L) dt}, \quad (6)$$

where $h(T_U)$ is the enthalpy of the warm fluid entering the regenerator, $h(T_L)$ is the enthalpy of the cold fluid entering the regenerator, P_c and P_h are the durations of the cold and hot flow periods in the regenerator,

\dot{m}_c and \dot{m}_h are the absolute values of the mass flow rates into the regenerator at the cold and warm ends, and t is time. The denominator can be simplified if the system operates at constant pressure or the gas in the system is assumed to be ideal, because enthalpy for an ideal gas depends only on temperature. Mass flows at each end of the regenerator for a compressible fluid are not equal; thus, for convenience the mass flow measurement is referenced to the cold end of the regenerator. Equation (6) can then be simplified to

$$\lambda = \frac{\int \dot{m} h_r dt}{m[h(T_H) - h(T_L)]} \quad (7)$$

where m is the total mass of gas that flows in one half of the cycle at the cold end of the regenerator. Substituting heat capacities into Eq. (7) results in

$$\lambda = \frac{\int \dot{m} C_p T dt}{m[C_p(T_H) T_H - C_p(T_L) T_L]} \quad (8)$$

If a mean or constant value of C_p is assumed, Eq. (8) reduces to

$$\lambda = \frac{\int \dot{m} T dt}{m \Delta T} \quad (9)$$

where ΔT is defined as $T_H - T_L$. For an ideal gas, the heat capacity is independent of temperature and pressure. The numerator of Eq. (9) can be measured anywhere in the regenerator. It is convenient in the apparatus being used to measure it at the cold end of the regenerator.

Equations (5) and (9) suggest two different ways in which the ineffectiveness of the regenerator can be evaluated. The numerator of Eq. (5) can be calculated if the heat load at the cold end of the regenerator can be measured. The numerator of Eq. (9) can be determined if instantaneous measurements of the mass flow rate and temperature in the regenerator can be made. The maximum possible heat transfer rate can be calculated from the known boundary conditions and the measurement of the instantaneous mass flow rates over one cycle. In this study, for comparative purposes, the ineffectiveness is calculated using both relations.

DISCUSSION

The enthalpy flow in the regenerator can be measured directly with the apparatus. This is achieved with the use of laminar-flow heat

exchangers called isothermalizers. These are placed between the cold ends of the regenerator and pulse tube¹ (see Fig. 1). The isothermalizers are immersed in liquid nitrogen baths which isolate the excess enthalpy flow in the regenerator. This enthalpy flow is monitored by measuring the increase in the boil-off rate from the liquid nitrogen bath. A water-cooled heat exchanger at the warm end of the regenerator and the isothermalizer regulates the entrance conditions at both ends of the regenerator. Absolute pressure is also monitored at the warm ends of the regenerator and the pulse tube.

The mass flow rate at the cold end of the regenerator is determined experimentally by two different techniques. One method allows determination of the mass flow rate from the pressure drop across the isothermalizers and from the absolute pressure. The other method utilizes constant temperature anemometry.⁷ This technique infers mass flow rate from the measurement of the heat transfer from a heated wire. However, constant temperature anemometry is sensitive to temperature changes and requires corrections for any temperature fluctuations. Therefore, temperature is measured close to the anemometer with a resistance thermometer.⁸ Both the anemometer and the resistance thermometer are constructed from 4 μm platinum-coated tungsten wire. The wires are supported by specially designed probes inside the 3 mm stainless steel tubing connecting the regenerator to the pulse tube (see Fig. 2). The anemometer has a response time of approximately 20 μs while the resistance thermometer has a response time of approximately 260 μs . Such fast responses provide excellent resolution of the mass flow rate and temperature. These measurements, in turn, permit evaluation of the effectiveness, number of transfer units, pressure drops, and friction factors in the regenerator. Initial regenerator ineffectiveness values, calculated from Eqs. (5) and (9), as

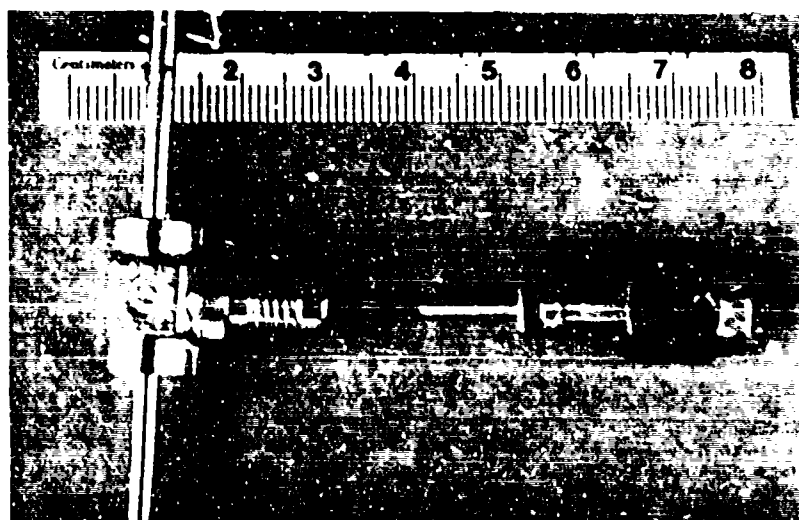


Fig. 2. Photograph of the modified tungsten resistance probe and the modified vacuum fitting.

well as the uncalibrated output from the anemometers are provided in the following section.

RESULTS

The test apparatus with helium as the working fluid was operated at a mean pressure of 2.2 MPa. The warm end of the regenerator was cooled with water to 290 K and the cold end of the regenerator was cooled to liquid nitrogen temperatures. For these operating conditions helium gas closely follows ideal gas behavior and the assumptions leading to Eq. (9) are valid. The compressor supplying the oscillating pressure in the refrigerator has a swept volume of 25 cm³ and was run at 7.0 Hz. The test regenerator was 100 mm long and was constructed from 304 stainless steel tubing with a diameter of 15.9 mm and a wall thickness of 0.3 mm. The heat storage matrix in the regenerator was made from stacked disks of 304 stainless steel wire cloth woven from 0.053 mm diameter wire. The wire cloth has 7.9 openings per millimeter. The porosity of the matrix, defined as the matrix's open cross sectional area divided by the regenerator cross sectional area, is 0.63. The orifice is an adjustable metering valve and was opened three turns.

A plot of dynamic mass flow rate as calculated from the pressure drop across the isothermalizer and the gas temperature at the cold end of the regenerator is presented in Fig. 3. The total mass moved through the cold end of the regenerator during one-half cycle was 4.8 mg. The additional liquid nitrogen boil-off, due to the passage of gas through the isothermalizer, was 0.827 mg/cycle. This boil-off represents an average heat load rate of 1.1 W. With assumptions of fixed boundary temperatures (the upper end cooled with water to 290 K and the lower end at 80 K, from an average value of Fig. 3) and constant heat capacity, the ineffectiveness of the regenerator was computed to be 0.032 using Eq. (5).

In Fig. 3 negative flow rates represent gas flowing out of the cold end of the regenerator and positive flow rates represent gas flowing into the cold end of the regenerator. The plot shows conclusively that the temperature of the fluid flowing into the regenerator is not isothermal as was originally assumed. Heating and cooling jumps of the gas occur shortly after the flow reversal at the cold end when the mass flow rate is low. These are due to the non-negligible void volume of the connecting tubing. The jumps are linked by relatively isothermal regions that fluctuate approximately only ± 0.5 K. Multiplying the mass flow rate by the temperature and integrating the product over a cycle allows evaluation of the numerator in Eq. (9). The ineffectiveness calculated thus is 0.0097, a factor of three lower than the previous calculation. This disagreement between values of effectiveness needs further investigation. The dynamic enthalpy fluctuation, calculated by multiplying the above product by the heat capacity is shown in Fig. 4. The average enthalpy rate from this plot is 0.35 W, again lower by a factor of three than that calculated by the boil-off method.

Figure 5 shows the simultaneous output of the voltage from the

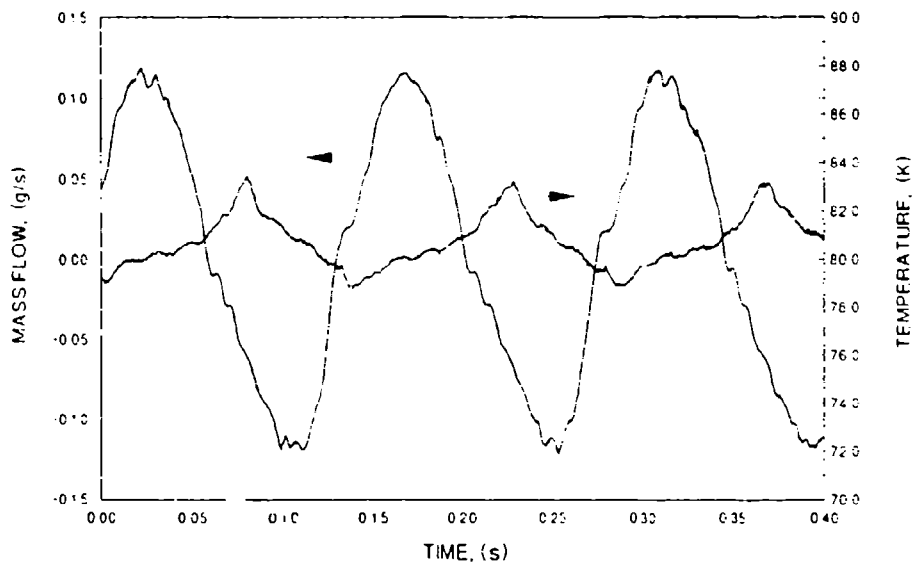


Fig. 3. The gas temperature and mass flow at the cold end of the regenerator.

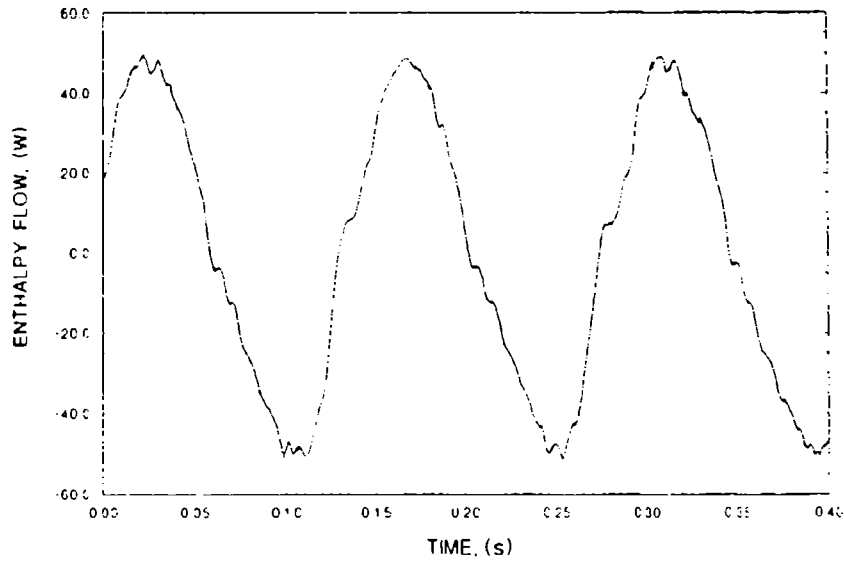


Fig. 4. Plot of the instantaneous enthalpy flow at the cold end of the regenerator.

anemometer and the absolute value of the mass flow rate as functions of time. This plot reveals the fast response of the anemometer and its capability of resolving turbulence in the 3 mm tubing following the regenerator. A comparison of the maximum and minimum outputs for the two different sensors shows a phase discrepancy between the flow readings. The minimum anemometer voltage output, representing zero flow, is not constant. This is attributed to fluctuations in temperature at the sensor and clearly demonstrates the need for temperature measurement for correction of the readings from the anemometer as well. Figure 6 shows the measured absolute pressure at the warm ends of the regenerator and pulse tube and the difference between these two pressures.

CONCLUSION

Real-time measurements of the important operating parameters in an orifice pulse tube refrigerator have been achieved. Initial measurements have yielded a value for the ineffectiveness of the regenerator during actual refrigerator operation. A more careful comparison of the boil-off and instantaneous enthalpy flow methods for measuring ineffectiveness needs to be performed. The measurements also allow evaluation of the dynamic pressure drop and friction factor in the regenerator.

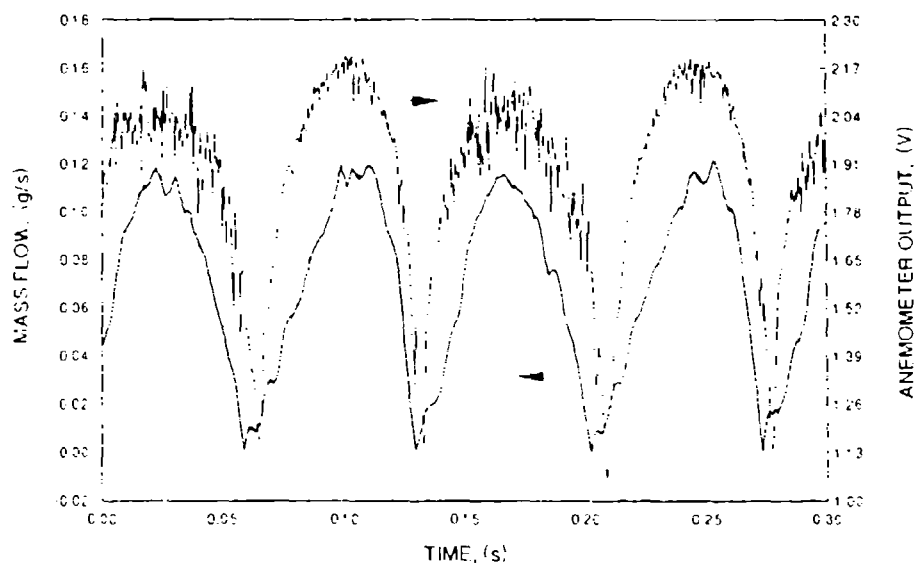


Fig. 5. Simultaneous output of the voltage from the anemometer and the absolute value of the mass flow rate as calculated from the pressure drop across the isothermalizer at the cold end of the regenerator as functions of time.

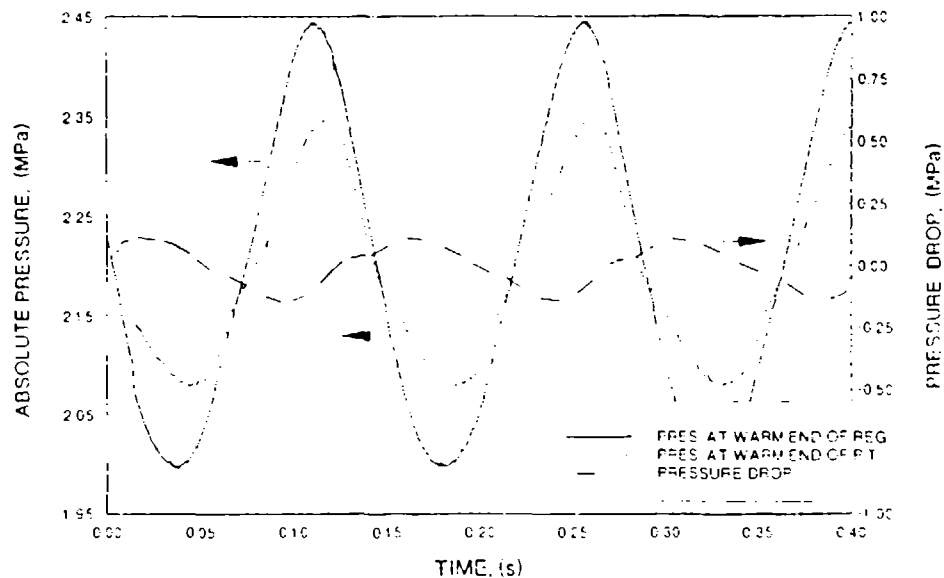


Fig. 6. Absolute pressure at the warm end of the regenerator and pulse tube and the difference of these two pressures as functions of time.

REFERENCES

1. W. Rawlins and R. Radebaugh, "An Apparatus for the Measurement of Regenerator Performance in Pulse Tube Refrigerators," Advances in Cryogenic Engineering, Vol. 35, Plenum Press, New York, 1990, p. 1213.
2. R. Radebaugh and S. Herrmann, "Refrigeration Efficiency of Pulse Tube Refrigerators," Proceedings of the Fourth International Cryocoolers Conference, 1986, p.119.
3. R. Radebaugh, J. Zimmerman, D.R. Smith, and B. Louie, "A Comparison of Three Types of Pulse Tube Refrigerators: New Methods for Reaching 60 K," Advances in Cryogenic Engineering Vol. 31, Plenum Press, New York, 1986, p. 779.
4. R. Radebaugh, K. Chowdhury, and J. Zimmerman, "Optimization of a Pulse Tube Refrigerator for a Fixed Compressor Swept Volume," Proceedings of the Fifth International Cryocoolers Conference, 1988, p. 113.

5. W.M. Kays, and A.L. London, Compact Heat Exchangers. McGraw-Hill, New York, 1984.
6. R. Radebaugh, D. Linenberger, and R.D. Voth, "Methods for the Measurement of Regenerator Ineffectiveness," Refrigeration for Cryogenic Sensors and Electronic Systems, NBS Special Publication 607, 1981, p. 70.
7. A.E. Parry, Hot Wire Anemometry, Clarendon Press Oxford, 1982.
8. W. Rawlins, R. Radebaugh, and K.D. Timmerhaus, "Monitoring Rapidly Changing Temperatures of the Oscillating Working Fluid in a Regenerative Refrigerator," to appear in Applications of Cryogenic Technology, Proceedings of Cryo '90, Plenum Press.

CERAMIC COMPOSITE REGENERATOR MATERIALS

W.N. Lawless
CeramPhysics, Inc.
921 Eastwind Drive, Suite 110
Westerville, Ohio 43081

ABSTRACT

A concept is discussed for inexpensive and durable composite materials for regenerator applications which have specific heats equivalent to, or larger than, the recently developed Er-based alloys. These composites involve loading powders of spin-frustrated magnetic spinels into a cesium iodide matrix. Powders are used because a grain-size effect broadens the very large specific heat maxima of the spinels. Additionally, the specific heat maxima of the spinels can be temperature-shifted by doping. Thermal data on the spinels and CsI are presented. Cesium iodide was chosen for its metallic-like thermal conductivity at low temperatures and for its ease of fabrication.

INTRODUCTION

The volumetric specific heat of the regenerator matrix material plays a crucial role in determining the power-temperature characteristics of regenerative cryocoolers.¹ Such cryocoolers operating in the He-temperature range and using Pb spheres in the regenerator are widely used in cryopumps, shield-cooling of MRI magnets, etc. However, the specific heat of Pb decreases rapidly below about 15 K, in contrast to the specific heat of pressurized He gas. As a result, the power-temperature curves of these cryocoolers also decrease rapidly below this temperature.

The Gd-Rh alloys have larger specific heats than Pb below 15 K and were introduced in 1975 as potential regenerative materials.² However, these alloys are very expensive and difficult to fabricate. More recently, researchers in Japan have developed Er-based alloys for regenerator applications.³ These alloys can be fabricated into spheres³ which result in improved regenerator efficiencies compared to Pb spheres.⁴ Although these Er-based alloys are less expensive than the Gd-Rh alloys, materials costs are still high, and brittle-fracture problems have been observed in regenerator operation.⁵

This paper describes a new ceramic-composite approach to regenerator materials. The volumetric specific heats of these composites may be considerably larger than those of the Er-based alloys in certain temperature ranges below 15 K, and materials costs are about 50 times smaller.

CERAMIC-COMPOSITE MATERIALS

The ceramic materials central to this approach have two phases; the major phase is a chromite spinel exhibiting a high degree of spin-frustration, which contributes to a very large specific heat. The minor phase promotes ceramic formation, which otherwise does not occur. Inexpensive oxide powders are used to make these materials.

Applied programs aimed at the enthalpy-stabilization of Nb_3Sn ⁶ and of $NbTi$,⁷ as well as fundamental physics studies of spin-frustration,⁸ have been based on these ceramics. Following the usage in these previous programs, these ceramics are here designated as "SCIC" and "SCID".

Volumetric specific heat data for the SCIC and SCID ceramics are compared in Fig. 1 to data for the Er-based alloys, GdRh, and Pb. These ceramics have very large specific heat maxima ($\sim 1.5 \text{ MJ m}^{-3} \text{ K}^{-1}$) at 8 and 10.7 K, respectively, which are independent of fields up to 15 T.⁶

The temperatures of the specific heat maxima of these ceramics can be shifted by doping, and an example of this is shown in Fig. 1 for a 2%-Fe doped SCIC ceramic (6.3 K). The dopants V, Mo, and Gd are effective in raising the peak temperature of SCID about 3.5 K.⁸

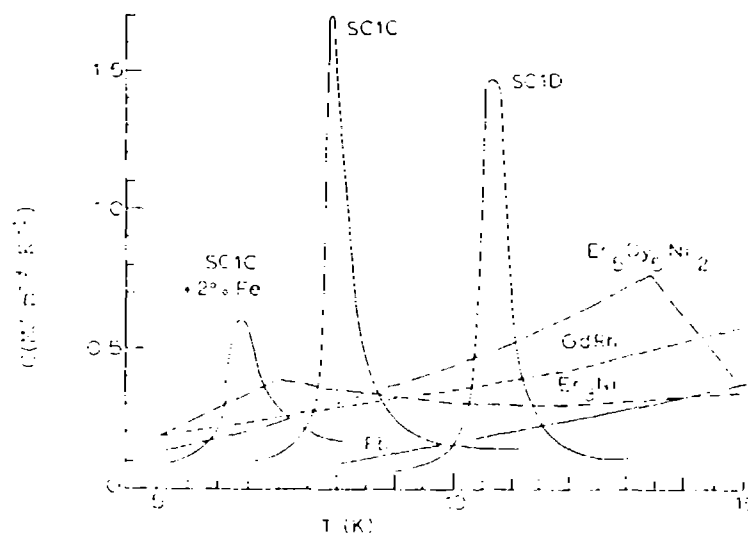


Fig. 1. Volumetric specific heat data for the SCIC and SCID ceramics in bulk form compared to GdRh, Pb, and two of the Er-based alloys. An example of 2% Fe-doping in the SCIC ceramic is also shown.

Although no studies have yet been made of these ceramics as regenerator materials, a large specific heat database exists on these ceramics under different conditions.⁶⁻⁸ Examples of some volumetric specific heat data from these earlier programs are collected in Fig. 2 compared to GdRh. For the ceramics shown in Fig. 2 the specific heat maxima range from $0.25 \text{ MJ m}^{-3} \text{ K}^{-1}$ at 5.9 K to $3.0 \text{ MJ m}^{-3} \text{ K}^{-1}$ at 12.3 K (truncated in Fig. 2, sample e).

Of particular importance to the composite approach, it has been found that the specific heat maxima of these ceramics can be "broadened" by grain size (independent of doping). An example of this broadening is shown in Fig. 2 for a very fine-grain powder of SC1D (sample f).

The SC1C and SC1D ceramics are very hard and tough materials from which small spheres ($\sim 2 \times 10^{-4} \text{ m}$ diam) can be made by a gravel process⁹ or other methods.¹⁰ Therefore, it would be possible to use a series of the ceramics shown in Fig. 2 in a "graded" regenerator wherein the spatial distribution of the spheres is chosen to match the heat capacity to the temperature distribution across the regenerator.

However, preliminary testing of SC1C spheres in a regenerator⁵ has shown time-dependent phenomena. This is due to the very small thermal conductivities of these ceramics, which limit the frequency at which the cryocooler can be operated. Thermal conductivity data for the SC1C and SC1D ceramics are shown in Fig. 3; owing to the very large specific heats of these ceramics (Fig. 1) the thermal diffusivities are very small in the neighborhood of the specific heat

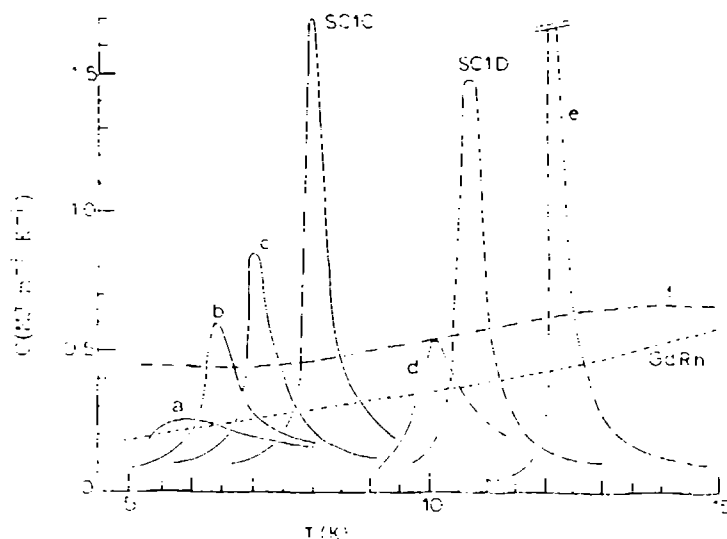


Fig. 2. Examples of volumetric specific heat data measured on ceramic samples from previous programs compared to data for GdRh. The sample identifications are: a, b, and c are Fe-doped sample of SC1C; d is a Nb-doped sample of SC1D; e is a high-purity SC1D sample; and f is a very fine-grain powder of SC1D (140 Angstrom).

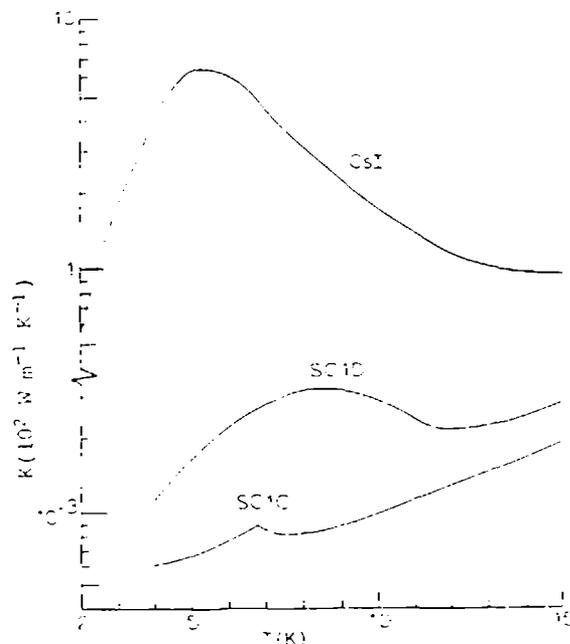


Fig. 3. Thermal conductivity data for the SC1C and SC1D ceramics and for CsI (note scale break). The ceramics have very small conductivities, whereas CsI has a near-metallic thermal conductivity.

maxima. This hinders the ability to make use of the large specific heats of these ceramics in the regenerator application.

The small thermal conductivities (diffusivities) of these ceramics suggest a composite approach, wherein the ceramic powders are dispersed into a high-thermal-conductivity matrix material at about the 65 vol% level (to insure connectivity in the matrix material). This approach has the additional benefit that the grain size of the powder can be used to broaden the specific heat maxima, as illustrated in Fig. 2 (sample f).

The matrix material should ideally have a large thermal conductivity and a large specific heat, and small spheres of the composite should be easily fabricated and durable. Cesium iodide appears to satisfy these requirements. Thermal conductivity data for CsI¹¹ are shown in Fig. 3, and one can see that this material has a near-metallic thermal conductivity at low temperatures. The T^3 -boundary scattering limit shown in Fig. 3 for CsI below 4 K corresponds to a phonon mean free path $\sim 3 \times 10^{-4}$ m.¹¹ In the ceramic-composite spheres suggested here this mean free path might be shortened and lead to somewhat suppressed thermal conductivity values, but these values would still be about 10^3 times larger than those of the ceramics.

Volumetric specific heat data for CsI¹¹ below 15 K are compared in Fig. 4 with Pb. This halide has a relatively large specific heat — about 3 to 4 times

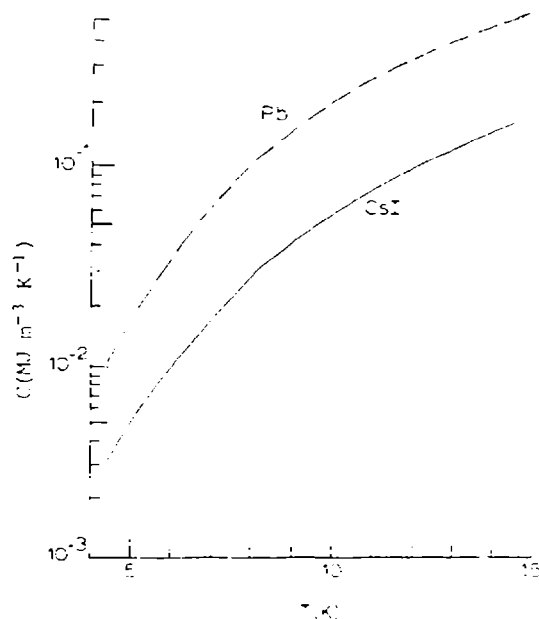


Fig. 4. Volumetric specific heat data for CsI compared to Pb.

smaller than Pb on a volumetric basis. Thus the specific heat of CsI in the composite would complement somewhat the very large specific heat of the embedded ceramic powder.

The fabrication of composite spheres using CsI as the matrix material should be straightforward, since CsI is ductile and can be hot-pressed to transparency at temperatures somewhat above room temperature.

DISCUSSION

A concept has been put forward here to embed powders of the SCIC and SCID ceramics in a CsI matrix to form composite spheres for regenerator applications. The positions of the specific heat maxima in these ceramics can be adjusted by doping, and the grain size of the powders in the composite can be used to broaden the maximum range. The CsI matrix has a large thermal conductivity, a complementary large specific heat, and is ductile enough to be fabricated by standard ceramic techniques near room temperature.

Both the thallos and cesium halides have large thermal conductivities and specific heats at low temperatures, but CsI has the largest thermal conductivity.¹¹ Moreover, CsI is the least expensive of these halides and is non-toxic. Cesium iodide is also favored from a hardness viewpoint, since in general the compressibility varies as the inverse square root of the Debye temperature¹² and the cesium halides have larger Debye temperatures (~ 150 K) than the thallos halides (~ 100 K)¹¹ or Pb (80 K).¹²

In this paper it was assumed that thermal resistance between the ceramic grains and the CsI matrix in the suggested composites will be minimal. However, there is some evidence that a Kapitza thermal resistance can occur at the interface between dissimilar solids at temperatures as high as 15-20 K due to acoustic-impedance mismatch.¹³ Testing will be needed to determine if such a mismatch exists in the composites suggested here.

Finally, enhancements in the specific heat at low temperatures have been observed in metals at very small particle sizes,¹⁴ and these enhancements may also play a role in the powders embedded in the composites discussed here.

In conclusion, the composites suggested here as regenerator materials may involve low materials costs, inexpensive fabrication methods, and larger regenerator heat capacities than are possible with either the GdRh or Er-based alloys. Research is needed, however, on the grain-size dependence of the specific heats of the ceramics and on the low-temperature thermal properties of the composites.

REFERENCES

1. G. Walker, *Cryocoolers* (Plenum Press, New York, 1984).
2. K.H. Buschow, J.F. Olijhoek, and A.R. Miedema, *Cryogenics*, May 1975, p. 261.
3. M. Sahashi, Y. Tokai, T. Kuriyama, H. Nakagome, R. Li, M. Ogawa, and T. Hashimoto, *Adv. in Cryogenic Eng.* 35, 1175 (1990).
4. R. Li, O. Yoshida, T. Hashimoto, T. Kuriyama, and H. Nakagome, *Adv. in Cryogenic Eng.* 35, 1183 (1990).
5. R.A. Ackerman, private communication.
6. Wright Patterson AFB Contracts #F33615-82-C-2227, -82-2229, -84-2418, and -86-2637; see also W.N. Lawless, C.F. Clark, and T.K. Gupta, *Adv. in Cryogenic Eng.* 30, 433 (1984).
7. NASA Contract # NAS1-18279. See also W.N. Lawless, C.F. Clark, and R. Boom, *Proc. 12th Int'l Cryogenic Eng. Conf.*, Southampton, 1988 (Butterworth & Co. Publ., Ltd.), p. 864.
8. Bolling AFB (AFOSR) Contracts #F49620-83-C-0129 and -86-C-004.
9. W.N. Lawless (unpublished).
10. J.N. Paranto and C.E. Patton, *Rev. Sci. Instrum.* 52, 262 (1981).

11. W.N. Lawless, Phys. Rev. *B30*, 6057 (1984).
12. E.S.R. Gopal, *Specific heats at low temperatures* (Plenum Press, New York, 1966).
13. K.W. Garrett and H.M. Rosenberg, J. Phys. D: Appl. Phys. *7*, 1247 (1974).
14. G.H. Comsa, D. Heitkamp, and H.S. Rade, Solid State Comm. *24*, 547 (1977).

Session IVA — Stirling Coolers I

Chairperson: Daniel Lehrfield, Magnavox

Co-Chairperson: Ron Ross, JPL

Session IVB — Joule-Thomson Coolers I

Chairperson: Javier Venesuala, Creare, Inc.

Co-Chairperson: John Barclay, ACA

Stirling Cooler Optimization

David Gedeon
Gedeon Associates
16922 South Canaan Road
Athens, Ohio 45701
(614) 592-5166

ABSTRACT

Stirling-cycle cryocoolers are accurately modeled with a one-dimensional finite-difference code named GLIMPS, and optimized with an adjunct program GLOP, which stands for GLimps OPTimization. GLOP is new, but GLIMPS has been in commercial use for a number of years. Both programs run on a personal computer. The GLIMPS cycle analysis includes realistic heat transfer and pressure drops in the heat exchanger as well as a number of parasitic loss calculations such as displacer leakage, shuttle heat transfer, cylinder-wall conduction, etc. The GLOP optimization driver can maximize efficiency (or any other objective function) subject to an arbitrary number of equality or inequality constraints. In practice, GLOP has produced designs for conventional one- and two-stage Stirling coolers and an orifice pulse-tube cooler. Some of these designs have been fabricated and tested.

OPTIMIZATION IN GENERAL

A simple quadratic function of two variables $f(x, y)$ might generate a surface as shown in figure 1. In unconstrained optimization we seek the point (x, y) for which f is minimum. The function f is called the *objective function*.

In constrained optimization we still seek the minimum f but restrict the search domain using *equality constraints* of the form $c(x, y) = 0$ or *inequality constraints* of the form $c(x, y) \geq 0$. For example, figure 2 shows the view from above at the quadratic objective function $f(x, y) = 2(x^2 - xy + y^2) + 6x$, subject to the linear inequality constraint $x + y > -1$.

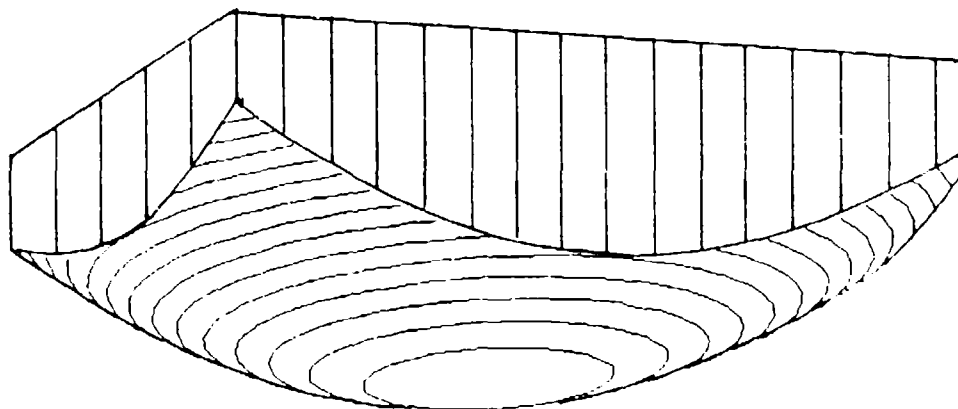


Figure 1: A typical surface generated by a quadratic function of two variables. The global minimum is evident.

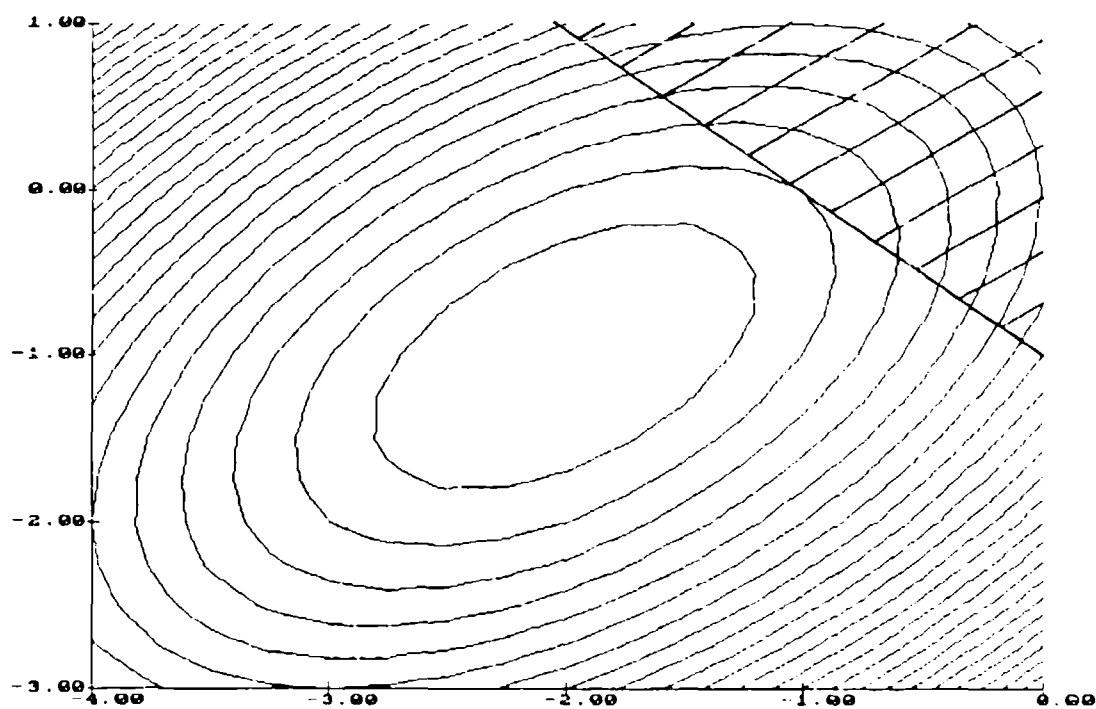


Figure 2: Level curves for the quadratic function $f(x, y) = 2(x^2 - xy + y^2) + 6x$ with the feasible region $x + y > -1$ shaded. The constrained minimum is, evidently, not the global minimum.

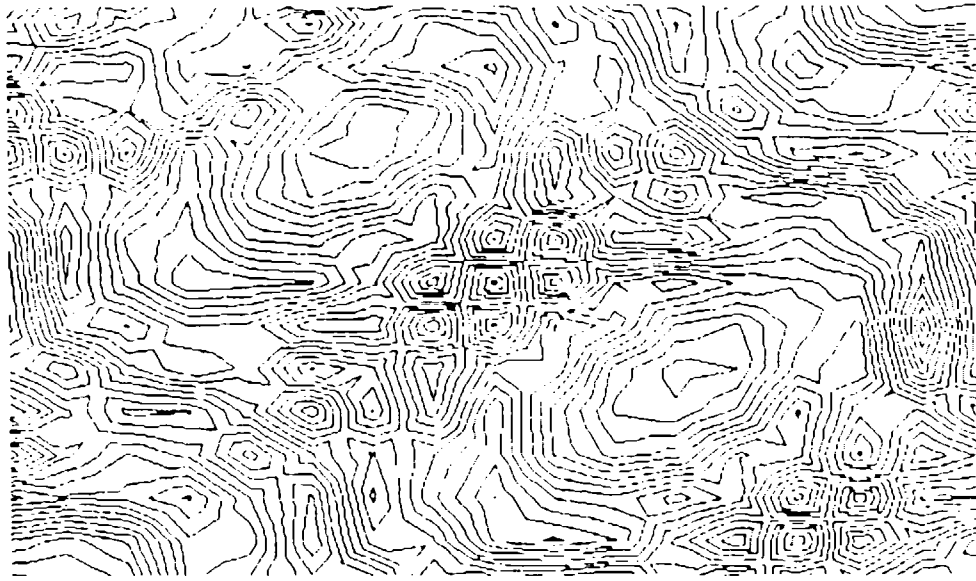


Figure 3: Level curves for a pathological objective function — unlike, we hope, a Stirling objective function.

When the search domain comprises more than two independent variables, we can no longer visualize the problem so easily, but the mathematical techniques for solving the problem are readily extended.

In optimizing Stirling cryocoolers we are faced with a objective function of many independent variables and usually several complicated constraints. The independent or *optimization* variables are things like geometrical specifications, temperatures, pressure and frequency. The objective function may be something like “efficiency” or “coefficient of performance”, both of which are a good deal more complicated than a simple quadratic function of the optimization variables. And the constraints may range from simple matters like “frequency equals 60 Hz”, to nonlinear interrelationships among variables like “net heat lifted equals 1 W”. Problems of this sort are known in optimization parlance as *general nonlinear programming problems*.

The question is: Does a typical **Stirling** objective function look similar to the quadratic function in figure 1, or does it look more like the pathological function in figure 3? If the latter, we are surely doomed. Fortunately, the answer is that **Stirling** objective functions tend to look more like figure 1. They are by no means simple quadratic functions, but there is generally only one peak to climb. The reason for this is that the optimization variables tend to cluster in small subsets of tightly coupled variables with only loose coupling between subsets. For example, dimensions for individual heat exchangers tend to be tightly coupled to other dimensions for the same heat exchanger, but loosely coupled to dimensions for other heat exchangers.

or to overall system dimensions like frequency or pressure. The upshot of this is that **Stirling** optimizations, while not trivial, are not all that difficult either.

THE STIRLING MODEL

The first requirement of optimization is for a mathematical model to represent the physical system to be optimized — in this case a **Stirling** cooler. The requirements for this model are that it be

1. Precise and repeatable
2. Reasonably fast
3. Including all significant phenomena

The reason for the first requirement is that optimization drivers are confused by noise in the objective function or constraint calculations. *Precision* here is used in the sense of minimum random fluctuation when the model is evaluated for nearby points, rather than the sense of absolute accuracy and fidelity to the physics. Accuracy and fidelity are part of the third requirement which is necessary if the optimization driver is to avoid drifting off into a region of the search domain where omissions in the model, previously thought to be minor, grow to catastrophic proportions.

I use the commercially available GLIMPS **Stirling** simulation model for my optimization work. This choice is not entirely surprising since I wrote the code, but it does seem to do a good job meeting the above requirements, and it has been in use long enough that its performance on a wide range of **Stirling** devices is well understood and documented.

The GLIMPS simulation algorithm is described in detail in reference 1. In broad strokes it is a personal-computer based finite-difference solution of the one-dimensional compressible gasdynamic equations plus the regenerator matrix solid energy equation. GLIMPS uses empirical formulations for friction factors and heat transfer coefficients in the **Stirling** heat exchangers as well as the expansion and compression space. The program derives its name from a loose acronym of "globally implicit simulation" which refers to its solution method whereby all space and time nodes of the computational grid are solved simultaneously in light of a time-periodic boundary condition. This feature allows GLIMPS to avoid the error introduced by the regenerator matrix slowly evolving to thermal equilibrium: — but never quite getting there — which plagues conventional time-stepping solution methods. The GLIMPS code comprises several separately-compiled and distinct Pascal *units* which may be linked together in various ways — a sort of library of **Stirling** model subroutines from which one may freely draw.

The GLIMPS model also includes a postprocessing stage wherein loss mechanisms and features external to the Stirling working gas may be factored into the objective function. This ability is very important in optimizations where the internal Stirling cycle is typically only a small part of a larger system. Most postprocessing needs are met by calls to a library of external-loss subroutines, another Pascal unit. Within this loss library are routines for calculating:

- Heat leakage down cylinder walls
- Gas leakage through seals between various spaces
- Displacer shuttle heat transfer
- Displacer appendix gap enthalpy losses due to pressure induced pumping and seal leakage
- Gas spring hysteresis loss
- Pumping loss in split-cycle connecting lines
- Secondary fluid performance for plain-tube as well as shell-and-tube heat exchangers
- Fin efficiency for finned heat exchangers
- Dynamic force-balance analysis for free (non-kinematic) pistons and displacers

THE OPTIMIZATION DRIVER

The second requirement for optimization is a controlling program to drive the optimization process. The driver I use is based on a sequential quadratic programming method developed by M. J. D. Powell². The Powell method solves the general nonlinear programming problem as a sequence of quadratic-programming subproblems (quadratic objective function and linear constraints). The idea is that in a localized region about any point in the search domain, a nonlinear problem resembles a quadratic programming problem. Powell shows how to use information from the actual nonlinear problem to define, and successively refine, a sequence of approximate quadratic problems, the solutions of which converge to the solution of the general nonlinear problem.

Powell leaves the choice of quadratic programming solver unspecified. After a review of the literature, I selected the dual-space method for strictly convex problems developed by D. Goldfarb and A. Idnani³. They specifically recommend use of their method with the Powell algorithm and report good performance.

GLOP

I coded the Powell method, as well as the Goldfarb and Idnani quadratic programming method, from scratch in Pascal as a number of separate program units which are linked together with units from the GLIMPS model into a complete executable program. I refer to the combination of the GLIMPS model and the optimization drivers as GLOP, which stands for GLIMPS optimization. GLOP runs under MS-DOS on a personal computer and can efficiently dispatch problems comprising up to about thirty optimization variables, with up to about the same number of combined equality and inequality constraints.

GLOP is structured for ease of use yet flexibility. All the code which has to do with the optimization driver and GLIMPS model is fixed in a number of pre-compiled units. The code which has to do with those aspects of the problem specific to the particular machine being optimized resides in a separate, relatively simple, program unit known as the *machine-specific* unit. The machine-specific unit is the only unit the GLOP user needs to modify to customize GLOP to his particular application. It has separate procedures in which one specifies the optimization variables, does postprocessing (generally by calls to the parasitic-loss library), calculates the objective functions and constraints, and appends any desired output to the default GLIMPS output listing. Pascal programming is required, but it is structured and usually amounts to making relatively minor modifications to existing examples.

Although GLOP came on-line only recently (early 1990), it has already optimized several **Stirling** coolers. Among these are:

- A 20 K, 200 mW, two-stage (stepped-displacer), free-displacer cooler
- A 65 K, 1 W, split-cycle, free-displacer cooler
- A 80 K, 300 W, split cycle, kinematic cooler
- A 255 K, 300 W, free-displacer, low-lift heat pump

A few GLOP-designed coolers have been fabricated and tested and feedback suggests they are performing well. Of course, validation and improvement of the GLIMPS model, especially in the sub 65 K realm, is an ongoing process.

Nonstandard **Stirling** coolers, like two-stage coolers or orifice pulse tubes, fall outside the standard GLIMPS model. However, they too can be successfully modeled and optimized within GLOP by using constraints to formulate various special boundary conditions in terms of standard GLIMPS variables. More on this later on.

Cryocoolers that are more non-**Stirling** than pulse tubes — those having a completely alien thermodynamic cycle — cannot be modeled with GLOP. However, the optimization-specific modules within GLOP don't care whether the objective function and constraints are **Stirling**-based or otherwise, and *could* be pressed into service for optimizing non-**Stirling** coolers. All that would be required would be to replace the GLIMPS thermodynamic model with the appropriate non-**Stirling** counterpart. The optimization-specific modules of GLOP are commercially available for this purpose.

THE POWER OF CONSTRAINTS

All realistic **Stirling** system optimizations involve constraints. A simple system might have only a few. A complex system may have dozens. To give some idea of the nature of these constraints, what follows is a compendium of examples, arranged in general categories. All of these come from actual examples formulated at one time or another within GLOP's machine-specific unit.

A typical constraint is written as a Pascal expression which is evaluated as a function of the optimization variables. The evaluation may involve a long sequence of computations (such as the GLIMPS simulation), but eventually winds up as a real numerical value, either positive, negative or zero. The optimization driver has the task of tweaking the optimization variables to force the constraint value to zero, in the case of an equality constraint, or merely non-negative, in the case of an inequality constraint.

ENERGY BALANCE

In most cases, the net amount of heat lifted at the cold end is a fixed specification for a **Stirling** cooler optimization. Accordingly, a typical equality constraint might be:

$$\text{constraint} = Q_{\text{actual}}/Q_{\text{required}} - 1;$$

where Q_{required} is the fixed target heat lifted and Q_{actual} is the actual value computed by the thermodynamic model. When the expression on the right evaluates to zero, the heat lifting is correct.

GEOMETRICAL

The pieces of a Stirling cooler must all fit together geometrically. For example, the regenerator plus heat rejector length might be equal to the displacer length. Or the regenerator frontal area might be related to some other frontal area. These sorts of things may be formulated as an equality constraints.

SUBSYSTEMS

Electric drive motors, secondary coolant loops, springs, etc., are all subsystems with their own design requirements. Motors may have a relationship among speed, mass and power output. Coolant loops may require a certain fluid mass flow rate to achieve required performance. Springs must provide axial and radial stiffness, yet not be overstressed or operate beyond their surge limit. All these sorts of things may be formulated as constraints.

For example, a design may call for a spring for which the diameter, number of turns, etc., are independent variables. We can easily calculate the axial stiffness K_{actual} and peak stress σ_{actual} as a function of these variables. Then, by choosing two independent variables as optimization variables and implementing the two constraints

$$\text{equality constraint} = K_{actual}/K_{required} - 1;$$

$$\text{inequality constraint} = 1 - \sigma_{actual}/\sigma_{allowed};$$

we can force the stiffness to come out to the required value (even if $K_{required}$ itself is a function of the optimization variables) and make sure the stress does not exceed the allowable limit. The optimization driver does the work, and we just watch.

Pressure walls are another example of subsystems with stress constraints. Typically we are concerned about hoop- or thermal-stress constraints. We may satisfy these by selecting the appropriate independent variables as input (such as wall thickness, length, pressure, etc.) and formulating constraints, as above, in terms of calculate stress vs allowed creep-rupture or fatigue stress.

DESIGNER WHIMS

We would like the objective function to truly represent that which we are trying to optimize. But, often, it fails to do that exactly. For example, we may specify mathematically that our goal is to optimize efficiency, but regenerator cost may grow unexpectedly and become an important issue. Rather than taking the trouble to formulate an objective function that encompasses our ultimate goal (such as:

"maximize efficiency but trade-off one efficiency point for every dollar saved in regenerator cost", or "just make me rich", or "bring happiness to the world") we usually introduce a stop-gap constraint to subdue whatever it is that is getting out of hand.

In this way we find ourselves putting arbitrary limitations on piston masses, displacer lengths, regenerator volume, and so forth. All of these whims may be easily formulated in terms of inequality constraints.

MODEL LIMITS

The GLIMPS model, being one-dimensional, and with rather coarse computational grid, cannot resolve certain phenomena. For example, it has no way of detecting flow maldistribution in regenerators brought about by jet penetration from tubes or poorly-designed manifolds. Nor does it adequately penalize low gas-flow tidal amplitudes in heat exchangers (mean-flow amplitude \ll heat exchanger length). Provided we can formulate constraints to quantify the things which we are trying to avoid, GLOP will avoid them.

BOUNDARY CONDITIONS

Occasionally we run into a problem where certain of the independent input variables to our thermodynamic model are not independent in our optimization problem.

Wall Temperatures

A good example of this in the GLIMPS model are heat exchanger wall temperatures which are normally fixed input variables. Often the true *fixed* temperatures are the ultimate source and sink temperatures, not the wall temperatures. So we need some way to adjust wall temperatures to meet our boundary conditions. As you may have suspected, constraints make this possible. The trick is to take wall temperatures as optimization variables for the sole purpose of satisfying temperature boundary conditions. For example, say that T_{source} is the fixed source temperature and T_{wall} is the cold-end wall temperature which we select as an optimization variable. Also assume that we can calculate in the GLIMPS postprocessor ΔT , the actual temperature difference between the ultimate source and the wall. Then the following constraint will do the job:

$$\text{equality constraint} = (T_{wall} + \Delta T)/T_{source} - 1;$$

Free-Piston Dynamics

Another example of using constraints to overcome fixed input variables is in the area of free-piston or free-displacer dynamics. Some **Stirling** coolers forgo kinematic linkages in favor of spring-supported components self-driven by gas forces. In such cases, the amplitudes and phase angles of the moving parts depend on a number of variables like: component masses, spring dimensions and frontal drive-areas, which we may take as optimization variables. We seek to adjust the optimization variables to make amplitudes and phase angles come out right. The guiding principle is that Newton's equation of motion can be embedded in a pair of constraints for each free component. By appropriately selecting optimization variables, the summation of forces on the moving component can be adjusted to equal the product of mass and acceleration, at least when all quantities are assumed to vary sinusoidally.

Pulse Tubes

An orifice pulse-tube cooler may be considered to be a **Stirling** cooler where the volume variation in the expansion space is determined, not by a piston or displacer, but by the flow through the orifice at the end of the pulse tube. Therefore, pulse tubes are fair game for the GLIMPS model, provided there is some way to insure that the expansion space volume variation is consistent with the volumetric flow through the orifice. Again, constraints make this possible. The trick is to take the expansion space volume amplitude and phase angle as optimization variables. Then one can calculate the difference between the volumetric flow rate at the actual expansion space endpoint, and that through the orifice as calculated from its velocity vs pressure-drop relationship. Expressing the amplitude and phase of the difference as two equality constraints allows GLOP to force the difference to zero.

Two-Stage Coolers

It is even possible to use constraints to match up boundary conditions for the first and second stage of a two-stage cooler. Normally GLIMPS models just a single compression and expansion space. A two-stage cooler, typically realized by a stepped displacer, has an intermediate expansion space at an intermediate temperature. This sort of device may be modeled by running successive GLIMPS simulations where the intermediate expansion space is the expansion space of the first-stage model and the compression space of the second-stage model. This requires matching of interstage gas temperatures, pressure and mass flow rate amplitudes and phases, and overall energy balance. Without going into the cumbersome details, equality constraints make it possible.

OFF-DESIGN MAPPING

After a design point is optimized, one often wants to investigate off design performance — at off-design frequency, temperature, etc. This is a separate use of GLOP compared to pure optimization. Satisfying constraints remains important, but the objective function is a dummy and has no effect on the outcome. Usually many of the constraints that were in place during the optimization process continue to hold — free-piston constraints and temperature boundary conditions, for example. Sometimes, however, the constraints are different. For a hermetically sealed system, the mean gas pressure may vary as a function of source or sink temperature. The condition that total system mass be constant governs the mean pressure in this case. In either case, equality constraints make it happen.

TYPICAL OBJECTIVE FUNCTIONS

Like the constraints, the objective function winds up in the GLOP machine specific unit as a Pascal expression. Evaluating this objective function typically requires the full resources of the GLIMPS simulation plus postprocessing, but eventually returns as a real numerical value. The optimization driver continually adjusts the optimization variables in order to minimize the objective function subject to the active constraints. That it *minimizes*, rather than *maximizes*, the objective function is no restriction since a minus sign converts a maximization problem to a minimization problem.

A typical objective function might be:

$$\text{minimize} = W_{input}/W_{norm};$$

where W_{input} is the net mechanical work input after parasitics and W_{norm} is the fixed rough expected value which serves to normalize the result to the order one. Important for this particular objective function would be that net heat input be fixed by way of an equality constraint.

An objective function may get as complicated as required. The only restrictions are that it be computable, reasonably smooth and have a minimum value (subject to the constraints). For example, an objective might be to minimize manufacturing cost, or size, or a combination of the two. However, I have found it good practice to keep the objective simple, and resolve cost, and size issues by way of inequality constraints.

TYPICAL OPTIMIZATION VARIABLES

Any input variable to the GLIMPS/postprocessor model is fair game as an optimization variable. Typical optimization variables include:

- Overall system variables such as temperatures, pressure and frequency
- Piston and displacer amplitudes and phase angles
- Cylinder frontal areas
- Heat exchanger dimensions
- Dimensions for secondary heat exchangers, drive motors, springs and other subsystems

The choice is dictated by what it is you are optimizing and the constraints you must satisfy. GLOP gives you complete freedom to choose. Generally speaking, every active constraint requires at least one optimization variable upon which it depends, and reduces the degrees of freedom in the search domain by one.

WORKING WITH GLOP

Provided that the problem you specify has a solution, GLOP will usually find it. Typical problems generally require about an hour or two of computing on a 386-based PC. GLOP generally moves to satisfy all the constraints very quickly, then plugs away at minimizing the objective function, rapidly at first, then more slowly as it approaches the optimum.

But still, optimization remains a bit of an art in spite of all the science. That is, optimization problems as specified by humans tend to produce results not expected. The problems are especially acute when several complicated nonlinear constraints come to bear at once. It is entirely possible for an objective function having a unique minimum in the absence of constraints, to have multiple extrema in the presence of nonlinear constraints. Nonlinear constraints can carve up the search domain into oddly shaped fragments or disjoint pieces. The art of optimization comes in grappling with the interrelationships among constraints and the objective function when things are not going well.

The best way I've found to deal with complex problems is to start simple and increase complexity gradually. For example, rather than invoking a large set of constraints all at once, it is better to leave many of them out at first, adding them a

few at a time in stages. In this way one can get a feel for the effect each constraint has on the outcome and be sure that the GLOP solution is meaningful.

However, be it art or science, GLOP is a powerful tool. It is not trivial to use, but neither is it too difficult. It demands some programming of the user, but returns infinite flexibility as the reward. GLOP optimizations tend to be self documenting, structured and maintainable, helping the designer evolve ever closer to the ideal where the optimization model is an accurate reflection of the total system being optimized.

REFERENCES

1. D. Gedeon, "A Globally-Implicit Stirling Cycle Simulation", *Proceedings 21st IECEC*, American Chemical Society, pp. 550-554. (1986)
2. M.J.D. Powell, "A Fast Algorithm for Nonlinearly Constrained Optimization Calculations", in: *Lecture Notes in Mathematics*, 630, *Numerical Analysis (Proc. Biennial Conf. at Dundee, 1977)*, Springer-Verlag (1978)
3. D. Goldfarb, A. Idnani, "A Numerically Stable Dual Method for Solving Strictly Convex Quadratic Programs", *Mathematical Programming*, 27, pp. 1-33, (1983)

DEVELOPMENT OF STIRLING CYCLE COOLER AND INTEGRATION OF THIS COOLER INTO A BIOLOGICAL STORAGE FREEZER

Russell C. Tipton
Forma Scientific, Inc.
Marietta, Ohio 45750

ABSTRACT

In both research and diagnostic laboratory applications, low temperature refrigeration of living biological systems and biomaterials is required to produce satisfactory preservations. A Stirling cycle cooler has been developed as the cooling source for such a biological storage freezer that will operate at 103 K. The heat exchange and control systems to incorporate this heat pump into a unitary appliance style storage freezer have also been developed. The primary design challenges include: achieving the required performance, life, manufacturability, and cost for the cooler; providing a control and power conditioning system to utilize nominal 220 V single phase alternating current power worldwide; and establishing heat exchange systems to uniformly cool a 0.23 m³ rectangular air space and dump the heat to ambient air in a laboratory setting. Key attributes implied by the product being an appliance are: continuous operation with only minimal routine unskilled maintenance for a minimum 5 years, aesthetically pleasing with noise and vibration levels suitable for an occupied laboratory, and minimal initial setup. The unique aspect of this work is that it is a commercialization of Stirling cycle technology bringing it out of the laboratory or highly specialized application.

INTRODUCTION

A storage freezer, figure 1, has been developed to operate at a temperature of 103 K. This product consists of three major assemblies: the heat pump to provide the cooling source; the cabinet and heat exchange systems to create a useable storage space cooled by the heat pump; and the electrical system to provide power conditioning, throttling of capacity, and monitoring of operation. This paper will begin by providing the overall product specifications and then address each subsystem in the order listed.

Biomedical laboratories, both research and diagnostic, utilize low temperature storage of raw materials and test products to provide long term preservation. Storage freezers used for this application need to have the attributes of an appliance:

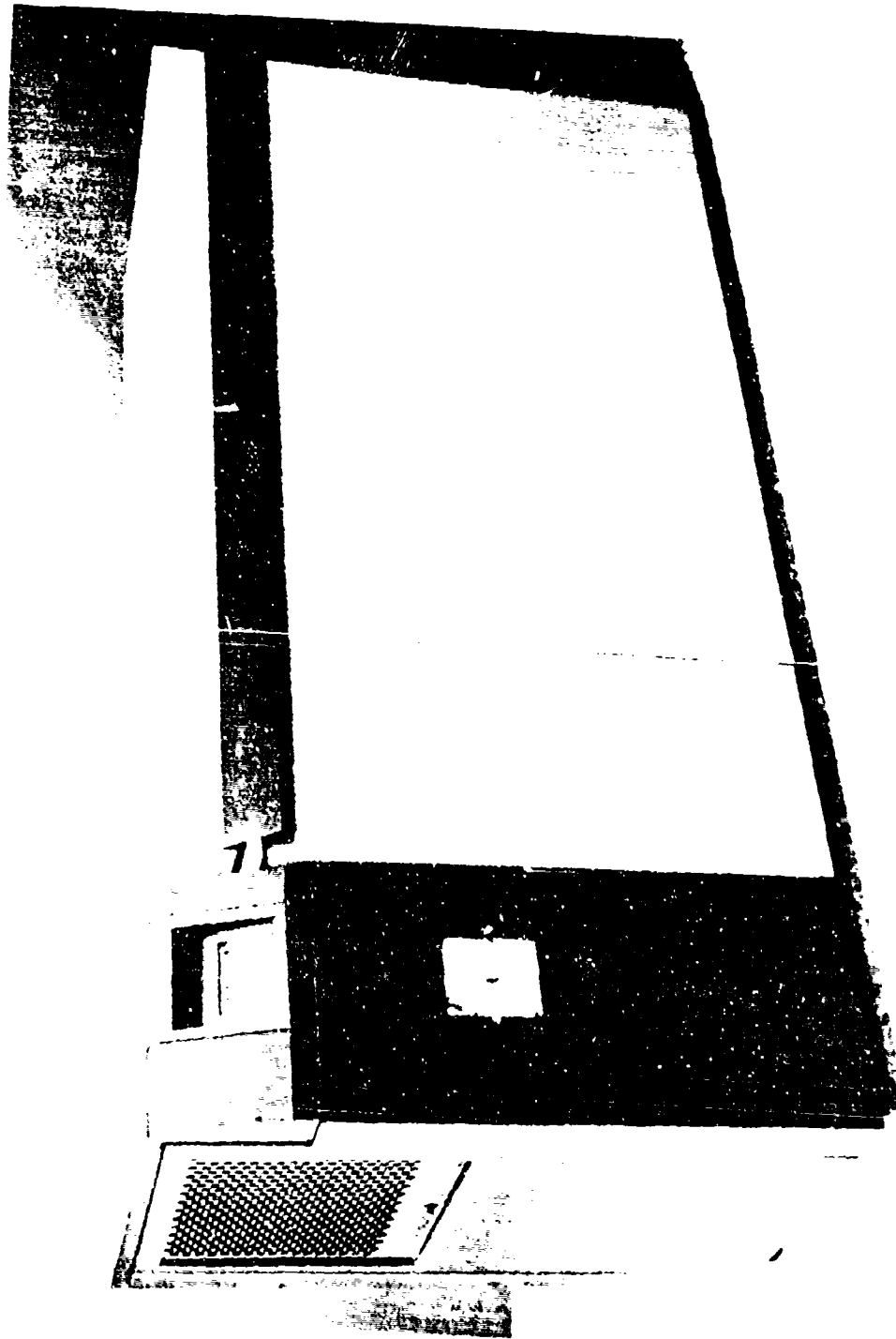


Figure 1. Storage Freezer Utilizing Stirling Cycle Cooling Source

1. Unitary in nature. Installation consists of uncrating, positioning, plugging in to adequate power source, and turning on the power switch.
2. Operate using commonly available electricity as the power source.
3. Operate continuously for a minimum of five years with only routine unskilled maintenance required.
4. Aesthetically pleasing appearance with noise and vibration levels suitable for an occupied laboratory.

PRODUCT SPECIFICATIONS

Figure 1 shows a prototype of the completed storage freezer. A Stirling cycle heat pump is used as the cooling source for this storage freezer. Table 1 shows the specifications for both the storage freezer and the heat pump.

THE HEAT PUMP FEATURES

The Stirling cycle has proven itself in the desired temperature range with laboratory size nitrogen liquefiers. However, these Stirling cycle coolers fall short in operating life and exceed cost levels to allow the target storage freezer selling price.

Figure 2 shows a completed heat pump developed for this application. Figure 3 is a cross-section of this heat pump. It is a form of the Beale free-piston¹ integral Stirling machine with other associated developments to provide solutions to the noted shortcomings in existing Stirling cycle equipment. Details of the design will be described in the following paragraphs.

The expansion and compression spaces are at opposite ends of the displacer. The heat acceptor, regenerator, and heat rejector are in a cylindrical shell configuration about the displacer. The displacer gas spring is centrally mounted on the warm end of the displacer. The fixed end of this spring is attached to the machine housing. The compression space is between the piston and displacer. The linear motor driving the piston consists of inner and outer laminations, coil, and magnets and is arranged peripherally around the piston. The piston spin motor is located centrally to the piston. The piston gas spring boundaries are formed by the piston and the outer laminations and supports. The most suitable working fluid for this application is helium.

Limits preventing the indicated life include: contamination of heat transfer surfaces by oil in oil-lubricated cryocoolers, leaks of helium working fluid, and mechanical wear of bearing and sealing surfaces. Free-piston configuration with gas springs², clearance seals, and hydrodynamic spin bearings on piston and displacer are used. These provide non-contact operation to eliminate wear other than that occurring during starting and provide lubrication without oil to minimize fouling problems. Center ports³ are used to locate the center of motion of the piston and displacer. In addition, the permanent magnet, high efficiency, linear motor^{4,5} driving the piston allows hermetic sealing of the heat pump to provide adequate containment of the helium. The displacer is spun by turbine fins⁶ at the warm end configured such that the helium flow into the compression space when the displacer is at the bottom of its stroke will flow past the blades imparting a spinning torque. The piston does not have the helium flow characteristics of the displacer to allow spin turbines. The piston is spun by an electric motor of drag cup rotor design. This has the required characteristics of low rotor mass and non-contact operation.

STORAGE FREEZER

CONFIGURATION	Chest
OPERATING TEMPERATURE	103 K
STORAGE CAPACITY	0.226 m ³
REFRIGERATION	Closed cycle, working fluid to be non-flammable and non-explosive at room temperature and atmospheric pressure
POWER SUPPLY	180 to 250 V 50 or 60 Hz single phase, 20 A service
DESIGN LIFE	5 Years continuous operation
AMBIENT CONDITIONS	
OPERATING	288 to 305 K 10 to 95% relative humidity (rh)
STORAGE	243 to 323 K 10 to 95% rh
SHIPMENT	Same ambient as storage; unit must withstand shipment by common carrier.
SOUND PRESSURE LEVEL	Maximum NC-55 at 0.9 m from freezer
VIBRATION LEVEL	2.5 E-03 m/s in storage space
PRESSURE	Working pressure of any vessel in system to be less than 3.5 E+03 kPa

HEAT PUMP

GENERAL DESCRIPTION	Long life Stirling cycle machine to provide constant temperature in a storage freezer. Unit to include mounting interface for both heater and cooler heat exchangers. Unit to be closed cycle and hermetically sealed.
WORKING FLUID	Non-flammable, nonexplosive at normal room temperatures.
TOTAL HEAT LIFTED	200 W from 100 K to 315 K 150 W from 90 K to 315 K
DESIGN LIFE	5 years
POWER SOURCE	180 to 250 V, 50 or 60 Hz, single phase
COEFFICIENT OF PERFORMANCE	30% of Carnot or greater

Table 1. Product Specifications

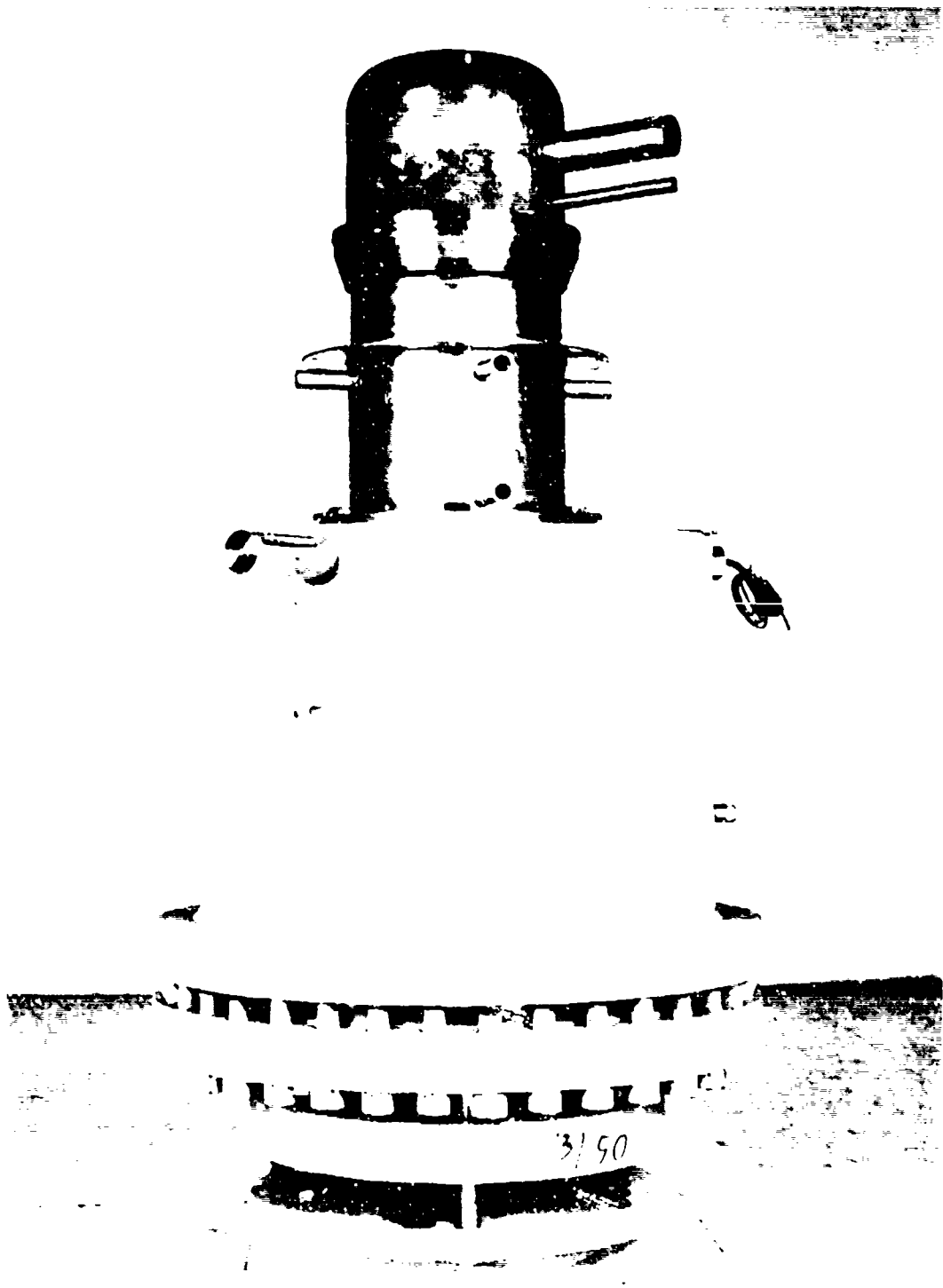


Figure 2. Free-Piston Stirling Cycle Heat Pump

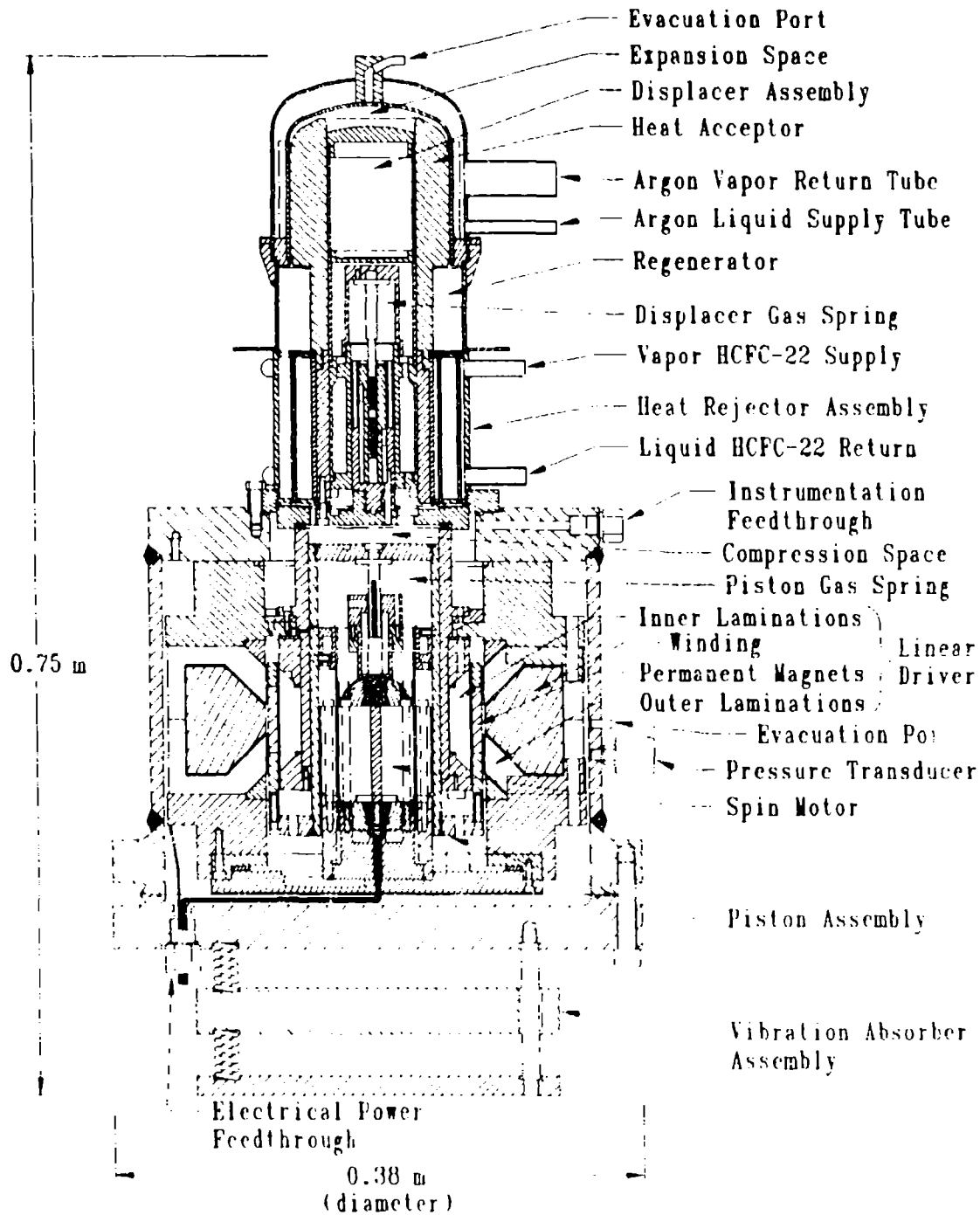


Figure 3. Free-Piston Stirling Cycle Heat Pump Assembly

Although highly inefficient, the starting torque can be supplied with high power input and then the power cut back to provide the very small running torque required and prevent overheating of the driver.

Stirling cycles are inherently quiet, but free-piston machines produce linear vibration forces. A tuned spring and mass vibration absorber is incorporated to minimize heat pump vibration that will be transmitted to the storage freezer.

The cost goals are achieved by a combination of manufacturing engineering and optimization and recent materials and processing developments. In general, the individual parts of a Stirling cycle heat pump can be made with standard manufacturing techniques. However, the purpose and requirements of the parts and assemblies are not commonplace. This requires unique combinations of manufacturing procedures with close scrutiny of the assumptions involved with each. Although the machine has two moving parts, there are a large number of pieces forming subassemblies. Over 3500 individual laminations are used in the linear motor. Subassemblies were defined to utilize known economical manufacturing capabilities and provide ease of assembly. For example, the rejector is made of stock pipe, tubing, and plate that is machined, assembled and vacuum brazed. Geometry of machined parts is selected to allow ease of fabrication. Tolerances are established to provide correct operation, interchangeable parts, and balance over-precision against final machining of assemblies. The primary material development is the Neodymium-Iron-Boron magnets of $2.07 \text{ E} + 05 \text{ kJ/m}^3$ peak energy density used in the linear motor. Another important development is in the adhesives, primarily epoxies, and sealants. The main use of adhesives is to assemble the multitude of pieces in the linear motor. The primary processing development is in CNC machining. Most of the parts in the heat pump are machined. Clearance seals and hydrodynamic bearings require close tolerance machining. In concept, the free-piston Stirling cycle heat pump is a pressure vessel with two moving parts enclosed. However, to provide gas springs, reference spaces for centering ports, and compression and expansion spaces, volumes of helium must be separated from each other. Thus, the pressure vessel requires relatively high tolerance interfaces with the internal components. CNC machining provides this cost effectively, also.

INTEGRATION OF THE HEAT PUMP AND STORAGE FREEZER

MECHANICAL

A characteristic of Stirling cycle machines is that the heat acceptor and rejector tend to be small cylindrical structures of relatively high heat flux and in close proximity to one another. As opposed to a vapor compression refrigeration system with compressor, condenser, expansion device, and evaporator all connected with tubing, a Stirling cycle heat pump is a compact machine enclosed in one pressure vessel. The evaporator is replaced by the heat acceptor and the condenser by the heat rejector. The fluid at both the low temperature heat source and high temperature heat sink in a storage freezer is air with its notorious heat transfer shortcomings. The temperature differentials between the source and sink should be minimized for most efficient operation. Phase change secondary heat transfer loops⁷ were included which can provide near isothermal high heat fluxes. Both of these have a reflux evaporator and condenser which are adaptations of heat pipe theory but rely on gravity to move the liquid.

The working fluid selected for the cold end is argon. This temperature is well within its liquid-vapor dome with a saturation pressure approximately 450 kPa.

Argon is non-flammable and otherwise non-reactive and is readily available. Its transport properties are not outstanding, but are acceptable. Design temperature differences are 10 K from air to argon and 3 K from argon to helium. Finned tubes, technology borrowed from HVAC industry, are arranged on the top of both the front and rear walls of the storage chamber to set up two natural convection loops as shown in figure 4. Air flow passages are built into the inventory system supports. Fin density increases from top to bottom so that the heat load for each tube is approximately the same and to allow space for frost build up on the upper fins. The tubes are sloped to provide gravity distribution of the liquid argon and sized so that the vapor/liquid counterflow stays in the laminar region as prescribed in heat pipe theory. The temperature drop of a falling film condenser for the argon was three times that desired. Augmented condensing surface as prescribed by Adamak⁸ was sized to achieve the desired temperature difference. Although optimized Adamak fins can require 1/15th the temperature drop of a falling film, manufacture of this is exceedingly difficult. The fins used are a compromise to allow machining practicality and desired performance. The liquid argon must be distributed to the multiple tubes in appropriate proportions. Typical liquid distributors rely on a pressure differential and do not have the vapor returning above the liquid in the same tube. Other than very small elevation changes, the argon system is isobaric. The liquid argon distributor used is a small pool with evaporator lead tubes proportionally distributed around the spillway of the pool.

The working fluid selected for the heat rejection system is HCFC-22. This also is nonflammable and otherwise nonreactive, has a reasonable saturation pressure at the temperatures of interest, and has good transport properties. Arrangement of the heat rejection system is shown in figure 5. A workable configuration to achieve the required helium and HCFC-22 surface areas is the shell and tube arrangement. Tubes are vertical and arranged in a cylindrical shell around the bottom of the displacer. Helium flows through the inside of the tubes and HCFC-22 liquid surrounds the tubes. The heat flux is between evaporation and pool boiling. The vapor exits from the top of this heat exchanger and flows up to a vertical tube plate fin heat exchanger. Here the vapor flows up the center of the tubes and condenses on the internal tube surface forming a falling film condenser. This liquid is collected and flows through tubes to enter the bottom of the shell and tube rejector. A blower pulls ambient air across the HCFC-22 condenser. Components are sized such that there is a 5 K temperature difference between the helium and HCFC-22 liquid and a 15 K difference between the HCFC-22 and the air.

ELECTRICAL

A power conditioning system was incorporated into the design for the following reasons. The available electrical power will have a wide range of voltage and two frequencies. However, the performance of the free-piston machine is tuned to a discrete frequency and the linear motor stroke is very dependent on the input voltage. Figure 6 shows the extent of electronic hardware required to allow the specified variability in the power source.

When the balances between size, cost, efficiency, and manufacturability were considered, 45 Hz was determined to be the best operating frequency for this machine. Performance of free-piston machines is tuned to one operating frequency. Stroke of piston and displacer in free-piston machines is not physically determined and varies with operating temperature and input power (voltage for a given motor).

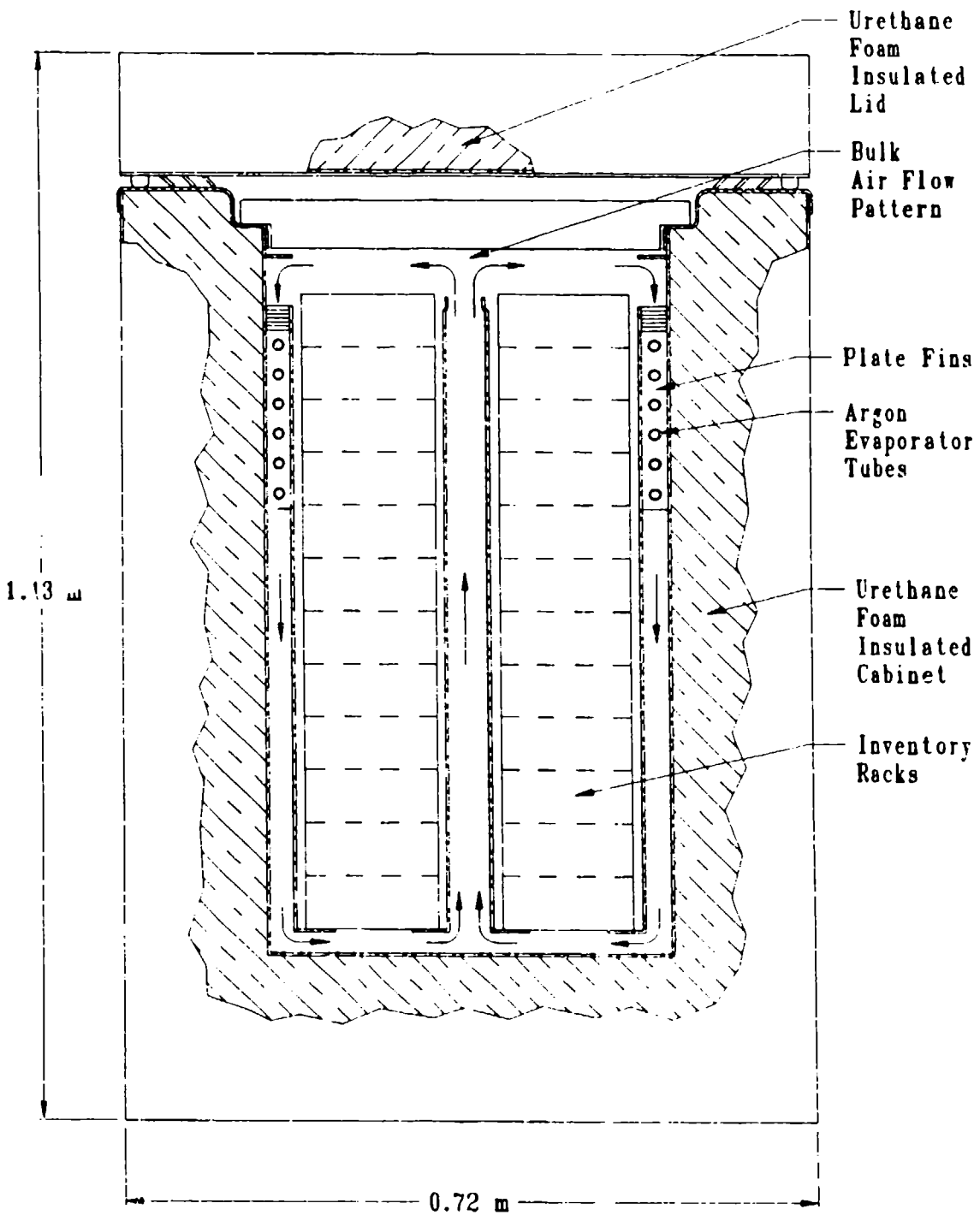


Figure 4. Storage Chamber Natural Convection Flow Pattern

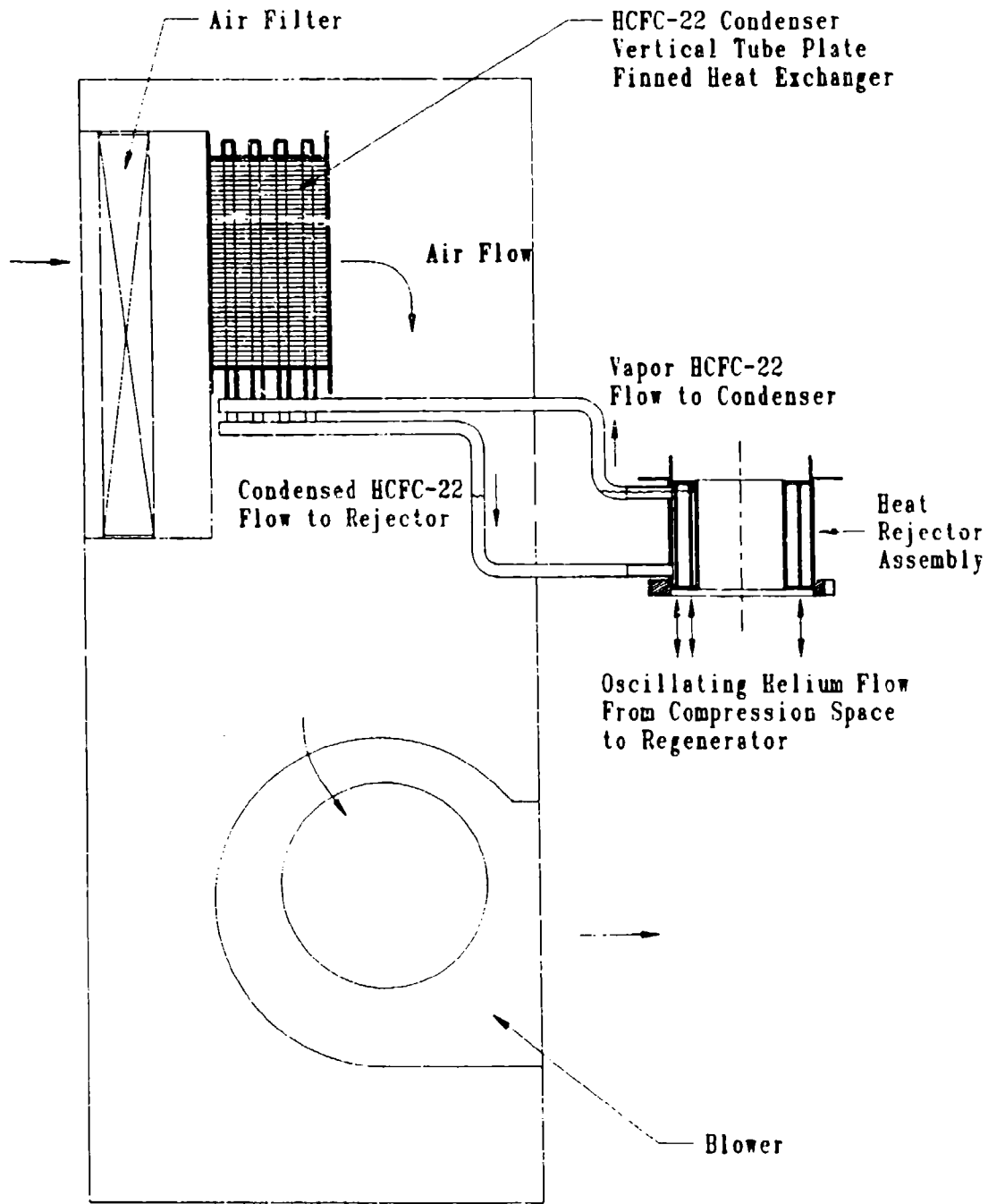


Figure 5. Heat Rejection System

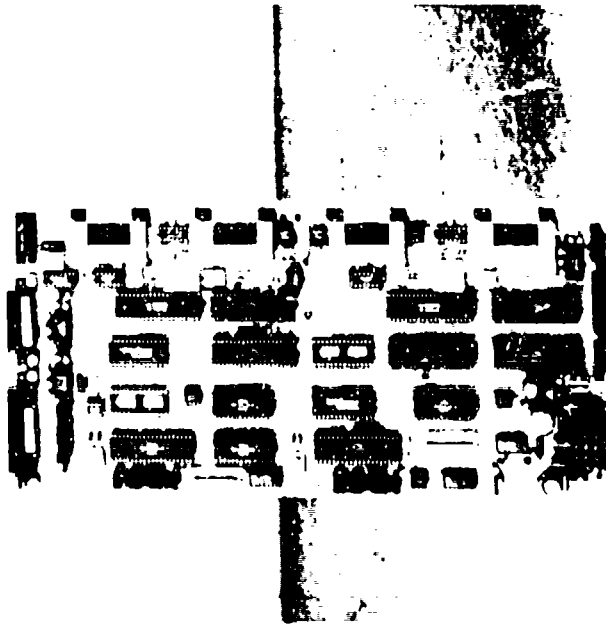
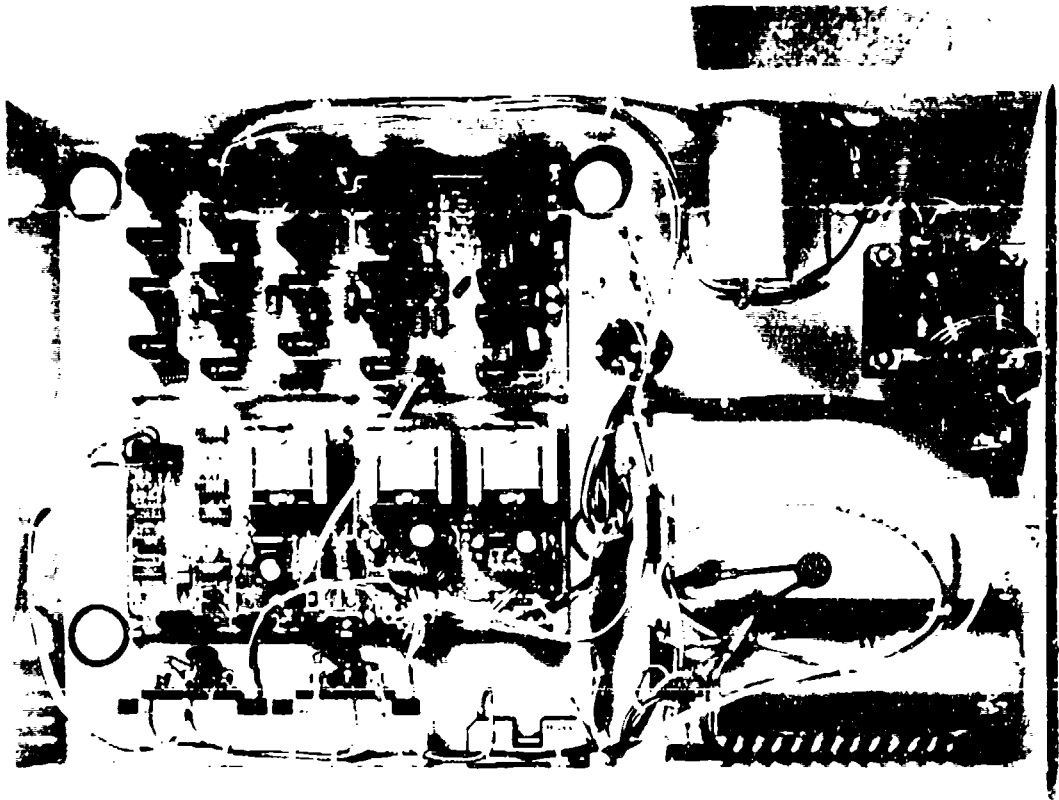


Figure 6. Control, Monitor, and Power Conditioning Electronics

Fortunately, the linear motor does not require a sine wave voltage but can operate quite efficiently with a square wave input voltage. Modern power electronics can rectify the incoming power and generate a constant frequency square wave output cost effectively. As this system is microprocessor driven, pulse width modulation was added for the cost of the software and a current sensor. This provides compensation for input voltage fluctuation as well as power modulation for both start up from room temperature and throttling of the heat pump for temperature control.

The drag cup rotor motor used to spin the piston requires two phase power at 32 Hz. This is generated in the same fashion as the linear motor power with an additional phase. Input voltage insensitivity is needed here also. Input to this motor is power not necessary for the thermodynamic cycle, but to provide the piston spin creating a hydrodynamic bearing. Starting torque of the piston is larger than spinning torque. Thus, throttling this motor after startup will provide the required spin and minimize heat added to the driver end of the heat pump.

With a microprocessor available, intelligent monitoring of the performance of the storage freezer is available for the cost of the sensors and signal conditioning. Temperature of the cold end is monitored and used to set input power limits during startup and to troubleshoot freezer operation. The temperature of the storage cabinet is monitored and used to set input power to the heat pump in normal operation. The temperature of the vapor HCFC-22 leaving the rejector is monitored and used to set condenser fan speed and to troubleshoot freezer operation. Helium pressure is monitored to detect helium leaks. Current to both the linear motor and spin motor is monitored to control power level with the pulse width modulation routines. Linear motor current is also used in troubleshooting the freezer operation. With a troubleshooting procedure, the items discussed can isolate problems to specific areas of the freezer without disassembly. Unfortunately, by the time heat pump performance degrades to the point to be noticed in the data taken above, the moving components of the heat pump will be destroyed. Infrared optical sensors to detect spinning of both the piston and displacer have been included to detect heat pump problems before irreparable damage can occur.

STATUS

This project has followed the normal fashion of predicting the number and level of technical risks and then proceeding to resolve issues as they arise. The cabinetry, heat exchange systems, controls, and power conditioning have the least risk and have proceeded in a straight-forward manner.

The heat pump has the highest risks to success. The design to achieve the required performance has been completed and demonstrated. Several areas relating to manufacturability and life are being addressed presently. The input power limit to prevent demagnetization in this application must be determined experimentally. Prior to charging the heat pump with helium, internal moisture levels must be reduced to a very low level for cryogenic temperatures. This free-piston Stirling machine requires individual volumes separated by orifices or clearance seals. Thus, practical evacuation is difficult. Procedures combining vacuum baking of subassemblies, evacuation, and purging are being developed.

Two aspects relating to the precision parts for clearance seals and spin bearings are receiving further attention. Achieving and maintaining concentric fits

for the displacer and ensuring dimensional stability of these parts is critical to preventing wear and performance degradation.

SUMMARY

The development of a Stirling cycle cooler and its integration into a biological storage freezer have been discussed. Developments during the last several decades in Stirling cycle configurations and analysis, power electronics and microprocessor based control systems, materials, machining, and manufacturing processes have allowed this.

REFERENCES

- 1.W.T. Beale, "Stirling Cycle Type Thermal Device," United States Patent 3,552,120 (1971).
- 2.W.T. Beale, J.G. Wood, and D.R. Gedeon, "Spring and Resonant System for Free-Piston Stirling Engines," United States Patent 4,183,214 (1980).
- 3.W.T. Beale, "Center-Porting and Bearing System for Free-Piston Stirling Engines," United States Patent 4,404,802 (1983).
- 4.R.W. Redlich, "Electromechanical Transducer Particularly Suitable for a Linear Alternator Driven by a Free-Piston Stirling Engine," United States Patent 4,602,174 (1986).
- 5.W.T. Beale and C.G. Scheck, "Electromechanical Transducer Particularly Suitable for a Linear Alternator Driven by a Free-Piston Stirling Engine," United States Patent 4,623,808 (1986).
- 6.W.T. Beale, "Hydrodynamic Lubrication System for Piston Devices Particularly Stirling Engines," United States Patent 4,330,993 (1982).
- 7.R.C. Tipton, "Laboratory Freezer Appliance," United States Patent Pending (1990).
- 8.T. Adamak, "Bestimmung der Kondensationsgrößen auf feingewellten Oberflächen zur Auslegung optimaler Wandprofile," *Wärme-und-Stoffübertragung*, vol. 15, (1981).

CONSIDERATIONS IN USING JOULE-THOMSON COOLERS

Glenn E. Bonney and Ralph C. Longsworth
Science Center, APD Cryogenics Inc.
1833 Vultee Street / Allentown, Pennsylvania 18103

ABSTRACT

Much has been learned from experience about considerations that are important in the design and use of JT cooling systems. This paper presents a discussion of some of the parameters that are important in system design and operation such as the effect of contaminants in the gas, heat transfer ΔT between the liquid cryogen and the dewar wall, dewar thermal effects, temperature stability with demand flow and fixed flow control, and the use of selected gas mixtures. Practical aspects of using JT coolers focus on the gas supply system and operative procedures that are needed to avoid having contaminants freeze out and also provide long-term reliability.

INTRODUCTION

Joule-Thomson coolers (a.k.a. JT cryostats) provide a fast-acting source of refrigeration by expanding a compressed gas isenthalpically to achieve temperatures in the range of the gas's saturation pressure. They ideally lend themselves to miniaturization for lightweight, portable applications. They require little maintenance, and have a very long shelf life. Cryostats can be designed with a fixed high flow rate for fast cooldown followed by a short run, or with demand flow control for moderately fast cooldown and extended run time.¹ They are essentially vibration and noise free. Most JT cryostats can operate in any orientation, and in very severe thermal and G-load environments.

The JT cryostat typically comprises an inlet gas connection, a particle filter, a counterflow heat exchanger, and a nozzle. It may also include an exhaust gas connection. Strictly speaking, the term "cryostat" means these items are assembled and mounted in a dewar. The dewar typically comprises a vacuum-insulated container, having an inner containment for the counterflow heat exchanger and exhaust gas, and a "cold end" mounting for the device to be cooled.

JT cryostats can be applied as open- or closed-cycle refrigerators. Either one requires a supply of pure, high-pressure

gas. The open-cycle gas is supplied either from a small high-pressure bottle for portability, or continuously from a compressor. Conversely, the closed-cycle gas is recycled from an initial stored quantity. The exhaust gas is directly collected, compressed to high pressure and resupplied to the JT cryostat.² A multi-stage compressor is required for the closed-cycle system. This adds bulk, requires relatively high input power and cooling, reduces reliability, and inhibits fast cooldown. Consequently, most JT cryostats are applied as open-cycle coolers.

Having a JT cryostat cool a device such as an IR detector in a satisfactory manner requires an understanding of some of the problems that can be encountered and the design and operating procedures that have to be considered to avoid such problems. This paper discusses the following factors that have been found to be the most significant:

- Gas purity
- Gas supply system
- Handling
- Temperature stability
- Heat transfer of liquid cryogen
- Dewar effects.

In addition, a brief description is presented on the general characteristics of using a gas mixture.

Gas Purity

The gas type, supply pressure, ambient temperature, volume, and JT cryostat design determine what operating conditions will result. Most constituents in the gas that have freezing points warmer than the saturation temperature, or particulates which could physically restrict gas flow, are contaminants that can prevent successful operation.³ Particulates can permanently restrict flow if they become lodged in the heat exchanger inlet passage or nozzle. Condensible contaminants that crystallize in the upper temperature region of the heat exchanger inlet passage are usually carried downstream where they collect and restrict the nozzle. For a given concentration of condensible contaminant, the "dew" point temperature increases with increasing pressure, thus freezing sooner at higher operating pressures and lower ambient temperatures.

The susceptibility of a JT cryostat to clogging is dependent on the nozzle size and flow rate. We define the nozzle size by the parameter C_0 which is the flow rate of nitrogen (N_2) in sL/min that is measured when the supply pressure is 7 MPa exhausting to 0.1 MPa with both the JT cryostat and gas at 20-24 C. It has been found that an orifice smaller than 0.07 mm or a flow rating, C_0 , less than 0.5 sL/min will require a higher gas purity than is practical to achieve. Clogging of a fixed nozzle occurs either abruptly during cooldown, or cyclically during operation in which the flow declines like a damped

oscillation. Several methods have been tried to impede clogging of fixed flow JT cryostats by trapping the solid or frozen contaminants in the cold end of the heat exchanger with large flow area labyrinths⁴ or thread filters.⁵

Demand flow JT cryostats are more tolerant to contaminants because their temperature-sensitive flow control nozzle will increase flow in response to the warming caused by clogging, thereby purging contaminants. We have found that the minimum acceptable purity for N₂ entering a nominal 200 mW demand flow JT cryostat must be at least 99.998% (as total assay), and the maximum acceptable levels for the common contaminants in N₂ are found to be: 2 parts per million by volume (ppmv) water vapor (H₂O), which is equivalent to a dew point of -71 C at 0.1 MPa; 2 ppmv carbon dioxide (CO₂) or carbon monoxide (CO); 3 ppmv total hydrocarbons (THC); 3 ppmv chlorofluorocarbons (CFC); and, 6 μm maximum diameter particles. Typically, air, oxygen (O₂), argon (Ar), helium (He), and neon (Ne) do not affect performance at low concentrations. It is found that by doubling the cryostat's nominal cold flow rate, and thereby halving the available run time from a fixed gas volume, operation is acceptable with 4 ppmv H₂O. As the level of H₂O is further increased, the frequency of temperature excursions also increases.

There are no general industrial, military, or federal purity specifications for JT gases at present. A few specific military and commercial JT cooler specifications coincide with the minimum acceptable levels described. Mil-P-27401, Grade C N₂ is sometimes specified, but its purity does not meet the acceptable levels described. Industrial gas suppliers present purity in a variety of ways.⁶ Most of them use grade names and total purity assay. "Commercial purity", > 99.995%, contains up to 10 ppm H₂O. "Ultra-pure carrier" grade, > 99.998%, or "ultra-high purity", > 99.999%, typically contain < 2 ppm H₂O. However, grade names and purities vary among suppliers and gases, and the total purity may be based on a weight analysis which may appear purer than a volume analysis (ppmv = ppmw x MW gas / MW impurity). Also, the total purity assay may not include all the impurities pertinent to the application. Some industrial gas suppliers will provide an actual impurity analysis. Unfortunately, the analysis may not detect the low levels required, and it may not be for the gas as it exists in the actual vessel being supplied. Furthermore, impurities will outgas from the vessel's internal surfaces as the supply pressure decreases during use, changing the purity ratios. From a practical stand point it has been found that all of these gases can be used satisfactorily if a clean adsorber is used in the gas supply line. Higher purity gases reduce the frequency of having to regenerate the adsorber.

Gas Supply System

It is essential that all contaminants in the gas supply system be either eliminated or reduced to acceptable levels. The gas supply

system typically consists of the gas source, a pressure regulator, adsorbers with filters, and an interconnecting line to a small gas bottle, a start valve, and another gas line to the cryostat (See Figure 1). The gas source is typically a pressurized tank purchased from a gas supplier, but it may be compressed locally from a low pressure gas source, ambient air, or a liquid cryogen, and purified. For gas compression, non-oil-lubricated compressors are recommended to minimize hydrocarbon contamination.

The gas supply system design should consider the following:

- (1) Safety: Capable of operating safely with the intended gas and pressure. Consideration must be given to the maximum working pressure at the high temperature ambient, the number of filling/venting cycles, applicable transportation codes, burst fragmentation, and fire safety (Ref.: ASME Sec. VIII, Div. 1; ANSI B31.5; DOT Hazardous Materials Regulations; Mil-STD-454; Mil-STD-1522).
- (2) Leak Tightness: For short-term applications, a soap solution leak check is acceptable with the system pressurized with the process gas at the working pressure @ 21 C. For long-term applications, a He mass spectrometer should be used with the system pressurized with He to the maximum working pressure. Thermal cycling beforehand at high- and low-temperature ambients is recommended.
- (3) Permeation: Minimize permeation by using corrosion resistant metals and metal sealed joints.

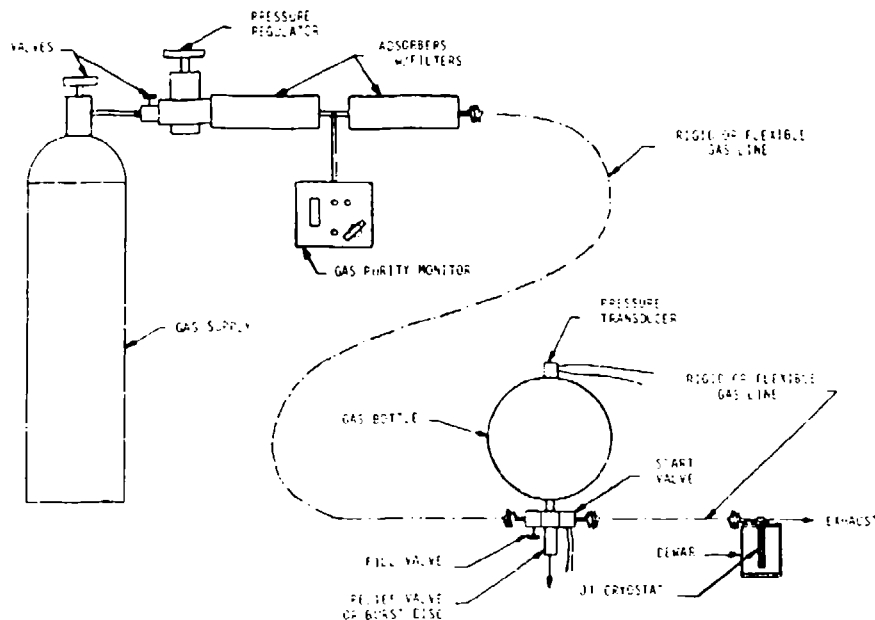


Fig.1. Typical JT Open-Cycle Refrigeration System

- (4) Cleanliness: Cleaned for oxygen use is preferred.
- (5) Simplicity: Minimize the number of joints, connections, dead flow volume, and internal surface area.
- (6) Outgassing: Use low vapor pressure materials, such as metals, and purge the system prior to use. A typical outgassing rate of 1×10^{-5} torr L sec⁻¹ cm⁻² at 1 L/min flow represents a 1 ppm level of impurity.⁷

The choice material for interconnecting plumbing in most applications is austenitic stainless steel (AISI 300 series) for strength, corrosion resistance, and non-magnetism. Easy machining type 303 has poor welding characteristics to other stainless steels. Types 321, 316L, and 304L are better choices for welded joints because they will have minimal grain boundary chromium carbide precipitation during welding, and therefore better resistance to corrosion and cracking. Passivation and electropolishing are preferable post-weld treatments because they enhance corrosion resistance, and remove micron-sized particles and crevices.

Copper and copper alloys outgas more than stainless steel and have been found to promote contamination abruptly after long-term use. Copper (Cu) oxidizes readily and continually in air. After the corrosion penetrates to the internal surface, H₂O permeates directly into the process gas. The plumbing must then be replaced. For these same reasons, a JT cryostat should be stored in a dry, inert environment to reduce corrosion of any copper in the heat exchanger.

Polymeric and elastomeric materials (i.e. plastics, Teflon, Nylon, silicone, nitriles, rubber, etc.) should also be avoided in JT gas systems. They are hygroscopic, and have high permeation and outgassing rates. They are fundamentally a source of hydrocarbon and chlorofluorocarbon contaminants. It is important to understand the properties of such materials which may exist in valves or pressure regulators.

Seamless tubing is preferred for interconnecting piping, although welded and drawn tubing is acceptable. All tubing, valves, gauges, and regulators should be leaktight and clean. Cleaning should consist of purging, scrubbing, vapor degreasing, or ultrasonic cleaning with solvents such as ethanol (denatured) or methanol, followed by Freon (TF or TMC) or 1,1,1 trichloroethane, followed by a pure N₂ purge at < 7 MPa. Vacuum baking afterward is beneficial.

All joints and connections in the plumbing should be inert-gas welded (e.g. TIG), fluxless brazed (e.g. vacuum), or dry metal sealed (e.g. Swagelok fittings, metal o-rings, MS or AN fittings, indium gaskets, etc.). Tapered pipe threads should be avoided because they can develop leaks without a sealant, and most pipe sealants contain Teflon. However, if pipe threads are used, an epoxy adhesive is a preferred

sealant. Elastomeric o-ring seals should be avoided. However, if they are used, the o-ring material should be carefully selected (e.g. Viton is acceptable for some applications), vacuum baked, and a very thin film of very low vapor pressure grease (e.g. Apiezon N) applied to the o-ring. Should a joint require soldering or brazing with an acid flux, such as with stainless steels, it is very important to use the least active flux possible. Neutralize the acidic residue immediately after making the joint (e.g. hot distilled water has been found to work better than many formulated neutralizers), then promptly clean as previously described.

An adsorber is required in the gas supply system. Adsorbers typically contain a molecular sieve which will adsorb primarily H₂O, and to a much lesser extent CO₂ and trace oils. The adsorber will improve or maintain the gas purity for a period of time, after which it begins to break through with contaminants. The amount of adsorbed H₂O is a function of the inlet gas purity, adsorbent mass, and initial adsorbent dryness. A typical adsorber, 32 mm diameter x 160 mm long and capable of operating @ 60 MPa, has a rating of 45.3 kSL of processed gas with 10 ppmv H₂O inlet purity. Adsorbers which have not been exposed to oils or other hydrocarbons can be regenerated by heating and purging, or vacuum baking, and re-used many times. If the adsorber breaks through with hydrocarbons due to excess exposure, then it has to be replaced. For long-term operations, it is recommended that two adsorbers be placed in-line downstream of the gas source, and routinely rotated with a third adsorber (i.e. the upstream adsorber is withdrawn and regenerated, the downstream adsorber is moved upstream, and the third, regenerated adsorber is placed in the vacant downstream position). It is recommended that a gas purity monitor be located between the two adsorbers to detect early breakthrough of the upstream adsorber.

A filter is required in the gas supply system downstream of every adsorber, unless a filter is part of the adsorber. Filters typically remove smaller particles from a gas than from a liquid. Therefore, it is important to understand the filter being used, and the pressure drop it imposes at the anticipated flow rate. APD Cryogenics supplies a porous stainless steel filter integral with their adsorbers and on the gas inlet of every JT cryostat. These filters typically have a 1 um nominal and 3 um absolute gas filtration rating.

The most direct method of identifying unacceptable levels of contaminants in the gas supply system is by using a gas purity monitor. It is important to routinely sample the gas purity nearest the JT cryostat. The APD Cryogenics gas purity monitor, p/n 250106D, will freeze up within 5 min if > 2 ppmv H₂O or > 1 ppmv CO₂ is present in 35 MPa N₂ (See Figure 2). Although it has not been calibrated for other contaminants, it is more sensitive to them than are most cryostats, providing a quick go no-go gage of overall gas purity. A hygrometer, gas chromatograph, or other gas sampling devices can be employed to gain a more complete analysis.

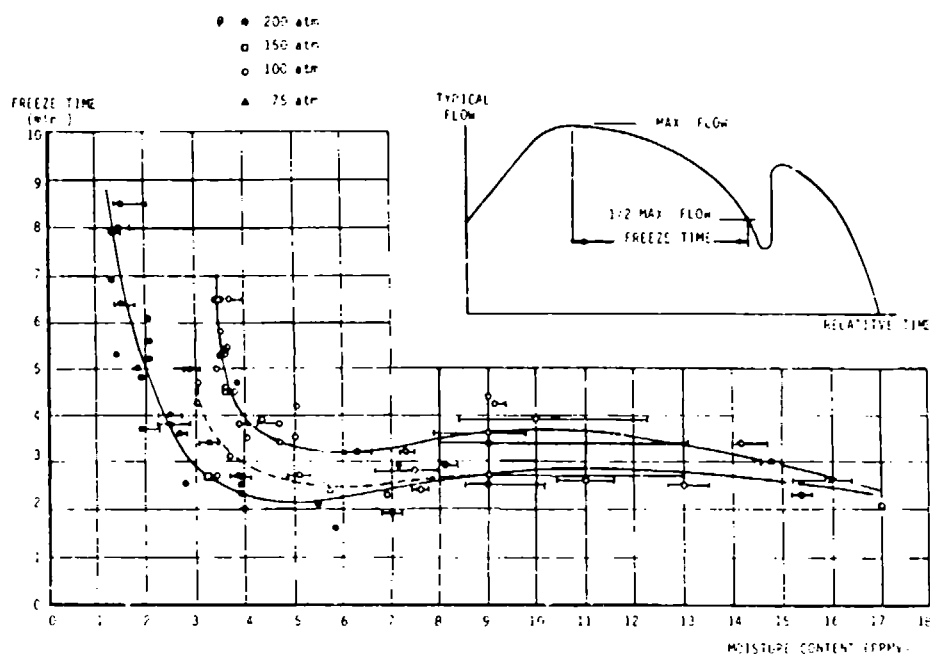


Fig.2. Gas purity monitor.
Freeze time vs. moisture content in nitrogen.

Handling

It is important to minimize the exposure of JT Cryostats to H_2O and other contaminants. Various storage methods can be employed to control their exposure. Unprotected storage in a typical laboratory is inadequate. The first improvement would be to seal the JT cryostat in a water vapor-proof bag. A dust-free package of dessicant could be sealed inside the bag to adsorb H_2O . A second improvement would be to seal the JT cryostat in a room temperature dry box, either purged with pure N_2 or dessicated. A third improvement would be to store it in a heated dry box, thereby degassing the surfaces. A fourth improvement would be to store it in a vacuum oven, thereby withdrawing the outgassed vapors. An oil-less, two-stage 30 L/min diaphragm pump @ < 25 torr on an oven at 70 C has been found to reduce the H_2O level to a few ppmv. It is important to keep the vacuum pump as close as possible to the oven, and the overall system clean and leaktight. Oil-lubricated vacuum pumps should be limited to 0.20 torr, and have a foreline trap to inhibit oil from backstreaming into the oven.

Before operating a J cryostat, purge the gas supply system and cryostat for several minutes with the pure process gas @ < 3 MPa. This flushes air and outgassed contaminants from the piping system. It is

also important to properly warm up the JT cryostat and dewar after each operating cycle. Cryopumping can occur on the exhaust side of the heat exchanger which can condense H₂O into the cold end area as it warms. This H₂O can freeze on the nozzle on subsequent cooldowns and cause erratic performance. Such adverse effects can be controlled by exhausting to a controlled dry environment, by using exhaust check valves to prevent backstreaming, or by continuing the supply gas at the end of the operating period at reduced pressure, < 3 MPa, until the cold end is > 273 K. Low level contaminants in the gas supply may accumulate, and backstreaming may occur during long operating periods (i.e. days/weeks). Therefore, it is usually necessary to warm up the system periodically.

When a JT cryostat has been exposed to excess H₂O, vacuum baking @ < 25 torr and < 80°C overnight is recommended. Alternately, it can be purged with pure N₂ at < 3 MPa. Contaminants that accumulate in a porous filter are difficult to completely remove, and usually require replacing the filter. Purging or vacuum baking may temporarily clean a path through a filter loaded with condensible contaminants, but the residual boundary contaminants will continue to mix with the incoming purer gas. Flushing with a liquid solvent is not recommended because the liquid will flush trapped particles downstream, and the solvent will be difficult to remove from the filter afterward.

Temperature Stability

The temperature stability of a JT cryostat-cooled dewar and load is dependent upon stable heat loads and a stable flow. Changes in heat load result in a change in the ΔT between the device being cooled and the liquid cryogen. Changes in flow rate have a small effect on heat transfer ΔT as discussed in the next section, but do change the pressure drop in the exhaust side of the heat exchanger. A change in the pressure of the liquid, whether it is caused by a change of pressure drop, altitude, or a valve in the vent line, will cause a change of temperature. For LN₂ at 77.4 K the change is 0.088 K/kPa. The nozzle flow is a sonic compressible gas condition, proportional to supply pressure and nozzle temperature as $P/T^{0.5}$. Therefore, as the supply pressure varies, as a pressure regulator fluctuates, or as a demand flow nozzle varies, so will the stability of the cold end temperature. These effects may cause a slow temperature change as the gas supply pressure decays in a bottle or a rapid change if the demand flow control adjusts suddenly.

A fixed flow JT cryostat or a dual-orifice type will generate an excess amount of liquid cryogen. The steady flow rate and excess liquid provide very stable temperatures, usually < 0.2 K/s variations. A demand flow JT cryostat will generate liquid cryogen proportional to the heat load, minimizing gas consumption, but the flow rate will vary, causing temperature fluctuations. Improved design and manufacturing of demand flow JT cryostats has resulted in routine temperature stability of < 5 K above the saturation temperature while maximizing gas

utilization. Better stability, within 1 K of the saturation temperature, can be obtained by increasing the average flow rate after cooldown, thus trading gas consumption for stability. This also reduces the susceptibility to clogging.

Heat Transfer of Liquid Cryogen

Gas consumption is minimized by designing the dewar cold end to have the lowest thermal mass and steady-state heat losses possible while providing the required structural support. For cylindrical plug-in JT cryostats, this is accomplished in general by minimizing the diameter of the heat exchanger sleeve. However, if the cold end cap is bonded directly to the end of the minimum diameter sleeve then the surface area may not be great enough to reduce the heat transfer ΔT to an acceptable level across the liquid film produced by the cryostat.

Figure 3 shows the design of a test sleeve that has been used to measure the heat transfer ΔT and test results for sleeves having inside diameters of 3.30 mm and 5.18 mm. Accurate measurements are obtained by brazing a flat copper plate to the end of a 0.076 mm wall stainless steel tube. The temperature of the liquid in the sleeve is determined by measuring the pressure in the heat exchanger mandrel, P1, which has no gas flow. The temperature of the copper end piece is determined by measuring the pressure of liquid in the vapor bulb, P2, which is machined into the copper. Tests were run with N_2 at supply pressures in the range of 34 MPa to 10 MPa using fixed flow JT cryostats and a demand flow type all venting to 0.10 MPa. Measurements were also made with LN_2 in the sleeves. The sleeves had static losses of about 200 mW to which additional heat was applied via heater wire wound on the copper end piece. Test results show that the ΔT is greater for the smaller diameter sleeve, as expected, and is less for the high velocity liquid produced by the cryostat than for static LN_2 . In either case the ΔT can be significant.

The data for the demand flow JT cryostat includes the ΔT due to pressure drop in the heat exchanger exhaust which tends to be small relative to the heat transfer ΔT . Conversely, for fixed flow JT cryostats the elevation of the saturation temperature due to pressure drop in the heat exchanger exhaust can be larger than the heat transfer ΔT , especially at high supply pressures. Actual values are a function of the heat exchanger design and nozzle size. An elevation of 1.6 K was measured for the 3.30 mm dia. cryostat at 34 MPa supply pressure.

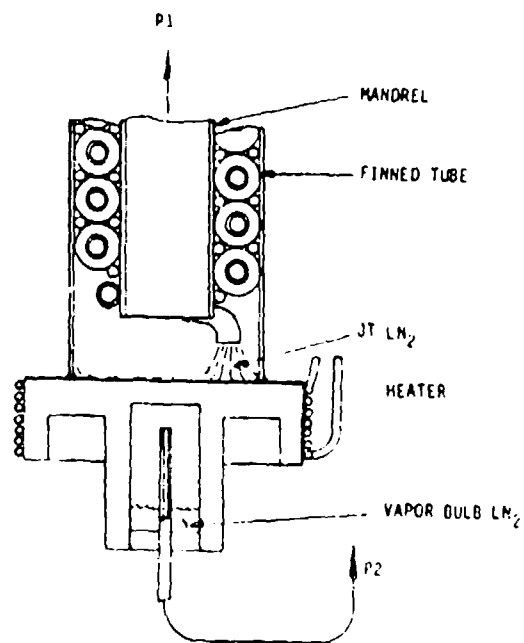
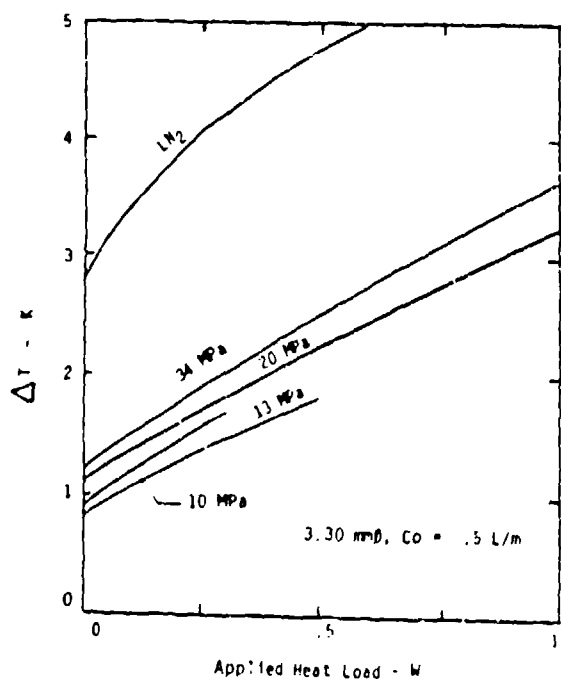
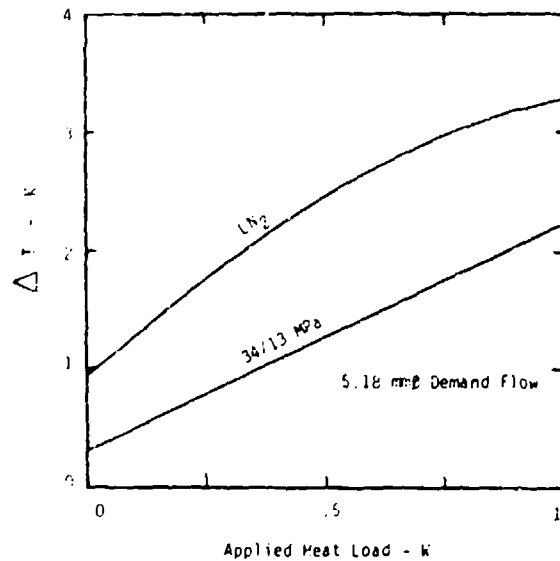
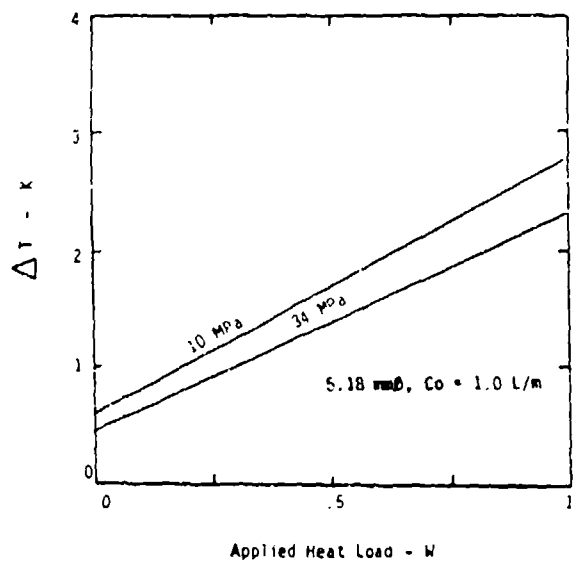


Fig.3. Measured values of the temperature difference between the LN₂ in the cryostat sleeve and LN₂ in a vapor bulb in copper end cap vs. applied heat load. Static dewar loss is 0.2 W.

Dewar Effects

The dewar is essentially a vacuum-insulated container. Proper dewar design for JT cryostats should include the following:

- (1) For cylindrical plug in, finned-tube JT cryostats: A bore with ± 0.0127 mm diameter tolerance, straightness within 0.001 mm/mm of length, and a depth such that the nozzle tip installs within 0.5 - 1.5 mm of the inside face of the cold end.
- (2) Minimized conduction heat losses entering the cold end, with vacuum insulation $< 1 \times 10^{-3}$ torr over the ambient temperature range for the intended life, and radiant heat shielding.
- (3) Minimized cold-end volume, maximized heat transfer surface area, and minimized load thermal mass. For complex load geometries, the component materials should have high thermal diffusivity, and the arrangement should attempt to minimize thermal gradients especially during cooldown. It has been found that demand flow JT cryostats will regulate flow (i.e. refrigeration) according to the local heat load which may be much less than the total load, thus extending the cooldown. This is due to poor thermal communication between the total load and the cooler.

The thermal response of a plug-in JT cryostat in a given dewar can be characterized by measuring the following:

- (1) the temperature sensor's sensitivity with respect to temperature, its repeatability, and stability with liquid cryogen inside the dewar bore;
- (2) the cooldown time from the ambient temperature by injecting liquid cryogen into the dewar bore; and
- (3) the steady state heat loss over the lower cold end half of the bore using a liquid cryogen. (Plot the volume of boiloff gas vs. time. Calculate the ave. boil-off rate during the "lower half" period, ignoring the non-linear rate near the end. Multiply by the latent heat of vaporization and the NTP density for the cryogen used. For LN₂: heat loss [mW] = boil-off rate [sL/min] x 3862.)

Gas Mixtures

A large number of gas mixtures have been tested in JT cryostats of different efficiencies. In general, it is found that adding a gas such as CH₄ to N₂ provides a refrigeration effect approximately in proportion to the sum of their separate refrigeration effects, but the operating temperature can be closer to the saturation temperature of the

colder constituent. If the heat load is increased, or the efficiency of the heat exchanger is decreased, then the saturation temperature increases toward the higher temperature constituent. Adding a gas such as hydrogen (H_2) or Ne to N_2 can reduce the boiling temperature below 77.4 K while venting to atmospheric pressure.

Figure 4 shows the results of a test with a mixture of 0.1 Ne/0.45 Ar/0.45 N_2 from a 60 mL bottle charged to 42 MPa using a fixed flow JT cryostat venting to 0.10 MPa and a repeat test with pure N_2 . The following observations apply to this test and are generally true for all of the tests with mixtures:

- (1) Initial cooldown is faster, but the time to 80 K is the same for the mixture compared with pure N_2 .
- (2) There is a time delay for the mixture to reach minimum temperature due to the time it takes to reach equilibrium concentrations in the liquid.
- (3) The temperature increases with time after reaching minimum temperature because the heat load is increasing relative to the rate at which refrigeration is produced. The increasing temperature is superimposed on a small decrease in temperature due to the decreasing gas pressure from a fixed volume and decreasing pressure drop in the heat exchanger exhaust as the flow rate decreases.*
- (4) The temperature of the mixture rises at the end of the test toward the NBP of the higher temperature constituent, in this case Ar, and holds there while the residual liquid, rich in Ar, evaporates.

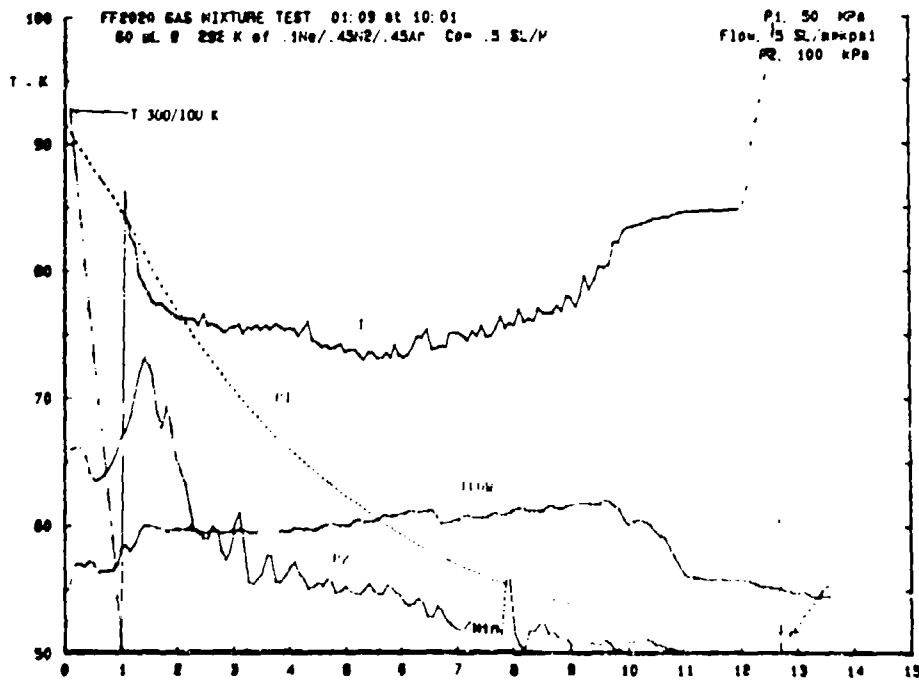
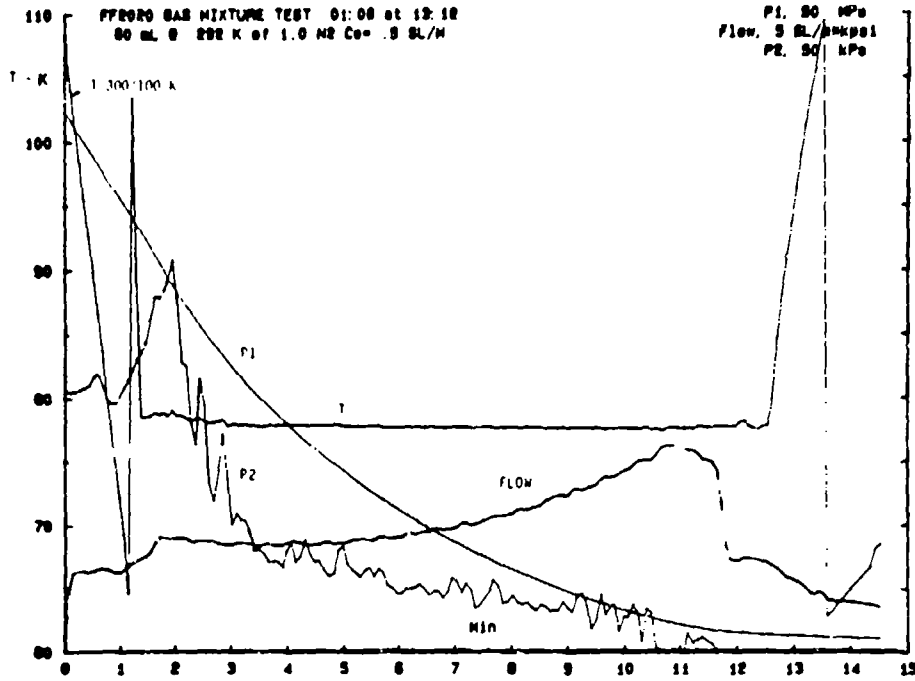


Fig.4. Temperature, T, bottle pressure, P1, pressure over the liquid, P2, and normalized flow vs. time for pure N₂ (upper) and a mixture of .1 Ne/.45 N₂/.45 Ar₂ (lower) venting to atmospheric pressure.

SUMMARY

JT cooling systems are relatively simple and versatile but have frequently presented problems for the user because of their sensitivity to contaminants. It is hoped that the experience which is presented in this paper will help users design and operate JT systems with a high degree of success.

REFERENCES

1. Longworth, "Advances in Small Joule-Thomson Coolers," Cryogenic Engineering Conference, 1989.
2. Little, "Advances in Joule-Thomson Cooling," Cryogenic Engineering Conference, 1989.
3. Hughes and Herr, "Mariner Mars 1969 ir spectrometer: Gas delivery system and JT cryostat," Cryogenics, September 1973.
4. General Pneumatics Patent No. 4,631,928 and/or 4,738,122.
5. APD Cryogenics Patent No. 4,653,284.
6. Krippene, Kurek, and Samuels. "The Nines Mirage," Pittsburgh Conference and Exposition, 1989.
7. Kanno and Ohmi, "Components Key to Developing contamination Free Gas Supply," Microcontamination, December 1988.
8. Longworth, "Comparison of Multi-Component Gas in Single-Circuit JT Heat Exchanger with Multi-Gases Multi Circuits," JPL Gas Mixture Conference, December 1989.

CHARACTERIZATION OF COOLANTS FOR JOULE-THOMSON CRYOCOOLERS

B. Maytal* and S. W. Van Sciver
Applied Superconductivity Center, University of Wisconsin
Madison, Wisconsin 53706 USA

ABSTRACT

The main thermodynamic characteristics of a coolant for the Joule-Thomson cryocoolers include: the isothermal and isenthalpic Joule Thomson effects $(\Delta h)_T$, $(\Delta T)_h$ and the normal boiling temperature T_{boil} . The present paper describes general trends in the candidate gases for Joule-Thomson cryocoolers. Correlations are presented for the generalized integral inversion curve and for $(\Delta h)_T$ as a function of boiling temperature. The potential use of gas mixtures adds a new dimension to the coolant selection process.

NOMENCLATURE

c_{po}	specific heat, J/(mole K)	Q	heat load, W
\underline{h}	molar enthalpy, J/mole	T	temperature, K
$\underline{h}^{\text{IG}}$	molar enthalpy of an ideal gas, J/mole	T_{boil}	normal boiling temperature, K
\underline{h}^{R}	molar enthalpy departure from ideal gas, J/mole	T_c	critical temperature, K
$(\Delta h)_T$	isothermal J-T effect, J/mole	T_r	reduced temperature, T/T_c
P	pressure, Pa	$(\Delta T)_h$	isenthalpic J-T effect, J/mole
P_c	critical pressure, Pa	Z	compressibility, PV/RT
P_r	reduced pressure, P/P_c	μ	J-T coefficient, $(\partial T/\partial P)_h$, K/Pa

*On sabbatical leave from RAFAEL and TECHNION-Israeli Inst. of Technology, Haifa, Israel.

INTRODUCTION

The Joule-Thomson (J-T) cryocoolers based on Linde-Hampson liquefaction process are widely applied in cold electronics, night vision and guidance systems¹ and (more specific type) space applications.² In most cases, they are constructed as compact finned or miniature photolithographically processed³ heat exchangers with or without a flow regulating mechanism. However the physical description does not include one of the most important components that of the coolant. The thermodynamic characteristics are a significant feature for the design and operation of a J-T cryocooling system. The present paper represents an attempt to summarize some of the main thermodynamic parameters of candidate coolants and their interrelation.

MATCHING SYSTEM REQUIREMENTS: T_{boil} , $(\Delta h)_T$ and $(\Delta T)_h$

The Joule-Thomson cryocoolers for sensors have to meet three principal and fundamental demands: (a) sensor operation temperature, (b) gas consumption and (c) cooldown rate (or period). The various systems might be classified according to the emphasis on each of those demands. For example, low gas consumption systems which are not concerned about the cooldown period or fast cooling down system⁴ for short operation where the gas consumption is of little importance. In between there are many other weighted combinations of these demands. The characteristics of a coolant are directly derived from the above systems requirements. Three coolant factors describe the ability to meet those requirements:

(a) Sensor's Operation Temperature

The designed sensor temperature is chosen to provide the optimal performance of the device. Possible sensor temperature are mainly the normal boiling temperatures: T_{boil} of liquefied gases. In practice two additional construction details should be taken into account: (1) thermal resistance between coolant bath and sensor and (2) back pressure resulting from hydrodynamic resistance of outlet flow. Higher back pressure will increase the boiling temperature.

Figure 1 shows the discrete normal boiling temperatures which are available using liquefied pure coolants. Any intermediate temperature among those is unachievable. The wide gap between Neon (27.1 K) and Nitrogen (77.4 K) of course, cannot be bridged by any pure coolant. (One possible solution using gas mixtures will be discussed later.)

(b) Gas consumption

The energy-based specific refrigeration content of a coolant is well represented

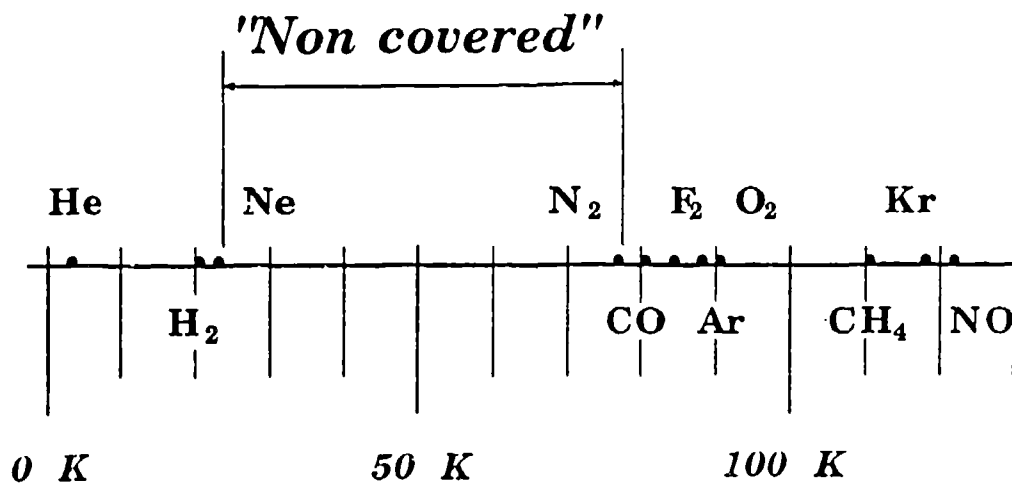


Fig. 1: Cryogenic available discrete temperatures of pure boiling liquefied coolants.

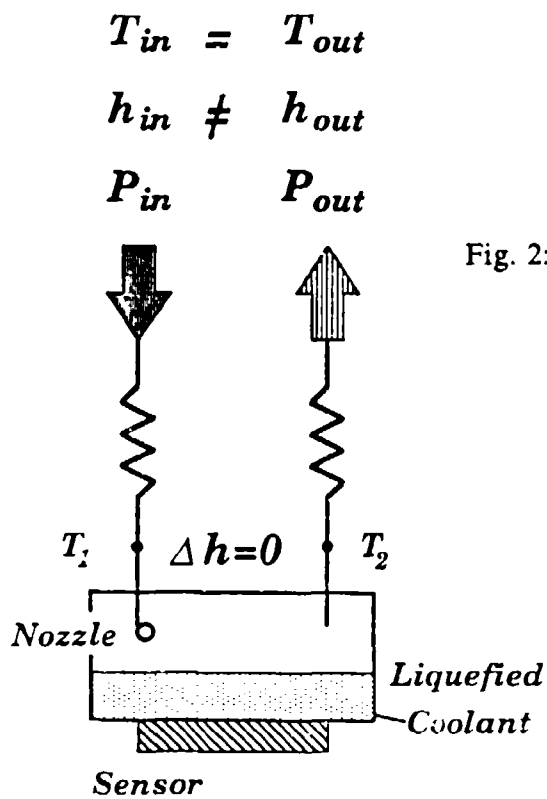


Fig. 2: Schematic illusion of ideal J-T cryocooler (and notation).

by the isothermal Joule-Thomson effect, $(\Delta h)_T$, defined through notations on Figure 2:

$$(\Delta h)_T \equiv h_{out} - h_{in} = h(0.1 \text{ MPa}, T) - h(P, T)$$

Applying the First Law of Thermodynamics for an open system and assuming an ideal heat exchanger of equal outlet and inlet temperatures one gets:

$$Q = \dot{n} (\Delta h)_T$$

A given heat load (Q) is carried through a smaller molar flowrate (\dot{n}) by a coolant of higher $(\Delta h)_T$. A smaller compressor will be sufficient for the same mission. There are application of autonomous operation: pressurizing through a storage vessel. Reduction in the gas consumption will result in reduced volume or weight of the vessel and simplify the logistics of vessel's supply. It is advantageous to use molar quantities because similar number of moles of different coolants might be contained at a same vessel.

(c) Cooldown rate

Just at the very beginning of the cooldown process, the "driving force" is the temperature drop for isenthalpic expansion through the nozzle, $(\Delta T)_h$. That process is a transient phenomenon of the heat exchanger while being forced through the temperature difference $(\Delta T)_h$ between the cold and hot streams. The $(\Delta T)_h$ is the integral isenthalpic Joule-Thomson effect which is a state dependent coolant feature. For similar flowrates the higher $(\Delta T)_h$ coolant will result in a more rapid cooldown of the cryocooler. Following the notation of Figure 2 let T_1 and T_2 be the inlet and outlet nozzle temperatures. They fulfill the isenthalpic relation:

$$h(T_1, P) = h(T_2, 0.1 \text{ MPa})$$

and

$$(\Delta T)_h = T_2 - T_1$$

THE INTEGRAL JOULE-THOMSON EFFECT, $(\Delta T)_h$

The Linde-Hampson liquefaction system is controlled by the J-T integral rather than by the differential form, $\mu = (\partial T / \partial P)_h$. However, most of the data available in physics and engineering likewise is processed in the differential form. These two are interrelated through the line integral over the isenthalpic curve:

$$(\Delta T)_h(P, T) = \int_P^{0.1 \text{ MPa}} \mu(P, T) dP$$

The inversion curve has been prepared for many gases and modeled by some generalized equations of state.¹⁰ An integral inversion curve in terms of reduced temperature and pressure is plotted in Figure 3. The graph displays the locus of states (pressure for each temperature) which will exhibit an overall cooling down effect, while expanding isenthalpically from any P_r to $P_r = 0.0$.

Following the law of corresponding states, the generalized integral inversion curve can be displayed in terms of reduced parameters for all gases with similar acentric factors (in the sense of ref. 5). N_2 , Ar and CO are examples of low acentric factor gases (correspondingly $\omega = 0.04, 0., 0.049$). Fifteen experimental values⁶ representing $(\Delta T)_h = 0$ have been correlated in Figure 3. The solid line which is the proposed generalized integral inversion curve is written:

$$T_r = 5.2292 - 0.10510 \cdot P_r + 5.6442 \cdot 10^{-4} \cdot P_r^2$$

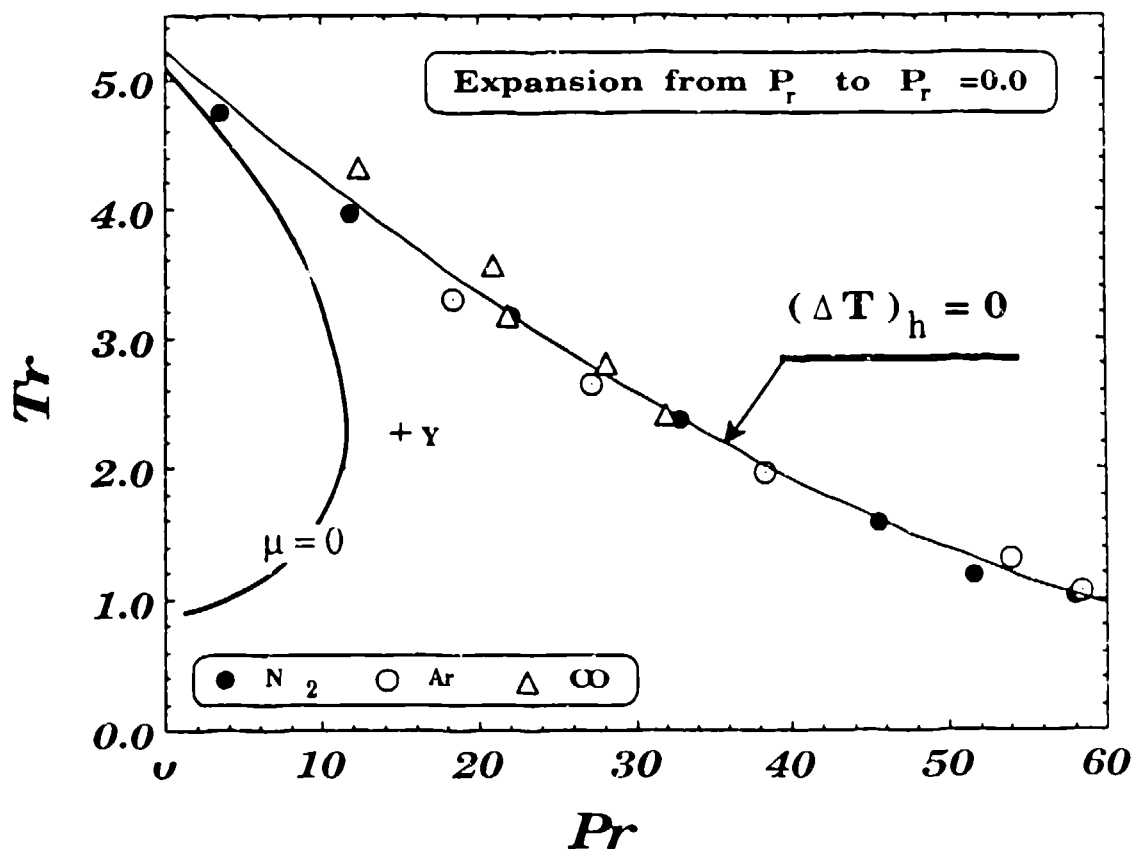


Fig. 3: Generalized integral (and differential) Joule-Thomson inversion curves. Points for N_2 , Ar and CO based on ref. 6.

A correlation factor of 0.993 is obtained for these data. The generalized differential inversion curve is also shown following the correlation proposed in ref. 10. Both curves should coincide at the maximum inversion temperature ($P_r \rightarrow 0$); however, some deviation is observed since the data is obtained from various experimental sources.

The integral cooling zone contoured by $(\Delta T)_h = 0$ is larger and includes the differential one obtained from setting $\mu = 0$. For instance, nitrogen in the state of 50 MPa and 300 K is represented in Figure 3 by point Y corresponding to $P_r = 14.73$ and $T_r = 2.37$. That state is out of the differential cooling zone so it will heat up through differential expansion. However through integral expansion to 0.1 MPa ($P_r = 0.0$) it will still cool down.

The $(\Delta T)_h$ may serve for ordering the coolants (Table 1) according to their cooling down rates. Argon, having a more negative $(\Delta T)_h$ will cool down faster than nitrogen. That is in accordance with practice using for fast cooldown applications⁷ Argon or in sequenced operation followed by nitrogen. The positive $(\Delta T)_h$ helium based on ref. 8 means that under the mentioned conditions the Joule-Thomson "cryocooler" will heat up. (The results of an experiment to demonstrate the effect are shown in Figure 4. Temperature rises at three rates according to the applied helium pressure.)

Table 1: Ordering of coolants through their integral isenthalpic J-T effect $(\Delta T)_h$ at 30 MPa and 300 K. (Based on Peng-Robinson equation of state.¹⁵)

He	+ 18.7 K
N ₂	- 41.5 K
F ₂	- 45.9 K
CO	- 47.8 K
O ₂	- 65.8 K
NO	- 70.5 K
Ar	- 81.8 K
CH ₄	- 107.8 K

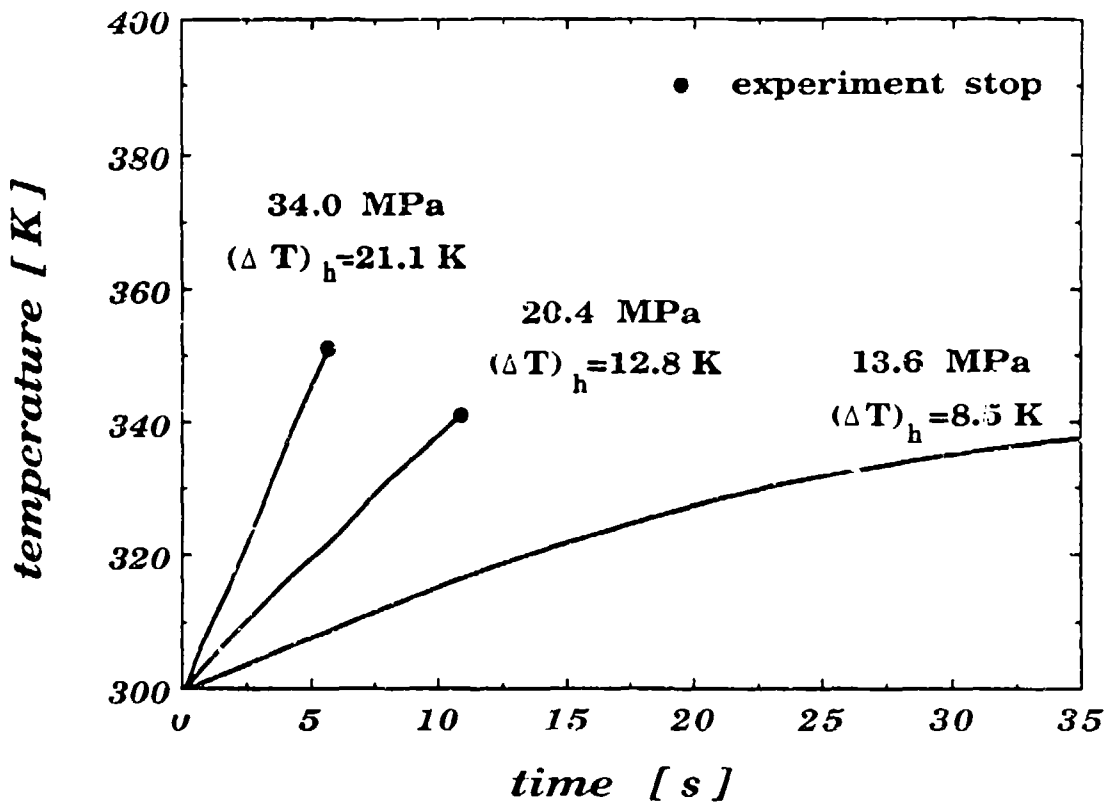


Fig. 4: Heating up by helium expansion through a Joule-Thomson "cryocooler" (experimental results).

Furthermore, different states of the same coolant or two coolants at different states (Table 2) are comparable through $(\Delta T)_h$ for their cooling down rates. At the above example: nitrogen at (50 MPa, 300 K) will cool down at the same rate as argon at (30 MPa, 300 K). (The benefit of pressurizing up to 60 MPa might be longer operation at the same vessel's volume). Or, argon at (20 MPa, 300 K) has a similar cooling down rate as nitrogen at (30 MPa, 235 K).

INTERDEPENDENCE of $(\Delta T)_h$, $(\Delta h)_T$ and T_{boil}

(a) ΔT_h and $(\Delta h)_T$

For any gas, the general relation was proven⁹

$$(\Delta T)_h = \frac{(\Delta h)_T}{c_{po}}$$

Table 2: Integral isenthalpic J-T effect $(\Delta T)_h$ for nitrogen and argon at various states (reference 6)

$(\Delta T)_h$ (K)					
T = 300 K			P = 30 MPa		
P	nitrogen	argon	T	nitrogen	argon
10 MPa	-18.7	-35.5	290 K	-40.7	-86.5
14 MPa	-25.0	-47.0	280 K	-44.0	-92.5
20 MPa	-31.3	-62.2	270 K	-47.6	-99.5
30 MPa	-37.7	-80.5	260 K	-51.5	-107.2
40 MPa	-39.0	-90.4	250 K	-55.6	-115.4
50 MPa	-37.6	-94.0	240 K	-60.0	-124.2

where c_{po} stands for the specific heat at the low outlet pressure (after Joule-Thomson's expansion). It is a good approximation for any ambient temperature assuming c_{po} is nearly temperature independent. Let us compare two states of the same coolant or a group of coolants with similar heat capacities like monoatomic gases (18 J/mole K) or bi-atomic gases (28 J/mole K). We may conclude that a higher $(\Delta h)_T$ involves a higher $(\Delta T)_h$. Put another way: a coolant with higher cooling content is also faster at cooling down. In the general case of an imaginary gas, without information about the c_{po} we cannot apply the above conclusion with the same evidence. However, for all known gases of low boiling temperatures the above conclusion is fulfilled.

(b) $(\Delta h)_T$ and T_{boil}

Comparing $(\Delta h)_T$ for different gases, an assumption should be made about the common basis in terms of the applied pressure. Following the law of corresponding state we may assume for that purpose pressurizing by $P_r \sim 10$. At that reduced pressure the largest isothermal integral Joule-Thomson effect is achieved for $1.2 < T_r < 3$. The differential inversion curve is the locus of maxima of isenthalpic lines at P-T plane. The above range of reduced temperatures is adequately comprehensive for most cryogenic sensor's cooling, starting liquefaction at $290 \text{ K} < T < 320 \text{ K}$. On Figure 5 $(\Delta h)_T$ is described as function of T_{boil} for sixteen coolants at 310 K and $P_r = 10$. For each coolant it was calculated through the three parameters Peng-

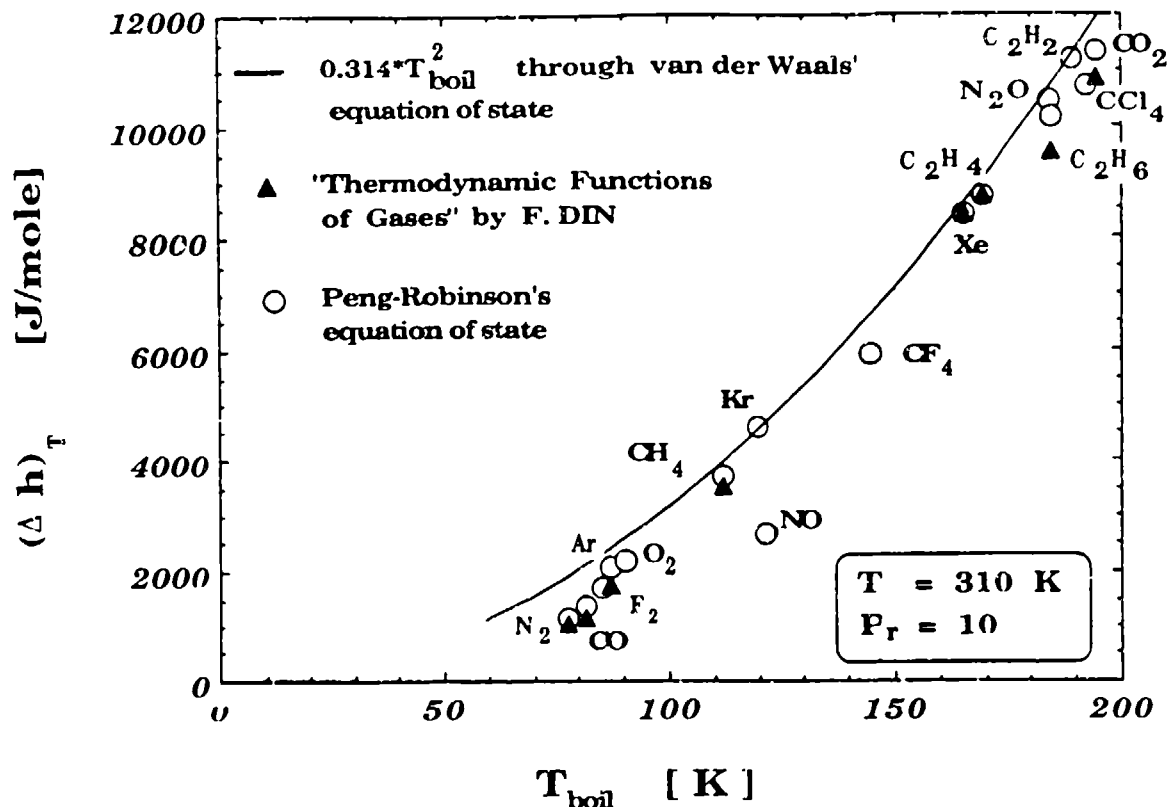


Fig. 5: Integral isothermal Joule-Thomson effect $(\Delta h)_T$ for different pure coolant as function of their boiling temperatures.

Robinson¹⁵ equation of state and compared to some (experimental) data.⁶

The general observed trend in applicative terms is: a coolant of lower liquefaction temperature is less refrigeration content. The solid line represents an approximated expression derived in Appendix through the two parametric van der Waals equation of state:

$$(\Delta h)_T = 11.72 \frac{R}{T} \cdot T_{boil}^2$$

GAS MIXTURES

The search for a proper mixture is very attractive because of the additional degrees of freedom in coolant design or choice. Some of the points that make it very

special are:

(a) Bridging the gaps between the discrete normal boiling temperatures of pure substances. For example: a sensor optimally performing at 65 K have to be cooled by liquefied mixture, because there is no pure coolant between nitrogen (77.4 K) and neon (27.1 K).

(b) Possible more refrigeration content mixture than a pure substance having the same boiling temperature. Koepp¹¹ showed experimentally that integral isenthalpic J-T effect for mixtures was at least equal to the molarly weighted mean effect of the pure components. Alfeev¹² pointed out the improved efficiency in mixtures operated J-T coolers. Little¹³ reports on a mixture of halon, hydrocarbons and nitrogen being more efficient and faster than nitrogen itself at 80 K.

(c) Generally the cooler design is not affected by the use of mixtures instead of pure coolants, which means that the same technology and hardware can be applied.

CONCLUSIONS

The thermodynamic parameters of pure coolants T_{boil} , $(\Delta T)_h$ and $(\Delta h)_T$ are interconnected. Both $(\Delta T)_h$ and $(\Delta h)_T$ are increasing functions of T_{boil} . Mixing of pure coolants is a source for new coolant with new pseudo-critical parameters.

APPENDIX

Real gas enthalpy departure from the ideal gas model, \underline{h}^R , can be formulated¹⁴ through its compressibility, Z , as:

$$\frac{\underline{h}^R(P, T)}{RT} = \frac{\underline{h}(P, T) - \underline{h}^{IG}(P, T)}{RT} = -R \cdot T_r \cdot \int_{P_r=0, T_r}^{P_r, T_r} \left(\frac{\partial Z}{\partial T_r} \right) \frac{dP_r}{P_r} \quad (1a)$$

For simpler drawing of the general trend we may avoid the differences of molecules' acentric factors and apply the two parameters van der Waals equation of state. Recalling that \underline{h}^{IG} is only temperature dependent we get:

$$\begin{aligned} (\Delta \underline{h})_T &= \underline{h}^R(P_{\text{out}}, T) - \underline{h}^R(P_{\text{in}}, T) \\ &= \left[-\frac{27}{64} \frac{R \cdot P_r}{T \cdot Z} \cdot T_c^2 + (Z-1)RT \right]_{P_{r,\text{in}}}^{P_{r,\text{out}}} \quad (2a) \end{aligned}$$

where $P_{r,in} = P_{in} / P_c$ and $P_{r,out} = 0.1 \text{ MPa} / P_c$.

Let us assume $P_r \sim 10$. (For cases of $1.2 < T_r < 3.0$ it gives the maximum Joule-Thomson effect.) From compressibility data we get $Z (P_r \sim 10) \sim 1$. Assuming empirically $T_{boil} \sim 0.6 T_c$ and $P_{r,in} \gg P_{r,out}$ we get from (2a)

$$(\Delta h)_T = 11.72 \cdot \frac{R}{T} \cdot T_{boil}^2 \quad (3a)$$

It should be remarked that for $T_c < 100 \text{ K}$ the term in equation (2a) that includes T_c^2 is not big enough in comparison to $(Z-1) RT$, so that relation can not be applied.

REFERENCES

1. Walker, G., "Miniature Refrigerators for Cryogenic Sensors and Cold Electronics," in: *Monographs on Cryogenics*, Oxford University Press, Oxford, UK (1989).
2. Hughes, J. L. and Herr, K. C., "Mariner Mars 1969 Infrared Spectrometer: Gas Delivery System and Joule-Thomson Cryostat," *Cryogenics*, vol. 13 (1973), p 513.
3. Little, W. A., "Microminiature Refrigeration," *Review of Scientific Instruments*, vol. 55 (1984), pp. 661-80.
4. Clarke, J. D., Dunn, W. A. E. and Gowlett, "Fast Cool Down I.R. Detectors," presented at *IEEE*, London (June 3-5, 1986).
5. Pitzer, K. S., *J. Am. Chem. Soc.*, vol. 77 (1955), p. 3427.
6. Din, F., *Thermodynamic Functions of Gases*, Butterworths, London (1961).
7. Hart, R. R., "Minicooler Systems for Fast Cooldown Applications," Technical Memorandum TM 1341, Hymatic Eng. Co. Ltd., Redditch, Worcester, UK.
8. McCarty, R. D., NBS Tech. Note 1029, U.S. Govt. Print Office (1980).
9. Gustaffsson, O., "On the Joule-Thomson Effect for Gas Mixtures," *Physica Scripta*, vol. 2 (1970), pp. 7-15.
10. Gunn, R. D., Chueh, P. L. and Prausnitz, J. M., "Inversion Temperatures and Pressures for Cryogenic Gases and their Mixtures," *Cryogenics*, vol. 6 (1966), p. 324.
11. Koeppe, W., "Zum Thomson-Joule Effekt von Gassen und Gasgemischen," (Joule Thomson Effect of Pure Gases and Gas Mixtures), *Kaltetechnik*, vol. 11 (1959), p. 363.
12. Alfeev, V. N., Brodyansky, V. M., Yogodin, V. M., Nikolsky, V. A. and Ivatsov, A. V., Dutch Patent Application No. 7106470 (Nov. 14, 1972).

13. Little, W., "Integrated Cryogenic Chip Carrier for High Speed CMOS and Superconducting Devices," *Proc. Symp. Low Temperature Electronics and High Temperature Superconductors*, The Electrochemical Society, Pennington, NJ, USA, (1987).
14. Sandler, S. I., *Chemical and Engineering Thermodynamics*, John Wiley and Sons, New York (1989).
15. Peng, D. Y. and Robinson, D. B., "A New Two Component Equation of State," *Ind. Eng. Chem. Fund*, vol. 15 (1976), p. 59.

RECENT DEVELOPMENTS IN CLOG RESISTANT AND DEMAND FLOW CRYOSTATS

J. W. Prentice, G. Walker, and S. G. Zylstra
General Pneumatics Corporation
Western Research Center
Scottsdale, AZ 85260

ABSTRACT

A cryostat composed of a special anti-clogging Joule-Thomson (J-T) expansion nozzle combined with demand flow regulation, derived by the use of materials with different coefficients of thermal expansion, was developed in the recent past. This new type of cryostat has proved to be remarkably rugged and highly resistant to blockage by contaminants in the gas flow. In addition, the cryostat has displayed surprisingly stable temperature characteristics.

The new cryostat design has now been applied to a variety of systems with different fluids and special requirements over a range of refrigeration capacities. This paper will discuss some of the interesting situations and problems encountered in devising new variations of the basic design. Recent applications include use of liquid cryogen working fluid, modular designs, and variable capacity systems.

INTRODUCTION

Development of the General Pneumatics (GP) patented cryostat design has progressed at the Western Research Center since the previous paper "A Non-Clogging, Temperature-Sensitive, Closed-Cycle Linde-Hampson Cryocooler"¹ presented at the Fifth International Cryocooler Conference held in 1988. Following fabrication and testing of a cryostat for NASA capable of producing up to 37 Watts of refrigeration at 85 K when supplied with nitrogen at 13.8 MPa, attention was turned toward producing a 1/4 Watt common module size cryostat, shown in Figure 1.

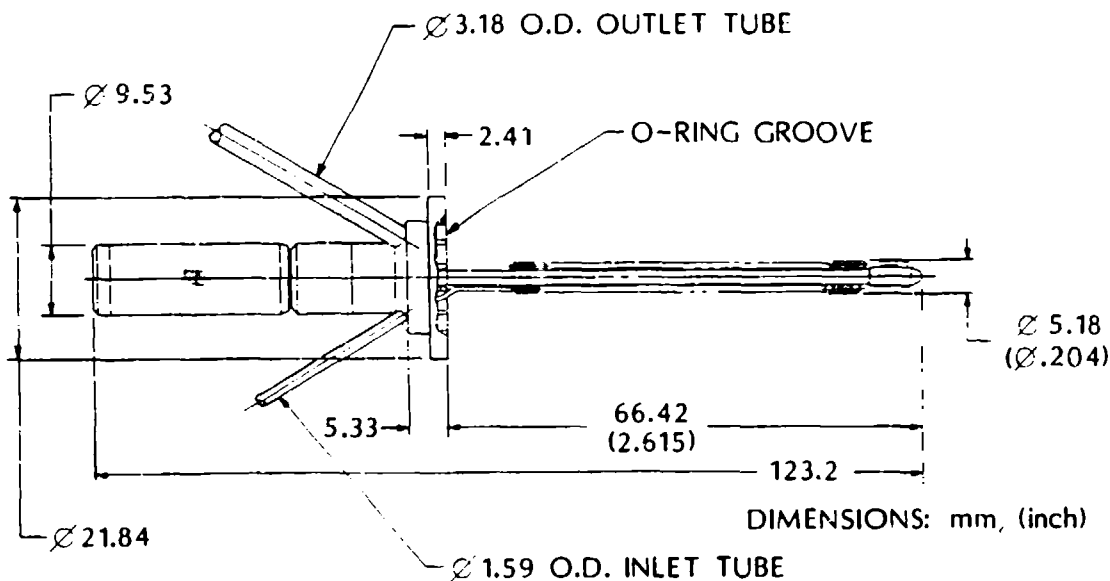


FIGURE 1. COMMON MODULE SIZE CRYOSTAT

Additional low capacity cryostats have been fabricated for use with nitrogen, argon, mixed gases, and liquid methane. Proposed uses have included deriving refrigeration while venting liquid hydrogen, to replacing a two-gas cooldown system with a single demand flow cryostat.

DESIGN FEATURES

Each of the GP cryostat designs are unique to the field of cryogenics in that they feature a clog resistant J-T isenthalpic expansion nozzle. Additionally, the flow (hence, refrigeration capacity) is controlled by optional combinations of a demand flow feature and a manual micrometer-like adjuster. As experience has been gained, these and other features along with the related fabrication techniques have been refined.

NOZZLES

The nozzle of the cryostat converges to an annular orifice formed by a tapered core. Circumferential grooves machined into the tapered core provide turbulence which allows wider flow passages and helps to break up and clear contaminants. This action combined with the large annular circumference relative to the flow area provides the patented clog resistant characteristic of the nozzle.

The included angle of the converging nozzle geometry influences adjustments to the mass flow rate. A 30 degree included angle increases the flow area more for each linear movement of the core than does a 15 degree angle. No appreciable difference in refrigeration capacity has been noted when comparing the 15 and 30 degree angles. Nozzle angles are therefore chosen based on flow control requirements.

During testing of a non-demand flow GP cryostat with a 30 degree nozzle, it was noted that the mass flow of the liquid methane working fluid increased slightly as the temperature at the nozzle decreased. The cause of the variation has been identified as the unexpected decrease in the kinematic viscosity with temperature. As the temperature decreased the dynamic viscosity increased, but the density increased more dramatically. Thus, the flow increased.²

DEMAND FLOW REGULATION

Demand flow regulation is the ability of a cryostat to achieve and maintain its refrigeration temperature with minimal flow while subjected to varying heat loads. The optional GP demand flow feature is achieved by differential thermal contraction of the materials supporting the nozzle and its core.

GP cryostats have been tested that regulated from an initial cooldown flow of 18 standard liters per minute (slpm), measured at the exit, to 3 slpm after achieving liquid nitrogen temperature. This was calculated to be a change from 5.2 to .9 watts of refrigeration based upon a 7% liquid yield. By using thermally active 304 stainless steel and thermally inactive Invar 36 in conjunction with a 15 degree included angle nozzle these cryostats can maintain their heat loaded temperature well within 1 K.

MANUAL FLOW REGULATION

Micrometer manual flow regulation has been provided for both demand flow and non-demand flow cryostats. When used with the demand flow feature it enables the user to set the initial flow which determines the rate of cooldown and then, if needed, to set the lower limit of the flow at the refrigeration temperature. When used with a non-demand flow cryostat it allows for accurate adjustment of refrigeration capacity within its range of heat loads.

Several micrometer configurations have been designed using differential threads to provide as much as 3024 equivalent threads per inch (108/112 pitch). One design using brass against stainless at the thread interface was found to bind at liquid methane temperatures near 111 K. Differential contraction in the longitudinal direction was suspected as the cause. The most recent micrometer design avoids this problem by using Inconel 718 against 316L stainless and by using a more tolerant 70/72 pitch differential thread (2520 equivalent threads per inch). Also, the thread arrangement allows the slightly more thermally active stainless threads (16×10^{-6} m/m·K) to contract away from the Inconel threads (13×10^{-6} m/m·K).

HEAT EXCHANGERS

GP cryostats employ helically wound finned tube heat exchangers constructed of 70/30 copper/nickel alloy. The heat exchanger is formed by wrapping the finned tubing around an inner sheath tube. A polyester thread is co-wound above and below the finned tubing to provide spacing and to direct the flow close to the finned tube. The number of wraps determines the overall length of the heat exchanger.

The internal diameter of the heat exchanger tube carries the high pressure flow to the nozzle. The configuration of the external finned or low pressure side primarily determines the effectiveness of the contra-flow heat exchanger. Effectiveness can be calculated by the equation ³:

$$\epsilon = \frac{T_{c2} - T_{c1}}{T_{h1} - T_{c1}}$$

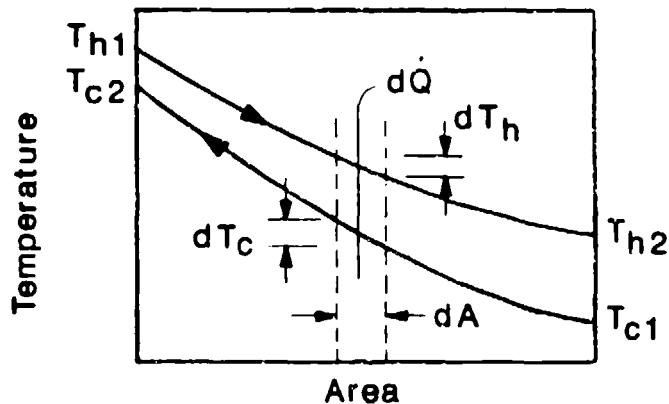


FIGURE 2. EFFECTIVENESS

As the effectiveness approaches 100%, additional wraps of the finned tube have less influence due to the reduced temperature difference between the high and low pressure sides of the heat exchanger near the high temperature end.

The pressure differential (ΔP) across the length of the return flow side primarily affects the temperature at the nozzle. Increasing the ΔP increases the temperature. Considerations that influence the ΔP are the return flow area, the size and existence of a co-winding, the flow rate, the density of the working fluid, and the overall length of the heat exchanger.

GP cryostat #527DA0017 (Figure 3) was tested with several lengths of heat exchanger and two sizes of co-winding over a range of flow rates using nitrogen supplied at 13.6 MPa. For nominal flow rates of up to 20 slpm, heat exchanger lengths of 35 or more wraps provided 97 to 99% effectiveness. One cryostat with 39 wraps produced refrigeration at a maximum flow of 22 slpm. With the same cryostat, 43 wraps did not improve the heat exchanger effectiveness, but did extend the maximum flow rate to 24.5 slpm. Another configuration with 29 wraps was found to have an effectiveness of 92.3 to 98.5% depending upon the flow rate. Increasing the diameter of the co-winding from .127 mm to .254 mm increased the effectiveness by an average 2%.

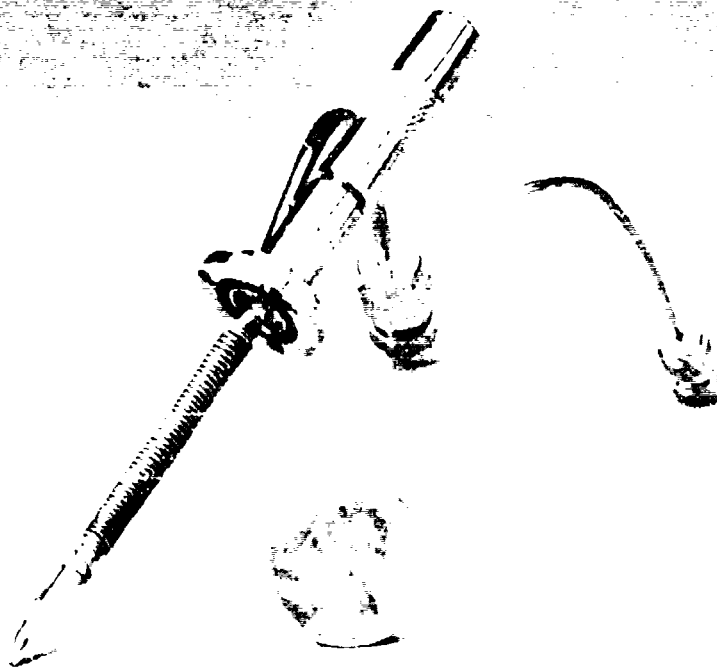


FIGURE 3. CRYOSTAT #527DA0017

MODULAR CRYOSTAT

The concept of a modular cryostat was proposed by Jack Jones of the Jet Propulsion Laboratory at a meeting that took place in January 1990. It was suggested that a cryostat could be designed with a precooling boss such that a series of like cryostats could be linked together, each one precooling the next (Figure 4). In this configuration cryogenic temperatures could be reached effectively in low pressure systems.

The first prototype modular cryostat was produced under a contract with Aerojet ElectroSystems (Figure 5). The design objectives using argon as the working fluid and the initial test results are enumerated in the following paragraphs.

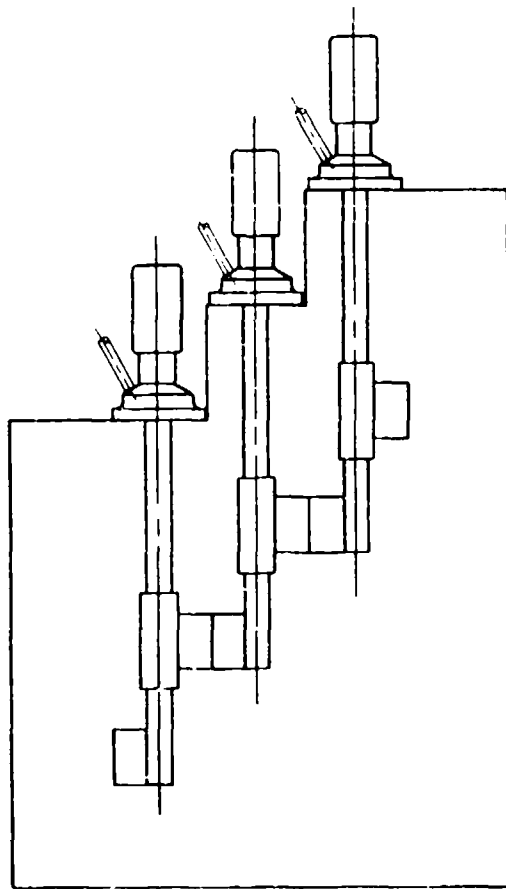


FIGURE 4. MODULAR CRYOSTAT CONCEPT

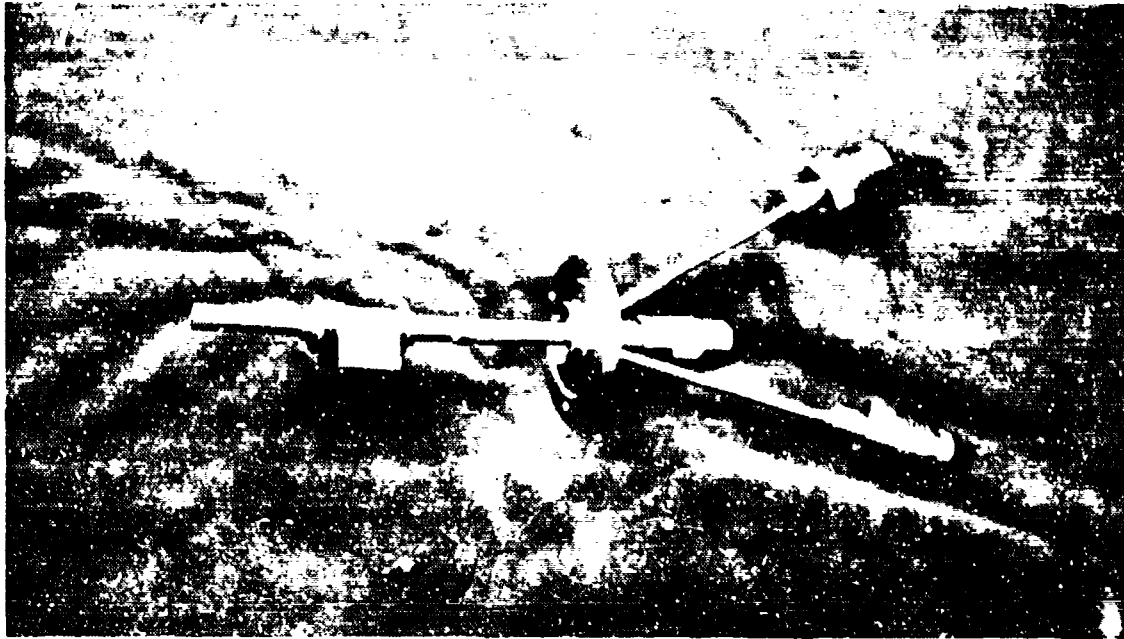


FIGURE 5. MODULAR CRYOSTAT

REFRIGERATION CAPACITY

It was desired that the refrigeration capacity at the cold end of the cryostat would be approximately 1 Watt at 90 K for each 0.01 grams per second of argon flow over the range of .01 to .07 g/s. For a latent heat of vaporization equal to 162 Joules/gram this implies a minimum required liquid yield of 61.7 %. Argon enters the cryostat at 4 MPa from 300 K. It can be shown on a Temperature vs. Entropy (T-S) diagram (Figure 6) that only 4% liquid yield would be produced by a J-T cryostat under these conditions.³ Therefore, the modular cryostat was designed to include a precooling section referred to as the condenser.

CONDENSER

The condenser was positioned to divide the finned-tubing heat exchanger into an upper and lower section. The location was determined by thermodynamic analysis and confirmed by the T-S diagram. Argon gas enters the condenser at near 165 K having been cooled by the sensible heat extraction of the upper heat exchanger. Argon leaves the condenser as saturated liquid near 130 K. Additional heat is removed by the lower heat exchanger before the liquid is introduced to the isenthalpic expansion of the nozzle.

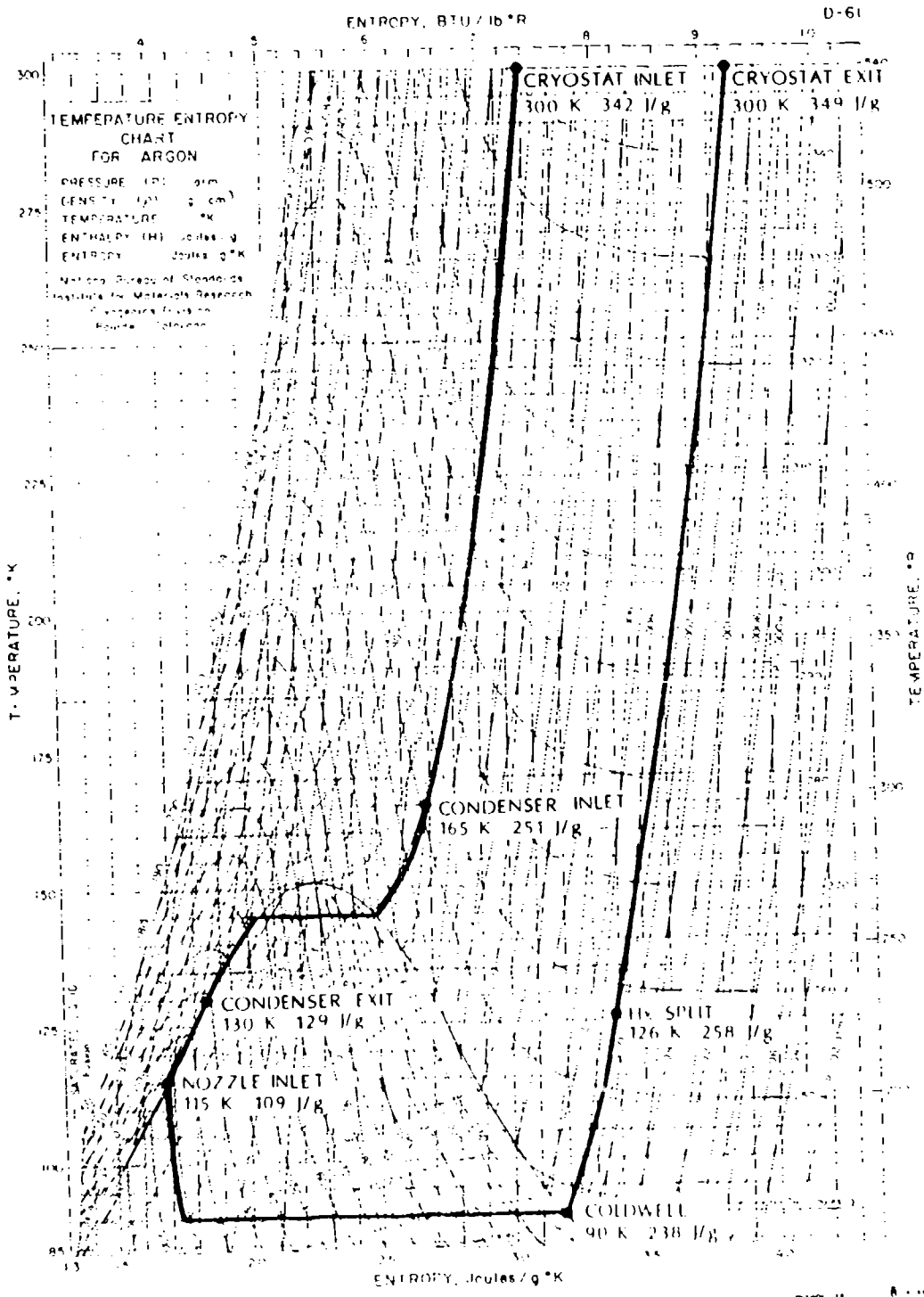


FIGURE 6. T-S DIAGRAM

NOZZLE

The working fluid passing through the clog resistant nozzle expands to the pressure of the coldwell producing a mixture of liquid and vapor. The pressure is dependant upon the outlet tube pressure plus the return flow pressure drop of the heat exchanger.

HEAT EXCHANGER

The heat exchanger was designed to minimize the return flow pressure drop to 6.8 KPa (1 psi), thus insuring a refrigeration temperature of 90 K or less. During testing the pressure was measured to be slightly more than 6.8 KPa for the maximum flow rate of .07 grams/second.

It was determined that the effectiveness of the upper heat exchanger could be as low as 80%. Any difference between the actual and 100% can be made up by extracting more heat through the condenser. Furthermore, any inefficiencies in the lower heat exchanger would pass on refrigeration to the upper heat exchanger and enhance its efficiency.

TEST CONFIGURATION

The test equipment was configured to measure the resultant refrigeration capacity at the anticipated 90 K temperature cold end. An Omega Pt100 RTD inserted into a small copper block fitted around the coldwell provided temperature measurements. Correction to these measurements was needed to compensate for inadequate thermal anchoring.⁴ The power required to vaporize the liquid argon, (refrigeration capacity), was determined from multiplication of the voltage and current applied to a carbon resistor inserted into the copper block.

The rate of heat extraction from the condenser was also determined. A copper bar attached to the condenser by a #6-32 UNC screw provided a heat transfer conduit to a liquid nitrogen heat sink. The sink was fabricated by silver soldering a 3.18 mm (.125 in.) stainless steel tube coiled around a 19 mm (.75 in.) diameter copper rod. A Minco heater button was attached to the copper bar to balance the heat load of the liquid nitrogen flow through the tube. An RTD was potted into the #6 screw to monitor the temperature at the condenser. In this way the heat extracted could be calculated as the heat capacity of the liquid nitrogen flow minus the heat load of the heater button required to maintain the desired temperature at the condenser (Figure 7)



FIGURE 7. HEAT TRANSFER CONDUIT

An inverted belljar was adapted to provide vacuum insulation around the cryostat and the condenser heat sink (Figure 8).



FIGURE 8. BELL JAR TEST CONFIGURATION

TEST RESULTS

Test results indicate that both the modular cryostat and the test equipment functioned in predictable manner. With argon supplied from 300 K at 4 MPa the cryostat was able to produce additional refrigeration at 90 K in excess of the amount provided by the condenser at 130 K. Below is a table of test results.

Argon Flow (gram/sec)	Total (90 K) Refrigeration (Watt)	Condenser (130 K) Heat Extracted (Watt)	Refrigeration Gained (90 K) (Watt)
.013	0.74	0.5	.24
.019	1.96	1.5	.46
.030	2.60	2.1	.50

SUMMARY

As experience is gained with the clog resistant nozzle it continues to prove its capability in varied applications. The demand flow and micrometer adjustment features are of additional benefit wherever temperature stability and flow control are required. It is anticipated that the most recent development, the modular cryostat, will enable cryogenic temperatures to be reached effectively with low pressure systems.

REFERENCES

1. K. Hedegard, G. Walker, S. Zylstra, "Non-Clogging, Temperature-Sensitive, Closed-Cycle Linde-Hampson Cryocooler," Proc. ICC, Monterey, Calif. (August 1988) p. 25-34.
2. Graham Walker, *Miniature Refrigerators for Cryogenic Sensors and Cold Electronics*. Clarendon Press, Oxford (1989) p. 23-35.
3. Randall F. Barron, *Cryogenic Systems*. Oxford University Press, New York, (1985) p. 69-73, 121-131.
4. Guy K. White, *Experimental Techniques in Low-Temperature Physics*. Clarendon Press, Oxford (1989) p. 100-102.

INITIAL DISTRIBUTION

DTIC (12 copies)

Stephen Abush
ADP Cryogenics Inc.
1833 Vultee Street
Allentown PA 18103
215-791-6700

Robert Ackermann
General Electric Corp. Res. & Dev.
P.O. Box 8, Bldg. K-1, EP-123
Schenectady NY 12301
518-387-6730

Frank S. Adams
TSA
2401 Bristol Court S.W.
Olympia WA 98502
206-984-1677

Sol Aisenberg
Raytheon New Product Center
63 Second Avenue
Burlington MA 01803
617-270-2300

Les Albiol
Air Force
P.O. Box 92960
Los Angeles CA 90009
213-363-6878

John A. Alvarez
Perkin-Elmer
2771 North Garey Avenue
Pomona CA 91767
714-593-3581

Tamirisa R. Apparao
Penn State University
Dept of Mechanical Engineering
University Park PA 16802
814-863-4652

Louis F. Aprigliano
David Taylor Research Center
Code 2812
Annapolis MD 21402-5067
301-267-2484

M.D. Atrey
Department of Mechanical Engineering
Indian Institute of Technology, Powai
Bombay- 400 076, India

Zdenek F. Backovsky (Stan)
Rockwell International Corp.
P.O. Box 3644
Seal Beach CA 90740
213-797-3759

James R. Baker
David Taylor Research Center
Code 2712
Annapolis MD 21402-5067
301-267-2634

Michael Balister
National Radio Astronomy Observatory
2015 Ivy Road
Charlottesville VA 22903
804-296-0365

Dr. John A. Barclay
Astronautics Corporation of America
5800 Cottage Grove Road
Madison WI 53716-1387
608-221-9001

Steven Bard
JPL
MS 157-102
Pasadena CA 91109
818-354-4487

Martin Bareiss
AEG, Aktiengesellschaft
Theresienstr. 2
Germany Heilbronn
017131/6212-81

Edward L. Bartlett, Jr.
General Dynamics
234 Broadway
Norwich CT 06360
203-433-2214

William H. Baumgart
Hughes Aircraft Co.
2000 El Segundo Blvd.
El Segundo CA 90245
213-636-0912

Bill Baungret
Hughes Aircraft
P.O. Box 902, EO/ESI/A290
El Segundo CA 90245

Luc Bauwens
Mitchell/Stirling Machines/Sys, Inc.
2550 Ninth Street
Berkeley CA 94710
415-845-2528

Trevor P. Benson
Dowty Weapon Systems
Site 25, Cheltenham Road East
England GL2 90N
011-44-452-714-382

David M. Berchowitz
Sunpower, Inc.
6 Byard Street
Athens OH 45711
614-591-2221

Robert E. Bernert, Sr.
3 Pleasant Street
Thermax, Inc.
S. Dartmouth MA 02748
508-999-1231

Peter K. Bertsch
CTI-Cryogenics
266 Second Avenue
Waltham MA 02254
617-622-5389

David P. Bloomfield
Analytic Power Corporation
123 South Street
Boston MA 02111
617-542-6352

Glenn E. Bonney
APD Cryogenics Inc.
1833 Vultee Street
Allentown PA 18103
215-791-6740

John D. Bowes
Ford Aerospace
3825 Fabian Way
Palo Alto CA 94303
415-852-6869

Douglas A. Bowker
Private Consultant
P.O. Box 13506, Sinoville 0129
Pretoria SA
27-12-572547

Peter E. Bradley
NIST
325 Broadway/M.S. 583.30
Boulder CO 80303
303-497-3465

Thomas W. Bradshaw
Rutherford Appleton Laboratory
Chilton, Didcot Oxon OX11 0QX
U.K.
(0) 235 821900 x6149

G.W. Brassell
Nuclear Filter Technology, Inc.
409 Corporate Circle
Golden CO 80401
303-278-1888

R. Warren Breckenridge
Arthur D. Little, Inc.
20 Acorn Park
Cambridge MA 02140
617-864-5700 x5870

Jeffrey A. Bruning
Consultant, Nichols Research Corp.
Rt. 1, Box 692
Leasburg MO 65535
314-245-6670

Warren Buckles
Superconductivity, Inc.
P.O.Box 56704
Madison WI 53705
608-831-3700 x112

Stan Buller
R.G. Hansen & Associates
631 Chapala Street
Santa Barbara CA 93101
805-564-3388

Connie Burke
WRDC/FIVP
Wright-Patterson AFB OH 45433
513-255-4853

William W. Burt
TRW Space & Technology Group
One Space Park (R1/1126)
Redondo Beach CA 90278
213-814-0411

Robert Buzerak
Loral Aeronutronic Corp.
Ford Road
Newport Beach CA 92658
714-720-4966

Steven R. Carolus
Carelton Technologies Inc.
10 Coghram Drive
Orchard Park NY 14127
716-662-0006 x283

Constantin Carpetis
German Aerospace Research Est. (DLR)
Pfaffenwaldring 38-40
D-7000 Stuttgart-80 Germany
(0711) 6862-427

Stephen H. Castles
NASA/GSFC
Code 713
Greenbelt MD 20771
301-286-5405

James N. Chafe
David Taylor Research Center
Code 2712
Annapolis, MD 21402-5067
301-267-2149

Chung-Kin Chan
One Space Park R1/1126
TRW Space and Technology Center
Redondo Beach CA 90278
213-813-9414

Dr. Fang Chen
Oak Ridge National Laboratory
P.O. Box 2008
Oak Ridge TN 37831-6070
615-574-0712

William E. Chen
General Electric Company
3001 W. Radio Drive
Florence SC 29501
803-678-9222

Yeu-Ching Chen
The Perkin-Elmer Corporation
2771 N. Garey Avenue
Pomona CA 91767
714-593-3581 x4719

James E. Chenoweth
Air Force Wright Aeronautical Labs
AFWAL/FIEC WRDC/FIVP
Wright Patterson AFB OH 45433-6533
513-255-4853

Jean-Claude Christeler
Balzers
8 Sagamore Park Road
Hudson NH 03051
603-889-6888

Y.K. Chuah, Manager
Industrial Technology Research Inst
Bldg. 64, 195, sec. 4., Chung Hsin Rd.
Chutung, Taiwan 31015
886-35-916279

F.J. Cogswell
Boreas, Inc.
175-U New Boston Street
Woburn MA 01801
617-937-9080

Richard M. Colgate
Colgate Thermodynamics
14 Nassau Street
Princeton NJ 08542
609-921-8770

Marc B. Connally
Air Force Astronautics Lab.
AL/RKLB
Edwards AFB CA 93523
805-275-5327

Peter Coyle
Loral Fairchild Systems
9 East Haddon Avenue
Oaklyn NJ 01807
609-858-1361

J. Alan Crunkleton
Boreas, Inc.
175-U New Boston Street
Woburn MA 01801
617-937-9080

Mr. Jeffrey D. Dalton
Naval Weapons Ctr
Commander, Code 36213
China Lake CA 93555-0001
619-939-1694

Marc David
Cryophysics
9 Rue Dallery
Jouy-En-Josas France 78350
33-1-39-56-00-66

Lt. Col. Thomas M. Davis
Air Force Space Technology Center
AFSTC/SW
Kirtland AFB NM 87117
505-846-6243

Anthony J. Degregoria
Astronautics Corp. of America
5800 Cottage Grove Road
Madison WI 53716
608-221-9001

Ronald den Heijer
Koch Cryogenics International B.V.
Achtseweg Noord 5, Building AQ
Acht, The Netherlands 5651 CG
+31-40-766425

Peter C. Dent
Lake Shore Cryotronics, Inc.
64 East Walnut Street
Westerville OH 43081
614-891-2243

F. David Doty, President
Doty Scientific Inc.
600 Clemson Road
Columbia SC 29223
803-788-6497

Lionel R. Duband
University of California, Berkeley
Department of Physics
Berkeley CA 94720
415-642-3618

Stephen B. Dunn
AFSTC/SWS
Kirtland AFB NM 87117
505-846-5803

Allen L. DeForrest
Hughes-Santa Barbara Research
75 Coromar Drive/Bldg. 32/M.S. 28
Goleta CA 93117
805-562-7220

James Eastwood
Allied-Signal Aerospace Company
2525 West 190th Street
Torrance CA 90509
213-512-3361

David B. Eisenhaure
Satcon Technology Corporation
12 Emily Street
Cambridge MA 02139
617-661-0540

Donald M. Ernst
DTX
780 Eden Road
Lancaster PA 17601
717-569-6551

Ralph Fenn
Satcon
12 Emily Street
Cambridge MA 02139
617-661-0540 x271

Michael D. Fennell
Energy Science Laboratories
6888 Nancy Ridge Drive
San Diego CA 92121
619-552-2035

Rod Fernandez
Ball Aerospace Systems Group
P.O. Box 1062
Boulder CO 80308-1062
303/939-6784

James H. Firkins
RSRE Mod. P.E.
St Andrews Road, Malvern
WORCS, MR14 3PS England
0684 894630

Marvin L. Firmin
The Aerospace Corporation
P.O. Box 9045
Albuquerque NM 87119
505-846-7062

Frank B. Fisk
AFSTC/SWS
Kirtland AFB NM 87117
505-846-5803

Terry N. Fleener
Ball-Electro Optics Cryo Div.
P.O. Box 1062
Boulder CO 80306
303-939-4413

Dr. Thomas M. Flynn
Ball Aerospace
P.O. Box 1062-M.S RA/3
Boulder CO 80306
203-939-4787

Don Formiller
Hughes Aircraft Company
3100 W. Lomita Blvd. P.O. Box 2999
Torrance CA 90509-2999
213-517-6204

Paul B. Forney
Lockheed Missiles & Space
3251 Hanover St.
Palo Alto CA 94304
415-424-2121

Howard Fraser
United Technologies Carrier
P.O. Box 4803
Syracuse NY 13221
315-432-3452

Kelly P. Gaffney
USAF
Space Technology Center
Kirtland AFB NM 87117
505-846-9752

John M. Gary
NIST
325 Broadway, Mail Code 719
Boulder CO 80303-3328
303-497-3369

David Gedeon
Gedeon Associates
16922 South Canaan Road
Athens OH 45701
614-592-5166

R. Andrew Gerrick
McDonnell Douglas Space Systems
5301 Bolsa Avenue
Huntington Beach CA 92647
714-896-4391

Peter E. Gifford
Cryomech, Inc.
1630 Erie Boulevard East
Syracuse NY 13210
315-475-9692

George Giggey
Raytheon Corporation
55 Barefoot Road
Northboro MA 01532
508-393-7300

David Glaister
Aerospace Corporation
P.O. Box 92957-M.S. M4908
Los Angeles CA 90009
213-336-6716

Charles D. Glenn
Glenn Company
1610 Manton Court
Campbell CA 95008
408-378-0570

Kimberly Godshalk
Tektronix
P.O. Box 500-M.S. 50-324
Beavertown OR 97077
502-627-5444

Lt. Col. Craig Golart
WRDC/FIVP
4049 Meridell Drive
Beavercreek OH 45430-2060
513-255-4063

Harald Gotthardt
Leybold AG
Bonner Strasse 498
5000 Cologne, 51 Germany
221-347-1010

Geoffery F. Green
Code 2712
David Taylor Research Center
Annapolis MD 21402-5067
301-267-3632

Kenneth E. Green
Loral Infrared & Imaging Systems
2 Forbes Road
Lexington MA 02173
617-863-3528

Youfan Gu
Univ of Colorado/Dept of Chem Engr
Campus Box 424
Boulder CO 80309
303-492-7680

Dr. Wilfred Gully
Hughes Aircraft Company
2999 W. Lomita Blvd.
Torrance CA 90505
213-517-5664

Marvin E. Gunn, Jr.
U.S. Department of Energy
1000 Independence Ave, SW, CE-232
Washington, DC 20585
202-586-5377

Ulrich Haefner
Leybold AG
Bonner Strasse 498
5000 Cologne, 51 Germany
221-3471203

Mark Hanes
Hughes Aircraft
3100 Lomita Blvd.
Torrance CA 90505
213-517-6771

George M. Harpole
TRW R1/1022
One Space Park
Redondo Beach CA 90278
213-812-0397

John T. Harvell
CTI-Cryogenics
266 Second Avenue
Waltham MA 02254
617-622-5314

George C. Haverly
General Electric Astro Space
(M4018) 230 Goddard Blvd.
King of Prussia PA 13406
215-354-3775

Ben P. Helvensteijn
Sterling Federal Systems
1121 San Antonio Rd.
Palo Alto CA 94303
415-604-5521

John B. Hendricks
Alabama Cryogenic Engineering Inc.
P.O. Box 2470
Huntsville AL 35804
205-536-8629

Edward L. Hershberg
Tektronix
P.O. Box 500, M.S. 50-324
Beaverton OR 97077
503-627-1593

Dr. John Hess
The Hebrew University of Jerusalem
706 N. 6th Avenue
Tucson AZ 85705
602-624-2243

Yu Hiresaki
Suzuki Shokan Company, Ltd.
2-8-52 Yoshinodai
Kwagoe, Saitama, Japan 350
0492-25-7551

Ryochi Hirose
Kobe Steel Ltd.
MIT NW-14 2508, 170 Albany St.
Cambridge MA 02139
617-253-4161

Bill J. Horsley
Ball Aerospace
P.O. Box 1062
Boulder CO 80306
303-939-6673

Prof. B.J. Huang
National Taiwan University
Dept. of Mechanical Engineering
Taipei, Taiwan 10764
02-363-0231 x2410

Charles A. Hull
GE Aerospace
French Road
Utica NY 13503
315-793-6382

Takashi Inaguchi
Central Research Lab/Mitsubishi Elec.
1-1, Tsukaguchi-Honmachi 8-Chome
Amagasaki, Hyogo, 661 Japan
06-497-7126

Donald Isaac
Lockheed Missiles and Space Co.
Research Lab/Dept. 92-40, Bldg. 205
Palo Alto CA 94304-1191
415-424-3350

Tim James, Ph.D.
STI
460 Ward Drive
Santa Barbara CA 93111-2310
805-683-7646

Dennis J. Janda
Astronautics Corp of America
Tech Center-5800 Cottage Grove Rd.
Madison WI 53716
608-221-9001

Sangkwon Jeong
MIT
77 Massachusetts Ave/Bldg. 41-208
Cambridge MA 02139
617-253-2273

Christopher I. Jewell
European Space Agency
P.O. Box 299, A.G. Noerdwijk
The Netherlands
(01719) 84309

Bradley Q. Johnson
Analytic Power Corp.
123 South Street
Boston MA 02111
617-542-6352

Dean L. Johnson
Jet Propulsion Laboratory
4800 Oak Grove Drive/M.S. 238-737
Pasadena CA 91109
818-354-1641

Bryan G. Jones
British Aerospace
FC 740, P.O. Box 5
Filton, Bristol BS127QW England
0272-368378

David A. Jones
The Aerospace Corporation
P.O. Box 92957, M/S M6-210
Los Angeles, CA 90009-2957
213-416-7183

Howard W. Jones
Mechanical Technologies Ltd.
968 Albany-Shaker Road
Latham NY 12110
518-785-2118

Peter F. Jones
The Aerospace Corporation
P.O. Box 9045
Albuquerque NM 87119
505-844-9969

Chad Joshi
American Superconductor Corp.
149 Grove Street
Watertown MA 02172
617-923-1122

Frank J. Kadi
Leybold Vacuum Products, Inc.
5700 Mellon Road
Export PA 15632
412-325-6547

Yoon-Myung Kang
Daikin Industries, Ltd.
3 Miyukigaoka
Tsukuba, Ibaraki, 305 Japan
298-58-5001

Ali Kashani
Sterling Federal Systems
NASA-Ames Research Ctr./M.S. 244-10
Moffett Field CA 94035
415-604-3663

Masakuni Kawada
Electrotechnical Laboratory
1-1-4, Umezono, Tsukuba-Shi
Ibaraki, 305 Japan
0298-58-5701

Thomas G. Kawecki
Naval Research Lab Code 8241
4555 Overlook Avenue
Washington DC 20375-5000
202-767-2851

Peter J. Kerney
CTI-Cryogenics
266 Second Avenue
Waltham, MA 02254
617-622-5391

Chi Shing Keung
Philips Laboratories
345 Scarborough Road
Briarcliff Manor NY 10510
914-945-6124

Katsunari Kikuchi
Sumitomo Heavy Industries, Ltd.
1 Kanda Mitoshiro-Cho, Chiyoda-Ku
Tokyo 101
03-233-9595

Glenn E. Kinard
Air Products & Chemicals, Inc.
7201 Hamilton Blvd.
Allentown PA 18195-1501
215-481-7902

Kenneth A. King
American Superconductor Corp.
149 Grove Street
Watertown MA 02172
617-923-1122

Peter Kittel
NASA
M.S. 244-10 Ames
Moffett Field CA 94035
415-604-4297

Richard Konian
IBM
Dept. A75, Bldg. 701, P.O. Box 950
Poughkeepsie NY 12602
914-435-1347

Stephen F. Kral
Astronautics Tech. Center
5800 Cottage Grove Rd.
Madison WI 53716
608-221-9001

George A. Kuhr
Hughes Aircraft
P.O. Box 902
El Segundo CA 90245
213-616-8926

Robert R. Lambert
General Electric Company
P.O. Box 915
Blue Bell PA 19422
215-354-7501

William N. Lawless
Ceramphysics, Inc.
921 Eastwind Drive/Suite 110
Westerville OH 43081
614-882-2231

David P. Laycock
RSRE Mod Pe
St. Andrews Road, Malvern
WORCS WR14 3PS England
0684 89-4936

Dr. Otto C. Ledford
Advanced Technology
222 N. Sepulveda Blvd., Suite 1310
El Segundo CA 90245
213-640-1050

Jeffrey H. Lee
Ball Aerospace
P.O. Box 1062, M.S. RA-3
Boulder CO 80306
303-939-5457

Daniel Lehrfeld
Magnavox Electro-Optical Systems
46 Industrial Avenue
Mahwah NJ 07430
201-529-1700

Robert M. Lerner
MIT Lincoln Lab
244 Wood Street
Lexington MA 02173-9108
617-981-2678

James M. Lester
Ball Aerospace Systems Division
P.O. Box 1062
Boulder CO 80306
303-939-4452

Robert Levenduski
Ball Aerospace Systems Group
P.O. Box 1062
Boulder CO 80308-1062
303-939-4194

James R. Lhota
The Aerospace Corp.
P.O. Box 92957 M2/248
Los Angeles CA 90009
213-336-5298

Anthony G. Liepert
Boreas, Inc.
175-U New Boston Street
Woburn MA 01801
617-937-9080

Dr. William A. Little
MMR Technologies Inc.
1400 North Shoreline Blvd/Suite A-5
Mountain View CA 99043
415-962-9620

Ralph C. Longworth
APD Cryogenics Inc.
1833 Vultee Street
Allentown PA 18103
215-791-6708

Chi Wun Lu
Taiwan University, Mechanical Eng.
National Taiwan University
Taiwan, R.O.C.

Jill Ludwigsen
Nichols Research Corp.
2201 Buena Vista SE, Suite 203
Albuquerque NM 87106
505-845-7364

James F. Maguire
Applied Eng. Technologies Ltd.
10 Tower Office Park, Suite 420
Woburn MA 01801
617-932-3221

Frithjof N. Mastrup
Hughes Aircraft Co.
2000 E. El Segundo Blvd/P.O. Box 902
El Segundo CA 90245
213-616-9647

Yoichi Matsubara
Nihon University
Atomic Energy Research Institute
Funabashi Chiba, 274 Japan
0474-69-5374

Ben-Zion Maytal
Univ. of Wisconsin-Madison
1500 Johnson Dr., Bldg. 811
Madison WI 53706
608-263-2141

Frank E. McCrea
Varian Associates
3560 Bassett Street
Santa Clara CA 95054-2704
408-496-2270

Kathleen M. McDermott
NIST
325 Broadway, MS 583.3
Boulder CO 80303
303-497-3952

James P. McGuire
NASA
Goddard Space Flight Center
Huntsville AL 20771
301-286-9170

Edward R. McLaughlin
Smithsonian Institute
60 Garden Street
Cambridge MA 02142
617-495-7362

Henry Meehan
Magnavox
46 Industrial Way
Mahwah NJ 07430
201-529-1700

Franc Megujar
Institut "Zoran Rant"
Kidriceva 66A
Skofja Loka, Yugoslavia
064-631-251

Gorken Melikian
United Technologies Research Ctr.
411 Silver Lane
E. Hartford CT 06108
203-727-7554

Janice Meredith
Lucas Aerospace
Shaftmoor Lane, Hall Green
Birmingham, B28 8SW, U.K.
011-21-707-7111

Grant Milbouer
Magnavox
46 Industrial Avenue
Mahwah NJ 07430-0615
201-529-1700

John Lester Miller
Martin Marietta
P.O. Box 179, M/S L8030
Denver CO 80201
303-971-6945

Archer Mitchell
Westinghouse Electric
10706 Eastwood Avenue
Silver Spring MD 20901
301-765-7232

Matthew Mitchell
Mitchell Stirling Machines Systems
2550 Ninth Street, Suite 207B
Berkeley CA 94710
415-845-2528

Raymond Moore
Koch Process Systems
20 Walkup Drive
Westboro MA 01581
508-898-0374

Timothy P. Moran
Astronautics Lab. RKL8
Edwards AFB CA 93523
805-275-5610

William C. Mulrone
Inst. for Defense Analysis
1801 N. Beauregard St.
Alexandria VA 22311
703-578-2746

Dwight M. Munk
ICI Advanced Materials
Wilmington DE 19897
302-886-3858

Hiroshi Nagano
Toyama University
3190 Gofuku Toyama 930
Toyko, Japan
0764-41-1271

Charles S. Naiman
Ice, Inc.
160 Lancaster Terrace
Brookline MA 02146
617-277-4184

Hideki Nakagome
Toshiba Corporation
4-1 Ukishima-Cho
Kawasaki-Ku, 210 Japan
044-288-8019

Ram Narayan
Magnavox
46 Industrial Avenue
Mahwah NJ 07430
201-529-1700

Rob E. Nast
Loral Fairchild Imaging Sensors
1801 McCarthy Blvd.
Milpitas CA 95035
408-433-2534

Theodore C. Nast
Lockheed Research Laboratory
3251 Hanover St./MS 92-40 Bldg. 205
Palo Alto CA 94304-1187
415-424-2401

Neno T. Nenov
UCIG-Linde
P.O. Box 44
Tonawanda NY 14150
716-879-2738

Martin Nisenoff
Naval Research Laboratory
4555 Overlook Rd., S.W. Code 6850.1
Washington DC 20375-5000
202-767-3099

Robert H. Norman
Allied-Signal Aerospace, Air Research
Los Angeles Division
2525 W. 190th Street, P.O. Box 2960
Torrance CA 90509
213-512-3343

Michael G. Norris
MIT
77 Massachusetts Ave/Rm 41-203
Cambridge MA 02139
617-253-2257

Dr. Takenori Numazawa
National Research Inst. for Metals
NW14-2508, MIT/FBNML
Cambridge MA 02139
617-253-4185

Rodney L. Oonk
Ball Aerospace Systems
P.O. Box 1062
Boulder CO 80306
303-939-4449

Anna H. Orłowska
Rutherford Appleton Laboratory
Chilton, Didcot Oxon OX110QX
U.K.
(0) 235 821900 x5717

Andrew P. Owen
Kollmorgen EOI
18 Bradco St.
Keene NH 03431
603-357-2582

Dr. Gottfried Pahler
AEG Aktiengesellschaft
Nachtsichtkomponenten Postfach 1134
D-7100 Heilbronn, Germany
7131/621299

Keith M. Parker
General Electric Company
3001 W. Radio Drive/P.O. Box F-23
Florence SC 29501
803-664-1650

Hsien-Sheng Pei (Jason)
Digital Equipment Corporation
30 Forbes Rd./M.S. NR05/J2
Northboro MA 01532
508-351-4913

Laurence B. Penswick
Stirling Technology Co.
2952 George Washington Way
Richland WA 99352
509-375-4000

Glen G. Pfeleiderer
Intermagnetics General Corporation
8 Robin Drive
Voorheesville NY 12186
518-765-2006

John R. Phillips
Harvey Mudd College, Eng. Clinic
260 E. Foothill Blvd.
Claremont CA 91711
714-621-8020

Michael J. Pickett
Koch Process Systems, Inc.
20 Walkup Drive
Westborough MA 01581-5003
508-898-0369

Richard L. Plambeck
University of California
Radio Astronomy Lab
Berkeley CA 94720
415-642-3441

David L. Potts
JSA International
1100 Massachusetts Ave.
Cambridge MA 02138
617-876-3838

Jerry W. Prentice
General Pneumatics Corporation
7662 E. Gray Rd, Suite 107
Western Research Center
Scottsdale AZ 85260
602-998-1856

Kenneth D. Price
Hughes Aircraft
2000 E. El Segundo Blvd.
El Segundo CA 90245
213-616-6863

Robert E. Priest
LLNL
7000 East Ave./P.O. Box 808, L-287
Livermore CA 94550
415-422-8677

Nachman Pundak
Ricor Ltd.
En Harod (IHUD)
Israel 18960
972-6-531703

Jeff R. Raab
TRW S&TG
One Space Park/M.S. 01/2070F
Redondo Beach CA 90278
213-404-0405

Dr. Ray Radebaugh
NIST
325 Broadway
Boulder CO 80303
303-497-3710

John F. Rasmussen
Lorel Infrared & Imaging Systems
2 Forbes Road
Lexington MA 02173
617-863-4543

Wayne C. Ravlins
NIST
325 Broadway/M.S. 583.3
Boulder CO 80303
303-497-5251

Peter Riggle
Stirling Technology Company
2952 George Washington Way
Richland WA 99352
509-375-4000

Dr. James C. Ripley, P.E.
Airesearch Los Angeles Division
2525 W. 190th Street, P.O. Box 2960
Torrance CA 90504-6099
213-512-4586

Pat R. Roach
NASA Ames Research Center
MS 244-10
Moffett Field CA 94035
415-604-3191

Gerald F. Robertson
Carrier Corporation
Carrier Parkway/P.O. Box 4808
Syracuse NY 13221
315-432-6287

George Robinson
19 Hemlock Lane
Acton MA 01720
508-263-4643

Ronald G. Ross
Jet Propulsion Laboratory
4800 Oak Grove Dr./M.S. 157-102
Pasadena CA 91109
818-354-9349

Robert T. Ruggeri
Boeing Aerospace & Electronics
P.O. Box 3999
Seattle WA 98124
206-773-8438

Carl J. Russo
American Semiconductor Corp.
149 Grove Street
Westtown MA 02172
617-923-1122

Samuel Russo
Hughes Aircraft Company
Bldg E55/M.S. 6232/P.O. Box 902
El Segundo CA 90245
213-616-9651

Roger D. Scarlotti
Bair Aerospace Systems Group
P.O. Box 1062
Boulder CO 80308-1062
303-939-5319

Richard L. Schapker
S2 Corporation
134 Farnum Street
N. Andover MA 01845
508-689-3973

Steve Schnurer
GE Medical Systems
3001 W. Radio Dr./P.O. Box F-23
Florence SC 29501
803-664-1648

James Gary Seyster
Allied-Signal
2525 W. 190th Street
Torrance CA 90509
213-512-2098

Julia I. Sheldon
Aerojet Electrotic Systems
1100 W. Hollyvale St./P.O. Box 296
Azusa CA 91702
818-812-1624

Neil I. Sherman
Aerojet Electrosystems
1100 W. Hollyvale St./P.O. Box 296
Azusa CA 91072
818-812-2698

William R. Shields
Janis Research, Inc.
2 Jewel Drive
Wilmington MA 01887
508-657-8750

Robert Shull
NIST
Bldg. 223, Room B150
Gaithersburg MD 20899
301-975-6035

Bill G. Simmons
Stirling Technology Company
2952 George Washington Way
Richland WA 99352
509-375-4000

Herbert Sixsmith
Create, Inc.
P.O. Box 71
Hanover NH 03755
603-643-3800

Matthew M. Skertic
Hughes Aircraft Co.
8433 Fallbrook Ave./Bldg. 270/M.S. 071
Canoga Park CA 91304
818-702-1566

Scot A. Slimon
General Dynamics
2 Oslo Street
Mystic CT 06355
203-433-2217

Joseph L. Smith, Jr.
MIT
77 Massachusetts Ave./Rm 41-204
Cambridge MA 02139
617-253-2296

Leroy M. Sparr
NASA/GSFC
Code 713.4
Greenbelt MD 20771
301-286-3811

W. Dodd Stacy
Create Inc.
P.O. Box 71
Hanover NH 03755
603-643-3800

Walter F. Stewart
Los Alamos National Lab
P.O. Box 1663/M.S. J576
Los Alamos NM 87545
505-665-1416

George Staubs
Dowty Weapon Systems
Sully Road/P.O. Box 5000
Sterling VA 22170
703-450-8296

Michael Superczynski
David Taylor Research Center
Code 2712
Annapolis MD 21402-5067
301-267-2149

Dr. Greg W. Swift
Los Alamos National Lab
P.O. Box 1663/M.S. K764
Los Alamos NM 87545
505-665-0640

Walter L. Swift
Create, Inc.
P.O. Box 71
Hanover NH 03755
603-643-3800

John A. Talbourdet
Loral Infrared & Imaging Systems
2 Forbes Road
Lexington MA 02173
617-863-3107

John Taylor
Polyflex Airtech/England U.K.
36, Cheltenham Trade Park, Arle Rd.
Cheltenham Glos GL51 8LZ
011-44-242-228878

Silas Teigland
Litton ILSD
2734 Hickory Grove, P.O. Box 4508
Davenport, IA 52808
319-383-6215

Ray Tervo
Clifton Precision
P.O. Box 4508
Davenport IA 52808-4508
319-383-6396

Niranjan Thatte
University of California, Berkeley
601 Campbell Hall
Berkeley CA 94720
415-643-6425

Peter J. Thomas
AFSTC/SWS
Kirtland AFB NM 87117
505-846-5803

Klaus Timmerhaus
University of Colorado/Chem. Engrg.
Campus Box 424
Boulder CO 80903
303-492-7680

Jesse D. Timmons
Bionetics Corporation
NASA Headquarters Code SED
Washington DC 20543
202-453-1750

Russell C. Tipton
Forma Scientific
Millcreek Road, P.O. Box 649
Marietta OH 45750
614-374-1863

Sasaki Toshiaki
Missho Iwai American Corp.
One Cambridge Center
Cambridge MA 02142
617-577-7260

Martin C. Trively
CECOM/NVEOL
Attn: AMSEL-RD-STD-ICT
Ft. Belvoir VA 22060-5677
703-664-1345

Emanuel Tward
TRW Space and Technology Inc.
R1/1126, One Space Park
Redondo Beach CA 90270
213-814-0409

Costas C. Tzemos
CVI Incorporated
P.O. Box 2138
Columbus OH 43216
614-876-7381

Javier A. Valenzuela
Create Inc.
Etna Road, P.O. Box 71
Hanover NH 03755
603-643-3800

Joseph P. Wachter
Ford Aerospace
3825 Fabian Way, MS/G79
Palo Alto CA 94303
415-852-5631

Philipp Wagner
Wagner Systems (PTY) Ltd.
P.O. Box 117, Plumstead 7800
South Africa
021-758011

Warren D. Waldron
Mechanical Technology Inc.
968 Albany Shaker Road
Latham NY 12110
518-785-2299

Graham Walker
University of Calgary
2500 University Drive N.S.
Calgary, Alberta, Canada T2N 1N4
403-220-5772

David A. Wallace
Stirling Technology Company
2952 George Washington Way
Richland WA 99352
509-375-4000

Joseph D. Walters
David Taylor Research Center
Code 2712
Annapolis MD 21402-5067
301-267-3632

Robert E. Warren
Hughes Aircraft Co.
P.O. Box 902 EO/EO1/C173
El Segundo CA 90245
213-616-9530

Alan Weeks
CTI-Cryogenics Inc.
266 Second Avenue
Waltham MA 02254-9171
617-622-5384

Harold Weinstock
AFSOR/NE
Bolling Air Force Base
Washington DC 20332-6448
202-767-4934

Ron White
Air Force Wright Aeronautical Labs
WRDC/FIVEA
Wright Patterson AFB OH 45433-6553
513-255-6078

Richard J. Williams
Aerojet Electronic Systems Div.
1100 W. Hollyvale St./P.O. Box 296
Azusa CA 91702
818-812-1864

William E. Wyche
AFSTC/SWS
Kirtland AFB NM 87117
505-846-5803

Ran Yaron
31 Mass. Ave.
Boston MA 02115
617-247-2019

Steven Glenn Zylstra
General Pneumatics Corporation
7662 E. Gray Road, Suite 107
Scottsdale AZ 88260
602-998-1886